



**Sediment transport in turbidity currents: internal
structure and flow energetics**

Sojiro Fukuda

**Submitted in accordance with the requirements for the degree of
Ph.D. Geography**

**The University of Hull
Faculty of Science and Engineering
Energy and Environment Institute**

December 2023

Abstract

This project investigates the material-transport dynamics of natural-scale turbidity currents. The sediment-laden gravity-driven flows are a dominant control on the sediment transport between continents and deep marine systems. The resulting sediment architectures are expected to record the previous millennia of environmental events such as tectonic events or relative sea-level changes. In spite of their importance as paleo-environmental record, and a key geohazard, their dynamics are still poorly constrained due to the limitations of observation, computational costs, and the destructive nature of turbidity currents. Indeed, key knowledge gaps include the internal structures and flow energetics of turbidity currents, which dictate the dynamics and thus sediment transport mechanics and deposits of such flows.

Data compilation and laboratory-scale experiments of turbidity currents, on which this work is based, have been conducted. The velocity and density profiles of pseudo-steady flows were gathered from laboratory experiments and natural-scale events to investigate the key factors that control the vertical flow structure. Laboratory experiments were designed to fill the gaps between the compiled data from the past literature and provide high-resolution observations.

The statistical analysis of pseudo-steady turbidity currents' compiled velocity and concentration profiles provides valuable insights into the material-transport dynamics. The empirical models for predicting flow velocity and concentration profile of turbidity currents are developed using machine learning techniques. Implications of the analysis and the developed models are that the internal structures of turbidity currents enhance their material-transport efficiency as the flow is decelerated.

The theoretical analysis of the energetics of turbidity currents revealed that the previous fluvial-based energetics theory significantly underestimated the sediment-load capacity of turbidity currents. The direct implication is that the traditional micro-scale turbulent energy production cannot explain the energetics of gravity currents.

To conclude, the findings of this thesis contribute to a better understanding of the material-transport dynamics of turbidity currents, identifying useful research areas for future works.

Intellectual Property

The candidate confirms that the work submitted is his/her own and that appropriate credit has been given where reference has been made to the work of others.

This copy has been supplied on the understanding that it is copyright material and that no quotation from the thesis may be published without proper acknowledgement.

© 2023 The University of Hull, Sojiro Fukuda

Acknowledgements

I wish to express my profound gratitude to the individuals and institutions whose support and contributions have made this work possible.

First and foremost, my heartfelt thanks go to my team of supervisors—Prof. Robert Dorrell, Assoc. Prof. Hajime Naruse, Dr. Elena Bastianon, Dr. Edward Skevington, Prof. Bill McCaffrey, and Prof. Daniel Parson. I am truly grateful for the opportunity they granted me and for their steadfast support throughout this project. Their patience, guidance, and support, both technically and emotionally, have been invaluable. Special gratitude to Prof. Robert Dorrell for his enduring patience and support as the main supervisor.

I extend my sincere appreciation to Assoc. Prof. Hajime Naruse for his support during a particularly challenging period, even from Japan. To Dr. Elena Bastianon, I am grateful for your support from the start of my project. Your guidance has been pivotal to its success. Dr. Edward Skevington, I appreciate your numerous technical insights and intensive support in drafting papers and the thesis. Prof. Bill McCaffrey, thank you for imparting not only scientific knowledge but also valuable English phrases and expressions. Prof. Daniel Parson, your constant support and encouragement have been truly motivating.

I also extend my thanks to all members and staff of the Energy and Environment Institute for their daily support, administrative assistance, and for maintaining a conducive studying environment in the university. My gratitude extends to the Turbidite Research Group (TRG) members for organising insightful events, meetings, and conferences that provided valuable geological perspectives. I want to express my appreciation to Dr. Brandon Murphy and the Total Environmental Simulator (TES) staff in The DEEP for allowing me to use the facility and for their intensive support during the flume experiments. Brandon's expertise was indispensable in designing and executing the flume experiments.

To my wife, Ami, thank you for your support throughout this project. Your decision to accompany me to the UK, facing numerous challenges, reflects our shared belief that these difficulties will transform into cherished memories. Embarking on a PhD may have been a personal decision, but moving forward, I am dedicated to devoting my life to you.

Contents

1	Introduction	1
1.1	Turbidity Currents	1
1.2	Theoretical Model	2
1.2.1	Navier-Stokes Equations	2
1.2.2	Reynolds-Averaged N-S Equation	4
1.2.3	Non-Dimensional Flow Characterisation	6
1.2.4	Turbulence Models	7
1.2.5	Rouse profile	9
1.2.6	Depth average Shallow water model	10
1.3	Mechanics of Turbidity Currents	13
1.3.1	Initiation	13
1.3.2	Anatomy of Turbidity Currents	15
1.3.3	Vertical Profile of Turbidity Currents	18
1.3.4	Relation between vertical profile and flow behaviour	21
1.3.5	Long-runout Turbidity Currents	21
1.3.6	Suspended load transport models	26
1.3.7	Sediment Deposition and Flow Properties	28
1.4	Morphology of Submarine Fan System	29
1.4.1	Morphology of Submarine Channel-levee System	31
1.4.2	Development of Channel-levee Systems	33
1.4.3	Flow Behaviour in Submarine Channels	34
1.5	Discussion	34
1.5.1	Significance of Flow Stratification	34
1.5.2	Equilibrium state of turbidity currents	36
1.6	Aim and research questions	37

2	Flume Experiment and Data Collection	39
2.1	Introduction	39
2.2	Data collection	39
2.2.1	Online data source	39
2.2.2	Estimation of characteristic flow parameters	43
2.3	Flume experiments	58
2.3.1	Experiment configuration	59
2.3.2	Velocity measurement	60
2.3.3	Particle-size distribution analysis	75
2.3.4	Monitoring of bed profile	91
3	Vertical Flow Structure	103
3.1	Introduction	103
3.2	Existing models for flow concentration profile	107
3.3	Characterisation of the vertical flow concentration profile	109
3.3.1	Methods	109
3.3.2	Results	121
3.4	Parameterisation of streamwise velocity profile	127
3.4.1	Correlation between the velocity and sediment concentration profiles	127
3.4.2	Prediction of velocity profiles	132
3.4.3	Validation of the prediction of the velocity profiles	135
3.5	Discussion	135
3.5.1	Significance of the natural-scale datasets for understanding velocity and concentration profiles of turbidity currents	135
3.5.2	Correlation between velocity and concentration profiles	136
3.5.3	Governing parameters for velocity and concentration profiles	137
3.5.4	Implications for material transport efficiency of turbidity currents	145
3.6	Conclusion	149
4	Sediment Transport Capacity of Long-runout Turbidity Currents	150
4.1	Statement and author contributions	150
4.2	Introduction	150
4.3	Data reduction	153
4.4	Turbidity current capacity	155
4.5	Discussion	158
4.5.1	Energy balance of TKE	158

5 Conclusion	166
5.1 Achievements	166
5.1.1 Flume experiments and data compilation	166
5.1.2 Time-averaged vertical flow concentration profile of turbidity currents	167
5.1.3 Time-averaged vertical flow velocity profile of turbidity currents	168
5.1.4 The energetics of turbidity currents	169
5.2 Implication of the results	170
5.2.1 Long-runout of turbidity currents	170
5.2.2 Material transport mechanics of turbidity currents	171
5.3 Future works	172
A Appendix Chapter	175
A.1 Drag coefficient	175
A.2 Flow power plot	176
A.3 Curve Fitting	178
References	181

List of Figures

1.1	Schematic diagram of turbidity currents	15
1.2	Lobe-and-cleft structure of turbidity currents	17
1.3	Vertical profiles of gravity currents and jet streams	20
1.4	Velocity profiles over different ratios of stratification types	20
1.5	Water entrainment functions	24
1.6	Schematic diagram of depositional sequence of turbidite	28
1.7	Acceleration matrix	29
1.8	Schematic illustration of submarine fan system	30
1.9	Schematic illustration of submarine channel-levee system (Nakajima and Kneller, 2013)	31
2.1	Schematic diagram of interpolation and extrapolation procedures	44
2.2	Interpolated and extrapolated flow profiles of the non-conservative flows	45
2.3	Interpolated and extrapolated flow profiles of the conservative flows	46
2.4	Time series of processed velocity fields of Congo events	50
2.5	Depth-averaged flow parameters of Event 01	51
2.6	Depth-averaged flow parameters of Event 04	52
2.7	Depth-averaged flow parameters of Event 05	53
2.8	Time-averaged vertical profiles of Congo's events	54
2.9	Log-log plot of layer-averaged flow concentration and initial concentration of the sediment-water mixture in the mixing tank of each experiment	55
2.10	Estimation of LDM-based particle size distribution from SHM	57
2.11	Schematic illustration of the flume setup for the experiments	58
2.12	UVP configuration	60
2.13	UVP time series data for Run 01	61
2.14	UVP time series data for Run 02	62
2.15	UVP time series data for Run 03	63
2.16	UVP time series data for Run 04	64

2.17 UVP time series data for Run 05	65
2.18 UVP time series data for Run 06	66
2.19 UVP time series data for Run 07	67
2.20 UVP time series data for Run 08	68
2.21 UVP time series data for Run 09	69
2.22 UVP time series data for Run 10	70
2.23 UVP time series data for Run 11	71
2.24 UVP time series data for Run 12	72
2.25 Turbulence analysis of Run 01	76
2.26 Turbulence analysis of Run 02	77
2.27 Turbulence analysis of Run 03	78
2.28 Turbulence analysis of Run 04	79
2.29 Turbulence analysis of Run 05	80
2.30 Turbulence analysis of Run 06	81
2.31 Turbulence analysis of Run 07	82
2.32 Turbulence analysis of Run 08	83
2.33 Turbulence analysis of Run 09	84
2.34 Turbulence analysis of Run 10	85
2.35 Turbulence analysis of Run 11	86
2.36 Turbulence analysis of Run 12	87
2.37 Particle size distribution in each run	88
2.38 Concentration measurement of each run	89
2.39 Schematic of peristaltic pump	90
2.40 Monitoring of aggradation rate in Run 01	91
2.41 Monitoring of aggradation rate in Run 02	92
2.42 Monitoring of aggradation rate in Run 03	93
2.43 Monitoring of aggradation rate in Run 04	94
2.44 Monitoring of aggradation rate in Run 05	95
2.45 Monitoring of aggradation rate in Run 06	96
2.46 Monitoring of aggradation rate in Run 07	97
2.47 Monitoring of aggradation rate in Run 08	98
2.48 Monitoring of aggradation rate in Run 09	99
2.49 Monitoring of aggradation rate in Run 10	100
2.50 Monitoring of aggradation rate in Run 11	101
2.51 Monitoring of aggradation rate in Run 12	102

3.1	Comparison between top-hat and stratified flow profiles	106
3.2	The visualisation of the shape factor ξ_ϕ based on the generalised Schlick's bias and gain function	115
3.3	Correlation of dimensionless parameters and fit parameters	117
3.4	Correlation of dimensionless parameters and fit parameters	118
3.5	Examples of curve fitting with different functions	124
3.6	Validation of the model with laboratory-scale data	126
3.7	Validation of the model with TYPE 1 data	128
3.8	Histogram of the height difference between velocity maximum and the inflection point of concentration profile	129
3.9	Scatter plots between the velocity maximum height and the inflection point of flow concentration	130
3.10	Velocity over concentration profiles	132
3.11	Model Validation of the flow velocity profile	133
3.12	Model Validation of the flow velocity profile	134
3.13	Shape variation of the concentration and velocity profile models	136
3.14	Fr_d dependency for the velocity and concentration profiles	138
3.15	Fr_d dependency for the velocity and concentration profiles	139
3.16	Dependency on β for the flow velocity and concentration profiles	141
3.17	Dependency on <i>beta</i> for the flow velocity and concentration profiles	142
3.18	Validation of the model with laboratory-scale data	143
3.19	Validation of the model with Congo test data	144
3.20	Froude and Rouse number dependency of weighting terms	147
4.1	Drag coefficient, C_D and densimetric Froude number, Ri of the compiled turbidity current data	154
4.2	Data reduction based on near-equilibrium thresholds	154
4.3	Sediment transport capacity for open-channel flows and turbidity currents	156
4.4	The turbulent flux coefficient, Γ as a function of Φ	158
4.5	Log-log plot of depth-integrated total production of TKE, against log-law production rate, $P_{II} = u_*^2 U$	159
4.6	Internal Energetics of gravity currents	162
5.1	Schematic diagram of internal flow structures of turbidity currents	170
A.1	Log-log plot of the estimated drag coefficient (Eq. 1.62) verses the top-hat drag coefficient (Parker et al., 1986) (Eq. A.1). The black dotted line represents the ideal linear line ($C_D = Rg\Phi hS/U^2$). The gray points indicate that those data points are excluded by the near-equilibrium criteria (Fig. 2 in the main text).	175

A.2 Sediment transport capacity for gravity currents without data reduction. Sediment concentration, Φ , versus dimensionless flow power, P_f/N_f for: a) all gravity current data with the log-law production term, P_f ; b) all gravity current data with the top-hat production term, P_{th} . Throughout, dilute, transitional and hyperconcentrated regimes are separated by gray solid lines. Parametric correlations of concentration and dimensionless flow power are depicted by black dotted curves. Symbol shapes as per Figure 1 in the main text.	177
---	-----

List of Tables

2.1	Summary of compiled sources	41
2.2	Experimental conditions	59
2.3	UVP configuration	60
3.1	Summary of compiled source	112
3.2	The candidate models of s_1 of the Congo-included model	122
3.3	The candidate models of s_2 of the Congo-included model	122
3.4	The candidate models of s_1 of the lab-included model	123
3.5	The candidate models of s_2 of the lab-included model	123
4.1	Fitted power-law correlation results	155
A.1	Summary of the compiled fluvial source.	178

Nomenclature

B	Buoyancy production term
N	Normalised buoyancy production term $N = B/\Phi$
R	specific gravity ($R = (\rho_s - \rho_a)/\rho_a$)
C_D	Drag coefficient
e_w	water entrainment function
E_z	diffusion coefficient
Fr_d	Densimetric Froude number
g	gravitational acceleration
\mathbf{g}	vector of gravity acceleration
G_i	gravitational potential energy
h	flow depth
K	depth-averaged turbulent kinetic energy
\mathbf{n}	Normal vector to a given surface
P	Total production of Turbulent Knetic Energy
p	pressure term
r_0	concentration ratio between the depth-averaged and the near-bed concentrations
Re	Reynolds number
Ri	Richardson number

S	Slope
S_c	Surface area of control volume
U	Depth-averaged streamwise flow velocity
\mathbf{u}	3-D velocity vector
u_i	velocity component of the i th direction
u_*	shear velocity
V	Depth-averaged vertical flow velocity
V_c	Control volume
w_s	particle settling velocity
x_i	coordinate of the i th direction
α	dimensionless coefficients of equations
β	Rouse number
δ_{ij}	Kronecker delta
ε	viscous dissipation of Turbulent Kinetic Energy
κ	von Karman coefficient
∇	nabla operator
ν	Kinematic viscosity
Φ	Depth-averaged volumetric flow concentration
ϕ	volumetric flow concentration
ρ_a	ambient water density
$\rho\Delta$	density difference between the ambient fluid, ρ_a and the flow, ρ_f
ρ_f	flow density
ρ_s	density of sediment particles
$\rho\Delta$	Buoyancy of the flow

$\tilde{\rho}$	Dimensionless flow density ($\tilde{\rho} = \rho_f/\rho_a$)
τ	shear stress
τ_b	bed shear stress
ξ_ϕ	structure function of flow concentration
ξ_u	structure function of streamwise flow velocity

Chapter 1

Introduction

1.1 Turbidity Currents

Turbidity currents, a type of submarine density flow, are one of the most important sediment-transport processes on Earth (Elmore et al., 1979; Piper et al., 1999; Wynn et al., 2002c; Meiburg and Kneller, 2010b). They are a primary mechanism for transporting sediment, nutrients, and pollutants from shallow to deep marine system (Pohl et al., 2020; Wells and Dorrell, 2021). Turbidity currents can traverse over 1000 km and transport over 100 km³ of sediment in a single event (Piper et al., 1999; Rothwell et al., 1998; Talling et al., 2007; Babonneau et al., 2010), yet the sediment-transport mechanism of these currents is still poorly understood. Submarine fans, a complex of the deposits from multiple density flows, are some of the largest and thickest sediment accumulations on the Earth's surface (Bouma et al., 1985; Nilsen, 2007). The huge complex of sediments can be an archive of, for example, past tectonic, biological, and climatic processes (Weimer and Link, 1991; Stow and Mayall, 2000; Covault, 2011). For instance, disastrous natural phenomena such as earthquakes can be an initiation factor of turbidity currents and thus, their deposits might record such events (e.g. Goldfinger et al., 2007). In addition, since the porosity of the deposits in submarine fans is relatively higher than the surrounding sediments, they can also be a potential oil and gas reservoir (Weimer and Link, 1991; Stow and Mayall, 2000; Covault, 2011).

When it comes to the management of geohazard risk, the destructive nature of turbidity currents means they pose a significant risk to marine infrastructure such as telecommunications and petroleum production facilities (Bruschi et al., 2006; Clare et al., 2015). Therefore, the understanding of submarine density flows from their initialization to their deposition is an important subject from scientific industrial and risk management perspectives. Here, the aim of this PhD project is a better understanding of the flow dynamics of turbidity currents, focusing on their energetics and material-transport mechanism.

1.2 Theoretical Model

Modelling represents a fundamental approach in enhancing our comprehension of natural phenomena. It simplifies the complexity of these phenomena into more manageable forms and allows us to make predictions. In this study, the focus is to develop a comprehensive model designed to predict the internal flow dynamics of turbidity currents. To achieve this, we will delve into existing theoretical models, particularly those derived from the Navier-Stokes equations. This exploration is crucial not only for understanding the foundational principles and methodologies employed in previous modelling but also for identifying the knowledge gaps.

The highest resolved numerical simulation which directly solves the Navier-Stokes equations numerically is called DNS (Direct Numerical Simulation). DNS requires the mesh size which is small enough to capture the smallest eddy in the target phenomenon. Thus, for a strongly turbulent flow, it requires vast number of grid points which makes it extremely computationally expensive. Therefore, researchers commonly use assumptions to introduce simple models of turbulence (e.g. Argyropoulos and Markatos, 2015, and the references therein), which provides methods for the practical prediction to advance understanding of fluid dynamics.

1.2.1 Navier-Stokes Equations

The Navier-Stokes equations are a description of the momentum conservation of viscous fluid (e.g. Navier, 1823; Stokes, 1845). Previously, the motion of fluid was approximated by the equations for ideal fluid, the Euler equation (Euler, 1755). By adding the viscous term to the Euler equations, the Navier-Stokes equations are achieved. The Navier-Stokes equations can be derived using the mass and momentum conservation of a control volume of fluid. Firstly, the equation of mass conservation can be derived considering a control volume of viscous fluid and its total advection. Using Gauss' theorem, the mass conservation can be described as,

$$\begin{aligned} \frac{\partial}{\partial t} \iiint_{V_c} \rho_f dV_c &= - \iint_{S_c} \rho_f \mathbf{u} \cdot \mathbf{n} dS_c \\ &= - \iiint_{V_c} \nabla \cdot (\rho_f \mathbf{u}) dV_c \end{aligned} \quad (1.1)$$

where ρ_f is the density of fluid and $\mathbf{u} = (u_1, u_2, u_3)$ is the three-dimensional velocity vector. Here the coordinate system is $\mathbf{x} = (x_1, x_2, x_3)$ in which x_1 is allocated to the streamwise direction and x_3 is allocated to the direction that is perpendicular to the bottom surface and streamwise direction. dS_c is small area on the surface of the control volume V_c . The equation (1.1) must be satisfied regardless of the size of the control volume, thus,

$$\frac{\partial \rho_f}{\partial t} + \nabla \cdot (\rho_f \mathbf{u}) = 0. \quad (1.2)$$

In the Lagrangian form, the equation (1.2) takes the form:

$$\frac{D\rho_f}{Dt} + \rho_f \nabla \cdot \mathbf{u} = 0 \quad \text{where} \quad \frac{D}{Dt} = \frac{\partial}{\partial t} + \mathbf{u} \cdot \nabla. \quad (1.3)$$

The equation (1.2) or (1.3) is called the equation of continuity. In the case of incompressible flow (discussed further below), since ρ_f is regarded as constant, only the advection term $\nabla \cdot \mathbf{u}$ will remain in equation (1.3).

Secondly, considering the total force which acts on the control volume, the momentum balance may be described as

$$\begin{aligned} \frac{D}{Dt} \iiint_{V_c} \rho_f \mathbf{u} \, dV_c &= \iiint_{V_c} \rho_f \mathbf{g} \, dV_c + \iint_{S_c} \mathbf{\Pi} \cdot \mathbf{n} \, dS_c \\ &= \iiint_{V_c} (\rho_f \mathbf{g} + \nabla \cdot \mathbf{\Pi}) \, dV_c \end{aligned} \quad (1.4)$$

where \mathbf{g} is the vector of gravity acceleration and $\mathbf{\Pi}$ is 3-D stress tensor that describes the surface forces which act on the control volume. The surface forces which act on viscous fluid are pressure and viscous friction. Here p denotes the pressure force which act on a unit area and λ and μ denote the bulk and dynamic viscosity coefficient respectively. Then, each component of $\mathbf{\Pi}$ can be written by (Stokes, 1845),

$$\Pi_{ij} = (-p + \lambda \nabla \cdot \mathbf{u}) \delta_{ij} + \mu \left(\frac{\partial u_i}{\partial x_j} + \frac{\partial u_j}{\partial x_i} - \frac{2}{3} \nabla \cdot \mathbf{u} \delta_{ij} \right) \quad (1.5)$$

where it is assumed that the stress of viscosity has a linear relationship with the velocity gradients. Stokes assumed that the bulk viscosity $\lambda = 0$ (Stokes' hypothesis) and from equation (1.4-1.5) and the Euler equation, obtained the momentum conservation of a viscous fluid (the Navier-Stokes equations)

$$\frac{D\mathbf{u}}{Dt} = \mathbf{g} - \frac{1}{\rho_f} \nabla p + \frac{1}{3} \nu \nabla (\nabla \cdot \mathbf{u}) + \nu \nabla^2 \mathbf{u} \quad (1.6)$$

where ν is the kinematic viscosity and given by μ/ρ_f .

In the case of the numerical models of turbidity currents, the currents can be assumed to be sufficiently dilute while they are traversing for a long distance ($\rho_a \langle \phi \rangle / \rho_f \ll 1$ where ρ_a denotes the standard fluid density; $\langle \phi \rangle$ denotes the sediment concentration), and particle-particle interaction can be regarded as negligible, which allows the use of the Boussinesq approximation (e.g. Bagnold, 1954; Parker et al., 1986; Kostic and Parker, 2006; Dorrell et al., 2013). The previous study of natural-scale turbidity currents (Simmons et al., 2020) observed several big events of super-dilute and pseudo-steady turbidity currents ($\langle \phi \rangle < 10^{-3}$) which last more than 5 to 10 days at Congo canyon. These observations also highlight the importance of a better understanding of the material-transport mechanics of pseudo-steady super-dilute turbidity currents. Having said that, it should be noted that turbidity currents can also be highly concentrated due to various reasons.

In such cases, the Boussinesq approximation cannot be applied. For instance, it has been implied (from rock records) that turbidity currents can drastically change its flow behaviour through entrainment of muddy sediment, increasing concentration and viscosity, so-called ‘Hybrid event’ or ‘flow transformation’ (e.g. Talling et al., 2004; Haughton et al., 2009; Kane et al., 2017). Those events mostly occur in the terminal lobes where the flow is rapidly decelerating or in the channel-lobe transition zone where the flow entrains large amount of muddy sediment due to the strong erosion during hydraulic jumps (e.g. Kane et al., 2017). Thus, although the Boussinesq approximation well represents the majority of the flow dynamics of turbidity currents, to fully consider the flow dynamics from the initiation to the deposition, the more complicated models for high-concentrated flows are required. Since those phenomena are out of scope of this study, hereafter, it is assumed that the flow is incompressible.

The Boussinesq approximation (Boussinesq, 1903) treats the flow as incompressible and of uniform density with the small variations in density only appearing in the gravitational forcing term. Under this approximation, the mass conservation of fluid (1.3) will be,

$$\nabla \cdot \mathbf{u} = 0, \quad (1.7)$$

and the momentum conservation for incompressible flow (1.6) takes following form:

$$\frac{D\mathbf{u}}{Dt} = \rho_{\Delta}\mathbf{g} - \frac{1}{\rho_a}\nabla p + \nu\nabla^2\mathbf{u}, \quad (1.8)$$

where $\rho_{\Delta} = (\rho_f - \rho_a)/\rho_a$ denotes the buoyancy of the flow. In Cartesian form, this may be expressed

$$\frac{\partial u_i}{\partial t} + u_j \frac{\partial u_i}{\partial x_j} = \rho_{\Delta} g_i - \frac{1}{\rho_a} \frac{\partial p}{\partial x_i} + \nu \frac{\partial^2 u_i}{\partial x_j \partial x_j}. \quad (1.9)$$

In the case of turbidity currents, the apparent gravity force is exerted by the density difference between flow ρ_f and ambient water ρ_a .

1.2.2 Reynolds-Averaged N-S Equation

DNS of the Navier-Stokes equations (1.8) is computationally expensive and is not practical for large scale phenomena such as turbidity currents. A common method to simplify the Navier-Stokes equations is to split the flow velocity into the ensemble-averaged value $\langle u \rangle$ and its turbulent part u' and similarly with the other components of velocity, the pressure, and the density. The equations governing these Reynolds-averaged quantities are called the Reynolds-Averaged Navier-Stokes (RANS) equations. First, the mean flow velocity

is defined as

$$\langle u \rangle = \int_{-\infty}^{\infty} u f(u) du, \quad (1.10)$$

where f denotes a probability density function. Then, the turbulent part, u' will be

$$u' = u - \langle u \rangle. \quad (1.11)$$

Next, the mean value of the product of two variables, for instance, $u_1 = \langle u_1 \rangle + u'_1$ and $u_2 = \langle u_2 \rangle + u'_2$ can be derived as follows.

$$\begin{aligned} \langle u_1 u_2 \rangle &= \langle (\langle u_1 \rangle + u'_1)(\langle u_2 \rangle + u'_2) \rangle \\ &= \langle u_1 \rangle \langle u_2 \rangle + \langle u_2 \rangle \langle u'_1 \rangle + \langle u_1 \rangle \langle u'_2 \rangle + \langle u'_1 u'_2 \rangle \\ &= \langle u_1 \rangle \langle u_2 \rangle + \langle u'_1 u'_2 \rangle \end{aligned} \quad (1.12)$$

where $\langle u'_1 u'_2 \rangle$ is not necessarily equal to zero while $\langle u'_1 \rangle = \langle u'_2 \rangle = 0$ by definition. By applying the equations (1.11) and (1.12) to (1.8), and considering the Reynolds-averaged equation, the RANS equation of momentum conservation is acquired,

$$\frac{D\langle u_i \rangle}{Dt} = \frac{1}{\rho_a} \frac{\partial}{\partial x_i} \left[\mu \left(\frac{\partial \langle u_i \rangle}{\partial x_j} + \frac{\partial \langle u_j \rangle}{\partial x_i} \right) - \langle p \rangle - (\rho_f - \rho_a) G_i \delta_{ij} - \rho_a \langle u'_i u'_j \rangle \right], \quad (1.13)$$

where G_i is the gravitational potential energy. Here, the momentum is transferred by three stress terms in the right-hand side of the equation: i) the viscous term, ii) isotropic pressure term, and iii) the apparent stress arising from the fluctuating velocity field. In Eulerian form, it may be written as

$$\frac{\partial \langle u_i \rangle}{\partial t} + \langle u_j \rangle \frac{\partial \langle u_i \rangle}{\partial x_j} = \rho_{\Delta} g_i - \frac{1}{\rho_a} \frac{\partial \langle p \rangle}{\partial x_i} + \frac{\partial}{\partial x_j} \left(\nu \frac{\partial \langle u_i \rangle}{\partial x_j} - \langle u'_i u'_j \rangle \right) \quad (1.14)$$

where $-\langle u'_i u'_j \rangle$ are referred as the Reynolds stress tensor. The components of $-\langle u'_i u'_j \rangle$ are

$$-\langle u'_i u'_j \rangle = \begin{pmatrix} -\langle u_1'^2 \rangle & -\langle u_1' u_2' \rangle & -\langle u_1' u_3' \rangle \\ -\langle u_1' u_2' \rangle & -\langle u_2'^2 \rangle & -\langle u_2' u_3' \rangle \\ -\langle u_1' u_3' \rangle & -\langle u_2' u_3' \rangle & -\langle u_3'^2 \rangle \end{pmatrix}. \quad (1.15)$$

The sum of the diagonal components of equation (1.15) is called Turbulent Kinetic Energy (TKE):

$$K = \frac{1}{2} \left(\langle u_1'^2 \rangle + \langle u_2'^2 \rangle + \langle u_3'^2 \rangle \right) \quad (1.16)$$

which is the mean kinetic energy per unit mass of the turbulent field. The rest of the components: $-\langle u'_1 u'_2 \rangle$, $-\langle u'_1 u'_3 \rangle$, $-\langle u'_2 u'_3 \rangle$, Reynolds shear stresses, are related to the velocity gradient of the flow. To solve the RANS and continuity equations, it is necessary to assume further relationships between the Reynolds stress and other flow parameters. The precision of the simulation results is greatly dependent on the choice of this model of turbulence (discussed in the section 1.2.4). The application of those turbulence models to turbidity currents requires intensive validations with more observational data.

1.2.3 Non-Dimensional Flow Characterisation

Non-Dimensional characterisation gives us a lot of benefits in various aspects. For example, by adjusting the non-dimensional parameters of governing equations to be the same value between the natural phenomenon and experiments, it is possible to observe the similar physical phenomenon at laboratory scale. However, it is difficult to adjust the all non-dimensional parameters consistently, so in most cases, experimentalists adjust only the major parameters. In this section, the important non-dimensional parameters of turbidity currents are introduced.

In the case of turbidity currents, the horizontal length scale (wave length) is much larger than the vertical length scale (flow depth), implying the flows are well described by shallow water theory (e.g. Parker et al., 1986; Dorrell et al., 2014), where characteristic velocity and length scales can be given by non-dimensional forms, e.g.:

$$\begin{aligned} \tilde{u}_i &= \langle u_i \rangle / U, & \tilde{x}_i &= x_i / h, & \tilde{t} &= tU / h, & \tilde{g}_i &= g_i h / U^2, \\ \tilde{\rho} &= \rho_f / \rho_a, & \tilde{\nu} &= 1 / \text{Re} = \nu / Uh, & \tilde{p} &= p / \rho_a U^2 \end{aligned} \quad (1.17)$$

The non-dimensional form of the Navier-Stokes equations is then,

$$\begin{aligned} \frac{\partial \tilde{u}_i}{\partial \tilde{t}} + \tilde{u}_j \frac{\partial \tilde{u}_i}{\partial \tilde{x}_j} &= \tilde{g}_i - \tilde{\rho} \frac{\partial \tilde{p}}{\partial \tilde{x}_i} + \tilde{\nu} \frac{\partial^2 \tilde{u}_i}{\partial \tilde{x}_j \partial \tilde{x}_j} \\ &= \frac{1}{\text{Fr}_d^2} - \tilde{\rho} \frac{\partial \tilde{p}}{\partial \tilde{x}_i} + \frac{1}{\text{Re}} \frac{\partial^2 \tilde{u}_i}{\partial \tilde{x}_j \partial \tilde{x}_j} \end{aligned} \quad (1.18)$$

where variables with tilde represent the non-dimensional value of corresponding flow parameters. From equation (1.18), the governing equations contain non-dimensional parameters. The densimetric Froude number (Fr_d) and Reynolds number (Re) introduced in the above equation (1.18) are the most fundamental non-dimensional parameters for density currents. Fr_d is the ratio between the velocity of flow and propagation of long wavelength waves. The following form is usually used:

$$\text{Fr}_d = \frac{U}{\sqrt{\rho \Delta g h}} \quad (1.19)$$

$$(1.20)$$

Re is the ratio of the inertia term to the viscosity term and given by,

$$\text{Re} = \frac{Uh}{\nu} = \frac{\rho_f Uh}{\mu} \quad (1.21)$$

If two density flows have the same values of Fr_d and Re, then, these flows are dynamically similar each other. However, adjusting both Re and Fr_d is difficult in many cases (e.g. Ettema et al., 2000; Sequeiros et al., 2010b). In cases of submarine density currents, for instance, Chikita (1989) reported, from direct observation data, a turbidity current where $\text{Re} \simeq 1.48 \times 10^7$; Meiburg and Kneller (2010b) calculated Re from the Grand Banks turbidity currents of 1929, and estimated it is $O(10^9-10^{10})$. On the other hand, Re at flume experiments conducted by Sequeiros et al. (2009), for example, is only around 2.0×10^4 which is at least three orders of magnitude smaller than the natural scale turbidity currents. Nevertheless, the value of Re acquired at flume experiments is still enough to be regarded as fully turbulent and thus, typically only Fr_d is adjusted (Sequeiros et al., 2009; Sequeiros et al., 2010b). When it comes to the density stratification of flow, the bulk Richardson number and gradient Richardson number are often used:

$$\text{Ri}_g = \frac{-g(\partial\rho_f/\partial z)}{\rho_f(\partial\langle u \rangle/\partial z)^2} \simeq \frac{gh\rho_\Delta}{U^2} \quad (1.22)$$

which is the ratio of the buoyancy and the flow shear stress. Ri_g is regarded as the instability of the flow stratification. For the advection–diffusion properties of the sedimentary phase, Peclet Pe and Schmidt Sm number are often used:

$$\text{Sm} = \frac{\nu}{D} \quad (1.23)$$

$$\text{Pe} = \frac{Uh}{D} = \text{Sm Re} \quad (1.24)$$

where D is diffusivity coefficient of sediment. Sm is the ratio of the sediment diffusion and viscosity. Pe is related to Sm and Re and it is the ratio between advection and sediment diffusion.

1.2.4 Turbulence Models

A better understanding of mixing process facilitates the accurate modelling of sediment suspension and therefore flow run-out of turbidity currents. While the direct observations have technical challenges to acquire high-resoluntional data of natural-scale turbidity currents, numerical simulation may provide prediction power even for the unreachable settings in the real world. As mentioned in the beginning of section 1.2, DNS solves the smallest eddy directly but is computationally expensive, and thus the application to the natural-scale phenomena is limited. By introducing appropriate turbulence models, the RANS equations can handle relatively larger scale phenomena in a relatively reasonable cost despite their limited accuracy (Meiburg et al., 2015). To solve the RANS equations (1.14), it is necessary to assume some relationships between

Reynolds stresses $-\langle u'_i u'_j \rangle$ and other flow parameters. This closure is commonly achieved by introducing a specific turbulence model such as mixing length model (Prandtl, 1925), Spalart–Allmaras model (Spalart and Allmaras, 1994), and standard k - ϵ model (Launder and Sharma, 1974). Based on the number of equations, these models are classified into some subgroups: zero-equation models (e.g. mixing length model), one-equation models (e.g. Spalart–Allmaras), and two-equation models (e.g. standard k - ϵ model) and so on (e.g. Markatos, 1986). In this section, the brief theory of turbulence modelling, mainly focusing on two-equation models are discussed. In the first step, Boussinesq (1877) assumed the following relationship:

$$-\langle u'_i u'_j \rangle = \nu_t \left(\frac{\partial \langle u_i \rangle}{\partial x_j} + \frac{\partial \langle u_j \rangle}{\partial x_i} \right) - \frac{2}{3} K \delta_{ij} \quad (1.25)$$

where ν_t is an eddy viscosity which describes the turbulent transfer of energy caused by the eddies, analogous to the viscosity of laminar flow caused by molecular friction. Substituting Eq.(1.25) into Eq.(1.14) gives:

$$\frac{\partial \langle u_i \rangle}{\partial t} + \langle u_j \rangle \frac{\partial \langle u_i \rangle}{\partial x_j} = g_i - \frac{1}{\rho_f} \frac{\partial \langle p \rangle}{\partial x_i} + \frac{\partial}{\partial x_j} \left[(\nu + \nu_t) \frac{\partial \langle u_i \rangle}{\partial x_j} \right] \quad (1.26)$$

The isotropic part of $\langle u'_i u'_j \rangle$ is absorbed into the pressure term as $\langle p \rangle \mapsto \langle p \rangle + \frac{2}{3} K$. The goal of turbulence models is to specify the relationships between the unknown parameter ν_t and other flow parameters.

The best-known zero-equation model uses a simple mixing length model. Prandtl (1925) considered the vertical flow velocity profile of two-dimensional ($\langle u_2 \rangle = 0$) open channel flow and introduced a mixing length l in which following relationship is satisfied:

$$\tau = -\rho_f \langle u'_1 u'_3 \rangle = \rho_f l^2 \left| \frac{d \langle u_1 \rangle}{d x_3} \right| \frac{d \langle u_1 \rangle}{d x_3} = \rho_f \nu_t \frac{d \langle u_1 \rangle}{d x_3} \quad (1.27)$$

$$l = \kappa x_3 \quad (1.28)$$

where τ is shear stress and κ is von Karman's constant of which value is 0.4. It should be noted that the equation 1.28 is only applicable in the near wall region. Based on this model, the velocity profile of open-channel flow near the wall will be

$$\frac{d \langle u \rangle}{d x_3} = \frac{u_*}{\kappa x_3} \quad (1.29)$$

and thus,

$$\frac{\langle u \rangle}{u_*} = \frac{1}{\kappa} \log \left(\frac{x_3}{z_0} \right) \quad (1.30)$$

the so-called law of the wall (Von Karman, 1930). u_* is shear velocity of flow and z_0 is the idealised roughness height at which flow velocity becomes zero. In reality, around the height z_0 , there is a turbulent–laminar

transition where the velocity decays linearly towards the bed.

In the case of two-equation models, the standard k - ϵ model (Launder and Sharma, 1974) and k - ω model (Wilcox, 1988) are widely used. Those models depict ν_t as,

$$\nu_t = \begin{cases} \alpha_{\epsilon 0} \frac{K^2}{\epsilon} & (k\text{-}\epsilon \text{ model}) \\ \alpha_* \frac{K}{\omega} & (k\text{-}\omega \text{ model}) \end{cases} \quad (1.31)$$

where $\alpha_{\epsilon 0}$ and α_* are empirical constant coefficients, ϵ is energy dissipation rate or equivalently ω is the dissipation per unit turbulence kinetic energy (Argyropoulos and Markatos, 2015). Two equation models require conservation equations of K and ϵ , or ω . For instance, the equations of conservation of K and ϵ are,

$$\frac{\partial K}{\partial t} + \langle u_j \rangle \frac{\partial K}{\partial x_j} = P - \epsilon + \frac{\partial}{\partial x_j} \left(\nu + \frac{\nu_t}{\alpha_k} \right) \frac{\partial K}{\partial x_j} \quad (1.32)$$

$$\frac{\partial \epsilon}{\partial t} + \langle u_j \rangle \frac{\partial \epsilon}{\partial x_j} = (\alpha_{\epsilon 1} P_k - \alpha_{\epsilon 2} \epsilon) \frac{\epsilon}{K} + \frac{\partial}{\partial x_j} \left(\nu + \frac{\nu_t}{\alpha_{\epsilon 3}} \right) \frac{\partial \epsilon}{\partial x_j} \quad (1.33)$$

where α_k , α_{ϵ} , $\alpha_{\epsilon 1}$, $\alpha_{\epsilon 2}$ and $\alpha_{\epsilon 3}$ are empirical constant coefficients of which values are 1.0, 1.3, 1.44, and 1.92 respectively. P is total-shear TKE production rate (e.g. Mansour et al., 1989; Argyropoulos and Markatos, 2015) and is given by

$$P = -\langle u'_i u'_j \rangle \frac{\partial \langle u_i \rangle}{\partial x_j} \quad (1.34)$$

This standard k - ϵ model is suitable for turbulent flows at high Reynolds numbers but cannot capture the flow behavior near the wall where viscous forces dominate (Argyropoulos and Markatos, 2015) and thus many scientists and engineers have proposed so-called ‘Low-Reynolds Number’ models (Patel et al., 1985). Also, it is known that the k - ω model is more accurate than the k - ϵ model for flow with strong pressure gradients and flow separation (Argyropoulos and Markatos, 2015). However, the k - ω models are known to have strong dependency of the solution on relatively arbitrary values specified for k and ω at the inlet (Menter, 2009). Advanced models can overcome this problem such as the Shear Stress Transport (SST) models of (Menter, 1993; Menter, 1994; Menter, 2009).

1.2.5 Rouse profile

In order to model the vertical profile of suspended sediment, (Rouse, 1937) considered turbulent diffusion by flow mixing in open channels. Although it is not directly relevant to seafloor turbidity currents, it is informative to understand the extant model for sediment suspension by turbulent flows. The shear stress of

open channel flows can be described as follows (Rouse, 1937)

$$\tau = \tau_b \left(1 - \frac{z}{h}\right) \quad (1.35)$$

Since $u_*^2 = \frac{\tau_b}{\rho_f}$, from equation (1.27) and (1.35) eddy viscosity is thus described as

$$\nu_t = \kappa u_* z \left(1 - \frac{z}{h}\right). \quad (1.36)$$

Considering the balance of diffusion and sediment fall out, the equation of diffusion can be expressed as,

$$w_s \langle \phi \rangle = -E_z \frac{\partial \langle \phi \rangle}{\partial z}. \quad (1.37)$$

where w_s denotes sediment fall velocity and E_z denotes the diffusion coefficient. Rouse (1937) considered that the diffusion coefficient E_z is equal to ν_t and thus, combining Eq.(1.36) with (1.37), the following relationship is acquired

$$\frac{1}{\langle \phi \rangle} \frac{\partial \langle \phi \rangle}{\partial z} = -\frac{w_s}{\kappa u_*} \frac{h}{z(h-z)} \quad (1.38)$$

By integrating Eq.(1.38) from near-bed specific height z_α to a specific height z , the well-known Rouse profile is acquired (Rouse, 1937).

$$\frac{\langle \phi \rangle}{\langle \phi_b \rangle} = \left(\frac{h-z}{z} \frac{z_\alpha}{h-z_\alpha} \right)^\beta \quad (1.39)$$

$$\beta = \frac{w_s}{\kappa u_*} \quad (1.40)$$

Where $\langle \phi_b \rangle$ is the near-bed sediment concentration and β is referred to as the Rouse number. Unlike open-channel flows where the shear stress is controlled only by the bed-shear (resulting in linearly varying τ ; see Eq. 1.35), the shear stress of turbidity currents are determined by the intricate interplay between the bed-shear and the shear between ambient fluid. Consequently, the velocity gradient becomes zero at the velocity maximum height, so the shear stress is also speculated to vanish near the velocity maximum, meaning that the equation 1.35 and thus the equation 1.36 do not hold for turbidity currents.

1.2.6 Depth average Shallow water model

Depth average shallow water models are derived by vertically integrating the Navier-Stokes equations for the description of fluid in which vertical scale is much smaller than horizontal scale. A consequence of the extreme

aspect ratio is that the pressure is hydrostatic to leading order, that is

$$\langle p \rangle = g(h - z)(\rho_s - \rho_a) \int_z^\infty \phi dz' \quad (1.41)$$

Further assuming that the variance of flow properties such as $\langle u_i \rangle$ is much smaller in vertical than the horizontal direction, the vertical flow profiles are regarded as uniform ('top-hat' model). Then, vertically Integrating the equation (1.26), following two-dimensional shallow water equations is acquired:

$$\frac{\partial U h}{\partial t} + \frac{\partial U^2 h}{\partial x} + \frac{\partial V U h}{\partial y} = gh\theta_x - gh \frac{\partial h}{\partial x} - \frac{\tau_{bx}}{\rho_f} + \frac{\partial}{\partial x} \left(\overline{\nu_t} \frac{\partial U h}{\partial x} \right) + \frac{\partial}{\partial y} \left(\overline{\nu_t} \frac{\partial U h}{\partial y} \right) \quad (1.42)$$

$$\frac{\partial V h}{\partial t} + \frac{\partial U V h}{\partial x} + \frac{\partial V^2 h}{\partial y} = gh\theta_y - gh \frac{\partial h}{\partial y} - \frac{\tau_{by}}{\rho_f} + \frac{\partial}{\partial x} \left(\overline{\nu_t} \frac{\partial V h}{\partial x} \right) + \frac{\partial}{\partial y} \left(\overline{\nu_t} \frac{\partial V h}{\partial y} \right) \quad (1.43)$$

$$\frac{\partial h}{\partial t} + \frac{\partial U h}{\partial x} + \frac{\partial V h}{\partial y} = 0 \quad (1.44)$$

where θ_x and θ_y are angle of bed slope given by:

$$\theta_i = - \frac{\partial \eta}{\partial x_i} \quad (1.45)$$

where η is height of bed. However, when it comes to turbidity currents, the vertical stratification is fundamental to the sediment transport mechanics (e.g. Abad et al., 2011; Dorrell et al., 2014) and it is known that these top-hat models result in poor prediction of the long-runout turbidity currents (Parker, 1982; Dorrell et al., 2014).

For a stratified flow, Dorrell et al. (2014) introduced some empirical structure functions, describing the vertical structures of flow velocity and concentration can be described as,

$$\langle u \rangle = \xi_u(z) U \quad (1.46)$$

$$\langle \phi \rangle = \xi_\phi(z) \Phi \quad (1.47)$$

where ξ_u and ξ_ϕ are the vertical structure functions of flow velocity and concentration respectively, satisfying the normalisation conditions

$$\int_0^\infty \xi_u(z) dz = \int_0^\infty \xi_\phi(z) dz = 1. \quad (1.48)$$

The implication of these structure functions in shallow water models can be observed in the depth-integrated

form of following terms:

$$\int_0^\infty \langle u_1 \rangle^2 dz = U^2 \int_0^\infty \xi_u^2 dz \equiv W_{u^2} U^2, \quad (1.49)$$

$$\int_0^\infty \langle u_1 \rangle \langle \phi \rangle d\eta = U\Phi \int_0^\infty \xi_u \xi_\phi dz \equiv W_{u\phi} U\Phi, \quad (1.50)$$

$$\begin{aligned} \int_0^\infty \langle p \rangle dz &= (\rho_s - \rho_a)gh \int_0^\infty \int_z^\infty \phi dz' dz \\ &= (\rho_s - \rho_a)gh \int_0^\infty z\phi dz \equiv \frac{1}{2}(\rho_s - \rho_a)gh W_P \Phi, \end{aligned} \quad (1.51)$$

where the double integral is calculated as

$$\begin{aligned} \int_0^\infty \int_z^\infty \phi dz' dz &= \left[z \int_z^\infty \phi dz' \right]_0^\infty - \int_0^\infty z \frac{\partial}{\partial z} \left(\int_z^\infty \phi dz' \right) dz \\ &= \int_0^\infty z\phi dz. \end{aligned} \quad (1.52)$$

The weighting parameters W_{u^2} , $W_{u\phi}$, and W_P arise due to the vertical stratification of a flow, each of which takes the following form (Dorrell et al., 2014):

$$W_{u^2} = \int_0^\infty \xi_u^2 dz \quad (1.53)$$

$$W_{u\phi} = \int_0^\infty \xi_u \xi_\phi dz \quad (1.54)$$

$$W_P = 2 \int_0^\infty z\xi_\phi dz. \quad (1.55)$$

These terms essentially describe the efficiency of momentum and material flux and the reduced hydrostatic pressure respectively. The first weighting term W_{u^2} represents the correlation between flow stratification and the momentum transport in a flow. In the same manner, $W_{u\phi}$ represents the correlation between the stratification and the material transport, and W_P represents the correlation between pressure gradients. Dorrell et al. (2014) demonstrated how a flow is channelised when the pressure gradient term $W_P < 1$, and flow stratification reduces the loss of suspended sediment due to the overspill. However, as Dorrell et al. (2014) noted, the empirical structure functions used in their model underestimate the flow stratification of natural-scale turbidity currents, resulting the poor prediction of channelised long-runout turbidity currents. Furthermore, the model in Dorrell et al. (2014) assumes the conservative flows where there is no exchange of suspended material through the flow interface. The sediment-laden turbidity currents are expected to show relatively strong stratification in the near-bed region due to the particle settling effects, which cannot be predicted by the current simplified structure functions (Abad et al., 2011; Dorrell et al., 2014). Therefore, there is a current need to develop new structure functions which better describe the dynamics of sediment-laden turbidity currents.

1.3 Mechanics of Turbidity Currents

1.3.1 Initiation

The initiation of turbidity currents depends on the formation of a sediment suspension (Meiburg and Kneller, 2010a). This sediment suspension can be triggered by various factors such as slope failures (Heezen and Ewing, 1952a; Ryan and Heezen, 1965; Gutiérrez-Pastor et al., 2009; Girardclos et al., 2007), plunging of a sediment-laden river flow to the bottom of lake or ocean (Eisma and Kalf, 1984; Geyer and Kineke, 1995; Mulder and Syvitski, 1995; Parsons et al., 2007; Piper and Normark, 2009), submarine volcanic eruption (Fiske, 1963; Mueller and White, 1992; White, 1996; Smellie and Hole, 1997; Fiske et al., 1998; Smellie, 1999; Mueller et al., 2000; White and Houghton, 2000), disturbance of seafloor sediment by Tsunami (Arai et al., 2013) and also anthropogenic activities (Xu et al., 2004; Iatrou et al., 2007; Talling et al., 2013). A better understanding of the initiation processes are essential to understand the stacking patterns of submarine fan systems and the evolution of submarine-channel networks. Also, the direct observation of turbidity currents would be extremely challenging without the knowledge of how and where turbidity currents are initiated. In this section, the detail of common and typical initiation processes which have been widely recognised are described: surge-like flows from slope failure and hyperpycnal flows from river floods (Normark and Piper, 1991; Mulder et al., 2003; Piper and Normark, 2009; Meiburg and Kneller, 2010b).

The initiation of a turbidity current is often linked to slope failure (Heezen and Ewing, 1952a; Ryan and Heezen, 1965; Van Den Berg et al., 2002; Mastbergen and Van Den Berg, 2003; Gutiérrez-Pastor et al., 2009; Girardclos et al., 2007). Hampton (1972) suggests a transition mechanism from slope failure through debris flow to turbidity current. The detached sediment firstly acts as a single block, but as it moves downstream, the block is jostled and agitated, which results in the collapse of the block and generates a debris flow. The further detachment of surface material from debris flow or mixing with ambient fluid by shearing may generate a turbidity current, which is called 'Flow transformation' (Houghton et al., 2009). The slope failure itself can be generally triggered by earthquakes or floods, therefore the depositional record created can be a good indicator of frequency of natural disasters. For example, Gorsline et al. (2000) reported that the depositional time of modern turbidites estimated by radiometric methods are matched with major floods or earthquakes in their study area.

River outflows into ocean or lakes and hypopycnal plumes may also initiate turbidity currents (e.g. Parsons et al., 2001; Parsons et al., 2007; Piper and Normark, 2009; Meiburg and Kneller, 2010b). Density currents generated by river outflow into oceans or lakes are classified based on their density difference between the current and ambient water: (1) homopycnal flow which refers the outflows from river mouths with negligible density difference and thus be mixed with ambient fluid rapidly, (2) hypopycnal flow which is less dense than the ambient fluid, and thus spreads above the ambient fluid due to its buoyancy and (3) hyperpycnal

flow which is denser than the ambient fluid, and it transforms into turbidity current running down on the seafloor (Bates, 1953). Although the concept of hyperpycnal flows was proposed in the earliest studies of turbidity currents (Bell, 1942), hyperpycnal flows at oceans were considered difficult to occur because the density of fresh water in river is much smaller than the one of ocean water (Bates, 1953; Wright, 1977). However, research in the past few decades clarify that the hyperpycnal flows are more common in small to medium scale rivers than previously thought (Mulder and Syvitski, 1995; Kineke et al., 2000; Parsons et al., 2001; McCool and Parsons, 2004). Mulder and Syvitski (1995) estimate the critical sediment concentration needed to make the plunging water denser than the ocean water (c.a. $36\text{--}42\text{ kg m}^{-3}$). Then, they estimated statistically the frequency of occurrence of hyperpycnal flows at 150 world rivers, clarifying that 81 rivers are capable of developing a hyperpycnal flow more frequently than once per hundred years. Furthermore, Parsons et al. (2001) demonstrated, experimentally, that even if the sediment concentration of the river outflow is less than the critical concentration estimated by Mulder and Syvitski (1995), the generated hypopycnal plume can initiate the hyperpycnal flow by the convective instability driven by some combination of heat diffusing out of the sediment-laden plume and particle settling within it.

Quasi-steady hyperpycnal flows have distinctive features compared with the flows initiated by slope failures (e.g., Mulder et al., 2003). Firstly, the duration of hyperpycnal flow events can last for months while the surge-type flows tend to last for only minutes to hours (Mulder and Alexander, 2001). Secondly, the sediment concentration of a hyperpycnal flow is lower than that of a surge-type flows. The initial sediment concentration of a hyperpycnal flow is $42\text{--}100\text{ kg m}^{-3}$ while the surge-type flow tend to possess initially $1300\text{--}1700\text{ kg m}^{-3}$ (Stacey and Bowen, 1988a; Kneller and Buckee, 2000). The relatively less dense hyperpycnal flows, therefore, are relatively slower than the surge-type currents even with the same angle of slope (Skene et al., 1997; Mulder et al., 1998; Alexander and Mulder, 2002). For example, Piper and Savoye (1993) and Mulder et al. (1997) estimated the mean flow velocity of turbidity current event. They reported that the mean flow velocity of the initiated debris flow in a steep slope ($1\text{--}5^\circ$) was $10\text{--}30\text{ m s}^{-1}$, while the velocity of subsequent turbidity current in a relatively gentle slope (less than 1°) was $7\text{--}8\text{ m s}^{-1}$ at the proximal area and $3\text{--}5\text{ m s}^{-1}$ at distal area. In contrast, the flow velocity of a hyperpycnal flow is typically around 1 m s^{-1} (Mulder et al., 2003). The importance of this initiation process is highlighted by its ability of generating pseudo-steady turbidity currents where large volumes of material may be transported over long flow durations, and thus it may play a vital role in terms of the evolution of submarine fan systems and material transport from shallow to deep ocean.

Other possible initiation mechanisms and the relationships between flow behaviour and initiation mechanisms are not so simple. For example, in the case of slope failures, Van Den Berg et al. (2002) and Mastbergen and Van Den Berg (2003) report that the gradual collapse of slope failure, so-called “breaching” is also capable of generating a sustained long-lived turbidity currents. In the recent direct observation of natural-

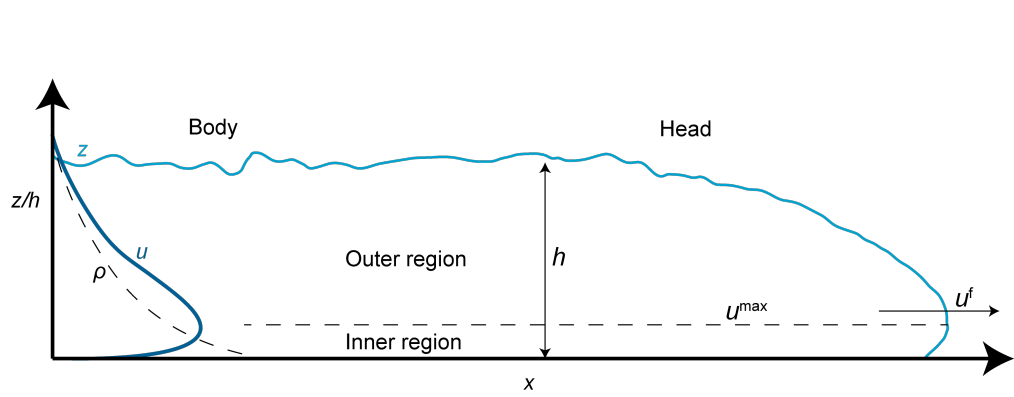


Figure 1.1: Schematic diagram of turbidity current (Modified after Meiburg and Kneller, 2010b)

scale turbidity currents at the Congo canyon (Simmons et al., 2020; Azpiroz-Zabala et al., 2017b) reported several pseudo-steady turbidity currents which last more than a week. Azpiroz-Zabala et al. (2017b) rules out earthquakes and wave height as the initiation processes of observed currents in Congo canyon, since there was no significant correlation with the flows. Although hyperpycnal river floods are common triggers for turbidity currents, the Congo River floods did not coincide with these currents and had low sediment concentrations as well. Other possible triggers, such as breaching, were considered, but Azpiroz-Zabala et al. (2017b) concludes that sustained turbidity currents are unlikely to result from sustained sources like river floods or breaching. Instead, Azpiroz-Zabala et al. (2017b) suggested that these currents may develop from a short-lived sediment source due to ‘flow stretching’ and an erosive frontal cell. More observations in Congo canyon and other settings are essential to validate those hypotheses.

1.3.2 Anatomy of Turbidity Currents

Turbidity currents have a structure that varies horizontally and vertically (Fig. 1.1). Turbidity currents are generally classified into two or three regions: head, body, and tail (e.g., Von Karman et al., 1940; Middleton, 1966b; Middleton, 1967; Benjamin, 1968). The structures and behaviours of Each part of the current have distinct features and play a significant role in the overall flow and transport processes (Kassem and Imran, 2001). Although it is controversial, the initiation mechanism may also relate to the flow structures. Traditionally, surge-type flows are considered to be triggered by slope failures, while prolonged flows are formed by river floods. Yet, the recent direct observation (Azpiroz-Zabala et al., 2017b) claims that even a small amount of sediment supply can generate prolonged turbidity currents by flow stretching and an erosive ‘frontal cell’. There are some knowledge gaps in the link between initiation processes and the flow structures for future studies. Initially, we consider the flow dynamics of the head and the body of turbidity currents.

Head

The fluid dynamics of head of turbidity currents has been studied extensively by theoretical analysis (Von Karman et al., 1940; Benjamin, 1968; Allen, 1971; Ungarish and Hogg, 2018), experiments (Simpson, 1972; Britter and Simpson, 1978; Simpson and Britter, 1979; Nogueira et al., 2014), and numerical simulations (Necker et al., 2002; Necker et al., 2005; Cantero et al., 2008; Borden and Meiburg, 2013). The first comprehensive theoretical analysis of the head of inviscid-turbidity currents was conducted by Benjamin (1968). This research showed that the occurrence of a head wave of density currents is theoretically impossible without any energy loss. Furthermore, it showed that the head wave must be broken at the rear of the head. The subsequent series of experiment-based studies (Simpson, 1972; Britter and Simpson, 1978; Simpson and Britter, 1979) and the theoretical analysis (Allen, 1971) revealed that the head of density currents play a significant role in terms of ambient fluid entrainment. Allen (1971) described the overhanging nose of density currents head, which was not considered in (Benjamin, 1968). They show that the ambient fluid entrainment rate at the head depends on the velocity profile in the boundary layer in the front of the head, the average height of the forefront point of the head, and the velocity of the head propagation. Furthermore, Allen (1971)'s detailed observations of flume experiments have shown that at the head of turbidity currents, two instability modes govern the mixing processes. Firstly, Kelvin-Helmholtz instabilities due to the gravitational and shear instabilities generate intermittent vortices (Britter and Simpson, 1978; Simpson and Britter, 1979). Secondly, convective instabilities are formed by incorporating ambient fluid beneath the current (Simpson, 1972). When the ambient less dense fluid is inserted beneath the denser fluid, it becomes gravitationally unstable. This instability creates the so-called "lobe and cleft" structure at the foremost region of the head (Fig.1.2). These instabilities are confirmed by the direct numerical simulation of lock-exchange type density currents (Necker et al., 2002; Necker et al., 2005; Cantero et al., 2008). Based on experiments, Kneller and Buckee (2000) show the head is relatively thicker and slower than that of the bodies. Thus, conventionally it is regarded that the head is fed sediments by the successive body (Kneller and Buckee, 2000). However, Azpiroz-Zabala et al. (2017b) proposed the new concept of head behaviour, a "frontal-cell" based on the direct observation of the natural-scale sustained turbidity current in the Congo Canyon, in which the faster, dense, and coarse-grained head runs away from the trailing body. They suggest that the frontal cell continuously erodes new sediment to replenish the sediment lost into the trailing body.

Body

The body of a turbidity current is generally regarded as a statistically uniform and steady region of the flow (e.g., Ellison and Turner, 1959; Middleton, 1966c; Garcia, 1993; Altinakar et al., 1996; Allen, 1971). Compared with the intensive studies of the head of turbidity currents, the body is less well studied despite potentially transporting more material and conducting more geomorphic work than the head. Based on

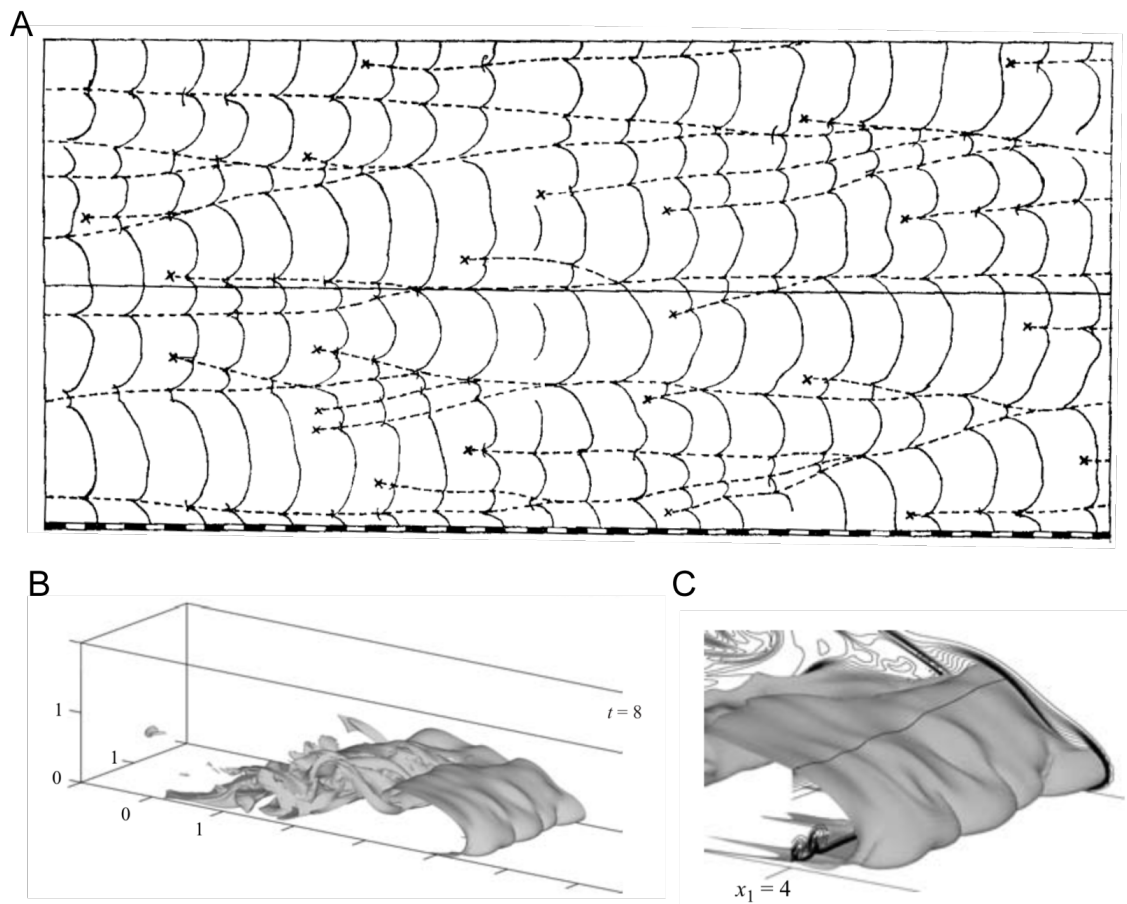


Figure 1.2: A) The sketch of the development of lobe-and-cleft structure (Modified after Simpson, 1972) and B,C) the 3D rendering of the results of numerical simulation of a density current in which lobe-and-cleft structure is well developed (Modified after Necker et al., 2005).

the flume experiments of surge-type flows, the maximal velocity of the body is faster than the speed of the head and thus, the body supplies the sediments to the head (Kneller et al., 1999; Kneller and Buckee, 2000; Sequeiros et al., 2018). In most cases, the features of the body and tail can be described by their vertical profile of velocity and sediment concentration. The vertical structures of the body can be roughly described as two layers: the lower thin dense layer near the base of the flows and the dilute upper layer which mixes with and entrains ambient fluid at the upper boundary (Ellison and Turner, 1959; Britter and Simpson, 1978; Simpson and Britter, 1979). Kassem and Imran (2001) report that these vertical structures of the body are responsible for sustained scour of and deposition on the basin floor. Recent research has demonstrated that the stratification of the flow is one of the most important factors in terms of the turbidity currents' ability to runout long distances without dissipation (Dorrell et al., 2014). An integrated study of the vertical profile of such flow states is lacking. Novel understanding may yet be concluded from the analysis of past experiments to analyse the relationships between vertical structure and other flow parameters.

1.3.3 Vertical Profile of Turbidity Currents

The typical velocity and density profiles of turbidity currents are expressed in Fig. 1.1. These vertical profiles have been measured by flume experiments (Ellison and Turner, 1959; Middleton, 1966c; Garcia, 1993; Altinakar et al., 1996; Buckee et al., 2001; Gray et al., 2005; Sequeiros et al., 2009; Sequeiros et al., 2010b; Cartigny et al., 2013; Tilston et al., 2015; Leeuw et al., 2018b), and by direct observations of natural-scale flows (Xu et al., 2004; Xu et al., 2010; Khripounoff et al., 2012; Liu et al., 2012; Dorrell et al., 2014; Hughes Clarke, 2016; Dorrell et al., 2014; Dorrell et al., 2016; Azpiroz-Zabala et al., 2017b; Dorrell et al., 2019). The vertical structures of the turbidity currents play a significant role in terms of flow behavior (e.g., Stacey and Bowen, 1988a; Stacey and Bowen, 1988b; Peakall et al., 2000; Abad et al., 2011; Dorrell et al., 2014; Dorrell et al., 2019).

The standard model for the velocity profile of a turbidity current is of a turbulent plane wall jet (e.g., Kneller and Buckee, 2000; Gray et al., 2005), differing from open channel flows where the velocity tends to increase monotonically with distance from the bed (e.g. Rijn, 1984). As depicted in Figure 1.3, turbidity currents can be divided into two layers by the velocity maximum: the lower shear layer, which shows a positive velocity gradient and the upper thick layer, which has a negative velocity gradient. The height of the boundary between these layers is controlled by the ratio of the frictional forces between the upper and lower boundaries (Middleton, 1966a; Kneller et al., 1997). Since the shear production of turbulence tends to zero at the velocity maximum, the turbulence intensities at this point become the lowest value within the currents, and this zone is called the 'slow diffusion zone' (Garcia, 1993; Kneller et al., 1999; Best et al., 2001; Buckee et al., 2001). This slow diffusion zone hinders sediment transport at the lower layer due to the strength of the stratification and the lack of turbulence production at the velocity maximum (Buckee et al., 2001). Advection and diffusion are also able to convey the vertical turbulent mixing through the velocity maximum, and thus, the effects of

this slow diffusion zone will be significant only in the case of strongly depositional flows. However, Dorrell et al. (2019) conclude that this is not a "slow-diffusion zone", but rather an eddy transport barrier. Such an eddy transport barrier is formed by internal waves, propagating mass and momentum towards the centre of the flow. The resultant steepening of shear and density gradients forms the eddy transport barrier, which inhibits the vertical motion of mixing events. Such internal wave mixing and eddy transport barriers are analogous to other processes dominated by flow scale mixing events, including density currents and (Coriolis forced) planetary jets (Fig 1.3).

The decay pattern of the upper-layer velocity is typically approximated by an exponentially decreasing Gaussian profile based on the flume experiments (Kneller et al., 1999; Sequeiros et al., 2010b) although the recent direct observation study (Xu et al., 2004) implies a linear velocity profile in the upper layer. The height of a maximum in the gradient of the concentration profile is close to the height of the velocity maximum in the experiment of Ellison and Turner (1959) in which the saline current flowed down a 14° slope. However, this trend is not observed in some other experiments (Altinakar et al., 1996; Garcia, 1993; Baas et al., 2005; Sequeiros et al., 2010b; Leeuw et al., 2018b). When there is a large gradient in the concentration profile, this implies the existence of a barrier to mixing, such as the aforementioned 'slow-diffusion zone' or 'eddy transport barrier'. Bo Pedersen (1980) suggested that the large density gradient only occurs in subcritical flows, but Garcia (1993) demonstrated that a large gradient of density at the velocity maximum can be observed both in supercritical and subcritical conditions. The same trends are also recognised in self-accelerating currents observed in experiments by Sequeiros et al. (2018). Recent direct observations of saline density currents (Dorrell et al., 2019) suggest that the internal waves propagate momentum towards the centre of the flow, which acts to steepen the density gradients, forming eddy transport barrier.

Various factors affect the vertical flow profile (e.g. Froude number, sediment concentration, bedform, basal sediment roughness and internal gravity wave). Garcia and Parker (1989) performed flume experiments with both saline and turbid currents. Their results show similar velocity profiles between saline and turbidity currents while showing different profiles before and after a hydraulic jump. In the case of subcritical flows, the dimensionless height of the velocity maximum is generally higher, and the velocity gradients are more gentle than under supercritical conditions (e.g., Garcia and Parker, 1989; Garcia, 1993). In the case of low-density turbidity currents, the dimensionless density profile shows relatively large deviations while the dimensionless velocity profile is almost constant (Stacey and Bowen, 1988a; Altinakar et al., 1996). However, in the case of high-density turbidity currents (e.g. concentrations at the basal layer between 45 and 65%), the dimensionless velocity profile of the lower dense part of the flow also shows different attributes compared with low-density ones (Fig. 1.4) (Postma et al., 1988; Cartigny et al., 2013). The highly concentrated basal layer tends to be a laminar flow. It shows high shear stress and fully damped turbulence, which results in a linear velocity profile below the velocity maximum (Fig. 1.4).

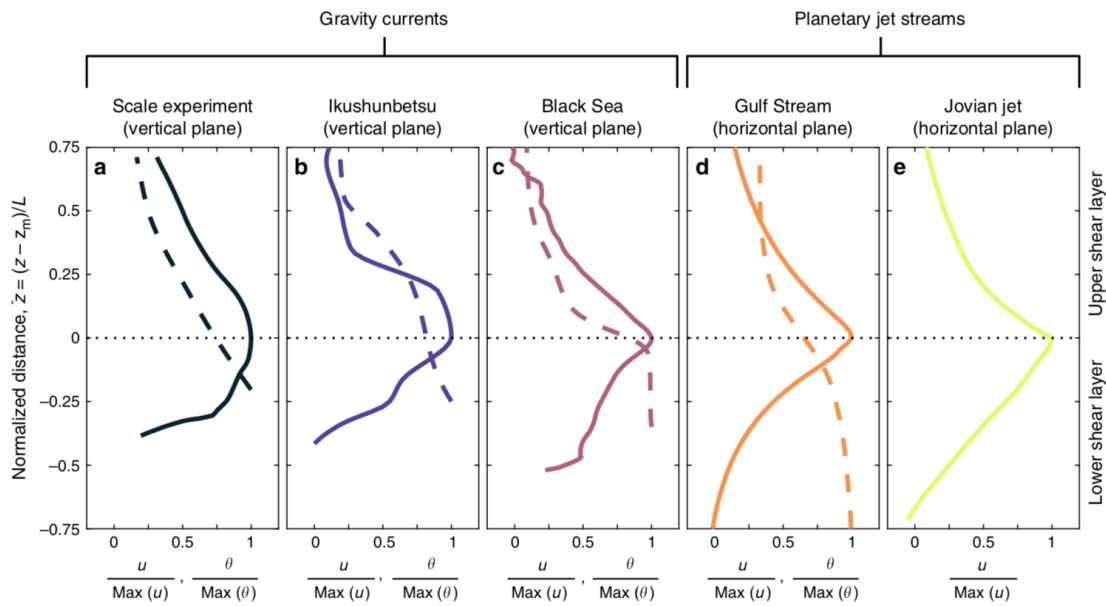


Figure 1.3: The comparison between the velocity profiles of flume experiments, direct observation of natural events, and planetary jet streams. Modified after Dorrell et al. (2019). The original symbols of the source are used in the figure: z_m is the velocity maximum height, L is the flow integral length scale, and $\theta = \rho_f/\rho_a - 1$ is the scalar transport term.

D. Velocity profiles over different ratios of stratification types

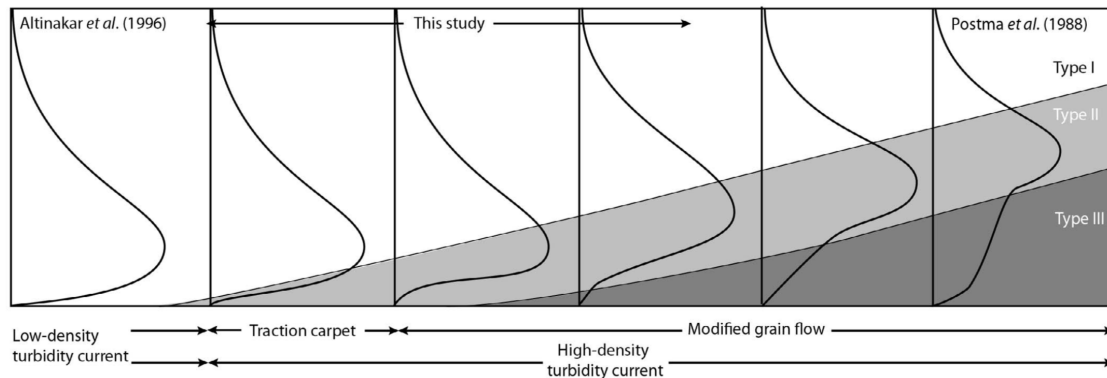


Figure 1.4: The variation of velocity profile depending on the vertical stratifications of the flow. Modified after Cartigny et al. (2013).

1.3.4 Relation between vertical profile and flow behaviour

The vertical structure of a turbidity current is one of the key controls of the flow along submarine sinuous channels (e.g. Stacey and Bowen, 1988a; Stacey and Bowen, 1988b; Peakall et al., 2000; Abad et al., 2011; Dorrell et al., 2014; Dorrell et al., 2019). The flow stratification controls the entrainment rate of ambient fluid and the erosion/deposition at the bottom flow interface (Stacey and Bowen, 1988a; Stacey and Bowen, 1988b; Dorrell et al., 2014; Luchi et al., 2015). The flow stratification is also a key control in the orientation of secondary flow circulation at the channel bends (Abad et al., 2011; Dorrell et al., 2013; Sumner et al., 2014). Although secondary circulation is a common phenomenon both in fluvial rivers and turbidity currents, it is known that turbidity currents show more complex and wide variation of the orientation of secondary circulation depending on their flow stratification (e.g. Azpiroz-Zabala et al., 2017a). The secondary flow circulation redistributes the suspended sediment and generates flow-scale circulation, which eventually breaks up into small eddies, supplying an additional source of turbulent kinetic energy (Abad et al., 2011; Dorrell et al., 2013; Sumner et al., 2014; Azpiroz-Zabala et al., 2017a). How these circulation cells are formed is fundamental to understanding the overspilling of turbidity currents and the evolution of sinuous submarine-channel networks.

1.3.5 Long-runout Turbidity Currents

Turbidity currents can runout over 1000 km downstream and create extremely long leveed channel (over 1000 km). The ability of turbidity currents to runout at such long distances is one of the enigmatic problems that remain to be solved. For subaerial currents, because the river is surrounded by an atmosphere, it does not entrain ambient air or thicken downstream. Furthermore, the water is strongly affected by gravity, and thus the current is well confined in the channel. However, in a subaqueous environment, density currents are surrounded by seawater and thus the currents entrain ambient water, which thickens and dilutes them downstream (Parker et al., 1986). In addition, the driving force of density currents is gravity, which exerts on the density difference between the currents and ambient water. Since this density difference is generated by sediments (or salt) suspended in the currents, the net gravity force becomes smaller as the currents get more diluted. One of the mechanisms which sustain the turbidity currents over long distances is the state of density currents called 'autosuspension' (Bagnold et al., 1962) in which a density current continuously erodes the basal sediments and does not deposit the suspended sediments.

To maintain the sediment in suspension, at least, the gravity energy generated by downslope motion must surpass the energy consumption due to the maintenance of suspended sediments. The numerical constraint of this condition can be expressed as:

$$Rg\Phi hU \sin \theta > Rg\Phi h w_s \cos \theta \quad (1.56)$$

where $R = \rho_s - \rho_a / \rho_a$ denotes the ratio of sediment particles' excess density against water density. If the slope θ is small enough, $\sin \theta \simeq \theta$ and $\cos \theta \simeq 1$. Applying these approximations to Eq.(1.56), the Knapp-Bagnold constraint (Knapp, 1938; Bagnold et al., 1962) can be obtained:

$$\frac{U\theta}{w_s} > 1. \quad (1.57)$$

where w_s is the settling velocity of the sediments. The autosuspension flow, indeed, must satisfy this constraint, but actual turbidity currents consume the majority of gravitational energy by the energy dissipation due to the fluid viscosity (e.g. Parker et al., 1986) and thus, this constraint is necessary but not sufficient. After Bagnold et al. (1962), Pantin (1979) and Parker (1982) consider the mass conservation of suspended load of a flow, and proposed a critical 'ignition' condition at which the flow reaches the autosuspension state. The conservation of suspended load can be described as

$$\frac{\partial \Phi h}{\partial t} + \frac{\partial U \Phi h}{\partial x} = w_s(e_s - r_0 \Phi) \quad (1.58)$$

where e_s denotes the coefficient of sediment entrainment, and r_0 denotes the concentration ratio of the suspended-sediment between the layer averaged value and the value near the bed:

$$r_0 = \frac{\langle \phi_b \rangle}{\Phi}. \quad (1.59)$$

Parker et al. (1986) add the following two equations to the equation (1.58) and proposed the depth-averaged model of turbidity currents:

$$\frac{\partial h}{\partial t} + \frac{\partial U h}{\partial x} = e_w U \quad (1.60)$$

$$\frac{\partial U h}{\partial t} + \frac{\partial U^2 h}{\partial x} = R g \Phi h \theta - \frac{1}{2} R g \frac{\partial \Phi h^2}{\partial x} - u_*^2 \quad (1.61)$$

where e_w denotes the entrainment rate of ambient fluid and u_* denotes the shear velocity of the flow. Equation (1.60) is the mass conservation of the flow, and the equation (1.61) is the momentum conservation of the flow. Using this 'three-equation' model, they showed that turbidity currents can realise autosuspension only if the current is in the state of self-acceleration. Self-acceleration is a positive feedback loop of a flow where the accelerated flow entrains more bed materials into suspension, which provides more driving force and thus further accelerates the flow.

To conduct the numerical simulation of turbidity currents by this three-equation model, the closures of four parameters r_0 , e_s , e_w , and u_* are needed. In the 'three-equation' model, they used a simple form to describe

the shear velocity u_* which is,

$$u_*^2 = C_D U^2 \quad (1.62)$$

where C_D is the dimensionless coefficient of bed drag regarded as a constant value in their paper. However, e_s is linked to u_* in their closures (equation (21) to (23) in their paper) and thus, e_s is also linked to the flow velocity U . As the flow accelerates, e_s becomes too large, and the consumption of turbulent energy exceeds the supply. As a result, the turbulence of the flow vanishes, and the flow dies (Parker et al., 1986). To overcome this shortcoming of the ‘three-equation’ model, Parker et al. (1986) assumes the relationship between the bed shear velocity u_* and layer-averaged turbulent kinetic energy K like bellow:

$$u_*^2 = \alpha_0 K \quad (1.63)$$

where α_0 is a constant coefficient. The conservation of this turbulent kinetic energy, K can be described as,

$$\frac{\partial K h}{\partial t} + \frac{\partial U K h}{\partial x} = u_*^2 U + \frac{1}{2} U^3 e_w - \epsilon_0 h - R g w_s \Phi h - \frac{1}{2} R g \Phi h U e_w - \frac{1}{2} R g h w_s (e_s - r_0 \Phi) \quad (1.64)$$

where ϵ_0 denotes the mean dissipation rate of turbulent energy which takes form:

$$\epsilon_0 = \alpha_1 \frac{K^{\frac{3}{2}}}{h}. \quad (1.65)$$

α_1 is a dimensionless coefficient related to the other flow parameters. Parker et al. (1986) considered the equilibrium state of the three- and four-equation models and introduced an ideal coefficient of bed friction C_{D*} that the equilibrium current would possess. From Eq.(1.62) and (1.63), C_{D*} will be

$$C_{D*} = \alpha_0 \frac{K}{U^2} \Big|_{\text{equilibrium}} \quad (1.66)$$

Then, using Eq.(1.65) and (1.66), the equation of conservation of K (1.64) with spatial equilibrium state will be

$$\alpha_1 = \frac{\frac{1}{2} e_w \left(1 - \text{Ri} - 2 \frac{C_{D*}}{\alpha_0} \right) + C_{D*}}{\left(\frac{C_{D*}}{\alpha_0} \right)^{\frac{3}{2}}} \quad (1.67)$$

They demonstrated that the flow is also able to reach the autosuspension state using the equation (1.58)–(1.61) and (1.64) which is called ‘four-equation’ model and they guessed that in the case of field-scale turbidity currents, this model shows better performance than the ‘three-equation’ model.

In the theoretical analysis of density currents by Ellison and Turner (1959), the ambient fluid entrainment rate

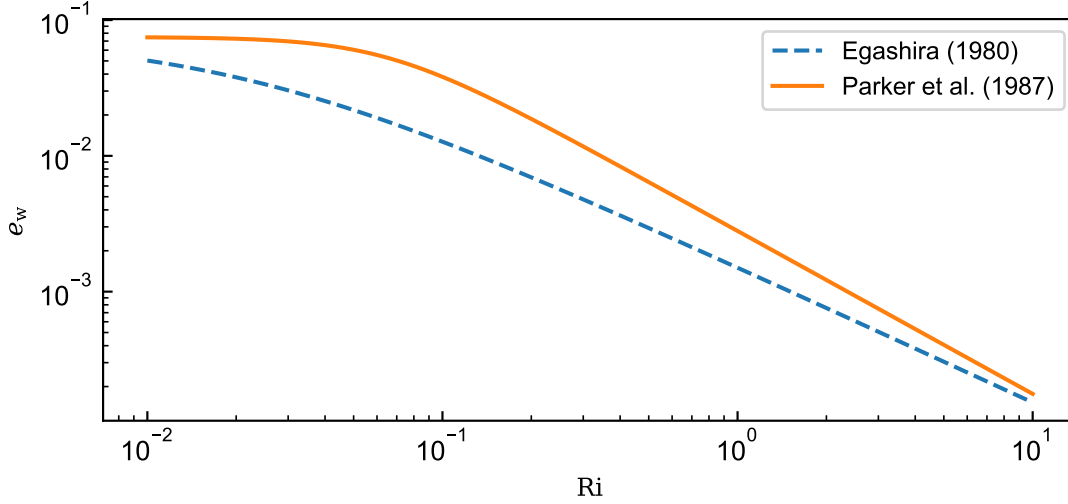


Figure 1.5: Empirical relationships of ambient fluid entrainment rate, e_w , and the Richardson number, Ri .

is assumed to be proportional to the velocity of the flow multiplied by an empirical function of the Richardson number, Ri . Following empirical relationships (Egashira, 1980; Parker et al., 1987) are widely used

$$e_w = \frac{0.00153}{0.0204 + Ri} = \frac{0.00153}{0.0204 + Fr_d^{-2}} \quad (1.68)$$

$$e_w = \frac{0.075}{\sqrt{1 + 718 Ri^{2.4}}} = \frac{0.075}{\sqrt{1 + 718 Fr_d^{-4.8}}} \quad (1.69)$$

As it is mentioned above, the entrainment of ambient fluid thickens and dilutes the current. Thus, it has been argued that long runout currents must be at very low Fr_d to suppress ambient water entrainment (Eq.1.68–1.69)(Toniolo et al., 2006a; Toniolo et al., 2006b). Although the existence of upstream-migrating large-scale bedforms in the deep-sea (discussed later) implies the supercritical flow condition (i.e. high Fr_d) (e.g. Postma and Cartigny, 2014), the super- or subcritical condition is based on the velocity difference between the flow and surface wave, and in the case of stratified flow, the supercritical condition does not necessarily require high Fr_d which rarely become bigger than unity (Dorrell et al., 2016).

Regarding r_0 , Parker et al. (1986) claimed that a constant value ($r_0 = 1.6$) approximates the data well. In the models, they used the empirical relationship from open-channel flows:

$$r_0 = 1 + 31.5 \left(\frac{u_*}{w_s} \right)^{-1.46} \simeq 1 + 8.23 \beta^{1.46} \quad (1.70)$$

The equation 1.70 means that the ratio of basal to depth-averaged concentration is determined by the Rouse number, β . However, as mentioned above, the Rouse profile is a theoretical model based on the open-channel vertical velocity profile, which differs greatly from density currents. The experiments by Garcia and Parker (1989) speculated that in the case of turbidity currents, r_0 is almost constant regardless of flow condition.

In many cases, r_0 is regarded as a constant value around 1.5–2.0 in the numerical simulation (Parker et al., 1987; Vrolijk and Southard, 1997; Kostic and Parker, 2006; Fildani et al., 2006; Cantero et al., 2012).

In the equilibrium state, currents must keep suspended sediment inside the flow; this constraint can be readily obtained from the momentum balance Eq.(1.61) assuming that U, Φ, h , and K are constant in time and space,

$$u_*^2 = Rg\Phi h\theta. \quad (1.71)$$

Also, from Eq. (1.58–1.60),

$$e_s = \phi_b \quad (1.72)$$

$$e_w U = 0. \quad (1.73)$$

It should be noted that Eq.(1.73) can be satisfied when $e_w = 0$, but in the case of density currents, e_w must be larger than zero. Therefore, it is theoretically impossible for the density currents to be equilibrium state. At the moment, let it assume that the flow almost (not perfectly) satisfies the Eq.(1.73). Then, from Eq.(1.64), the following constraint can be obtained (Parker et al., 1986),

$$u_*^2 U = Rg\Phi h U \theta = \epsilon_0 h + Rg w_s \Phi h. \quad (1.74)$$

Since the first term of right side is non-negative value,

$$Rg\Phi h U \theta > Rg w_s \Phi h. \quad (1.75)$$

The Knapp-Bagnold criterion can be obtained, dividing both side of this equation by $Rg w_s \Phi h$.

Even though these kinds of depth-averaged models can capture the fundamental mechanisms of density currents, such as self-acceleration in a laboratory scale, they are still not able to simulate the field-scale long-runout turbidity currents (e.g. Luchi et al., 2015; Luchi et al., 2018). Luchi et al. (2015) discussed the problems of depth-averaged models and showed theoretically that both 'three-equation' and 'four-equation' models cannot produce the sustainable long-runout turbidity currents in the field scale. The point is no matter how small the densimetric Froude number is, since the right side of the equation (1.60) is a positive value, the thickening and dilution of the flow is inevitable when the flow travels a long distance. Further, these models assume that the long-runout flow in natural scale is almost equilibrium, and their flow parameters temporally and spatially do not vary significantly. However, recent direct observation (Dorrell et al., 2019) implies that the internal waves within a statistically unstable current, for which the flow state varies temporally and spatially, might be a key control of flow sustainability.

One of the effective methods to avoid the dilution of the flow is introducing flow stratification into the numerical models. Regarding stratified flow, some of the layer-average values of the shallow water model must be reconsidered to describe the structure functions (Eq. 1.46–1.53). Dorrell et al. (2014) introduced the empirical closures for the shape functions from (Islam and Imran, 2010; Sequeiros et al., 2010b; Abad et al., 2011) into the ‘three-equation’ model. They demonstrated the significance of flow stratification by adapting their model to the Black Sea submarine channel. However, their improved model also failed to predict the flow behaviour along a natural-scale partially-confined submarine channel. They concluded that the current empirical shape functions still underestimated the flow stratification, and thus the improvement of shape functions is the key to improve the system-scale numerical modelling. Cantero et al. (2009) used DNS (direct numerical simulation) to investigate the internal flow structures of turbidity currents. Due to the water entrainment, there is no theoretical equilibrium state in a turbidity current. To enable the analysis of internal structures in stable turbidity currents, the model in (Cantero et al., 2009) introduced a ‘roof’ (a solid boundary where the velocity becomes zero) parallel to the bed, so preventing ambient water entrainment and creating a channel flow. Luchi et al. (2018) also conducted numerical simulation using the similar configuration of ‘Turbidity Currents with a roof model’ in Cantero et al. (2009), but they replaced the ‘roof’ with a free-slip upper boundary (the normal component of the flow velocity and the shear stress at the boundary are zero while the streamwise component of velocity is non-zero at the boundary), so that they can resolve the upward normal structure of the flow. They concluded that the steady-state turbidity currents self-partition themselves into two layers: the lower dense ‘driving layer’ and the upper dilute ‘driven layer’. The expanding upper dilute layer prevents the lower dense layer from getting diluted, and this mechanism may enable the flow to runout long distance (Luchi et al., 2018). The key research gap here is the lack of empirical shape functions which can accurately predict the mechanisms of flow separation into dilute upper and dense lower layers.

1.3.6 Suspended load transport models

Deposition and erosion of sediments are key controls in terms of development of depositional architectures such as submarine channel-levee networks and the sedimentary structures inside them. In addition, since the suspended sediments provide turbidity currents with their driving force, whether a flow is erosional or depositional inherently affects other flow parameters. When turbidity currents traverse for long distances, the bypass or self-acceleration state has been considered as a requirement for turbidity currents to keep sediment in suspension (e.g. Bagnold et al., 1962; Parker et al., 1986; Sequeiros et al., 2018). Therefore, the prediction of net erosional and depositional threshold is of key importance for understanding the hydrodynamics of turbidity currents.

Sediment transport models can be classified into three categories and their combinations: i) competence models (Komar, 1985; Kneller, 2003; Kubo et al., 2005; Lynds et al., 2014) that assume that the deposition rate is a function of flow stratification which scales with the settling to shear velocity ratio (Soulsby, 1997),

ii) flow power models (Velikanov, 1954; Bagnold, 1966; Celik and Rodi, 1991; García, 2008) that consider the balance between available flow power, defined as turbulent-kinetic-energy production rate, and the work done to keep sediments in suspension, iii) flux balance models (Garcia and Parker, 1991; García, 1993; Smith and Hopkins, 1971) that consider the sediment flux at the boundary taking into account the balance between the near-bed concentration and the settling velocity to the sediment entrainment rate, and iv) flow-power flux-balance model (Dorrell et al., 2018a), which is based on a flux-balance model but incorporates the new sediment entrainment function that takes the concepts of flow power models into account.

In a first competence model, the net erosion-deposition rate, is described as

$$w_s = \beta' u_* \quad (1.76)$$

where β' is an empirical Rouse parameter (Rouse, 1937). This relationship is widely used for describing the transition between bedload and suspended load (Soulsby, 1997). However, since in the dilute flow the turbulence is the dominant mechanism of keeping sediment in suspension, the net erosional-depositional threshold is known to be dependent on the flow concentration (García, 2008). Thus this model is unable to accurately capture the dynamics of erosion.

Flow power models assume that when deposition and erosion are in balance, the available flow power will be proportional to the work done to keep sediments in suspension (Velikanov, 1954; Bagnold, 1954). The flow power is proportional to the production rate of turbulent kinetic energy and it can be described as (Pope, 2000),

$$\Gamma(z) \propto -\rho_f \langle u'_1 u'_3 \rangle \frac{\partial \langle u_1 \rangle}{\partial z} \quad (1.77)$$

where Γ is the available flow power supply. In open-channel flows, the right-hand side of Eq.(1.77) will be proportional to $\rho_f u_*^3/h$ from the law of the wall (Eq.1.30), the turbulent-viscosity hypothesis (Eq.1.27), and the assumption of parabolic profile of eddy viscosity (Eq.1.36). Therefore, in the equilibrium state,

$$\rho_\Delta g w_s h = \alpha u_*^3 \propto U^3 \quad (1.78)$$

where left-hand term is the work done to keep sediment suspended in the currents and α is a constant coefficient. From equation (1.78),

$$\frac{U^3}{g R h w_s} \propto \Phi \quad (1.79)$$

Wan and Wang (1994b) measured the flow parameters of the Yellow Rivers and showed that equation (1.79) is well satisfied when the flow is dilute (volumetric sediment concentration < 10%). Still, they also find

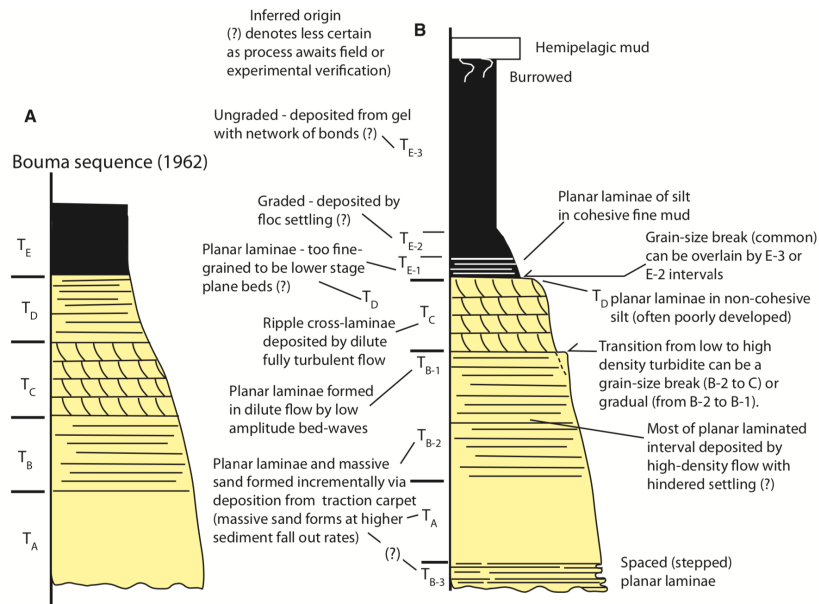


Figure 1.6: Schematic diagram of depositional sequence of turbidite, modified after Talling et al. (2012). A) Classical Bouma sequence. B) Revised Bouma sequence proposed by (Talling et al., 2012).

that when the flow concentration is higher than 10%, equation (1.79) is no longer satisfied since in such high-density flows, the turbulence is damped and is no longer the dominant sediment-support mechanism. However, turbidity currents do not satisfy the law of the wall in the upper layer of the flow. Thus, the profile of eddy viscosity is not a simple parabolic function. Thus, whether the equation (1.79) applies to the turbidity currents is doubtful.

1.3.7 Sediment Deposition and Flow Properties

In turbidity currents, larger grains preferentially settle in a layer-by-layer fashion (Talling et al., 2012). Since the sorting and mean grain size of deposited sediments depends on the flow parameters such as concentration near the bottom layer of the flow, grain size distribution of suspended sediments, and flow velocity (e.g. Kneller, 1995), the deposits, i.e. turbidites are expected to preserve the information of paleo-flow conditions. The classification schemes of sedimentary facies and possible mechanisms are reviewed in Talling et al. (2012).

The sedimentary structures of turbidites are firstly classified into 5 divisions, the so-called 'Bouma sequence' (Bouma, 1962): (T_A) structureless and sometimes graded sand with occasional erosional surface, (T_B) lower parallel laminated sand, (T_C) cross-laminated sand and silt, (T_D) upper parallel laminated sand and silt, (T_E) laminated mud. It should be noted that although the Bouma sequence is a well-known and ubiquitous feature in deep-marine settings, due to the nonuniform grain size distribution and flow transformations (Fisher, 1983), a complete sequence is rarely seen (Mulder and Hüneke, 2016). Whilst the Bouma sequence explains a part of typical sedimentary structures of turbidites, there are still other common intervals not covered by the Bouma sequence (Talling et al., 2012). To describe the variety of common intervals, new schemes for more

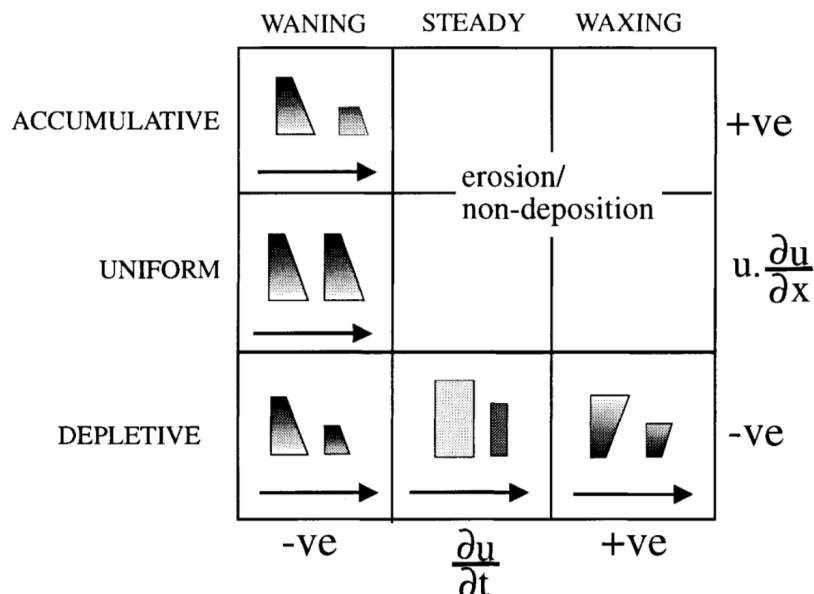


Figure 1.7: Acceleration matrix proposed by Kneller (1995).

detailed classification of depositional facies were proposed, such as Lowe sequence (Lowe, 1982) for the deposits for high-density flows, which partially corresponds to Bouma T_A division, and the classification scheme for 'fine-grained turbidite' defined by Stow and Shanmugam (1980) which mainly corresponds to Bouma T_{C-E} divisions. Some researchers also subdivided the conventional Bouma intervals (e.g. Piper, 1978; Talling et al., 2012). Talling et al. (2012) summarized the previous classification scheme for turbidite intervals and proposed a new sequence (Fig.1.6B).

The vertical succession of a turbidite generally records the passing body and tail of a flow over the deposits, in other words, the history of the deceleration of flow (Walker, 1965; Allen, 1991). Kneller (1995) proposed the 'acceleration matrix' (Fig.1.7), which explains the simple relationship between spatial or temporal velocity gradient and the resultant vertical grain-size distribution of the deposits. However, this matrix is too simplified and does not concern some important physical mechanisms of turbidity currents, such as vertical stratification and sediment source supply. First, if the sediment source was extremely well-sorted and is composed of almost a single grain size, the grain size distribution of resultant deposits must be the same regardless of the flow properties (Talling et al., 2012). Furthermore, since the sediment exchange at the bed is affected by the suspended-sediment concentration near the bed rather than the layer-averaged one (right term of Eq.1.58), the vertical density profiles of each grain size should be taken into account.

1.4 Morphology of Submarine Fan System

To advance understanding of real-world turbidity currents, it is helpful to understand the systems in which they are generated. Submarine fans are a complex of deposits from multiple density flows and are some

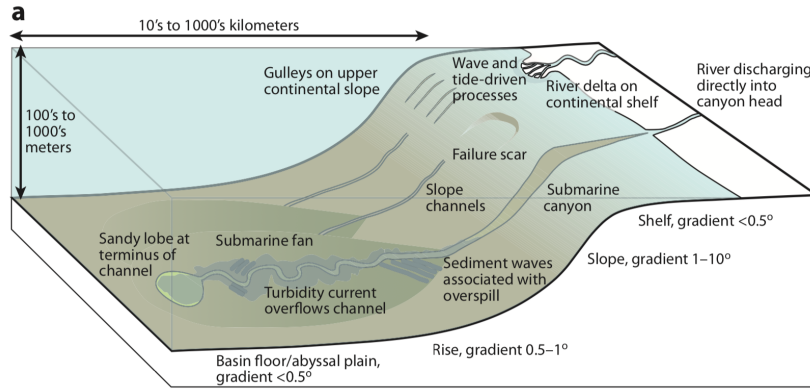


Figure 1.8: Schematic illustration of submarine fan systems (Meiburg and Kneller, 2010b)

of the largest and thickest sediments accumulations on the Earth's surface (Bouma et al., 1985; Nilsen, 2007). The huge complex of sediments can be archives of, for example, past tectonic, biological, and climatic processes (Weimer and Link, 1991; Stow and Mayall, 2000; Covault, 2011). Since the porosity of the deposits in submarine fans is relatively higher than the surrounding sediments, they can also be a potential oil and gas reservoir (Weimer and Link, 1991; Stow and Mayall, 2000; Covault, 2011). Therefore, the understanding of how a submarine fan system develops provides a lot of information of paleoenvironments and natural resources. Turbidity currents transport the sediments from shallow continental slopes to the deep sea. During the transport, these currents erode and deposit the sediment and create various sedimentary structures in the submarine fan system (Meiburg and Kneller, 2010b). This system is often associated with a subaerial river which is a potential sediment source (e.g. Ganges river associated with Bengal fan; Curray et al., 2002). Offshore of the river mouth, the erosional features range from a gully on the upper continental slope to submarine canyons which can be recognized on the modern seafloor. Submarine canyons are typically several kilometres wide and hundreds of meters deep (e.g. Inman et al., 1976). At the more downstream region, there are depositional architectures analogous to subaerial river deltas, such as sinuous leveed channels and sheet-like deposits on the abyssal plains (Fig.1.8). It has been recently recognised that a channel-lobe transition zone occurs at canyon/channel mouths and is commonly associated with a break of slope (Wynn et al., 2002b; Wynn et al., 2002a). This zone is characterised by a wide scattering distribution of scours and coarse sands and gravels (Wynn et al., 2002b; Wynn et al., 2002a; Dorrell et al., 2016). Typically, in the submarine canyon and channels, scours are aligned in a linear path, which is often associated with the hydraulic jumps of supercritical turbidity currents along cyclic steps or chutes-and-pools (e.g. Kostic et al., 2010). However, this cannot explain the synchronous deposition and erosion within adjacent scours in the channel-lobe transition zone. Dorrell et al. (2016) suggested that flow stratification significantly influences the dynamics of hydraulic jumps in these zones. In stratified gravity currents, seafloor scours and their associated hydraulic jumps affect the flow velocity profile and turbulent mixing processes downstream. As a result, not all scours in a channel-lobe transition zone exhibit active hydraulic jumps, and the presence and number of these jumps can

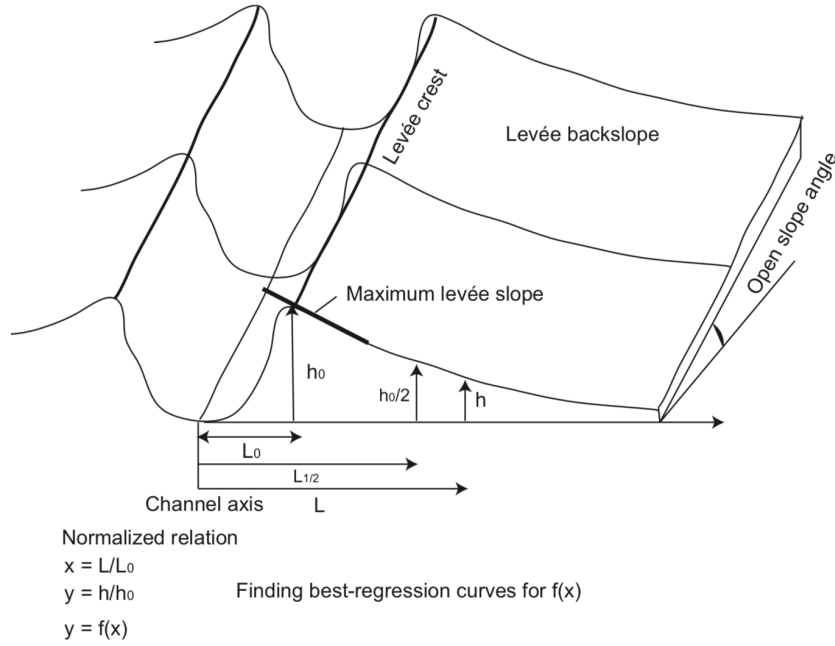


Figure 1.9: Schematic illustration of submarine channel-levee system (Nakajima and Kneller, 2013)

vary with the flow magnitude. Dorrell et al. (2016) also speculated that near-bed stresses do not significantly change downstream of a stratified hydraulic jump, implying that the bulk flow capacity for sediment transport remains relatively consistent. This helps explain why deposition areas are found downstream of broad scour zones in channel-lobe transition zones, as vertical turbulent mixing and maintained bed shear stresses enable sediment to bypass these regions.

One of the astonishing features of the submarine fan systems is the extremely long sinuous submarine leveed channels, which can extend for hundreds and thousands of kilometres (Wynn et al., 2007; Straub et al., 2008; Dorrell et al., 2015). The network of these self-organised channels creates a submarine fan, the largest lobe-shape deposit on our planet (Covault, 2011). The detailed morphology of submarine levees and channels and how they develop has been investigated by seismic data of modern fan (e.g. Nakajima et al., 2009; Nakajima and Kneller, 2013), ancient rock record (e.g. Covault et al., 2016) and numerical simulation (e.g. Dorrell et al., 2015). In this section, the morphological features and development of channel networks are introduced.

1.4.1 Morphology of Submarine Channel-levee System

Submarine channel-levee systems comprise channels as a conduit of density currents and levees formed by the deposits from overspilled turbidity currents (e.g. Nakajima and Kneller, 2013; Peakall and Sumner, 2015). Channel-Levee architectures might contain information about paleo flow conditions such as flow type and vertical flow profile (Skene et al., 2002). The base of channel and channel-fill deposits tend to be relatively coarse sandy sediments, while the levees are mainly composed of fine muddy sediments (e.g. Babonneau et al., 2010; Covault et al., 2016). This upward-fining trend of levees may reflect the vertical flow structure

of turbidity currents (Skene et al., 2002). Covault (2011) differentiated 20 modern submarine canyon and channel longitudinal profiles into three groups: i) convex, ii) slightly concave, and iii) very concave groups. They concluded that as a general trend, the longitudinal profile corresponds with a continental-margin type, distinct depositional architecture such as preexisting depositional relief and sedimentary processes by density currents (Covault, 2011).

The submarine channel's and external levee's detailed morphology can be described based on its cross-sectional features. Generally, the channel width ranges from hundreds of meters to a few kilometres, and its depth, which is defined as the length between the base of the channel and the top of the external levee (Fig.1.9), ranges from 10s meters to several hundreds of meters (e.g. Nakajima and Kneller, 2013) The outer external levee gradually decreases its levee slope as a function of the distance perpendicular to the channel axis. It has been argued whether the outer external levee shows exponential decay or power-law decay (e.g. Birman et al., 2009). Based on observation, Skene et al. (2002) examined the seismic profile of gentle-slope areas at six modern submarine channel-levee systems and assumed that the decay pattern was exponential. On the other hand, Kane et al. (2007) surveyed the Upper Cretaceous rock record and reported examples of submarine levees exhibiting power-law decay. Recently Nakajima and Kneller (2013) examined the seismic profile of several submarine channels at different slope angles and suggested a relationship between decay pattern and angle of slope: power law on steep slopes and exponential on gentle slopes or basin plains.

On the surface of submarine channels, upstream-migrating bedforms, so-called Crescent-Shaped Bedforms (CSBs) are common features (Smith et al., 2005; Smith et al., 2007; Xu et al., 2008; Paull et al., 2010; Paull et al., 2011; Paull et al., 2013). These upstream-migrating bedforms are often interpreted as cyclic steps generated by supercritical turbidity currents (Kostic, 2011a; Covault et al., 2014a; Hughes Clarke, 2016; Hage et al., 2018). Hughes Clarke (2016) reported the direct observation of turbidity currents at the prodelta slope off the mouth of the Squamish River. They concluded that the hydraulic jumps by supercritical turbidity currents are responsible for the development of crescent-shaped bedforms because the bedforms show upstream migration during the flow events and the thickening of flow which can be interpreted as hydraulic jumps are observed just after base of the lee slope.

Migrating sediment waves such as cyclic steps are the most common bedforms on the seafloor, including the submarine channels (Peakall et al., 2000; Kostic, 2011b; Covault et al., 2014b). Cyclic steps occur within flows which alternate supercritical and subcritical. Each step is bounded by hydraulic jumps where the depth-averaged Froude number is around unity (Parker et al., 1996; Kostic et al., 2010). Cyclic steps have two competing effects on sediment-transport efficiency (Sun and Parker, 2005). One of which is the cyclic transition from subcritical to supercritical, and this effect increases transport efficiency. Another effect is energy loss by hydraulic jumps, which reduce the efficiency. Sun and Parker (2005) concluded (although not always) that the existence of cyclic steps generally increases the sediment-transport efficiency in the case

of open channel flows. However, the numerical simulations of Hage et al. (2018) demonstrated that these crescent-shaped bedforms are well reproduced by fluvial models rather than the depth-averaged unstratified models for turbidity currents (Fildani et al., 2006; Kostic, 2011a; Cartigny et al., 2011; Covault et al., 2017). They observed that the lack of laminated sand unit (Bouma T_B division) implies higher near-bed sediment concentration of turbidity currents than the concentration predicted by depth-averaged flows. It is known that in the case of hydraulic jumps in stratified flow, the depth-averaged Froude number is almost always less than unity and sometimes shows different flow behaviour from fluvial currents (Baines, 1998; Dorrell et al., 2016). In stratified flow running along complex topography, because the speed of surface waves and thus the Froude number, is affected by the flow stratification, the depth-averaged Froude number does not provide accurate information about the flow state (Baines, 1998; Thorpe, 2010; Thorpe and Li, 2014; Dorrell et al., 2016). However, our understanding of hydraulic jumps in density-stratified gravity currents remains limited. This is important, and such transitions are crucial to explaining depositional products generated by rapidly decelerating flows, e.g. in the channel lobe transition zone (Dorrell et al., 2016).

1.4.2 Development of Channel-levee Systems

Submarine channel-levee systems develop thorough lateral migration and avulsion, which have some superficial similarities to fluvial systems. The avulsion, by which an active channel is abandoned and a new channel path is created, is a key control of the development of channel-levee systems. Avulsion creates complex channel-levee systems, making it difficult to predict the geometry and distribution of potential reservoir sediments (Kolla et al., 2007). While in some parts, submarine channel systems are similar to fluvial rivers, there are also some unique phenomena to submarine channels. For example, the stratigraphic records of fluvial settings are characterised by lateral accretion of pointbar deposits by channel migration. In contrast, the seismic profiles of submarine channels are characterised by vertical accretion by aggradational channel fill deposits (Jobe et al., 2016). This suggests the flow dynamics between fluvial and submarine settings are fundamentally different.

Avulsion can occur both by internal (autogenic) and external (allogenic) factors (e.g. Peakall et al., 2000; Dorrell et al., 2015). The candidates of allogenic factors responsible for avulsion are, for instance, seafloor uplift (Clark and Cartwright, 2011; Chiang et al., 2012), sea-level changes (Lopez, 2001; Maslin et al., 2006; Kolla et al., 2007) and channel destruction or occlusion by mass-transport events (Kolla et al., 2007; Wynn et al., 2007). Therefore, avulsion points and resultant channel-levee networks potentially possess the record of paleo-environment events. However, turbidity currents can be unconfined in a channel and avulse as channels develop even without these allogenic factors (Mohrig and Buttles, 2007; Dorrell et al., 2015). It is still poorly understood which factor (autogenic or allogenic) is more dominant in developing the channel-levee network. Furthermore, Dorrell et al. (2015) compared the history of relative sea-level change with the avulsion history. Using a simple mathematical model of channel development, they concluded that if the channel-levee system

is too immature, it is robust to allogenic factors. In contrast, as the system matures, it becomes sensitive to allogenic and autogenic factors. In some, such as the Amazon and Bengal fans, the avulsion seems to be concentrated on the upper part of the fan (e.g. Curray et al., 2002; Maslin et al., 2006) while others show a more complex distribution of avulsion points (e.g. Weimer and Buffler, 1988; Picot et al., 2016). Since the avulsion of submarine channels is linked to how the turbidity currents are confined inside the channels (Mohrig and Buttles, 2007; Dorrell et al., 2015), the flow behaviour inside the sinuous channels must be clarified to discuss the avulsion criterion and the resultant channel morphology.

1.4.3 Flow Behaviour in Submarine Channels

The flow behaviour of channelised turbidity currents is inherently unsteady and three-dimensional. As mentioned in the above section, migrating sediment waves such as cyclic steps are common in submarine channels. Due to the transition between super- and subcritical flow conditions over the cyclic steps, the flow velocity of turbidity currents should periodically fluctuate (e.g. Dorrell et al., 2016). The hydraulic jumps bounding each step mix the lower dense flow layer periodically (Dorrell et al., 2016). Furthermore, helical flow at channel bends, which arises due to the centrifugal forces and the pressure forces resulting from superelevation (Peakall and Sumner, 2015), also plays a significant role in mixing processes. Since the helical flow strongly affects the sedimentation processes within a channel, it can be one of the key control factors on how channels develop (Rozovskii, 1957; Peakall et al., 2000). In terms of the long-runout of turbidity currents, the helical flow and superelevation at channel bends are believed to reduce the effect of the ‘slow diffusion zone’/‘eddy-transport barrier’, which is mentioned in the vertical profile section (section 1.3.3) because these processes can vertically mix the stratified flow (Keevil et al., 2006; Straub et al., 2011; Azpiroz-Zabala et al., 2017b; Dorrell et al., 2018b).

1.5 Discussion

1.5.1 Significance of Flow Stratification

The flow stratification of turbidity currents is a key control on the flow behaviour in terms of entrainment of ambient fluid, the efficiency of sediment transport, the process of erosion and deposition, and thus the development of resultant deposits they create, as discussed above. Despite recent improvement in computational technology, high-resolution numerical simulation such as DNS and RANS is still too computationally expensive to apply to the field scale turbidity currents. One of the effective ways to assess the flow behaviour of field scale turbidity currents is to introduce vertical shape factors into depth-averaged shallow water models such as the three- and four-equation models of Parker et al. (1986). However, because this method requires an accurate parametrization of the profiles in terms of the flow parameters (which is not yet available) these models still provide a poor prediction (e.g. Dorrell et al., 2014). There are three key problems of current

depth-averaged shallow water models for turbidity currents: 1) it is not obvious how to calculate the flow height, 2) the suspended-sediment concentration is not described properly, and 3) the shape factors which are applied to models are inappropriate.

Firstly, the definition of flow height contains some difficulties since the actual upper boundary of a turbidity current is a three-dimensional structure and a gradual transition from turbid fluid to clear water rather than the distinct flat surface (e.g. Altinakar, 1988). Previously, in flume experiments, the measurement of this vague boundary has been conducted by the visual observation using dye to increase the contrast or/and using shadowgraph technique (Merzkirch, 1987), direct measurements with siphon tubes or acoustic backscatter. The direct measurements of flow concentration using siphon tubes or acoustic backscatter might be better than the subjective visual observation. However, even with these measurement methods, the flow height is difficult to observe. In the case of measurement with siphon tubes, it is able to measure the flow concentration at a specific height with high accuracy, but it is not suitable for detecting the height of the boundary. Since the transition between turbid fluid and clear water is gradual, the measurement with acoustic backscatter also contains a large uncertainty in terms of dilute flow. To avoid these problems, many researchers have been applying the momentum equations introduced by (Ellison and Turner, 1959) to calculate flow height and layer-averaged parameters from their measurement data, which are given by,

$$Uh = \int_0^{\infty} \langle u \rangle dz \quad (1.80)$$

$$U\Phi h = \int_0^{\infty} \langle u \rangle \langle \phi \rangle dz \quad (1.81)$$

$$U^2 h = \int_0^{\infty} \langle u \rangle^2 dz. \quad (1.82)$$

However, the flow height estimated by these equations (1.80–1.82) is always lower than the height where the flow velocity becomes zero. Thus, even though this method is more objective than other methods, the resultant flow height always underestimate the stratification of turbidity currents. Secondly, the suspended-sediment concentration ratio between near-bed and specific height r_0 is derived from the Rouse profile (Parker et al., 1986). However, as mentioned above, the Rouse profile is only appropriate for the equilibrium open-channel flow, which poorly captures the density stratification of turbidity currents. The assumption of a Rouse profile Eq.(1.35) implies a linear decay of shear stress. In the case of turbidity currents, on the other hand, the shear stress must be related to the flow profile. Here, I demonstrate how the shear stress for turbidity currents can be described with the vertical flow structures. The shear stress for turbidity currents can be described as

$$\tau = \tau_b f_1(\langle \phi \rangle, \tilde{z}) = \rho_f u_*^2 f_1(\phi, \tilde{z}). \quad (1.83)$$

where $\tilde{z} = z/h$ denotes non-dimensional specific height and $f_1(\langle \phi \rangle, \tilde{z})$ is a specific function of sediment

concentration. The assumption of Prandtl (1925) can be revised for turbidity currents as

$$\tau = \frac{\rho_f \nu_t}{h} f_2(\langle \phi \rangle, \tilde{z}) \frac{\partial \tilde{u}}{\partial \tilde{z}}. \quad (1.84)$$

where $f_2(\langle \phi \rangle, \tilde{z})$ is a specific function of sediment concentration and specific height. From Eq.(1.83) and (1.84),

$$\nu_t = \frac{u_*^2 f_1(\langle \phi \rangle, \tilde{z})}{\frac{\partial \tilde{u}}{\partial \tilde{z}} f_2(\langle \phi \rangle, \tilde{z})} h. \quad (1.85)$$

Since $\partial \tilde{u} / \partial \tilde{z}$ tends to zero at velocity maximum, from Eq.(1.85), it is clarified that f_1 and f_2 must satisfy following relationships,

$$\left. \frac{f_1(\langle \phi \rangle, \tilde{z})}{f_2(\langle \phi \rangle, \tilde{z})} \right|_{z \rightarrow z_{\max}} \rightarrow a \frac{\partial \tilde{u}}{\partial \tilde{z}} \quad (1.86)$$

If the specific description of the two unknown functions f_1 and f_2 are clarified, the appropriate profiles for the turbidity currents will be acquired.

1.5.2 Equilibrium state of turbidity currents

Since the driving force of turbidity currents is the excess density produced by suspended sediments, whether the flow is erosional or depositional, plays a significant role in flow sustainability and the development of submarine architectures. Recent theoretical models of suspended load transport (Dorrell et al., 2018a) successfully expanded the previous flux balance model by incorporating the concept of flow power and polydisperse suspensions, which suggests the sediment size distribution plays a dominant control on the net erosional-depositional threshold.

However, whether these models can be applied to turbidity currents is still questionable. It is known that the flow power models describe the equilibrium state of open-channel flows (Wan and Wang, 1994b; Maren et al., 2009); this model is based on some hypotheses that are not validated for the turbidity currents. First of all, the flow power model and other models assume that the flow is in equilibrium. Although the flow duration of turbidity currents can be a few days to weeks (Mulder and Alexander, 2001; Mulder et al., 2003), the turbidity currents are vertically mixed by various events through the submarine channels and continuously get diluted by entrainment of ambient water. Thus, what proportion of natural turbidity currents actually reach a near equilibrium state is still unknown. Thus, it is doubtful that a flow power model is suitable for turbidity currents. Secondly, in the flow power model, the available flow power, which is proportional to the TKE production rate, is assumed to be proportional to shear velocity cubed and thus flow velocity cubed. However, this assumption is based on open-channel flow theories: the law of the wall (Eq.1.30), the turbulent-viscosity hypothesis (Eq.1.27), and the parabolic profile of eddy viscosity (Eq.1.36). Both the law

of the wall and the parabolic profile of eddy viscosity are derived from the vertical flow profile of open-channel flow. Thus, it could be a poor approximation for turbidity currents. Thirdly, the flow power model assumes that the dominant particle-support mechanism is the turbulent motion of fluid and that other mechanisms, such as particle-particle interactions, are negligible. However, this transition of the dominant particle-support mechanism between turbulent motion and particle-particle interaction is still poorly understood. In the open-channel flow, the collapse of correlation between flow power and the work done to keep sediment in suspension has been observed in high concentration flow by Wan and Wang (1994b) in the Yellow River, China, whilst there are no observational data that show the transition to a particle-support mechanism for turbidity currents.

1.6 Aim and research questions

Aim: This project aims to understand the material-transport dynamics of natural-scale turbidity currents. As mentioned in the literature review, the sediment-laden gravity-driven flows play a dominant control in the sediment transport between continents and deep marine systems. The sediment architectures they create are expected to record the previous 100-1000s years-scale environmental events such as tectonic events or relative sea-level changes. In spite of the importance, how those submarine systems respond to the environmental changes is still poorly constrained due to the limitations of observation, computational costs, and the destructive nature of turbidity currents. Developing practical high-accuracy models requires a detailed understanding of the flow behaviours of turbidity currents and the dominant factors that affect morphological developments. I will deliver the aim to improve the understanding of the development of submarine fan systems through addressing the following research questions.

Question 1: What controls the vertical structure of turbidity currents and how does this affect flow dynamics?

Although the past 100 years of research into turbidity currents have assumed that turbidity currents are similar to fluvial rivers, as mentioned in section 1.5.1, the difference between the vertical structure of fluvial rivers and turbidity currents seems to be one of the key controls of the long-runout of turbidity currents and the evolution of channel-levee networks. The limitations of computational cost and observational techniques impede our better understanding of the relationships between vertical flow structures and channel evolution. Here, to analyse the variety of vertical flow profiles of turbidity currents, we gather the available dataset of flow profiles from the past literature on flume experiments. Statistical analyses of this dataset are expected to provide quantitative relationships between the flow structure and other flow parameters. This data compilation also allows us to analyse the differences in the sediment transport mechanics of turbidity currents compared with rivers.

Question 2: Is the energetics of turbidity currents similar to the rivers?

Due to the long-runout of turbidity currents, a better understanding of the energetics of the near-equilibrium turbidity currents is fundamental to predicting the material transport of turbidity currents. Equilibrium flow theory in open-channel flows is currently used in the models of turbidity currents without validation. While the first question focuses on the internal structures of the turbidity currents, here, the energy budget of turbidity currents is analysed. As mentioned in section 1.5, the concept of autosuspension is that the total shear production rate of TKE will be balanced with the work done to keep sediment in suspension. This energy balance is the least condition for a turbidity current to traverse a long distance. We investigate this energy balance, comparing the data of turbidity currents and rivers to understand how efficient turbidity currents are in material transport.

In the next three chapters, I address these questions. Firstly, in Chapter 2, I assemble a dataset of turbidity currents from the past literature on flume experiments and the direct observation of natural-scale events. I also present the set of large-scale flume experiments designed to fill the gaps in available data from the past literature. The following chapters are based on the combined dataset of turbidity currents from literature and newly conducted flume experiments. Secondly, in Chapter 3, I present the statistical analysis of vertical flow structures and the development of empirical models for predicting turbidity currents' flow velocity and concentration profiles to address research question 1. Finally, in Chapter 4, I present the theoretical analysis of the sediment-load capacity of pseudo-steady turbidity currents, comparing the compiled turbidity currents with fluvial data to address the research question 2.

Chapter 2

Flume Experiment and Data Collection

2.1 Introduction

In this chapter, the methodology used in this study is detailed. Firstly, the large part of the analysis is based on the compiled flow profiles dataset. The profiles are gathered from i) natural-scale turbidity currents, ii) laboratory-scale experiments from past literature, and iii) newly designed flume experiments conducted at the Total Environmental Simulator (TES), at The Deep. In the following section, the detailed methodology of data collection is elaborated.

2.2 Data collection

To address the research question of vertical flow structure of near-equilibrium turbidity currents, wide variety of measured dataset of density currents are compiled from literature. The target data is the time-averaged stream-wise flow velocity and concentration profiles measured from the prolonged body part of density currents. The criteria require choosing near-equilibrium datasets, therefore lock-exchange laboratory experiments are excluded, since in this type of experiments, the flows tend to lack the prolonged body and only consist of head and tail. Also, the data from the head or tail of turbidity currents are omitted from all sources. Although the criteria described above are applied for all the analyses in this project, more strict criteria are set when required in each chapter.

2.2.1 Online data source

source	TYPE	Slope (%)	Material	d_{50} (μm)	Φ_0 (vol.%)	Measurement tools
Michon et al. (1955)	I	0.3–3.6	Kaolinite	14.6	0.06–0.43	$\langle u \rangle$: MPCM $\langle \phi \rangle$: Siphon array (4–12)
Tesaker (1969)	I	5.0–12.5	Quartz Kaolinite	360–410 1.1–1.5* ⁴	1.60–16.3	$\langle u \rangle$: Velocity meters* ⁶ (3) $\langle \phi \rangle$: Siphon array (3)
Altinakar (1988)	I	1.0–2.96	Quartz Salt	14 / 32 –	0.13–0.47	$\langle u \rangle$: MPCM $\langle \phi \rangle$: Siphon array (16)
García (1993)	I	8	Silica	9	0.13–0.14	$\langle u \rangle$: MPCM $\langle \phi \rangle$: Optical probes
Packman and Jerolmack (2004)	I	1.0	Quartz Kaolinite	12 1.3	1.13	$\langle u \rangle$: ADV $\langle \phi \rangle$: Siphon array (6)
Amy et al. (2005)	I	5.2	Glycerol	–	–	$\langle u \rangle$: UVP array (8) $\langle \phi \rangle$: Siphon array (5)
Islam and Imran (2010)	I & II	0.0–8.0	Silt / Salt	25	0.61 / –	$\langle u \rangle$: ADV $\langle \phi \rangle$: Siphon array (20)
Sequeiros et al. (2010a)	I	0.85–5.0	Salt* ³	–	–	$\langle u \rangle$: ADV $\langle \phi \rangle$: Siphon array (10)
Sequeiros et al. (2010b)	I	5.0	Salt* ³	–	–	$\langle u \rangle$: ADV $\langle \phi \rangle$: Siphon array (10)
Cartigny et al. (2013)	II	12.3–21.3	Quartz	160	9.0–26.0	$\langle u \rangle$: Angled UVP $\langle \phi \rangle$: –
Varjavand et al. (2015)	I	1.25	Kaolinite	13.4	0.31–0.50	$\langle u \rangle$: Angled UVP $\langle \phi \rangle$: Siphon array (14)
Fedele et al. (2016)	I	8.7–17.6	Salt	–	–	$\langle u \rangle$: ADV $\langle \phi \rangle$: Siphon array (20)
Breard and Lube (2017)	I	15.8	Ignimbrite	250	–	$\langle u \rangle$: PIV $\langle \phi \rangle$: LC & PT
Leeuw et al. (2018a)	I & II	15.8–19.4	Sand	141	17.0	$\langle u \rangle$: Angled UVP $\langle \phi \rangle$: Siphon array (4)
Leeuw et al. (2018b)	II	19.4	Sand	131	17.0	$\langle u \rangle$: Angled UVP $\langle \phi \rangle$: –
Hermidas et al. (2018)	II	10.5–16.7	Quartz Kaolinite	150/46 0.18	9.0–21.0	$\langle u \rangle$: Angled UVP $\langle \phi \rangle$: –
Sequeiros et al. (2018)	I	9.0	Plastic	57	2.03	$\langle u \rangle$: Angled UVP $\langle \phi \rangle$: Siphon array (11)
Eggenhuisen et al.	I	7.0–14.0	Sand	130	17	$\langle u \rangle$: Angled UVP

(2020)						$\langle\phi\rangle$: Siphon array (4)
Farizan et al. (2019)	I	1.0	Kaolinite	11	0.07–0.25	$\langle u\rangle$: ADV $\langle\phi\rangle$: ADV
Kelly et al. (2019)	II* ¹	3.5	Salt	–	–	$\langle u\rangle$: ADV $\langle\phi\rangle$: –
Koller et al. (2019)	I* ²	0.9–2.6	Salt	–	–	$\langle u\rangle$: UVP array (10) $\langle\phi\rangle$: Siphon array (6)
Brosch and Lube (2020)	I	10.5	Ignimbrite	245	–	$\langle u\rangle$: PIV $\langle\phi\rangle$: LC & PT
Pohl et al. (2020)	I	14.1	Quartz	133	15.0	$\langle u\rangle$: Angled UVP $\langle\phi\rangle$: Siphon array (4)
Simmons et al. (2020)	I	0.7	Silt	9.9–11* ⁵	–	$\langle u\rangle$: ADCPs $\langle\phi\rangle$: ADCPs

MPCM: Micro-Propeller Current-Meter; UVP: Ultrasonic Velocity Profiler;

ADV: Acoustic Doppler Profiler; ADCPs: Acoustic Doppler Current Profilers

PIV: Particle Image Velocimetry; LC: s-beam Load Cell; PT: Pressure Transducer

Table 2.1: Summary of compiled sources. From the left, each column represents corresponding reference of the source, data type, slope of the bed at the measurement location, type of material used for generating the excess density of the flow, median particle size, initial volumetric concentration of material, and the type of equipment used for velocity and concentration measurement respectively. The figures in the parentheses represent the number of measurement devices in the array. *¹ Numerical simulation of Reynolds-averaged Navier-Stokes model. *² Limited information about concentration profiles reported in this study. *³ There are also experiments with sediment, but the availability of flow profiles is limited. *⁴ Original reported values of particle size from hydrometer analysis. *⁵ d_{50} from Event 1, 4, and 5 from the original source. *⁶ Velocity meters are special equipment that are designed for their particular study.

The compiled published sources are listed in the table 2.1. In total, 22 laboratory-experiment (2 of them are experiments of pyroclastic density currents), 1 numerical simulation, and 1 direct-observation source were gathered. Hereafter, the dataset is classified into the following two groups: i) TYPE I: dataset in which both velocity and concentration profiles are available, and ii) Type II: data in which only velocity profiles are available but concentration profiles. Each source uses different tools for vertical-profile measurement. For example, the velocity measurement of flume experiments can be categorised into 5 different types: Micro-Propeller Current-Meters (MPCMs), velocity meters, Ultrasonic Velocity Profilers (UVPs), Acoustic Doppler Velocity probes (ADVs).

The MPCMs are used in the experiments in 20th centuries. The typical micro-propeller has a cage diameter of 1.5cm, its measuring head consists of a five-blades rotor mounted on a hard stainless steel spindle. When the rotor is immersed in the water, the passage of the rotor blades past the gold wire tip slightly varies the measurable impedance between the tip and the tube. This variation is used to modulate at 15kHz carrier

signal generated within the indicating instrument which is in turn applied to the electronic detector circuits. Since an automatic compensation is made for the changes in liquid conductivity, the probe can be used for both type of gravity current experiments, regardless of the salt or sediment content in the liquid. On the other hand, one MPCM can only measure the one-direction velocity component at single point. Thus, multiple MPCMs are required to obtain the enough resolution to estimate the full vertical flow profile, which increases the flow obstruction. Further, the velocity range which MPCMs can measure is limited (cf. 2.0 to 150 [cm/s]) compared with other measurement tools which use ultrasonic signal.

The UVP (Ultrasound Velocity Profile) represents both a method and a device for measuring an instantaneous velocity profile in liquid flow along the ultrasonic beam axis by detecting the Doppler shift frequency of echoed ultrasound as a function of time. Since each UVP transducer can measure one projection of a complete flow field, simultaneous measurement with several transducers makes complete measurement of the flow field possible. In some of the laboratory-scale experiments of density currents (e.g. Cartigny et al., 2013; Leeuw et al., 2018a; Leeuw et al., 2018b; Hermidas et al., 2018; Eggenhuisen et al., 2020; Pohl et al., 2020), a single UVP probe is positioned in a certain angle tilted from the bed-normal direction at a certain height where the probes do not obstruct a flow. Then, assuming the bed-normal component of flow velocity is small, the streamwise velocity component is estimated from the angled UVP measurement. Alternatively, some of the experiments (e.g. Amy et al., 2005; Koller et al., 2019) use multiple UVP probes aligned parallel to the streamwise direction so that each probe can measure the true streamwise velocity component. The resolution of data (channel numbers in the measurement window) of each probe is dependant on the transmitting frequency of signal. The maximum measurable velocity component range is also limited by the transmitting frequency and pulse repetition frequency of the signal. Thus, there is a trade-off between measurable velocity range and the measurement resolution.

ADVs also measure the Doppler shift frequency by transmitting a pair of short sound pulses of a specific frequency into the water column. While the UVP transducer can measure one projection of a flow field, ADVs can measure the instantaneous velocity field in three different direction component by its three receiving probes. Thus, the one of the advantages of using ADVs is its ability to measure the instantaneous three-dimensional turbulent field of a flow. The major drawback of ADVs are that, generally, the measurement window is relatively smaller than UVPs, (which also depends on the signal frequency of each probe). Also, since ADVs have a relatively large head, it may obstruct the flow more than a single probe of UVP does.

For both UVPs and ADV, each source used a different number of probes, sampling rate, and angle of mounting. To perform consistent analysis, here, only the original measurement points are extracted from each source to minimise the errors. Then, a consistent interpolation and extrapolation method are applied to recover the full vertical profiles.

2.2.2 Estimation of characteristic flow parameters

Here, the detailed methodology of the estimation of characteristic flow parameters based on the compiled sources are elaborated. The process can be summarised into three steps: (i) Extraction of original measurement data from the compiled sources, (ii) the reconstruction of full flow profile of streamwise flow velocity and concentration, and (iii) the calculation of each flow parameters based on the estimated flow profiles and other meta data (such as the energy slope and the dimension of laboratory-scale channel). The data from the first step only provide discrete values of measured velocity and concentration at certain measurement heights in each experiment. However, to estimate the depth-integral or depth-averaged flow parameters, full continuous profiles are required. To this end, in the second step, the interpolation and extrapolation of discrete measurement points are conducted. Interpolation is a method of constructing a continuous function based on the range of a discrete set of known data points. On the other hand, extrapolation is a method of constructing a continuous function beyond the original observation range, of the value of a variable on the basis of its relationship with another variable. Interpolation is conducted to obtain the continuous profile within the range of original discrete data points, and then, the extrapolation is conducted to extend the continuous profile to the upper and lower interface of a flow. Once the full profiles are obtained, each characteristic flow parameters are calculated as the final step.

Extraction of original measurement data of flow profile Different procedures are required to extract the data from the different sources, depending on how the data was presented. The dataset gathered from literature provide (i) raw measurements or (ii) plots of the vertical profile. Hence two different methods are adopted in order to compare these datasets. In the first case, the raw velocity measurements are directly used to reconstruct the flow profiles. In the second case, original measurements point of vertical velocity and concentration profiles are extracted by using a graph-read software. However, some of the sources have less than three velocity or concentration values for each vertical-profile, which are not enough to apply the extrapolation method. Here, assuming that the potential errors due to the choice of interpolation and extrapolation near the elevation of maximum velocity are relatively small, a few data points are manually added near the original data points along the curve provided in each original source.

Estimation of full continuous flow profiles There are three steps to the procedure: i) data formatting, ii) estimation of flow height and near-bed concentration, and iii) interpolation and extrapolation. Detailed procedures of each step are described in this section.

The first step is formatting the data to prepare for the application of interpolation and extrapolation. This procedures include excluding the obvious noise or error data points, imposing the boundary conditions, and aligning each data point in a consistent order. Firstly, the data points which are below the bed height is omitted. The also the data points of which relative velocity to the background velocity show negative values

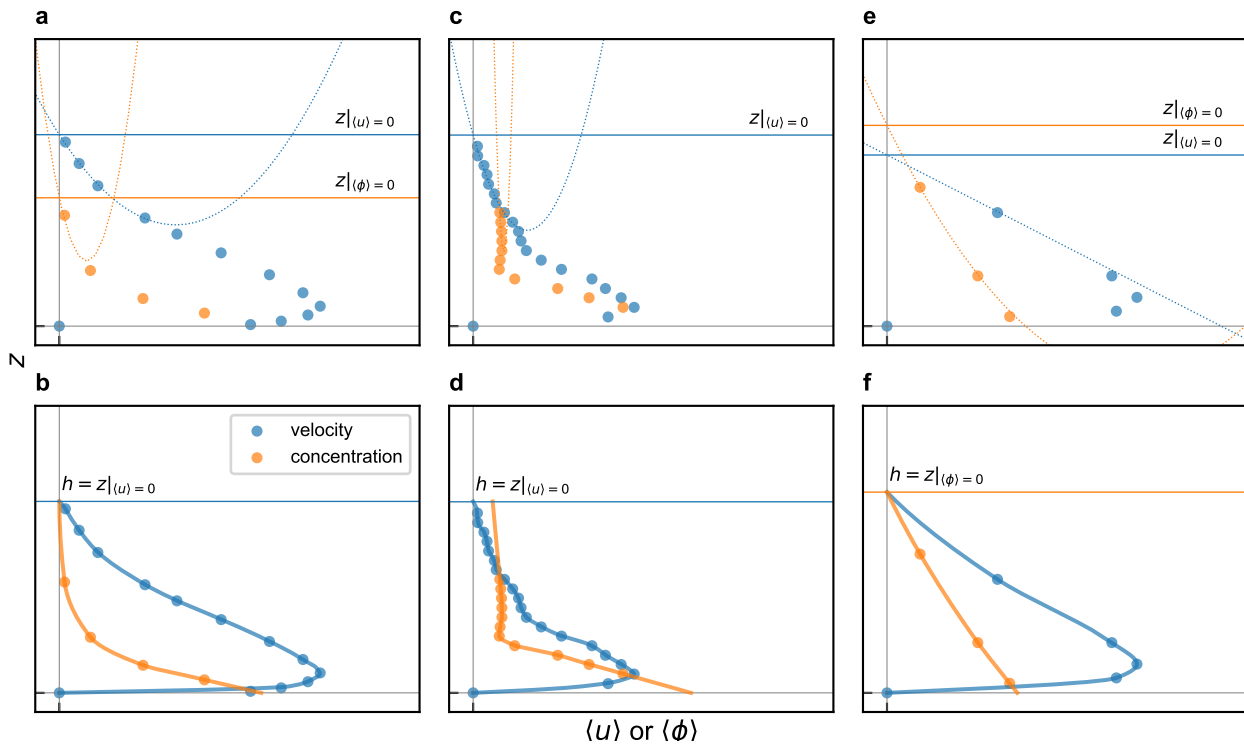


Figure 2.1: Schematic diagram of interpolation and extrapolation procedures in three different cases: a) b) $z|_{\langle \phi \rangle=0} < z_{u,n}$. c) d) $z|_{\langle u \rangle=0} < z|_{\langle \phi \rangle=0}$. e) f) $z_{u,n} < z|_{\langle \phi \rangle=0} < z|_{\langle u \rangle=0}$. Figures in the top row (a, c, e) visualise the two different flow heights ($z|_{\langle u \rangle=0}, z|_{\langle \phi \rangle=0}$) estimated from the raw measurement points, while Figures in the bottom row (b, d, f) visualise the finalised flow height and fully reconstructed velocity and concentration profiles based on the method described in the main text. Blue and orange markers represent the original measurement values.

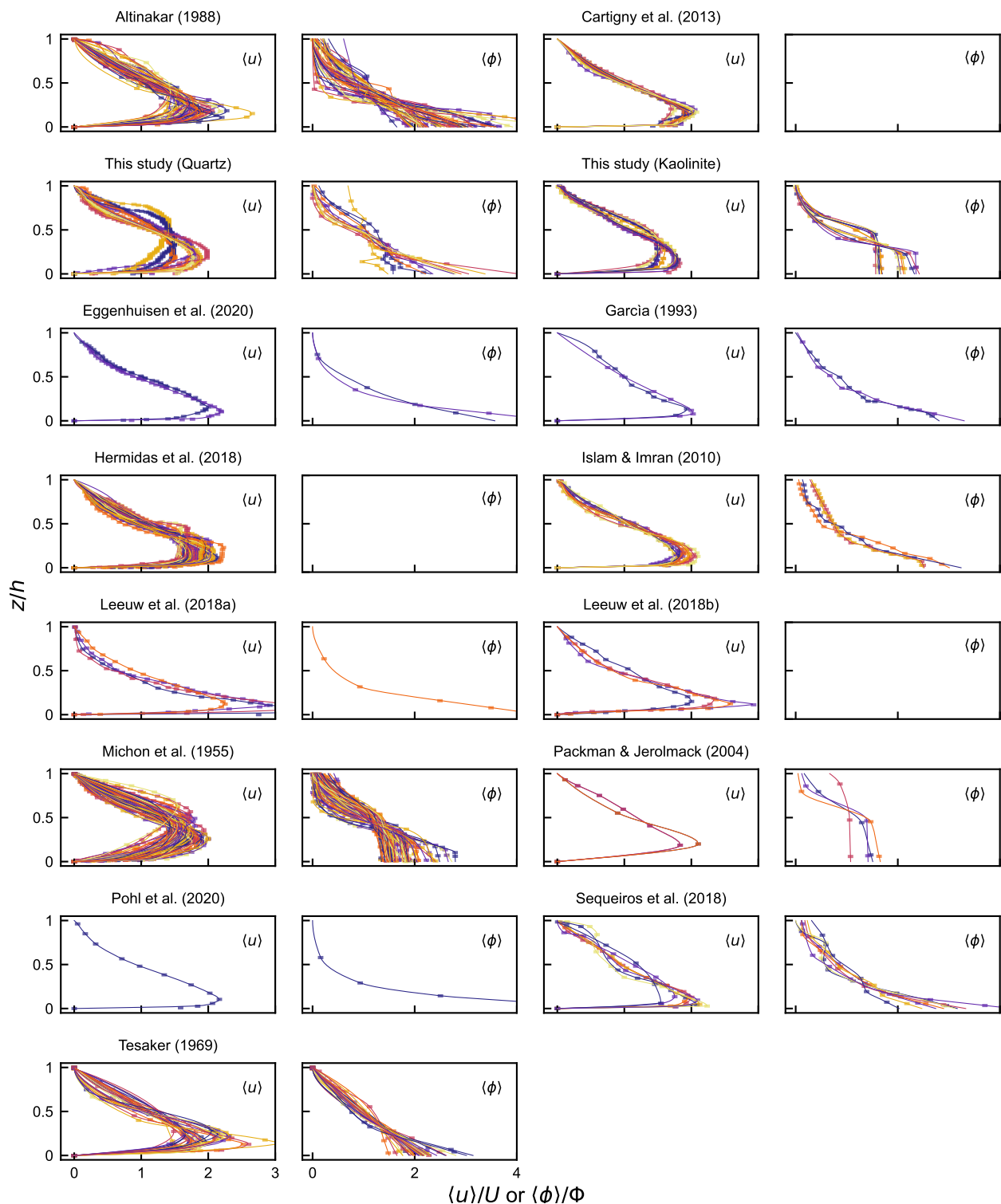


Figure 2.2: For each source, velocity profiles are plotted in the left figure, and concentration profiles in the right. X-axes are either flow velocity or flow concentration which are normalised by depth-averaged values, and Y-axes are elevation z which is normalised by flow height h .

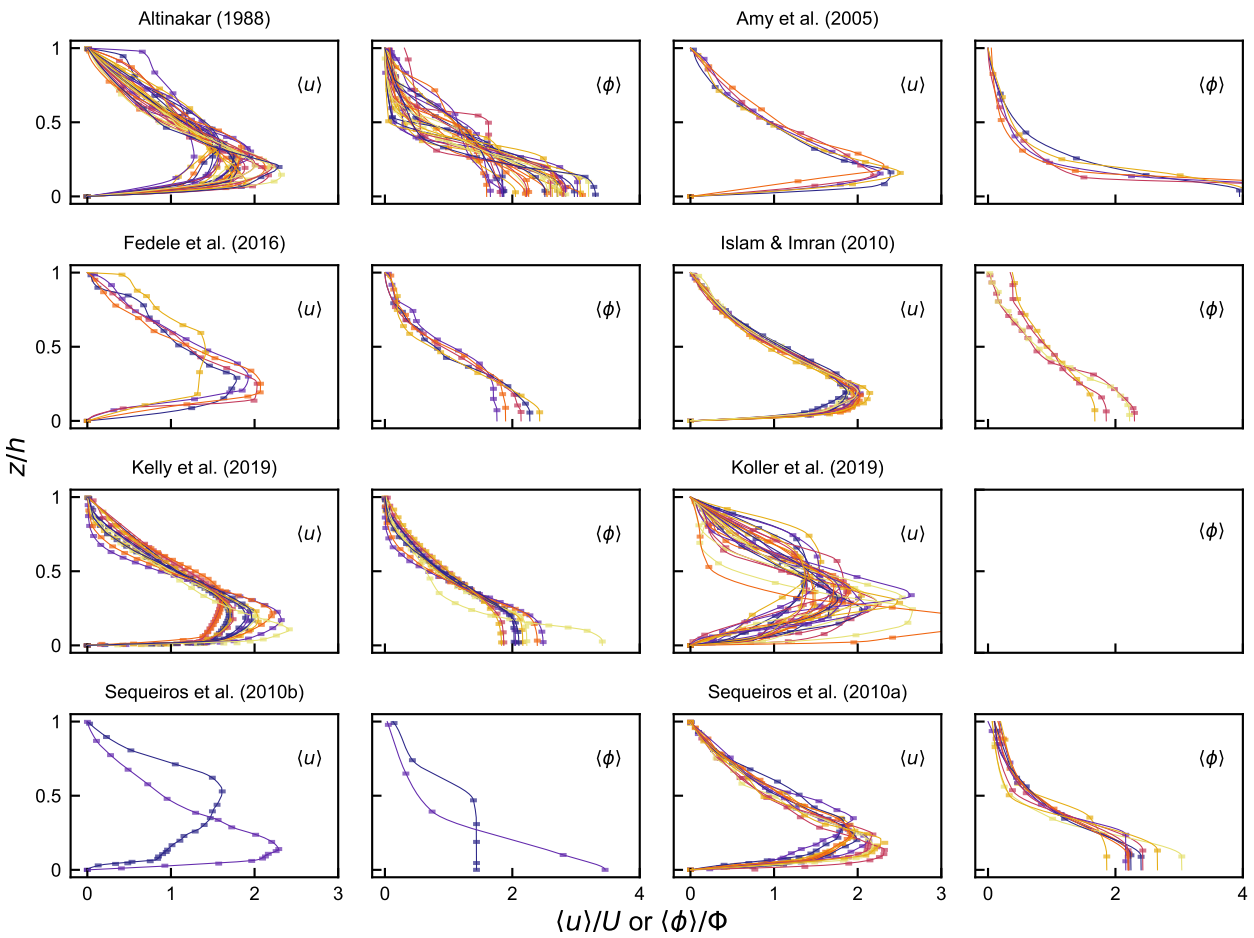


Figure 2.3: For each source, velocity profiles are plotted on the left, and concentration profiles are in the right figure. X-axes are either flow velocity or flow concentration which are normalised by depth-averaged values, and Y-axes are elevation z which is normalised by flow height h .

are omitted so that the return flow is excluded.

To impose the boundary condition, let $P_{\langle u \rangle} = [\mathbf{x}_{\langle u \rangle,1}, \mathbf{x}_{\langle u \rangle,2}, \dots, \mathbf{x}_{\langle u \rangle,n}]$ and $P_{\langle \phi \rangle} = [\mathbf{x}_{\langle \phi \rangle,1}, \mathbf{x}_{\langle \phi \rangle,2}, \dots, \mathbf{x}_{\langle \phi \rangle,m}]$ denote the lists of extracted coordinates from the velocity and concentration profiles. n and m denote the number of extracted measurement points of velocity and concentration profiles respectively, and $\mathbf{x}_{u,i} = (\langle u \rangle|_{z=z_{u,i}}, z_{u,i})$ and $\mathbf{x}_{\phi,i} = (\langle \phi \rangle|_{z=z_{\phi,i}}, z_{\phi,i})$ denote the i^{th} extracted point. The data points are aligned from the lowest to highest elevation so that $z_i < z_{i+1}$. That is, $z_{u,0}$ and $z_{\phi,0}$ are the lowest original measurement elevations and $z_{u,n}$ and $z_{\phi,m}$ are the highest measurement elevations. Then, we impose following boundary conditions.

$$\langle u \rangle|_{z=0} = \langle u \rangle|_{z=h} = 0, \quad (2.1)$$

which means that the streamwise flow velocity is assumed to vanish at the upper and lower interface. To impose the lower boundary condition ($\langle u \rangle|_{z=0} = 0$), an artificial data point $\mathbf{x}_{u,\text{bed}} = (0, 0)$ is inserted into $P_{\langle u \rangle}$.

The next step is to estimate the flow height, which is done in two steps: i) calculate $z|_{\langle u \rangle=0}$ and $z|_{\langle \phi \rangle=0}$, and then ii) evaluate the flow height based on a comparison between $z|_{\langle u \rangle=0}$ and $z|_{\langle \phi \rangle=0}$. Firstly, the interpolation of $P_{\langle u \rangle}$ and $P_{\langle \phi \rangle}$ is conducted using PchipInterpolator function from Scipy, a Python package. This function provides piecewise cubic Hermite interpolation (Fritsch and Butland, 1984). This interpolation method determines the derivative at a given point based on the signs of slopes of adjacent two data points. If the sign is different each other between adjacent points, then the derivative at the given point becomes 0, which prevents the overshooting (Fritsch and Butland, 1984). For instance, let $[x_0 < x_1 < \dots, < x_n]$, $[y_0, y_1, \dots, < y_n]$ denotes a specific x and y coordinates of a given dataset. Let f denotes the piecewise cubic interpolation function so that $f(x_i) = y_i$. The basic scheme of piecewise cubic interpolation is to choose the proper function, G , to describe the derivative values $f'_i(x_i)$ of a given points (x_i, y_i) (Fritsch and Butland, 1984). Here, the derivative of each point is calculated by following function

$$G(S_{i-1}, S_i, h_{i-1}, h_i) = \begin{cases} \frac{S_{i-1}S_i}{\alpha S_i + (1-\alpha)S_{i-1}} & \text{when } S_{i-1}S_i > 0, \\ 0 & \text{otherwise.} \end{cases} \quad (2.2)$$

$$\text{where } \alpha = \frac{1}{3} \left(1 + \frac{h_i}{h_{i-1} + h_i} \right) \quad (2.3)$$

where $S_i = (y_{i+1} - y_i)/(x_{i+1} - x_i)$ and $h_i = x_{i+1} - x_i$ denotes the slope of adjacent two points, One of the benefits of this interpolation method is that the profile is not oversimplified, by having the original data populating the interpolated curve. Let $f_{\langle u \rangle}(z)$ and $f_{\langle \phi \rangle}(z)$ denote the interpolated functions. Then, to obtain enough data points for subsequent data-processing, 500 data points are extracted from the interpolated

function as follow,

$$P_{f,\langle u \rangle} = [(f_{\langle u \rangle}(z_{fu,0}), z_{fu,0}) \dots (f_{\langle u \rangle}(z_{fu,499}), z_{fu,499})], \quad P_{f,\langle \phi \rangle} = [(f_{\langle \phi \rangle}(z_{f\phi,0}), z_{f\phi,0}) \dots (f_{\langle \phi \rangle}(z_{f\phi,499}), z_{f\phi,499})]. \quad (2.4)$$

It should be noted that the points $(f_{\langle u \rangle}(z_{fu,499}), z_{fu,499})$ and $(f_{\langle \phi \rangle}(z_{f\phi,499}), z_{f\phi,499})$ correspond to the original data points with the highest elevations, $\mathbf{x}_{\langle u \rangle, n}$ and $\mathbf{x}_{\langle \phi \rangle, m}$ respectively.

For the estimation of $z|_{\langle u \rangle=0}$ and $z|_{\langle \phi \rangle=0}$, quadratic-function curve fittings are conducted against a upper part of the both velocity and concentration profile (Fig. 2.1a,c,e). Although the higher polynomial curve fittings usually provide less residuals of fittings, they also tend to cause overshooting, especially for the extrapolation. Yet, since the linear fitting is too simple, and thus, here, quadratic (2nd-order polynomial) curve fitting is conducted to estimate $z|_{\langle u \rangle=0}$ and $z|_{\langle \phi \rangle=0}$. For the velocity profile, the range of curve fitting is between $z_{fu, u_{\max}}$ and $z_{fu,499}$, where $z_{fu, u_{\max}}$ is the nearest data point to the velocity maximum. For the concentration profile, the range is between $z_{f\phi,249}$ and $z_{f\phi,499}$, where $z_{f\phi,249}$ denotes the data point at the middle height of interpolated region. The best fit quadratic functions, g_u and g_ϕ are given as,

$$g_u(\langle u \rangle) = a_1 \langle u \rangle^2 + a_2 \langle u \rangle + a_3, \quad g_\phi(\langle \phi \rangle) = b_1 \langle \phi \rangle^2 + b_2 \langle \phi \rangle + b_3. \quad (2.5)$$

where (a_1, a_2, a_3) and (b_1, b_2, b_3) are the coefficients of best-fit curves determined by the least-square method, with the condition $a_1 > 0$ and $b_1 > 0$ imposed to avoid an unrealistic profile shape. Then, $z|_{\langle u \rangle=0}$ and $z|_{\langle \phi \rangle=0}$ are obtained as follow,

$$z|_{\langle u \rangle=0} = g_u(0), \quad z|_{\langle \phi \rangle=0} = g_\phi(\phi_{\text{ambient}}). \quad (2.6)$$

where ϕ_{ambient} is the flow concentration of ambient fluid. Then, the flow height is given by,

$$h = \begin{cases} z|_{\langle u \rangle=0} & \text{when } z|_{\langle u \rangle=0} \leq z|_{\langle \phi \rangle=0} \text{ or } z|_{\langle \phi \rangle=0} < z_{u,n}, \\ z|_{\langle \phi \rangle=0} & \text{when } z_{u,n} < z|_{\langle \phi \rangle=0} \leq z|_{\langle u \rangle=0}. \end{cases} \quad (2.7)$$

where the flow height is defined as the zero-velocity height when zero-concentration height is higher than zero-velocity height, or zero-concentration height is lower than the highest elevation of the valid original velocity measurement point. The latter case, $z|_{\langle \phi \rangle=0} < z_{u,n}$, sometimes happens when the number data points of density profile are inadequate. In this study, the original velocity measurements are regarded as more reliable than the extrapolated concentration curve. Thus, when $z|_{\langle \phi \rangle=0} < z_{u,n}$ (Fig. 2.1a,b), extrapolation of concentration profile is discarded and $z|_{\langle u \rangle=0}$ is used as the flow depth. Then, a new velocity point at flow height $\mathbf{x}_{\langle u \rangle, h} = (0, h)$ is inserted into P_u . For the concentration profile, the concentration at that flow height,

$\mathbf{x}_{\langle\phi\rangle,h}$ is not necessarily always ϕ_{ambient} . When $z|_{\langle u\rangle=0} \leq z|_{\langle\phi\rangle=0}$, the flow concentration at the flow height is estimated by a piecewise cubic Hermite interpolation of the original measurement points with $(0, z|_{\langle\phi\rangle=0})$. Let $f_{\phi}(z)$ denote the interpolated function. Then, flow concentration at flow height is given as $f_{\langle\phi\rangle}(z = h)$.

Now that the dataset from the literature has been formatted and the flow height has been computed, the final step is to interpolate and extrapolate the rest of the profiles. Extrapolation is required to estimate the near-bed concentration, $\langle\phi\rangle_{\text{bed}}$. For the non-conservative currents, the first-order polynomial curve fit is conducted against the lowest two data points. For the conservative flow, the lowest original measurement point $\langle\phi\rangle|_{z=z_{\phi,0}}$ is used as the near-bed concentration. Then, combining the original measurements points, near-bed points, and flow height points, the following completed data lists were obtained,

$$P'_{\langle u\rangle} = [\mathbf{x}_{\langle u\rangle,\text{bed}}, \mathbf{x}_{\langle u\rangle,1}, \dots, \mathbf{x}_{\langle u\rangle,n}, \mathbf{x}_{\langle u\rangle,h}], \quad P'_{\langle\phi\rangle} = [\mathbf{x}_{\langle\phi\rangle,\text{bed}}, \mathbf{x}_{\langle\phi\rangle,1}, \dots, \mathbf{x}_{\langle\phi\rangle,m}, \mathbf{x}_{\langle\phi\rangle,h}]. \quad (2.8)$$

Finally, by conducting piecewise cubic Hermite interpolation against $P'_{\langle u\rangle}$ and $P'_{\langle\phi\rangle}$, the full profile $\langle u\rangle(z)$ and $\langle\phi\rangle(z)$ were obtained. The full vertical concentration and velocity profile obtained following the method described here, and applied to each dataset considered in this study, are shown in Figure 2.2 (laboratory-scale non-conservative flows), 2.3 (laboratory-scale conservative flows), and 2.8 (natural-scale non-conservative flows).

Turbidity currents from Congo canyon The real-world dataset from Congo canyon is extracted from the publication by Simmons et al. (2020). Here, flow velocity and concentration structures are measured by Acoustic Doppler Current Profilers (ADCPs). In this study, to investigate the flow dynamics of quasi-equilibrium natural-scale turbidity currents, relatively long-duration (more than 5 days) events are chosen (Event 01, 04, and 05). Some long-duration events in which velocity and concentration fields drastically changed during the flow event (such as Events 8, 9, and 10 from the original source) are excluded.

Firstly, the moving averages of the velocity and concentration time series are calculated from each event (Supplementary Fig. 2.4). Then, the depth-averaged flow parameters, (flow velocity and concentration), are calculated from each averaged profile (Supplementary Fig. 2.5–2.7). Based on the gradient in time of the depth-averaged flow velocity, intervals of time for data compilation are selected so that the strongly accelerated or decelerated regions are excluded. Finally, from the selected window, mean depth-averaged flow parameters are calculated. To remove the background noise from each flow, the time-average background velocity with in the selected window is calculated for each run. Then velocity values lower than the background noise are excluded in the interpolation and extrapolation of profiles. The velocity relative to the time-averaged background velocity is extracted as the flow velocity measurements.

The original concentration profiles include some artifacts (Simmons et al., 2020). In events 1 and 4, sometimes concentration values suddenly increase near the interface with the ambient. Simmons et al. (2020) assumed

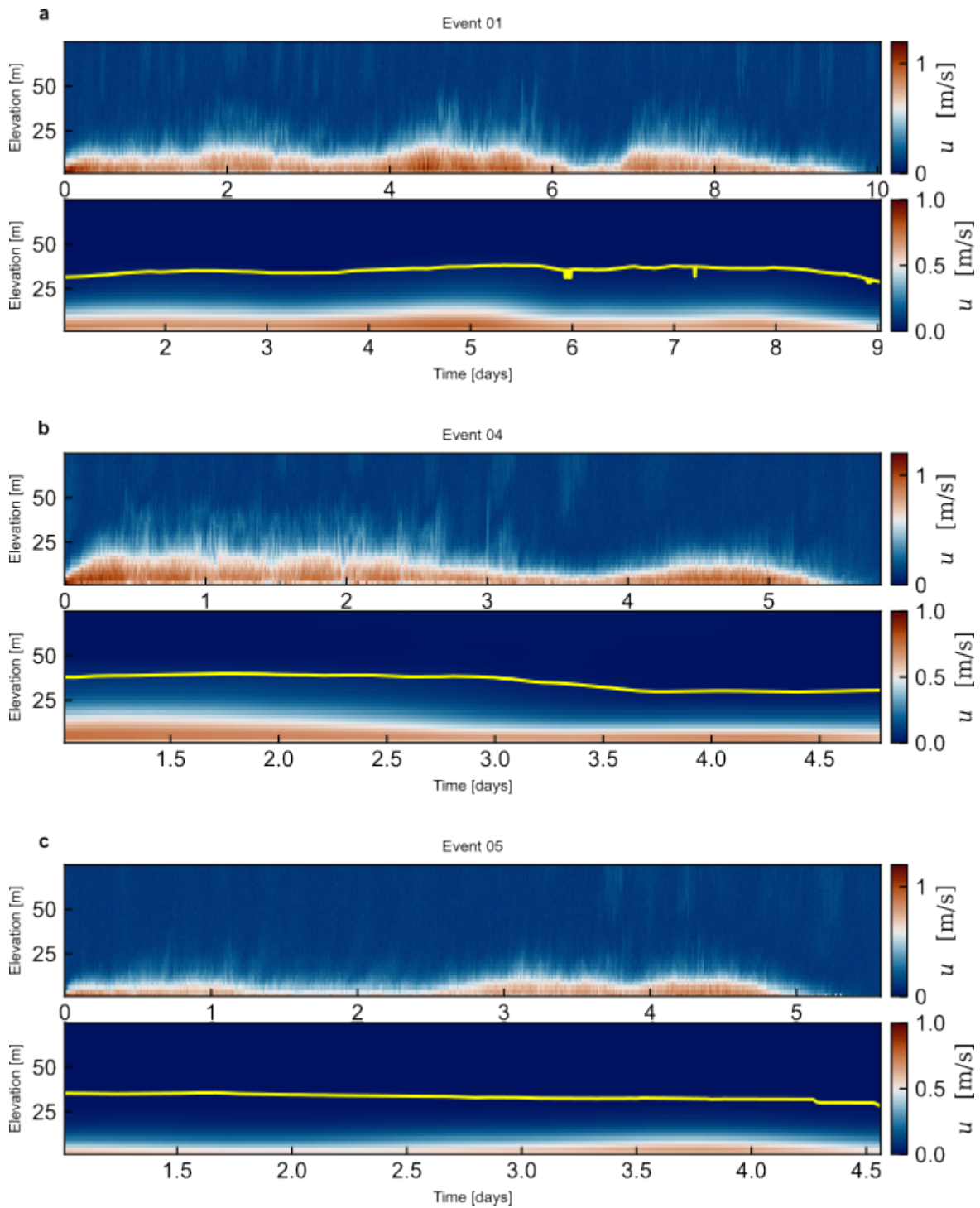


Figure 2.4: Time series of original and moving-averaged velocity field of the turbidity currents in the Congo system: a) Event 01, b) Event 04, c) Event 05. Yellow lines are the estimated flow height.

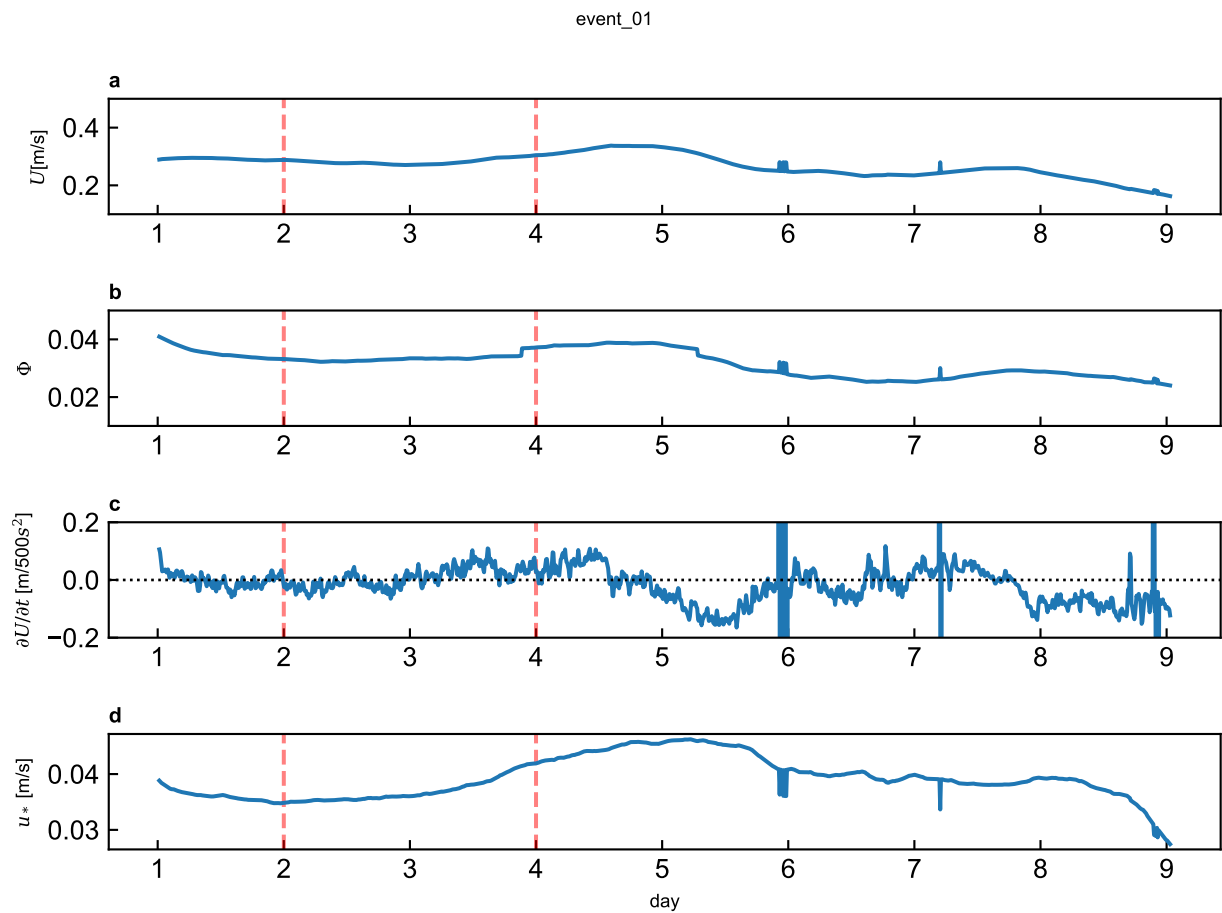


Figure 2.5: Depth-averaged flow parameters of Event 01 in Congo canyon. a) Depth-averaged flow velocity, b) depth-averaged flow concentration, c) time gradient of depth-averaged flow velocity [m/500s²] and, d) estimated shear velocity. The selected time interval is indicated by red dashed lines.

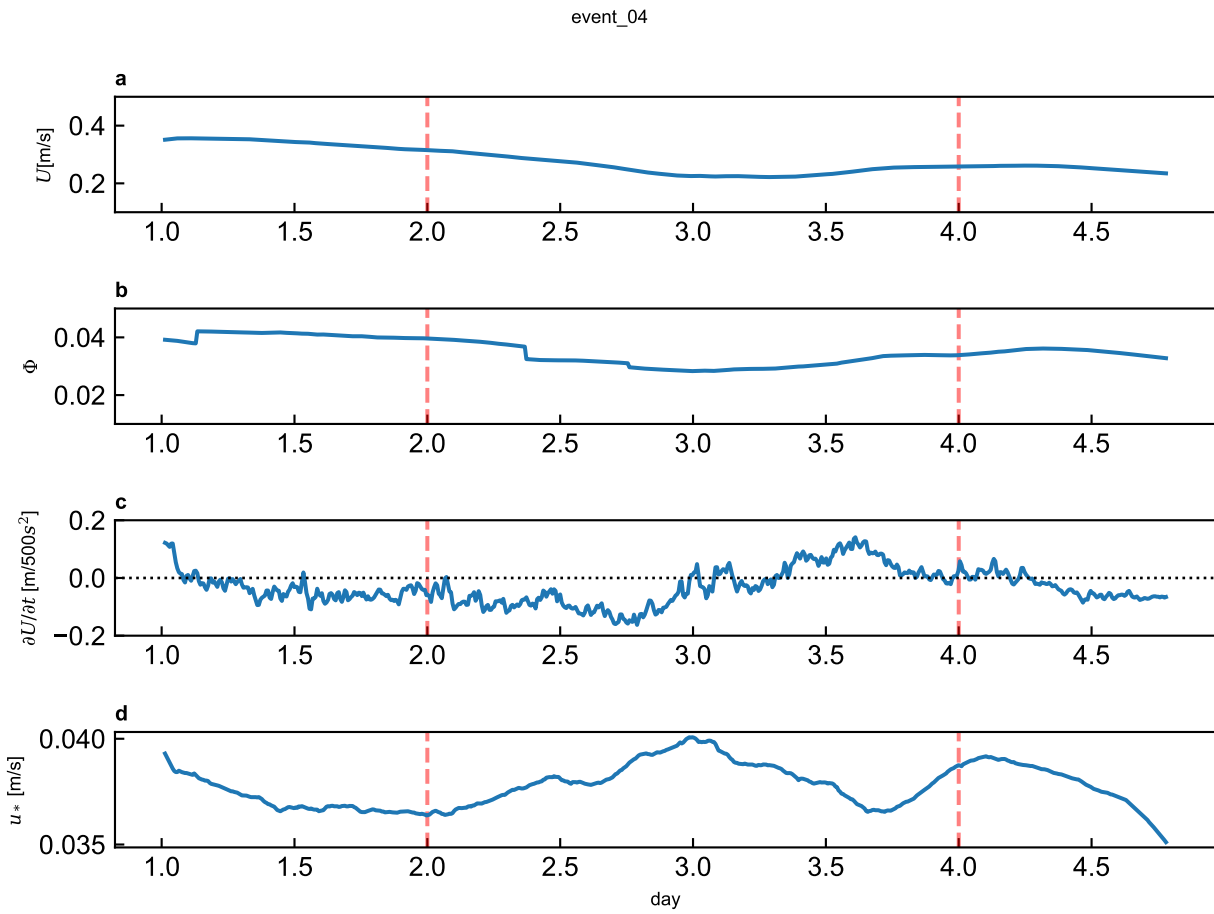


Figure 2.6: Depth-averaged flow parameters of Event 04 in Congo canyon. a) Depth-averaged flow velocity, b) depth-averaged flow concentration, c) time gradient of depth-averaged flow velocity [m/500s²] and, d) estimated shear velocity. The selected time interval is indicated by red dashed lines.

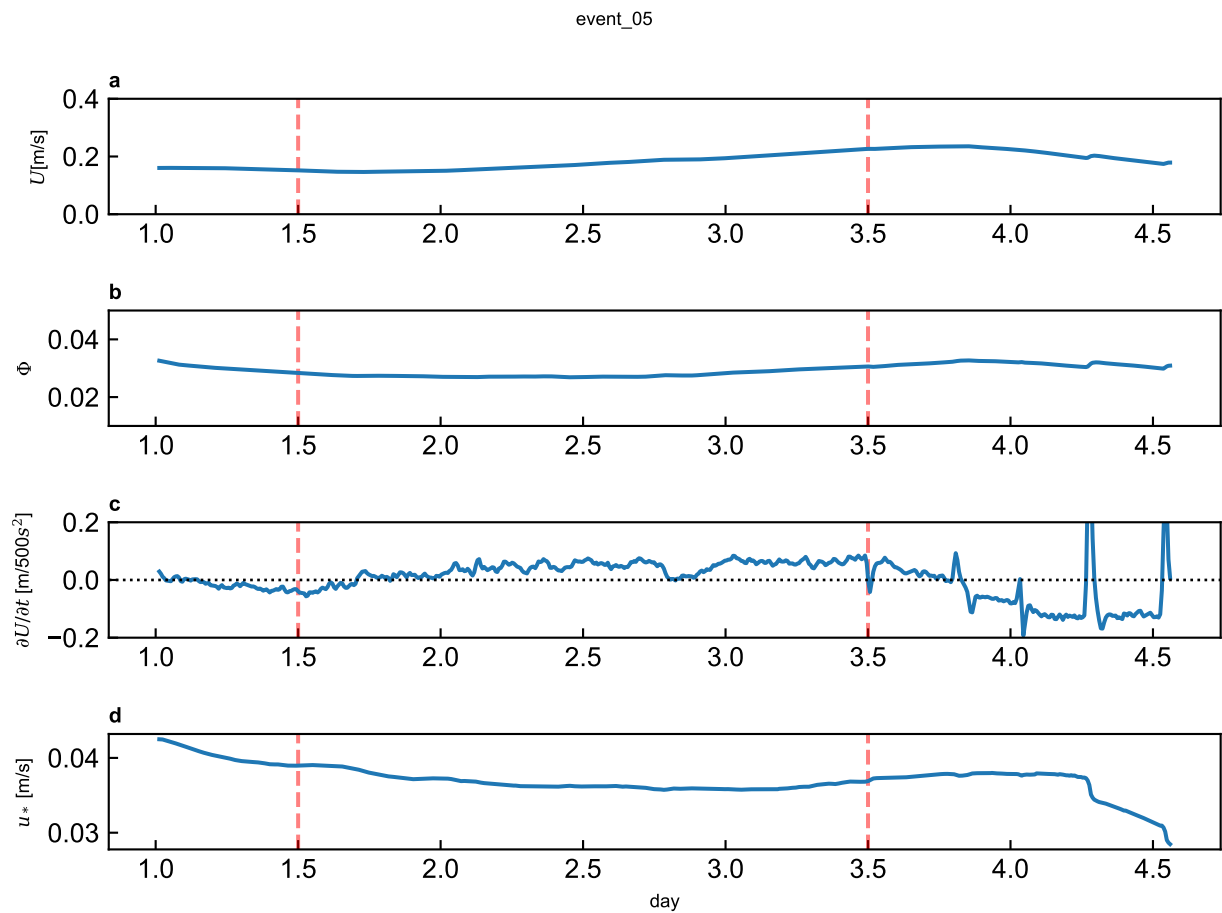


Figure 2.7: Depth-averaged flow parameters of Event 05 in Congo canyon. a) Depth-averaged flow velocity, b) depth-averaged flow concentration, c) time gradient of depth-averaged flow velocity [m/500s²] and, d) estimated shear velocity. The selected time interval is indicated by red dashed lines.

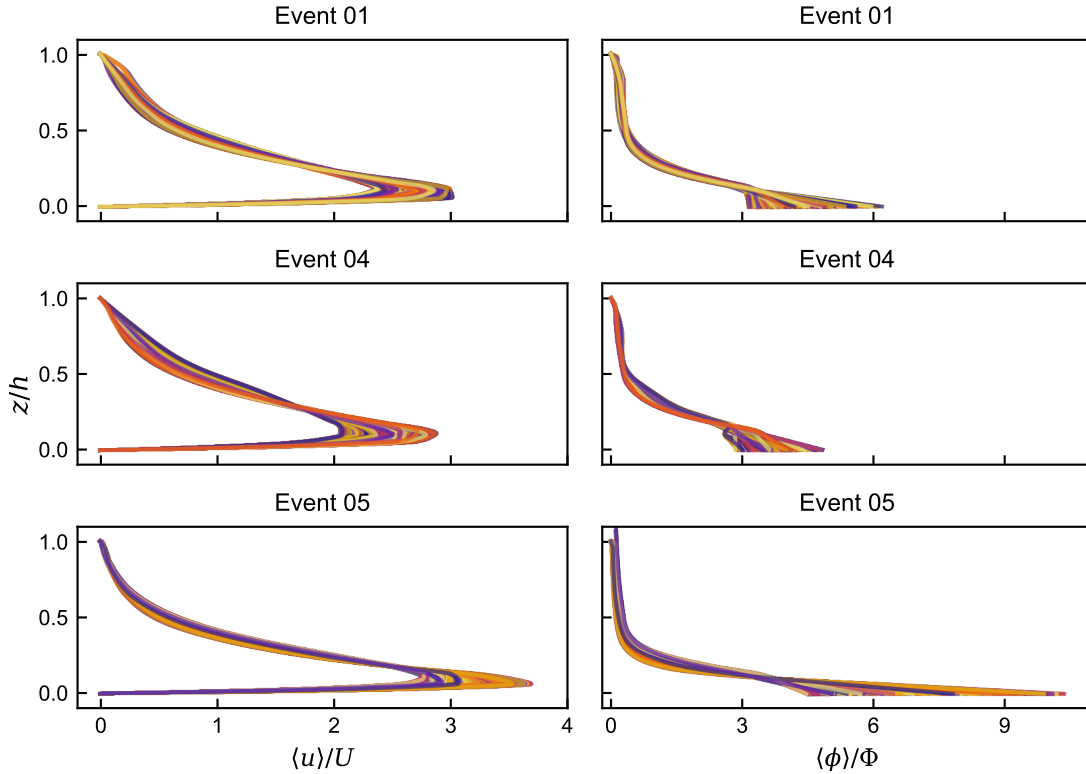


Figure 2.8: The moving-averaged flow profiles of Congo’s turbidity currents in the selected windows.

that this type of artefact is related to the backscatter from turbulent microstructure associated with gradients in either density, temperature, or salinity (Lavery et al., 2003). To exclude the artefacts, the peak value of the concentration near the upper flow interface is measured from Event 1 and 4. Then, in the upper half of the flow, the concentration lower than this peak is omitted; only the portion of the concentration data which is of higher concentration than the artefact is used for interpolation and extrapolation.

Estimation of depth-averaged concentration The TYPE II dataset (laboratory-scale experiment data in which only velocity profiles are available but not concentration profiles, see table 2.1) lack the data of flow concentration of each run. However, they reported the initial flow concentration (the concentration in the mixing tank). As a rule of thumb, as the higher the initial concentration is, the higher the depth-averaged flow concentration becomes if it is in the same setting of experiments. Yet, the detailed correlation between Φ and Φ_0 is unknown. If there is a clear correlation, the depth-averaged flow concentration of TYPE II dataset may be potentially reasonably estimated from the initial concentration, Φ_0 . Here, to estimate the correlation between depth-averaged flow concentration, Φ , and initial flow concentration in the mixing tank, Φ_0 , a regression analysis is conducted against those two parameters in TYPE II data (fig. 2.9). For the curve

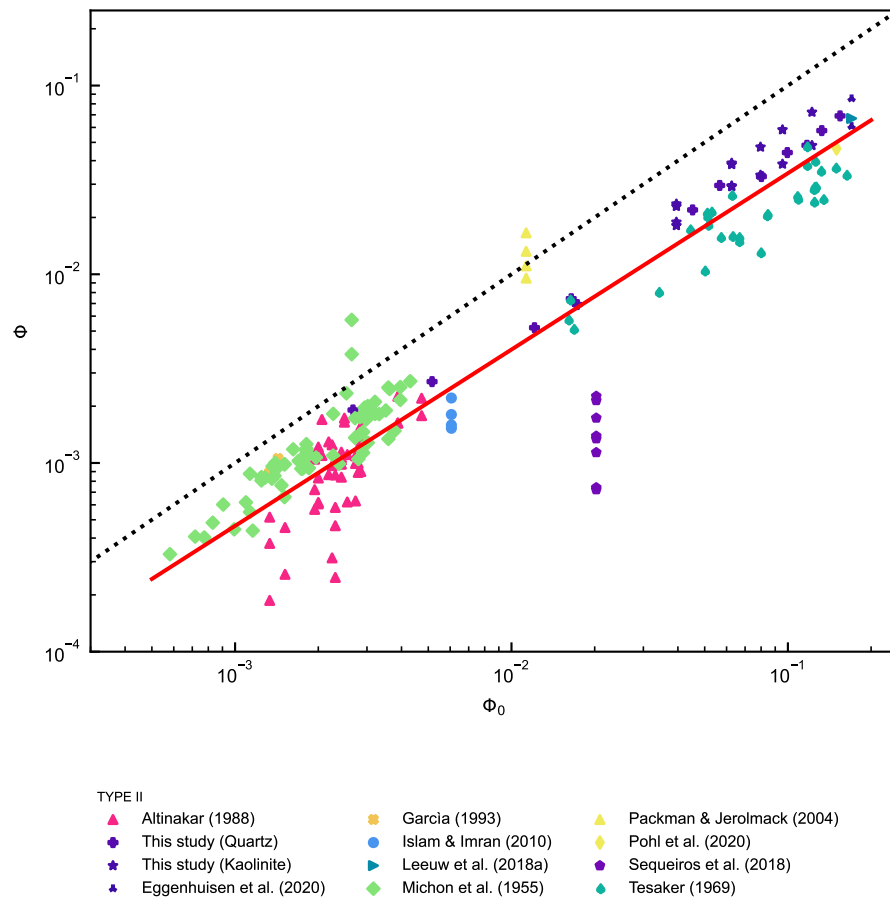


Figure 2.9: Log-log plot of layer-averaged flow concentration and initial concentration of the sediment-water mixture in the mixing tank of laboratory-scale data. The regression line (red solid line) was fitted to logarithmic values of Φ_0 and Φ , with a coefficient of determination $R = 0.88$. The gray dotted line represents $\Phi_0 = \Phi$.

fitting, orthogonal distance regression is applied. The best fit curve imply following relationship,

$$\Phi \simeq 0.30 \times \Phi_0^{0.94} \quad (2.9)$$

Among each single experiment setting, the correlation between Φ and Φ_0 varies. For instance, Michon et al. (1955), Tesaker (1969), and the experiments in this study show relatively clear correlation between Φ and Φ_0 . On the other hand, Altinakar (1988), Sequeiros et al. (2018), and Pohl et al. (2020) show relatively poor correlation. Overall, apart from Sequeiros et al. (2018), most of the data points show good agreements with the best fit curve (Fig. 2.9). Therefore, the depth-averaged flow concentration of TYPE II are estimated by the equation (2.9), assuming that TYPE II data follow the best fit curve in the Figure 2.9.

Particle-size distribution analyses The particle-size distribution is one of the most fundamental properties of suspended material of turbidity currents, which strongly affects the sediment-load capacity of a flow. The particle-size analysis in the compiled sources are either sieving combined with hydrometer method (SHM) or the laser diffraction method (LDM). SHM measures the settling velocity of the particles in a liquid. In SHM, the particles are assumed to be spherical and their sizes are calculated based on Stokes' law (Fisher et al., 2017). On the other hand, in LDM, the measured particles size is equivalent to that of a sphere giving the same diffraction as the particles. LDM can process each sample faster and provide more detailed information such as the number of particles and surface area, compared with SHM (Goossens, n.d.). Further, LDM provides high repeatability and reproducibility (Eshel et al., 2004).

Extensive comparison of SHM and LDM (Katayama, 1997; Vitton and Sadler, 1997; Konert and Vandenberghe, 1997; Lu et al., 2000; Goossens, n.d.; Di Stefano et al., 2010; Al-Hashemi et al., 2021; Lopez et al., 2021) has shown a large discrepancy between the measured proportion of clay-size particles. Although the discrepancy becomes negligible for sand-size particles in most cases, when comparing the size of the largest particles in a sample of silt to clay-size particles, the error can be up to two orders of magnitude (Lu et al., 2000). The particle-size difference of two orders of magnitude can result in up to 4 order of magnitude errors of settling velocity. Those measurement discrepancies are attributed to the density difference and shape variation of particles (Bah et al., 2009).

In this study, considering the high repeatability and reproducibility, particle size distribution from LDM is regarded as more reliable data than the SHM. Tesaker's experiment (Tesaker, 1969) used SHM to measure the particle size distribution of their clay sample, and the reported median particle size varies between 0.8–2.3 microns which is likely to be significantly below the true value. To mitigate this systematic error due to the different methodology, in this study, the following modification of reported particle size is conducted.

Firstly, the cumulative particle distribution curves of similar materials as Tesaker's experiments (Kaolinite clay) are extracted from the particle-size comparison studies between SHM and LDM (Di Stefano et al., 2010;

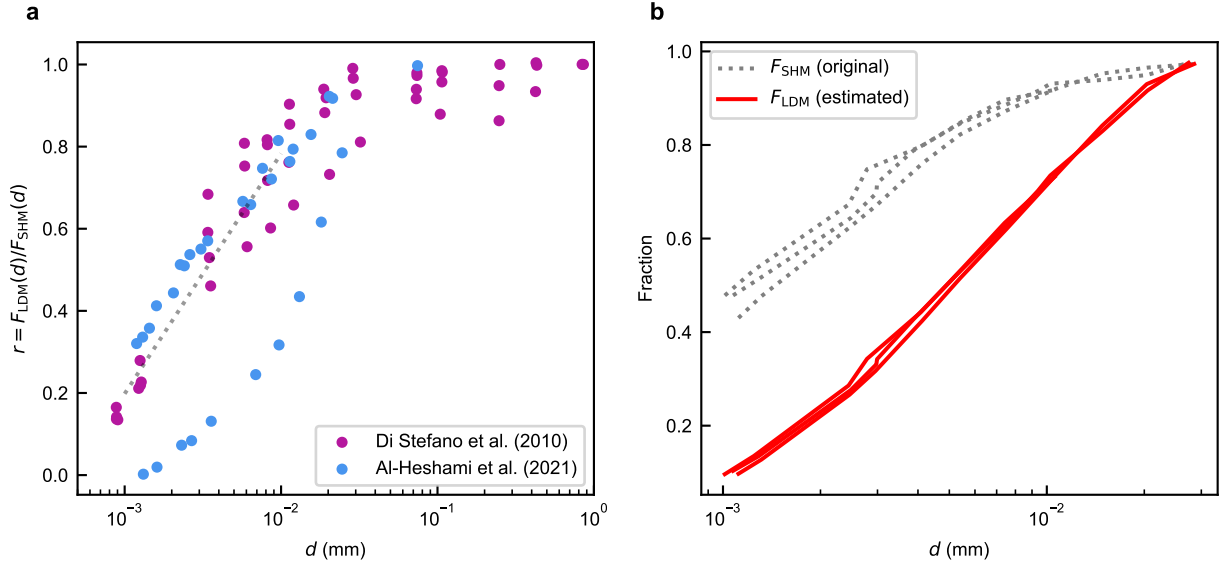


Figure 2.10: a) The ratio of particle sizes as measured by the Laser Diffraction method to that of the hydrometer analysis method. Gray dotted line represents the fitted curve. b) Modified particle-size distribution of Tesaker (Tesaker, 1969).

Al-Hashemi et al., 2021). Since the particle-size discrepancy between SHM and LDM could show different trends based on the type of clay minerals, only data was used where the material is mainly composed of Kaolinite. The cumulative particle distribution curve, $F(d_i)$ is defined as follow

$$F(d_i) = \sum_{k=0}^i f(d_k) \quad (2.10)$$

where d_i is the characteristic particle size of the i^{th} bin, N is the total number of bins, and $f(d_i)$ denotes the fraction of the i^{th} particle size class which is given as

$$f(d_i) = \frac{q_w(d_i)}{\sum_k q_w(d_k)} = \frac{q_v(d_i)}{\sum_k q_v(d_k)} \quad (2.11)$$

$$\text{where } q_w = \rho_s q_v \quad (2.12)$$

where $q_w(d_i)$ and $q_v(d_i)$ denotes the measured weight and volume of the particles in the i^{th} size bin. Let $r(d)$ denote the ratio of the cumulative fraction of particles measured by LDM to the one measured by SHM, such that

$$F_{\text{LDM}}(d) = r(d)F_{\text{SHM}}(d). \quad (2.13)$$

Figure 2.10a shows the calculated correlation between $r(d)$ and the particle size, d from the compiled sources (Di Stefano et al., 2010; Al-Hashemi et al., 2021). $r(d)$ increases monotonically as d increases until r saturates to unity at $d \simeq 3 \times 10^{-2}$ (Fig. 2.10a).

Here, the correlation between r and $\log d$ for fine particles ($d < 3 \times 10^{-2}$) is approximated by the linear curve fitting with the least-square method (Gray dotted line in Fig. 2.10a). Then, assuming $r \leq 1$, the empirical formula for r is given as

$$r(d) = \min [a \log_{10} d + b, 1] \quad (2.14)$$

where the correlation coefficients are $a = 0.58 \pm 0.04$ and $b = 1.95 \pm 0.09$ ($R^2 = 0.91$). Then, F_{LDM} of Tesaker's experiments (Tesaker, 1969) is estimated from the measured F_{SHM} by Equation (2.13) and (2.14) (Fig. 2.10b). Consequently, d_{50} shifted from around 1×10^{-3} mm to 4.98×10^{-3} on average (Fig. 2.10b). In the analysis of main text, 4.98×10^{-3} is used as the median particle size of Tesaker's experiments.

2.3 Flume experiments

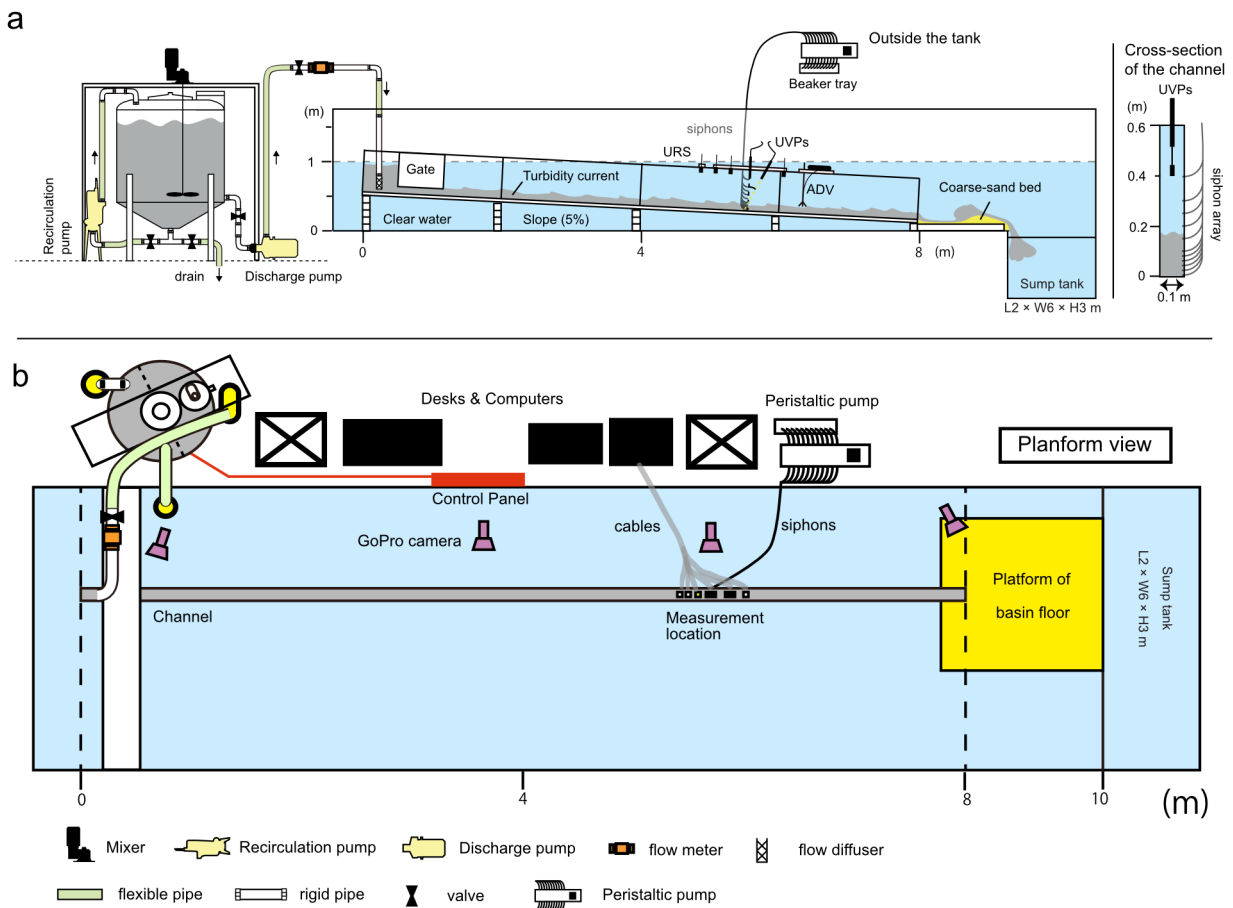


Figure 2.11: Schematic of experiment configuration. a) The sideview of the configuration. b) The planform view. Measurement location is at 4.7 m from the inlet (5.7 m downstream from the upstream end of the channel). The cross-section of the channel at the measurement location is depicted on the right side of the figure.

The experiments were conducted to study the internal flow structures of turbidity currents in an idealized channel (Cala et al., 2020) in the Total Environment Simulator, at the University of Hull.

Exp.	d_{50}	ϕ_0	Q	D_{flow}	T_{ambient}	T_{flow}	$\log_{10} \text{Re}$	Ri	Re_p
01	40	15.4	6	160	14.0	14.5	4.8	0.92	1.03
02	42	13.3	6	160	14.2	15.2	4.8	0.98	1.11
03	42	11.7	6	160	13.5	14.3	4.8	0.73	1.1
04	41	10.0	6	160	13.3	14.5	4.9	0.73	1.04
05	43	8.0	6	160	13.3	15.0	4.9	0.84	1.14
06	41	5.7	6	160	13.3	14.1	4.8	1.07	1.07
07	43	4.5	4	240	15.0	15.4	4.8	1.16	1.14
08	41	1.7	4	240	–	–	4.8	1.16	1.07
09	43	1.2	4	240	–	–	4.9	0.93	1.14
10	43	0.3	4	240	14.2	14.7	4.8	0.78	1.14
11	38	1.6	4	240	13.9	14.4	4.8	1.05	0.94
12	33	0.5	4	240	13.9	14.5	4.8	1.5	0.77
13	9.0	4.0	3.5	280	16.2	16.7	4.6	0.68	0.11
14	9.0	6.3	3.5	280	16.4	17.7	4.7	0.56	0.11
15	9.0	8.0	3.5	280	17.6	15.1	4.7	0.56	0.11
16	9.0	9.6	3.5	280	17.6	16.4	4.7	0.63	0.11
17	9.0	12.2	3.5	280	15.9	17.9	4.8	0.68	0.11

Table 2.2: Median particle size, d_{50} (μm), initial concentration in the mixing tank, ϕ_0 (vol.%), discharge rate, Q (l/s), total flow duration, D_{flow} (s), the temperature ($^{\circ}\text{C}$) of ambient water (T_{ambient}) and of the flow (T_{flow}), Reynolds number (Re), Richardson number (Ri), and particle Reynolds number (Re_p) are listed. T_{ambient} and T_{flow} are calculated by the acoustic doppler velocimeter (ADV) as time-averaged values. The turbidity currents for the experimental runs are characterized by either glass beads (01–12) or kaolinite (13–17).

2.3.1 Experiment configuration

The main channel is 8 m long, 0.1 m wide, 0.6 m deep with 5% slope, and it is submerged in a large water tank 12 m long, 6 m wide, 1 m deep filled with ambient water. At the downstream, the channel is connected smoothly to a region of coarse sand of area $3 \text{ m} \times 3 \text{ m}$ and 5 cm deep. A sump tank (2 m long \times 6 m width \times 3 m depth) is located at the downstream end of the large tank, to minimise backwater effects (Cala et al., 2020).

A large corn-shape mixing tank is built and used to generate turbidity currents. The volume is in total 1.36 m^3 inside of which the total effective volume for the experimental run is above the elevation of the fit for the discharge piping system and is approximately 0.97 m^3 . To keep the concentration vertically uniform, two different mixing systems are established: i) an electrical mixer with a 350 mm diameter impeller is inserted from the middle lid on the top of the tank which generates a strong vortex within the tank, and ii) a recirculation piping system with a pump is connected from the bottom fit of the tank to the manually-drilled fit on the top of the tank which generates vertical circulation mixing. Independently, another piping system is connected with a slurry pump (Ebara DWO 300) from the fit on the sidewall of the tank to the flow diffuser inserted upstream of the perspex straight channel. The (pumped) input rate is tested by adjusting the in-line valve, reading the flow rate from an electromagnetic flowmeter during test runs. Sediment-water mixtures are then fed into the flume from the mixing tank (Fig. 2.11).

The sediment concentration in the mixing tank and each flow are calculated from the wet and dry weight

of collected samples. Finally, the dry sample was analyzed by a laser particle sizer (Malvern Mastersizer) to estimate the detailed particle size distribution. Then, each experimental flow is discharged from the flow diffuser pointed upstream to create a sediment-water cloud which generates a turbidity current by its negative buoyancy. The initial conditions for each run are summarized in Table 2.2. Vertical velocity and density profiles are measured 4.7 m downstream from the inlet (Fig. 2.11).

2.3.2 Velocity measurement

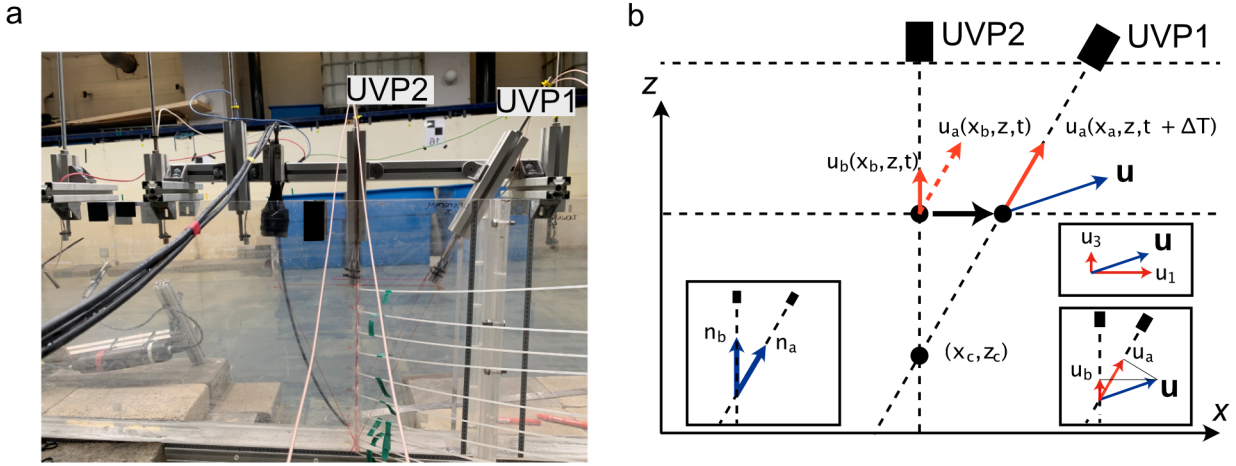


Figure 2.12: UVP configuration. 1) picture of the measurement location (cf. 5.7 meter downstream from the upstream end of the straight channel). The flow direction is from left to right in the picture. b) Schematic of the configuration of UVP probes. $z_c = 10$ (cm).

Parameter	UVP 1	UVP 2
Downstream distance (mm)	5853	5680
Bed-normal distance (mm)	400	400
Angle relative to bed-normal ($^{\circ}$)	30	0
Ultrasound frequency (MHz)	1	2
Speed of sound (m/s)	1480	1480
Velocity band width (mm/s)	1097.9	350
Velocity resolution (mm/s)	8.578	1.367
Maximum measurement distance (mm)	498.76	782.18
Number of channels	96	96
Sampling period (ms)	25	39
Window start (mm)	11.66	10.18
Window end (mm)	486.18	484.7
Channel distance (mm)	5	5
Channel width (mm)	2.96	1.48
Pulse repetition frequency (kHz)	1.483	0.946

Table 2.3: UVP configuration. The maximum measurement distance is set by the pulse repetition frequency, the frequency of the ultrasonic pulse into the fluid from the probes. Since the probe must receive the echo from previous pulse before it pings a new ultrasonic pulse into liquid, the maximum measurement distance increases with decreasing pulse repetition frequency.

Velocity measurements are made using two Metflow Ultrasonic Velocity Profilers (UVPs), mounted at different angles: bed-normal and 30 degrees to the bed-normal angle (Fig. 2.12 and Table 2.3). Since each UVP probe

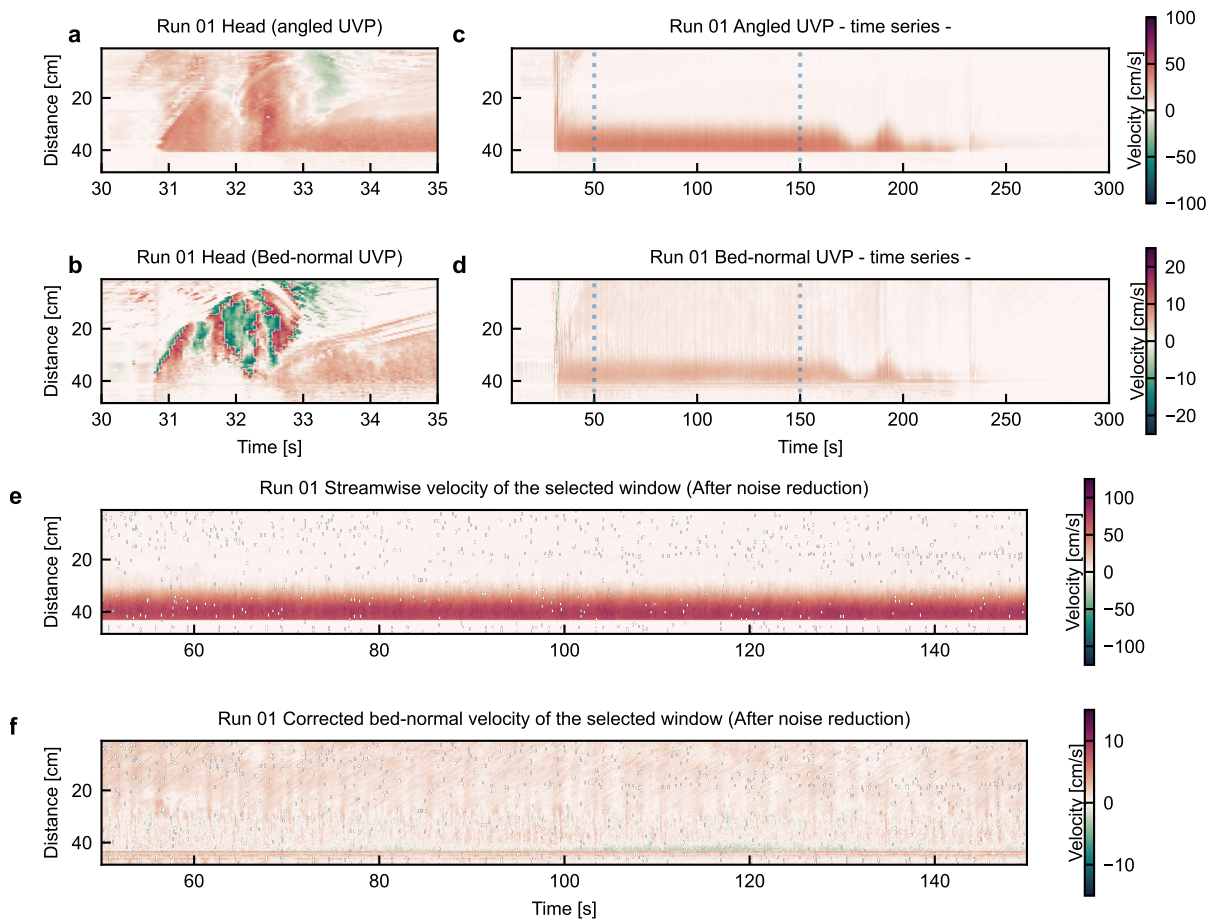


Figure 2.13: The time series UVP data of Run 01. a,b) The head region of the flow measured by angled and bed-normal UVP probes respectively. c,d) The time series of the entire event. The selected data range for calculations of time-averaged profiles are indicated by blue dotted lines. The streamwise (e) and bed-normal (f) velocity fields of the selected window were calculated from the equation (2.19) respectively.

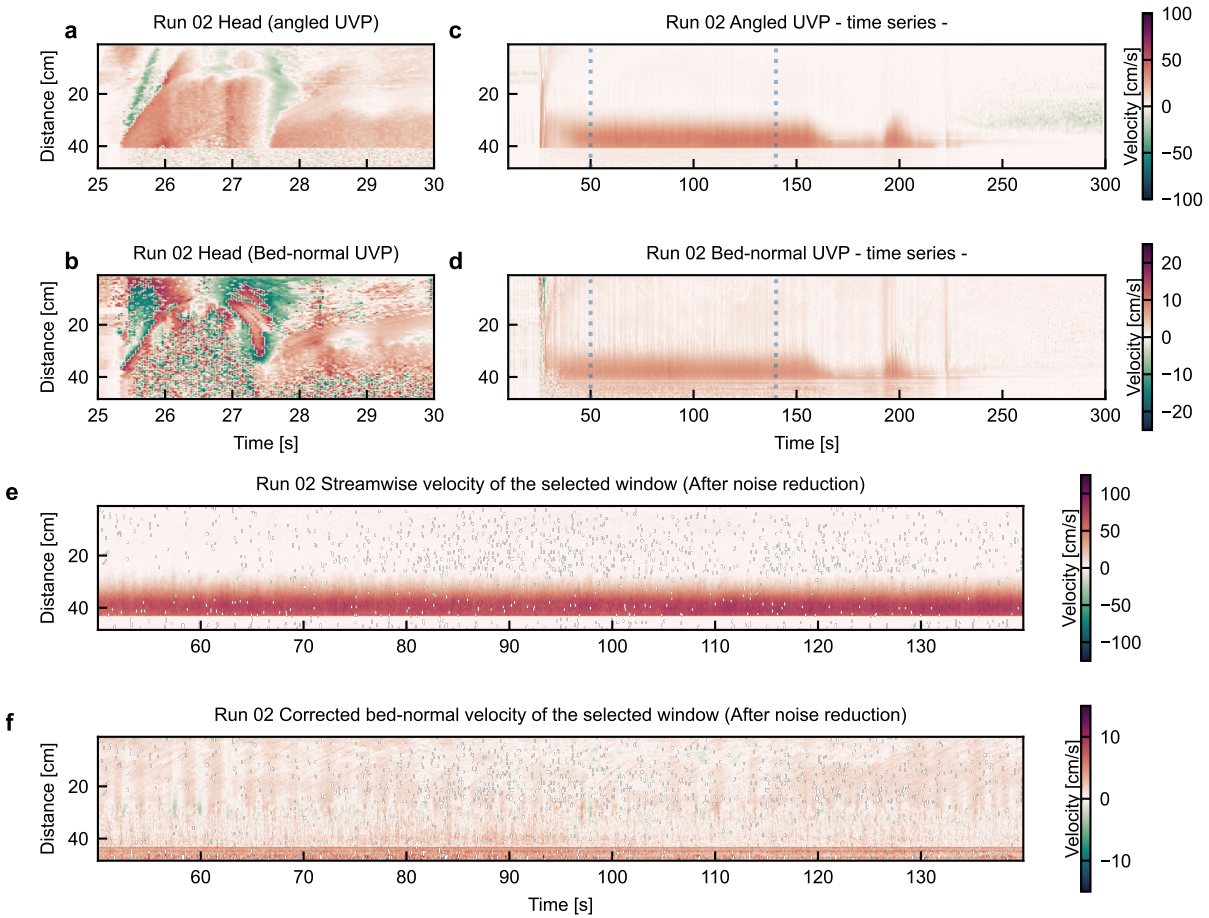


Figure 2.14: The time series UVP data of Run 02. a,b) The head region of the flow measured by angled and bed-normal UVP probes respectively. c,d) The time series of the entire event. The selected data range for calculations of time-averaged profiles are indicated by blue dotted lines. The streamwise (e) and bed-normal (f) velocity fields of the selected window were calculated from the equation (2.19) respectively.

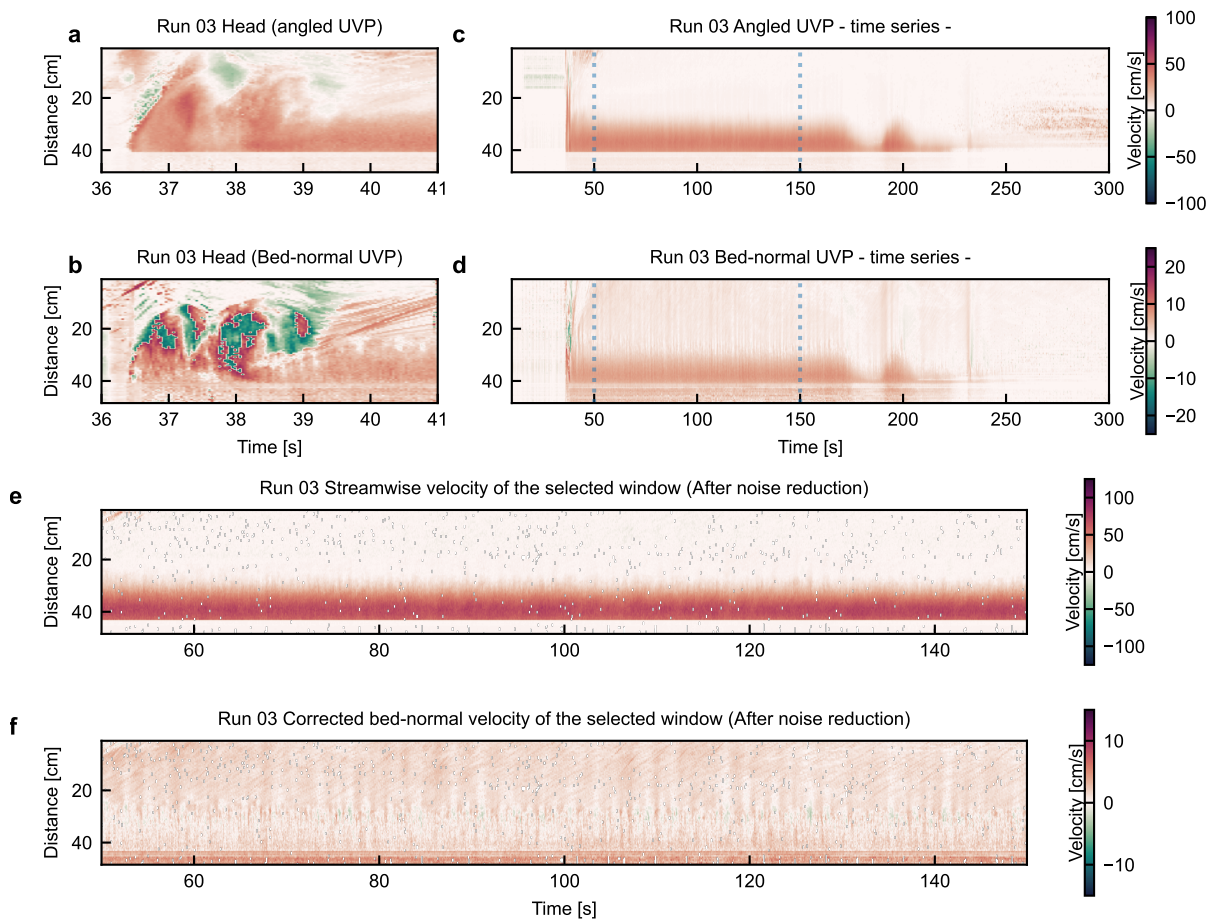


Figure 2.15: The time series UVP data of Run 03. a,b) The head region of the flow measured by angled and bed-normal UVP probes respectively. c,d) The time series of the entire event. The selected data range for calculations of time-averaged profiles are indicated by blue dotted lines. The streamwise (e) and bed-normal (f) velocity fields of the selected window were calculated from the equation (2.19) respectively.

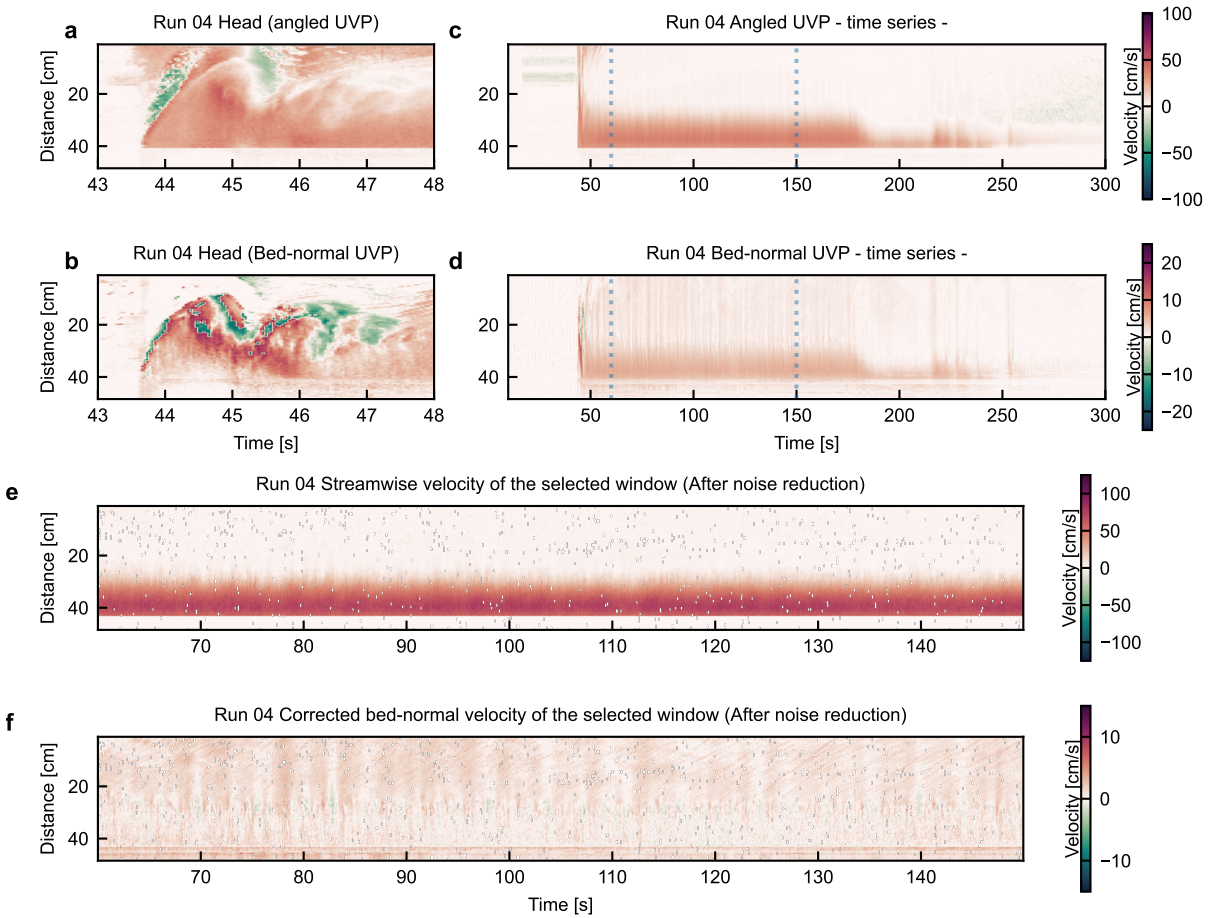


Figure 2.16: The time series UVP data of Run 04. a,b) The head region of the flow measured by angled and bed-normal UVP probes respectively. c,d) The time series of the entire event. The selected data range for calculations of time-averaged profiles are indicated by blue dotted lines. The streamwise (e) and bed-normal (f) velocity fields of the selected window were calculated from the equation (2.19) respectively.

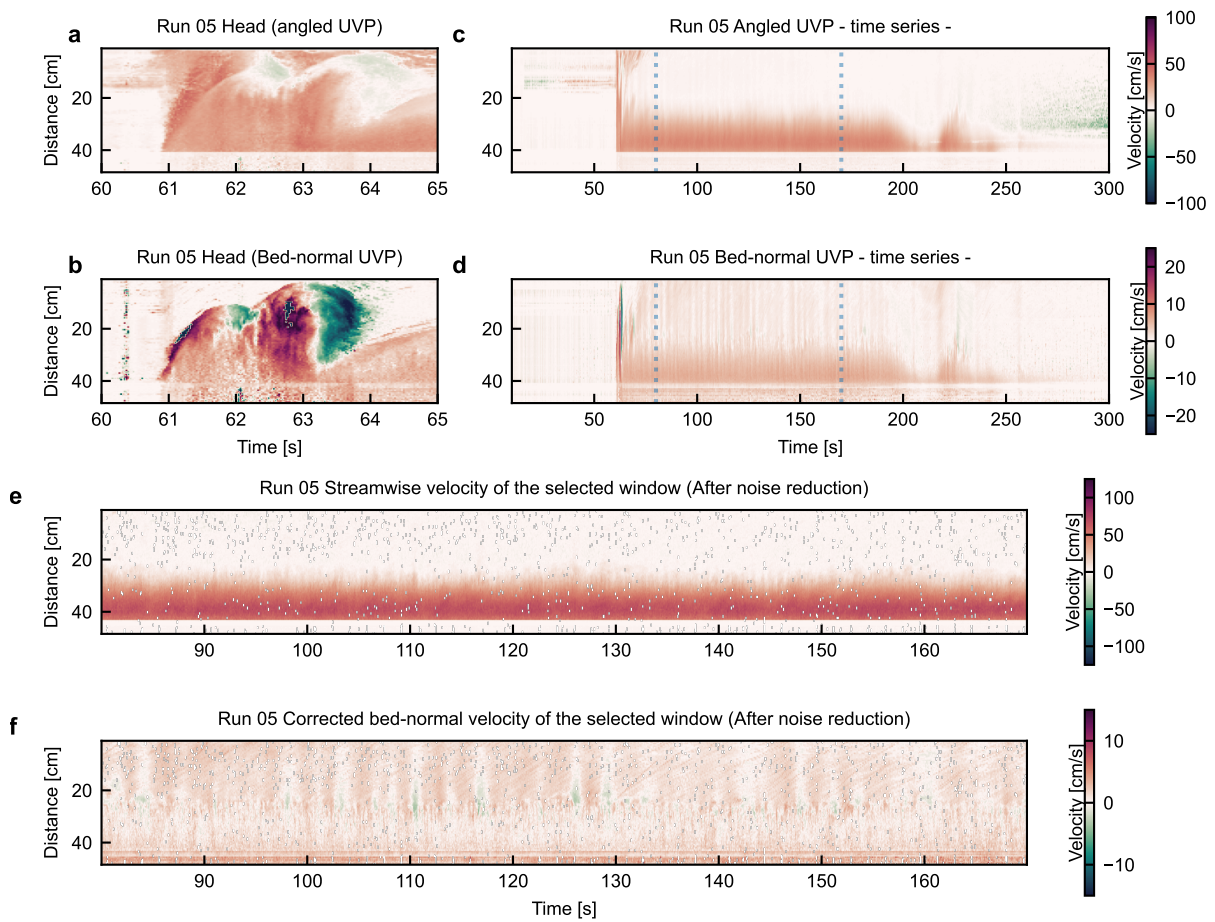


Figure 2.17: The time series UVP data of Run 05. a,b) The head region of the flow measured by angled and bed-normal UVP probes respectively. c,d) The time series of the entire event. The selected data range for calculations of time-averaged profiles are indicated by blue dotted lines. The streamwise (e) and bed-normal (f) velocity fields of the selected window were calculated from the equation (2.19) respectively.

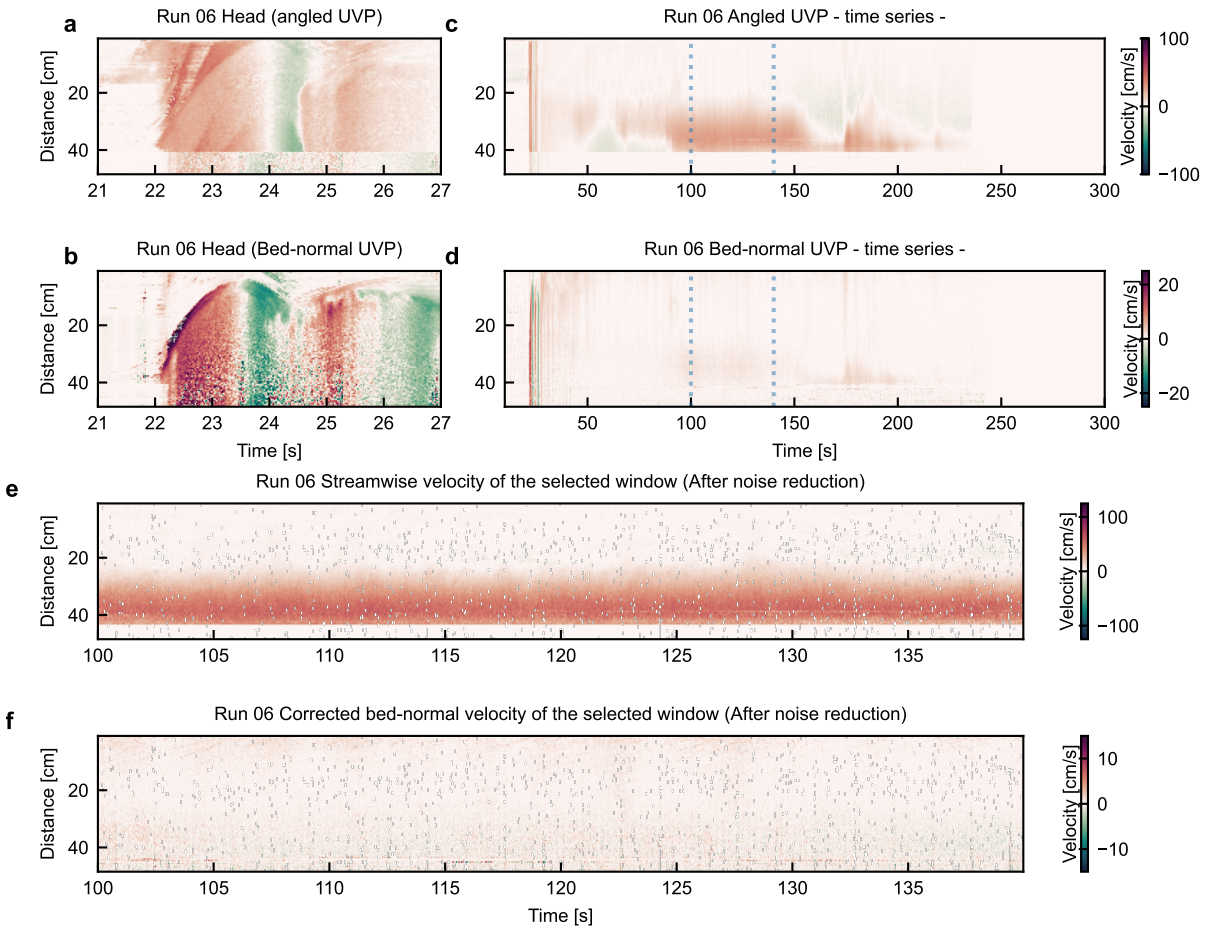


Figure 2.18: The time series UVP data of Run 06. a,b) The head region of the flow measured by angled and bed-normal UVP probes respectively. c,d) The time series of the entire event. The selected data range for calculations of time-averaged profiles are indicated by blue dotted lines. The streamwise (e) and bed-normal (f) velocity fields of the selected window were calculated from the equation (2.19) respectively.

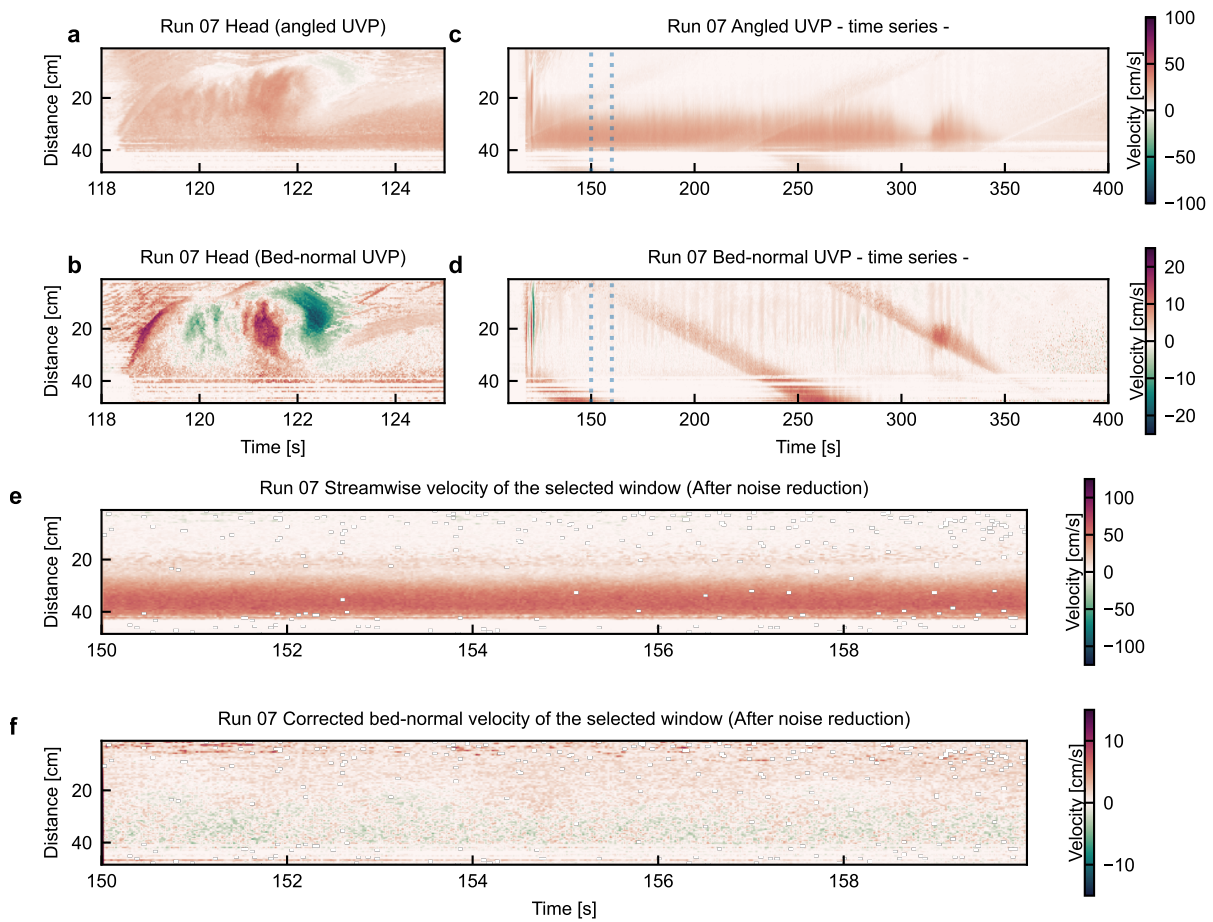


Figure 2.19: The time series UVP data of Run 07. a,b) The head region of the flow measured by angled and bed-normal UVP probes respectively. c,d) The time series of the entire event. The selected data range for calculations of time-averaged profiles are indicated by blue dotted lines. The streamwise (e) and bed-normal (f) velocity fields of the selected window were calculated from the equation (2.19) respectively.

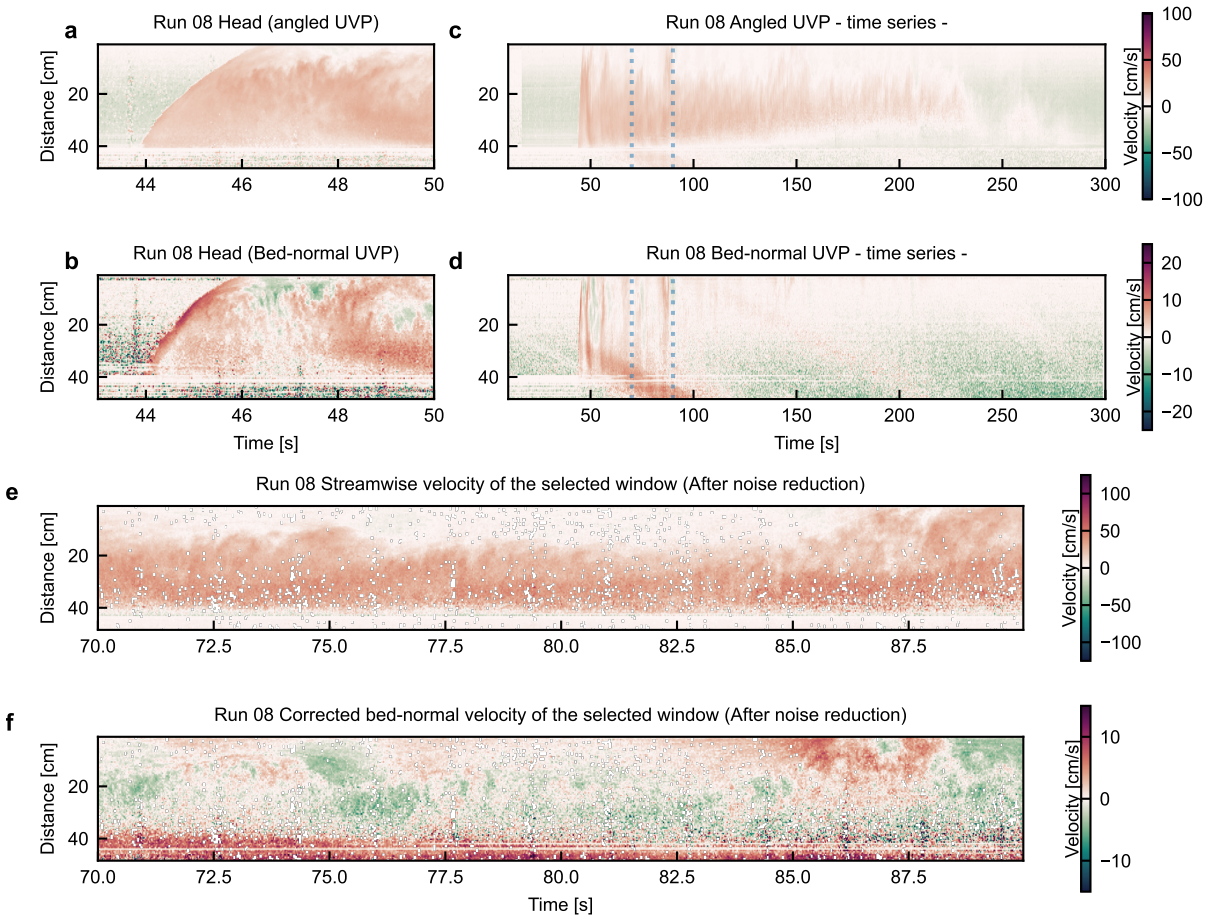


Figure 2.20: The time series UVP data of Run 08. a,b) The head region of the flow measured by angled and bed-normal UVP probes respectively. c,d) The time series of the entire event. The selected data range for calculations of time-averaged profiles are indicated by blue dotted lines. The streamwise (e) and bed-normal (f) velocity fields of the selected window were calculated from the equation (2.19) respectively.

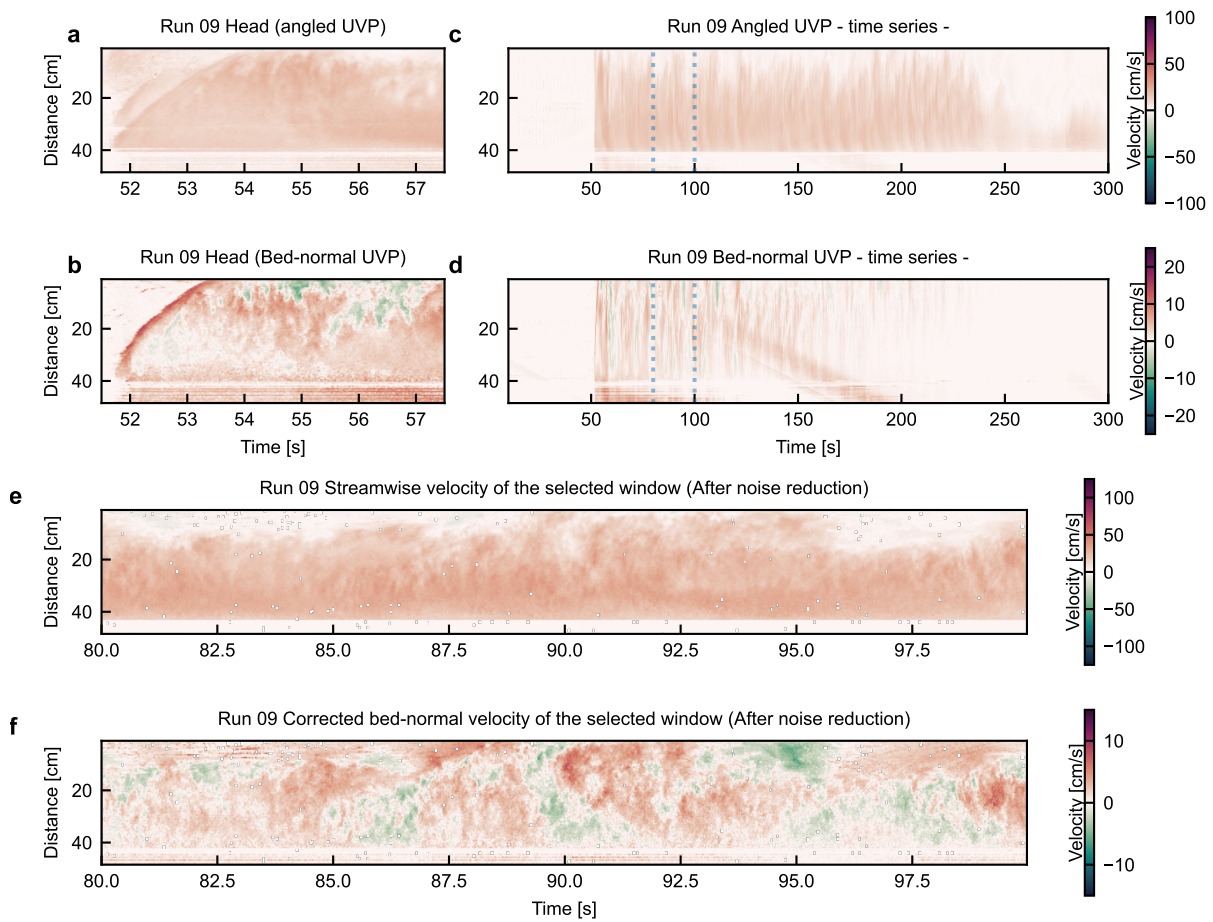


Figure 2.21: The time series UVP data of Run 09. a,b) The head region of the flow measured by angled and bed-normal UVP probes respectively. c,d) The time series of the entire event. The selected data range for calculations of time-averaged profiles are indicated by blue dotted lines. The streamwise (e) and bed-normal (f) velocity fields of the selected window were calculated from the equation (2.19) respectively.

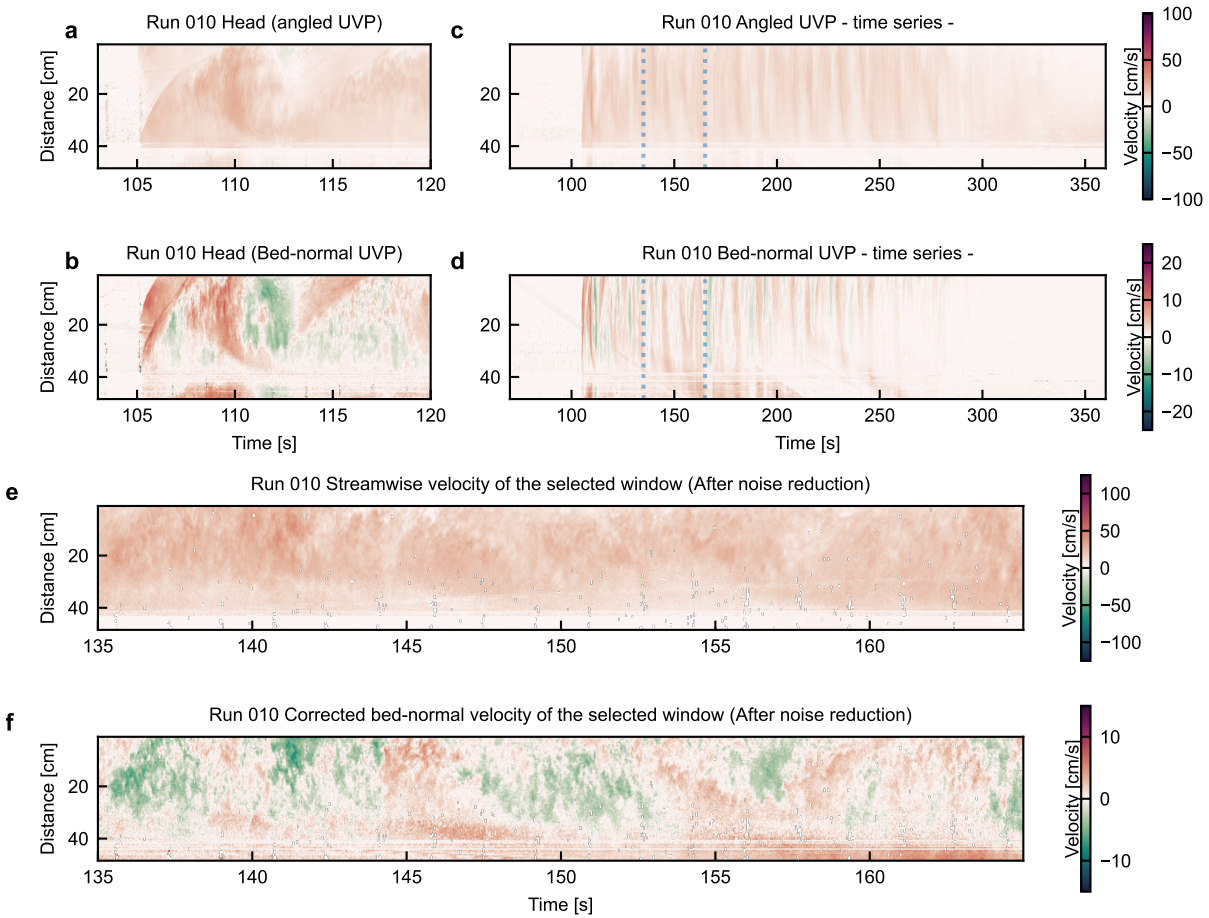


Figure 2.22: The time series UVP data of Run 10. a,b) The head region of the flow measured by angled and bed-normal UVP probes respectively. c,d) The time series of the entire event. The selected data range for calculations of time-averaged profiles are indicated by blue dotted lines. The streamwise (e) and bed-normal (f) velocity fields of the selected window were calculated from the equation (2.19) respectively.

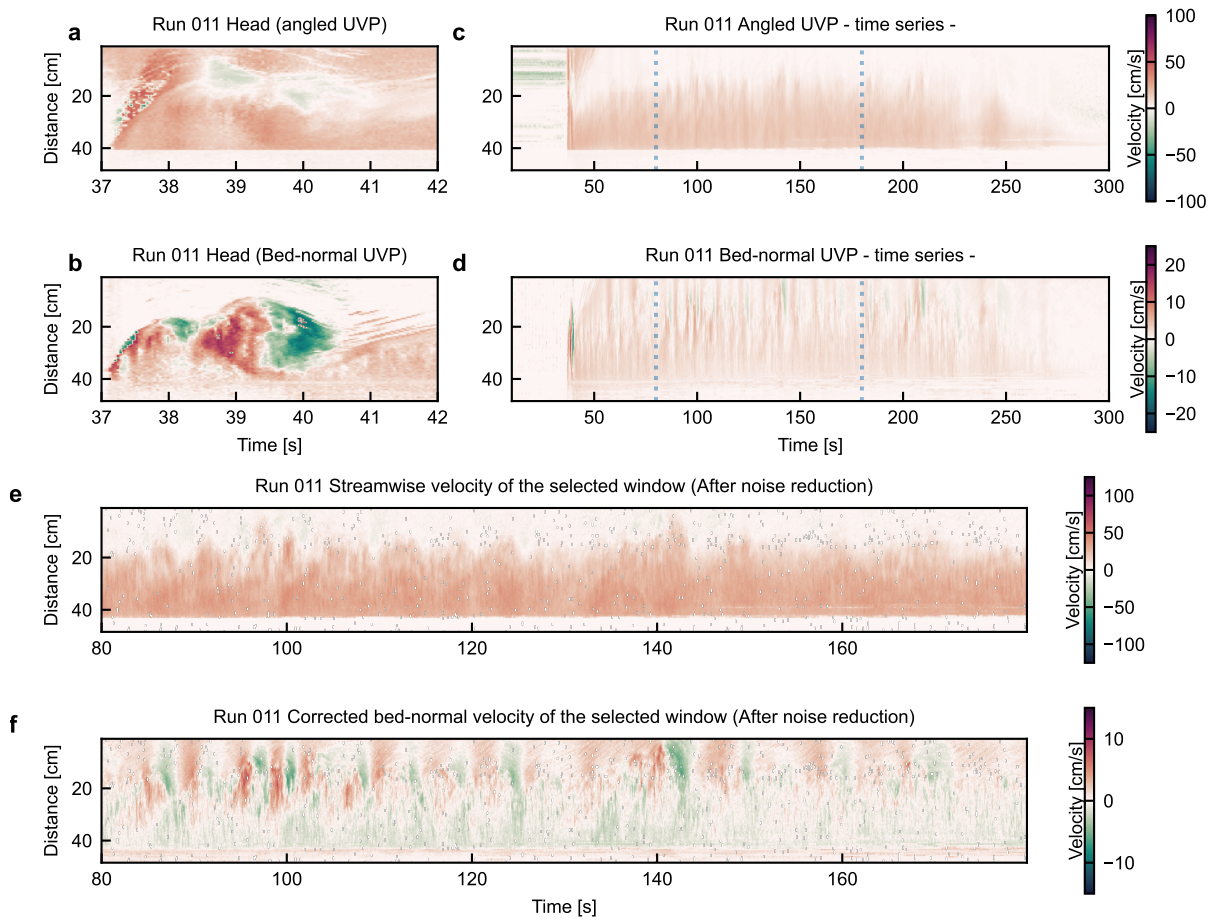


Figure 2.23: The time series UVP data of Run 11. a,b) The head region of the flow measured by angled and bed-normal UVP probes respectively. c,d) The time series of the entire event. The selected data range for calculations of time-averaged profiles are indicated by blue dotted lines. The streamwise (e) and bed-normal (f) velocity fields of the selected window were calculated from the equation (2.19) respectively.

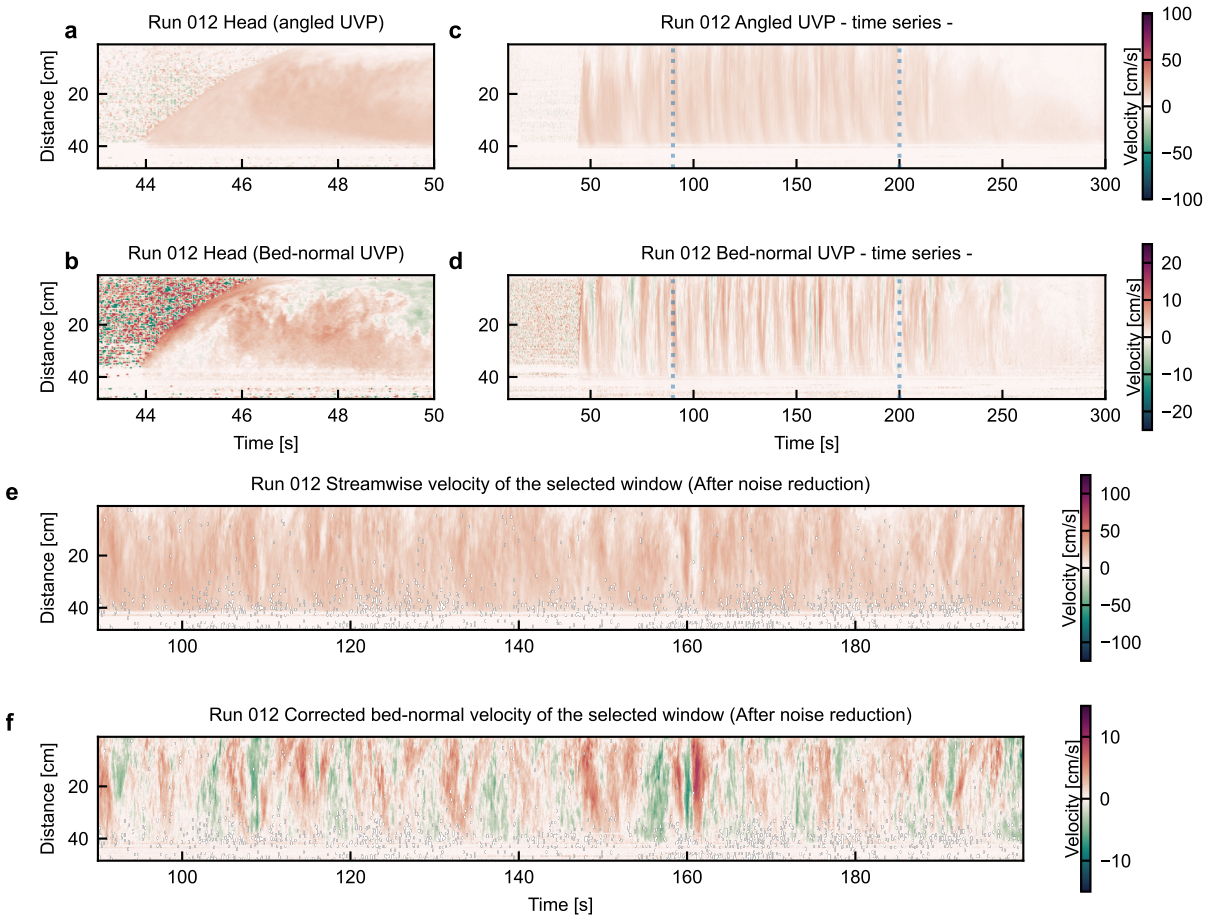


Figure 2.24: The time series UVP data of Run 12. a,b) The head region of the flow measured by angled and bed-normal UVP probes respectively. c,d) The time series of the entire event. The selected data range for calculations of time-averaged profiles are indicated by blue dotted lines. The streamwise (e) and bed-normal (f) velocity fields of the selected window were calculated from the equation (2.19) respectively.

can measure one direction component of flow velocity field, following procedures are made to estimate the streamwise and bed-normal components of flow velocity field from two UVP probes.

Here, we consider the two dimensional coordinates along the main channel, (x, z) where x is streamwise and z is bed-normal direction. let $\mathbf{u} = (u_1, u_3)$ denotes the two dimensional flow field where u_1 denotes the streamwise component and u_3 denotes the bed-normal component, and \mathbf{n}_a and \mathbf{n}_b denotes the vectors parallel to the angled and bed-normal UVP probes respectively so that,

$$\mathbf{n}_a = \begin{pmatrix} \cos 30 & \sin 30 \\ -\sin 30 & \cos 30 \end{pmatrix} \begin{pmatrix} 0 \\ 1 \end{pmatrix} = \begin{pmatrix} \sin 30 \\ \cos 30 \end{pmatrix} \quad (2.15)$$

$$\mathbf{n}_b = \begin{pmatrix} 0 \\ 1 \end{pmatrix} \quad (2.16)$$

Further, let $u_a(x_a, z, t + \Delta T)$ and $u_b(x_b, z, t)$ denote the measured velocities at a specific elevation, z , and a specific time, t , by angled and bed-normal UVP probes respectively.

$$u_a = \mathbf{u} \cdot \mathbf{n}_a = u_1 \sin 30 + u_3 \cos 30 \quad (2.17)$$

$$u_b = \mathbf{u} \cdot \mathbf{n}_b = u_3 \quad (2.18)$$

The raw measurement data of u_a and u_b for each run is listed in Figure 2.13–2.24. Solving eq. (2.17) and eq. (2.18) for u_1 and u_3 , the flow velocity field \mathbf{u} can be estimated as,

$$\mathbf{u} = \begin{pmatrix} u_1 \\ u_3 \end{pmatrix} = \begin{pmatrix} (u_a - u_b \cos 30^\circ) / \sin 30^\circ \\ u_b \end{pmatrix} \quad (2.19)$$

Except for the cross section, (x_c, z_c) (Fig. 2.12), there is a time shift of measurement between the bed-normal and angled UVP probes. At a specific elevation, z , the time shift, Δt for a flow to reach from x_b to x_a can be expressed as follow

$$\Delta t \simeq \frac{\Delta x}{\langle u_1 |_{z=z} \rangle} \quad (2.20)$$

$$\Delta x = (z - z_c) \tan 30^\circ \quad (2.21)$$

The precise values of $\langle u_1 |_{z=z} \rangle$ cannot be estimated without instantaneous measurement of u_a and u_b at the same coordinate and time. However, here, it is assumed that a flow is in near-equilibrium state where the flow velocity does not vary significantly in space and time. Especially, around the cross section area, (x_c, z_c) ,

we assume that the spacial and temporal variation of flow velocity is negligible. Then,

$$u_1|_{x,z,t} \simeq u_1|_{x+\Delta x,z,t} \quad (2.22)$$

Then, ΔT can be estimated with the equations (2.19) can be directly calculated from the UVP measurements.

To calculate eq. (2.19), following preprocessings of raw data are conducted.

Selection of data range From the original time series of u_a and u_b , the steady body part of each flow with less noise are manually selected (which are indicated by blue dotted lines).

Noise reduction The velocity data measured by UVPs are filtered to replace any spikes in the time series more than two standard deviations from the moving average. The detected spikes are often replaced by moving mean values (see Buckee et al., 2001; Keevil et al., 2006). In this study, the detected spikes are removed and left as blank data.

Adjusting time and elevation stamp The angled and bed-normal UVPs data have different sampling rate and number of channels (Table 2.3). To compute eq. (2.19), Piecewise Hermite cubic interpolation is conducted. Since the angled UVP has higher resolution, interpolation is conducted against the angled UVP data. The black data (of which original values are excluded in the noise reduction) in angled UVP is then replaced by this interpolation. From interpolated data, u_a which has the same time and elevation stamps as the bed-normal UVP data, u_b . Then, eq. (2.19) is calculated. The cells of u_a which has the same time and elevation as the blanked cells in u_b are ignored during this calculation. It should be noted that sometimes the angle of the bed-normal UVP slightly deviated from the bed-normal direction. In such case, the original time-series data of bed-normal UVP data is biased by the streamwise velocity component. In which case, the deviated angle is estimated from the photos and videos of the run.

Now, the estimated time series of streamwise and bed-normal components of the selected time range from each flow is obtained (Fig. 2.13–2.24).

Time-averaged streamwise flow velocity The representative time-averaged streamwise velocity profile, $\langle u \rangle$ for each run is calculated by taking the average of the equation (2.19) at each height over the selected time window (windows are shown by blue dotted lines in Fig. 2.13 – 2.24).

Potential errors in measurements It should be noted that the bed-normal UVP data, u_b , is sensitive to the small amount of error in the angle of the UVP probe. For instance, when the bed-normal UVP is tilted by 1 degree from the actual bed-normal direction, and the ratio of streamwise to bed-normal velocity component is 10, the error in bed-normal velocity estimation can be more than 15%, while the error in streamwise velocity

estimation based on the equation (2.19) is approximately 3%. The larger the ratio between streamwise and bed-normal velocities, the more significant the error in bed-normal velocity estimation becomes. When the ratio is 100, the error in bed-normal velocity exceeds 100%. From Figure (2.13 – 2.24), the ratio of streamwise velocity to bed-normal velocity in this experiment is roughly an order of 10 or more. Although the bed-normal UVP probe was carefully aligned in this experiment, the accuracy of the angle may be up to 1 degree due to the limitation of manual setup. This may make the instantaneous velocity field analysis unreliable, as shown in the next paragraph. Having said that, the main analyses of this project used only the time-averaged streamwise velocity data of which potential error is expected to be less than $\sim 3\%$. Therefore, the uncertainties due to the accuracy of the alignment of UVP probes are considered negligible in this study.

Turbulent analysis From the time-series of u_1 and u_3 (Fig. 2.13–2.24), the time-averaged flow velocity profile, $\langle u_1 \rangle$ and $\langle u_3 \rangle$ are estimated. From equation 2.20 and $\langle u_1 \rangle$ and $\langle u_3 \rangle$, the instantaneous velocity field, $(u_1(x, z, t), u_3(x, z, t))$, can be approximated. By subtracting the time-averaged values, $\langle u_1 \rangle$ and $\langle u_3 \rangle$, from u_1 and u_3 respectively, the time series of turbulent field, u'_1 and u'_3 , and thus the Reynolds stresses can be obtained (Fig. 2.25–2.36), which enables to calculate the shear production of turbulent kinetic energy (Eq. 1.34). However, the results imply the unrealistic negative values of total-shear production of TKE. This is presumably due to the poor estimation of time shift, ΔT which is a function of Δx and flow velocity. The another possible factor is the error in the angle of bed-normal UVP probe mentioned in the previous paragraph. As mentioned, the small amount of error in angle of bed-normal UVP probe can result in a significant amount of error of bed-normal velocity component. Ideally, $u_1(x, z, t)$ and $u_3(x, z, t)$ should be measured instantaneously, while in this study, the following relationship is assumed

$$u_a(x, z, t) = u_a(x + \Delta x, z, t + \Delta t) \quad (2.23)$$

Since the signs of u'_1 and u'_3 are changing in a second scale, the small errors in ΔT and Δx could result in opposite signs of Reynolds stresses. Thus, in this study, we concluded that the data of UVPs do not have enough accuracy for the precise estimation of turbulence fields and are only used for the estimation of time-averaged flow properties.

2.3.3 Particle-size distribution analysis

Two types of sediment-water mixture samples are collected during the experiments. First type is the samples from the mixing tank which are used for the estimation of initial concentration ϕ_0 , and the median size of suspended particles, d_{50} (Fig. 2.37). The other type is the samples from the body of each experimental turbidity currents which are used for the estimation of time-averaged flow concentration profile, $\langle \phi \rangle$, of each flow (Fig. 2.38). Suspended sediment samples from the experimental flows are collected using a multi-channel (24 channels) peristaltic pump (Watson Marlow, see Fig. 2.39) connected to a 12-siphon array at a constant

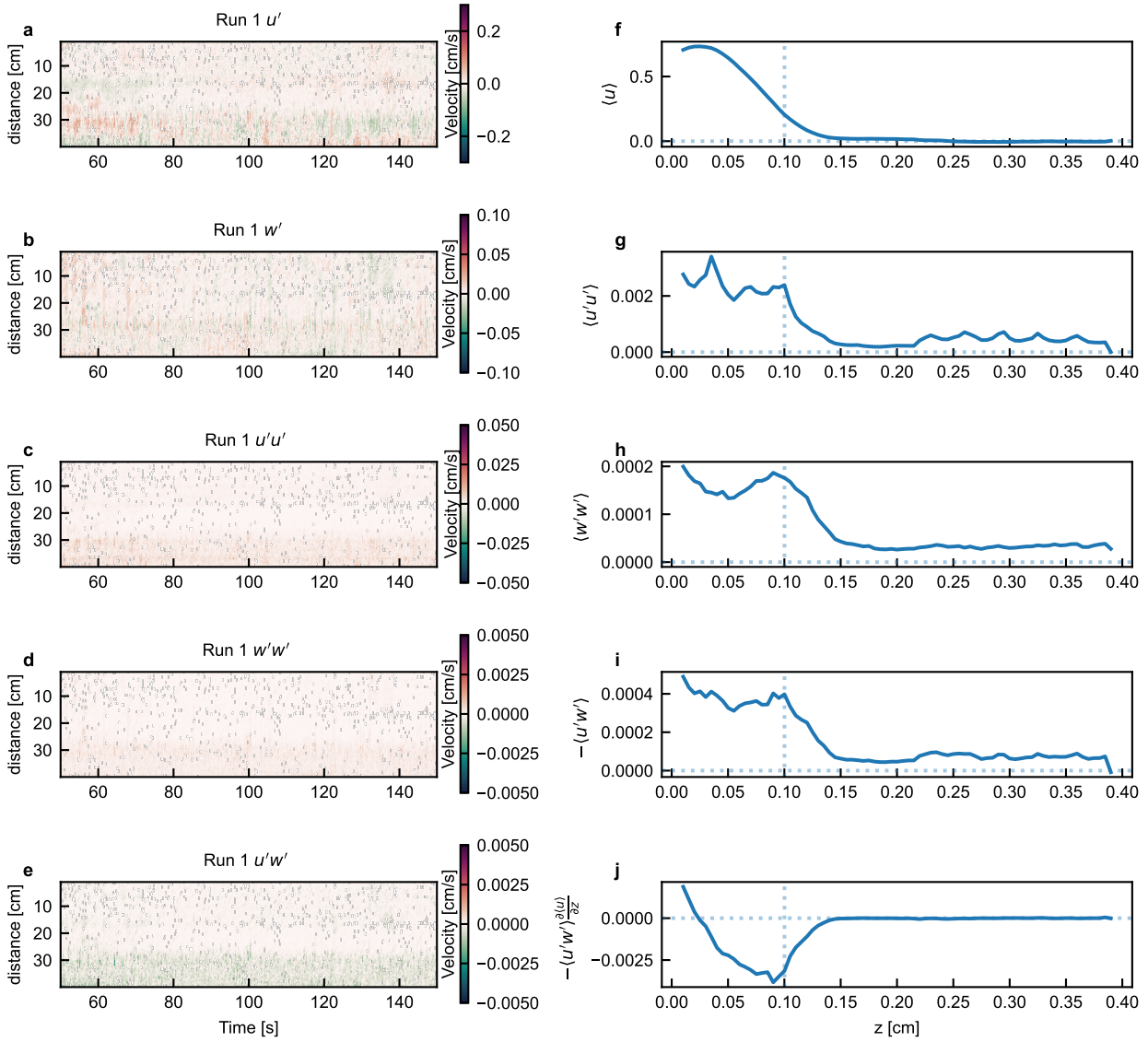


Figure 2.25: Turbulence analysis of Run 01. a) The time series of u' of the selected window. b) The time series of w' of the selected window. c) The time series of $u'u'$ of the selected window. d) The time series of $w'w'$ of the selected window. e) The time series of $u'w'$ of the selected window. f) time-averaged streamwise velocity profile. g) time-averaged Reynolds stress, $\langle u'u' \rangle$ profile. h) time-averaged Reynolds stress, $\langle w'w' \rangle$ profile. i) time-averaged Reynolds stress, $-\langle u'w' \rangle$ profile. j) Time-averaged TKE production rate at each height.

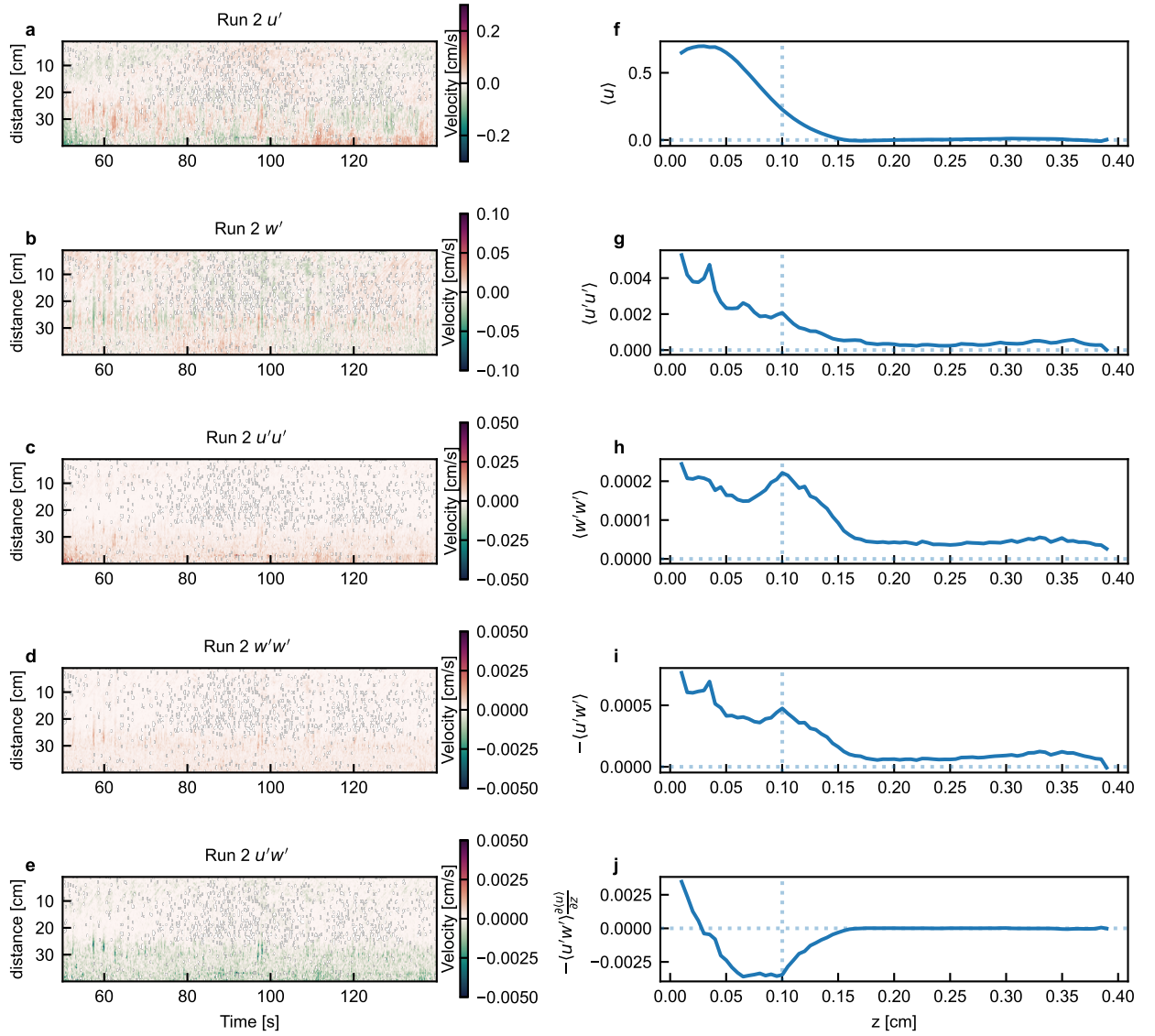


Figure 2.26: Turbulence analysis of Run 02. a) The time series of u' of the selected window. b) The time series of w' of the selected window. c) The time series of $u'u'$ of the selected window. d) The time series of $w'w'$ of the selected window. e) The time series of $u'w'$ of the selected window. f) time-averaged streamwise velocity profile. g) time-averaged Reynolds stress, $\langle u'u' \rangle$ profile. h) time-averaged Reynolds stress, $\langle w'w' \rangle$ profile. i) time-averaged Reynolds stress, $-\langle u'w' \rangle$ profile. j) Time-averaged TKE production rate at each height.

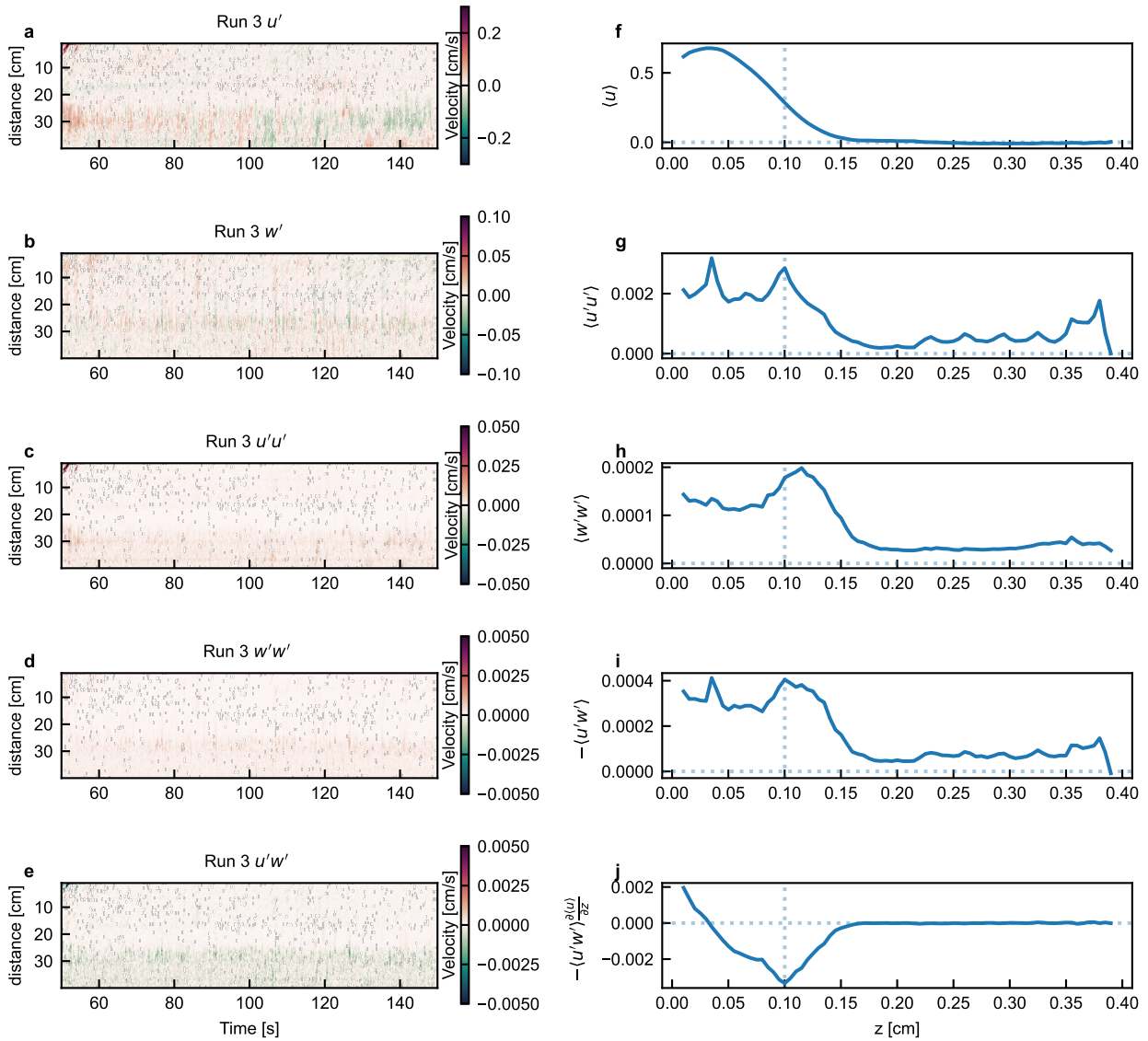


Figure 2.27: Turbulence analysis of Run 03. a) The time series of u' of the selected window. b) The time series of w' of the selected window. c) The time series of $u'u'$ of the selected window. d) The time series of $w'w'$ of the selected window. e) The time series of $u'w'$ of the selected window. f) time-averaged streamwise velocity profile. g) time-averaged Reynolds stress, $\langle u'u' \rangle$ profile. h) time-averaged Reynolds stress, $\langle w'w' \rangle$ profile. i) time-averaged Reynolds stress, $-\langle u'w' \rangle$ profile. j) Time-averaged TKE production rate at each height.

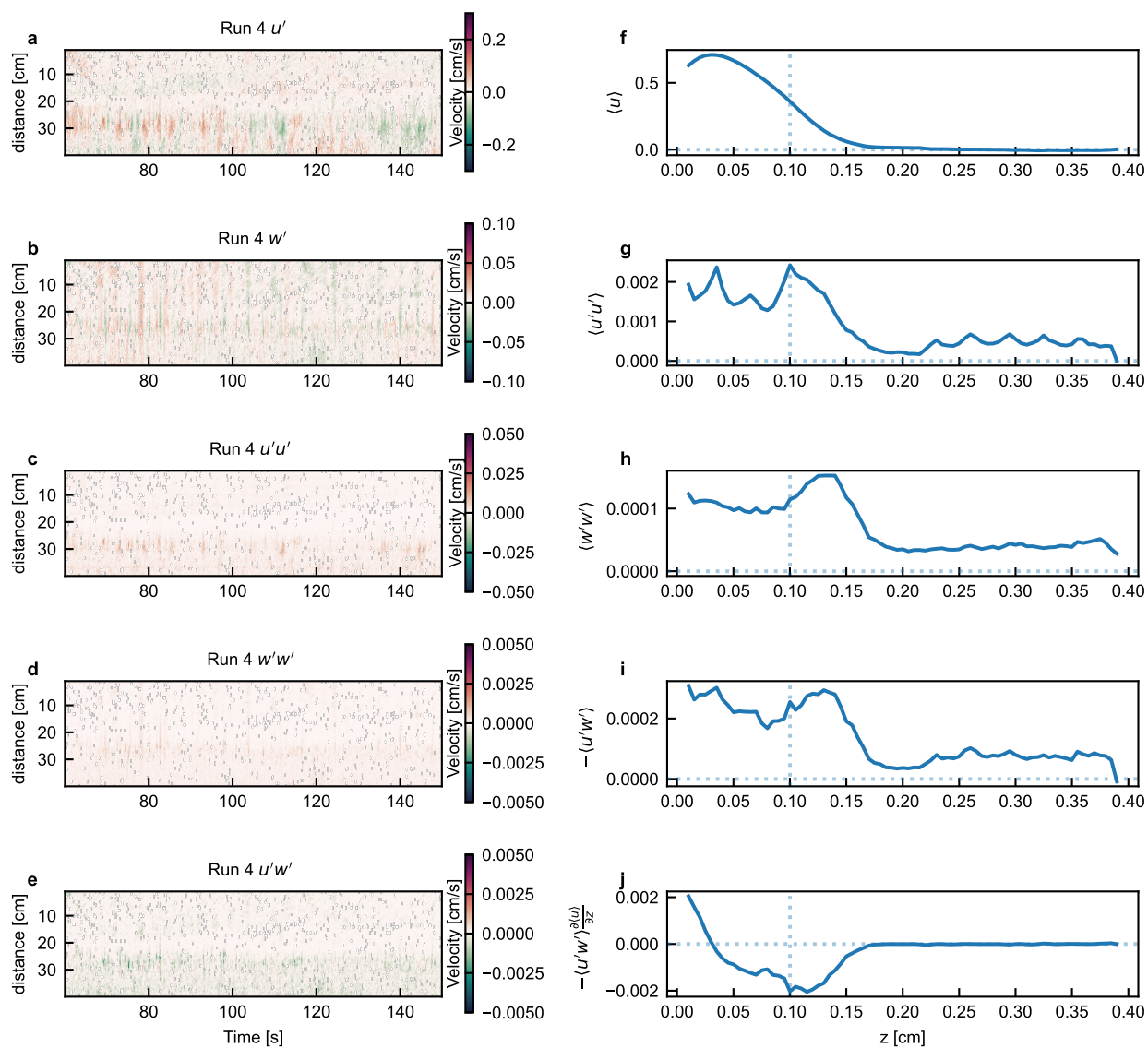


Figure 2.28: Turbulence analysis of Run 04. a) The time series of u' of the selected window. b) The time series of w' of the selected window. c) The time series of $u'u'$ of the selected window. d) The time series of $w'w'$ of the selected window. e) The time series of $u'w'$ of the selected window. f) time-averaged streamwise velocity profile. g) time-averaged Reynolds stress, $\langle u'u' \rangle$ profile. h) time-averaged Reynolds stress, $\langle w'w' \rangle$ profile. i) time-averaged Reynolds stress, $-\langle u'w' \rangle$ profile. j) Time-averaged TKE production rate at each height.

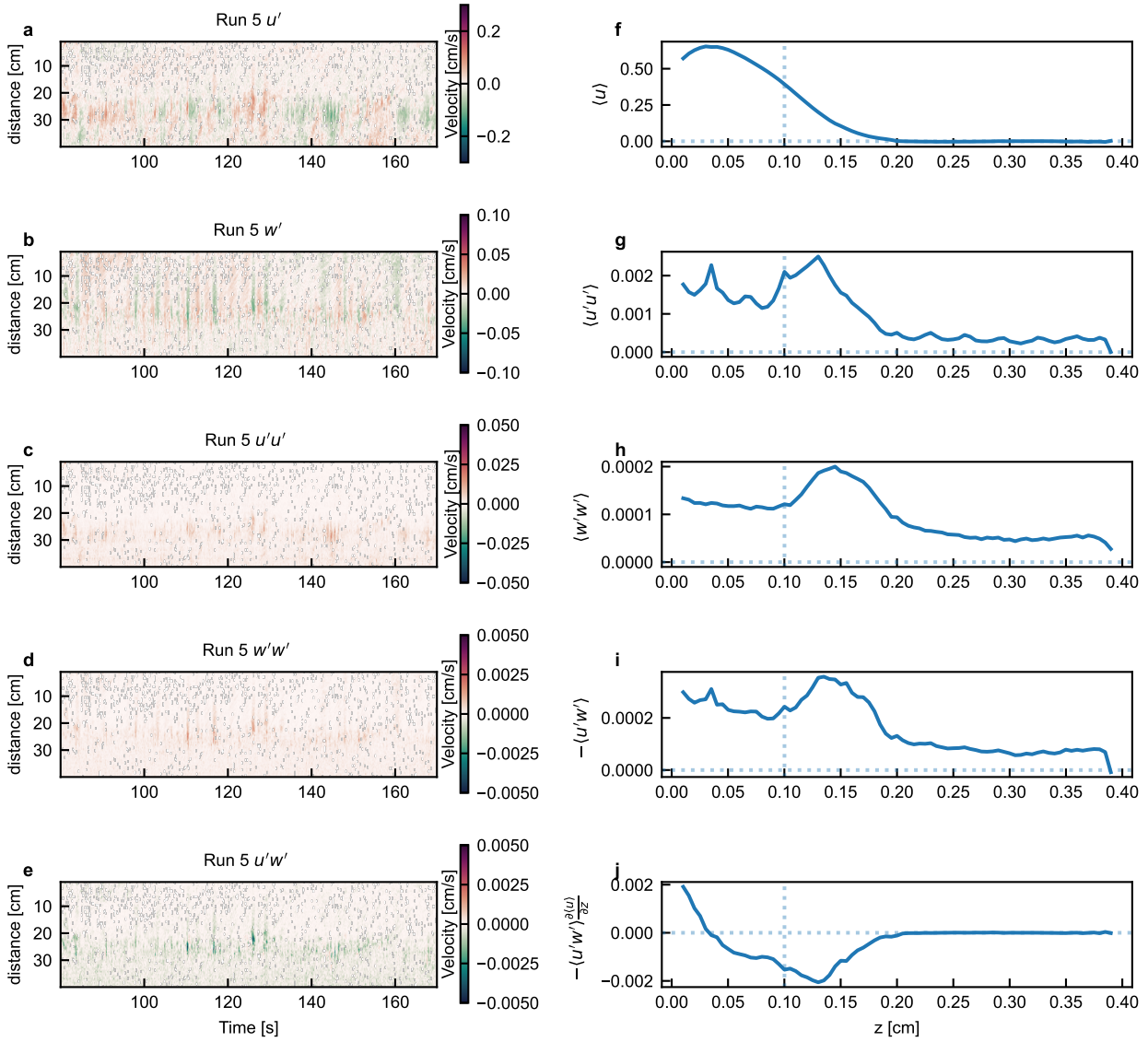


Figure 2.29: Turbulence analysis of Run 05. a) The time series of u' of the selected window. b) The time series of w' of the selected window. c) The time series of $u'u'$ of the selected window. d) The time series of $w'w'$ of the selected window. e) The time series of $u'w'$ of the selected window. f) time-averaged streamwise velocity profile. g) time-averaged Reynolds stress, $\langle u'u' \rangle$ profile. h) time-averaged Reynolds stress, $\langle w'w' \rangle$ profile. i) time-averaged Reynolds stress, $-\langle u'w' \rangle$ profile. j) Time-averaged TKE production rate at each height.

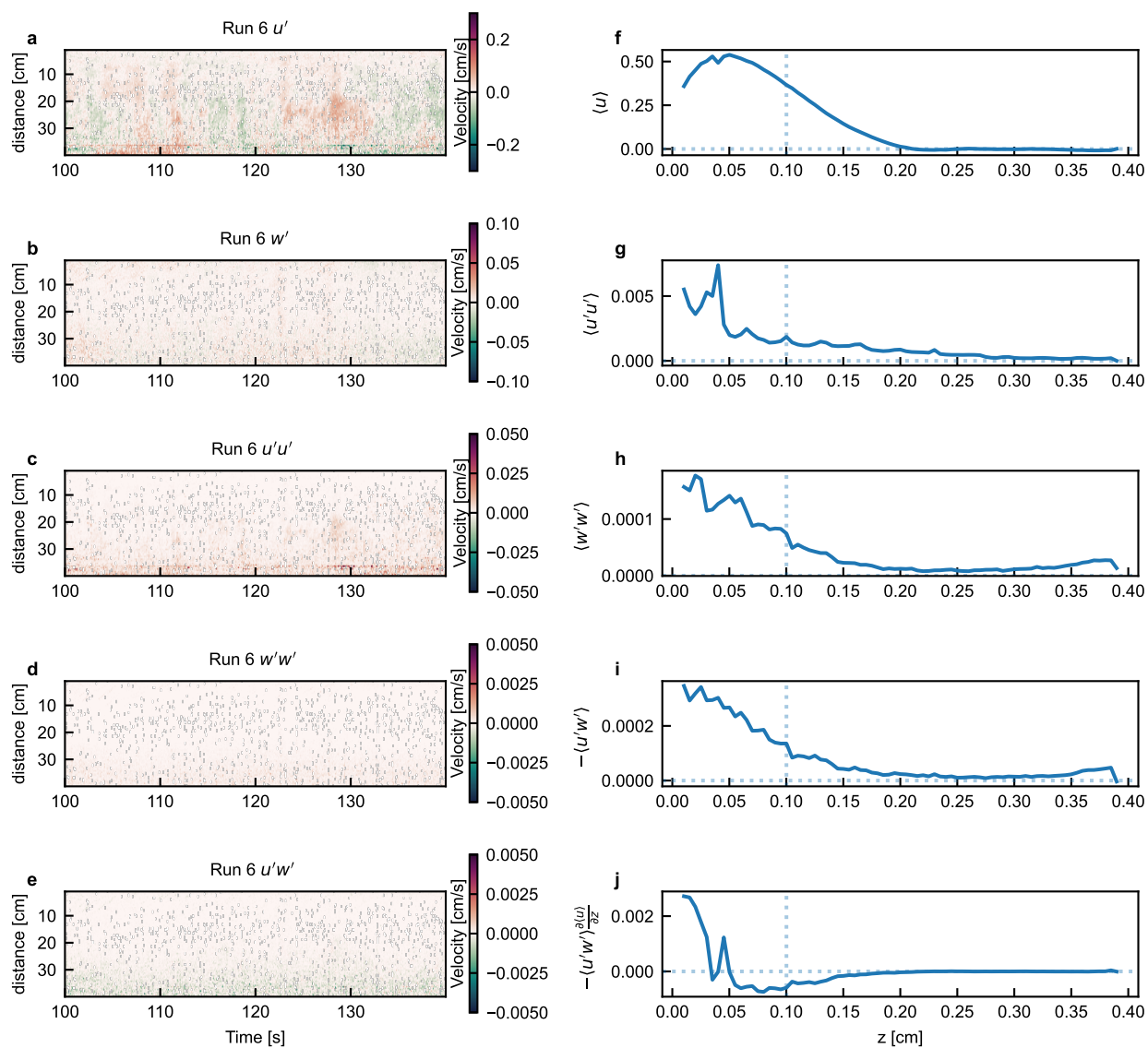


Figure 2.30: Turbulence analysis of Run 06. a) The time series of u' of the selected window. b) The time series of w' of the selected window. c) The time series of $u'u'$ of the selected window. d) The time series of $w'w'$ of the selected window. e) The time series of $u'w'$ of the selected window. f) time-averaged streamwise velocity profile. g) time-averaged Reynolds stress, $\langle u'u' \rangle$ profile. h) time-averaged Reynolds stress, $\langle w'w' \rangle$ profile. i) time-averaged Reynolds stress, $-\langle u'w' \rangle$ profile. j) Time-averaged TKE production rate at each height.

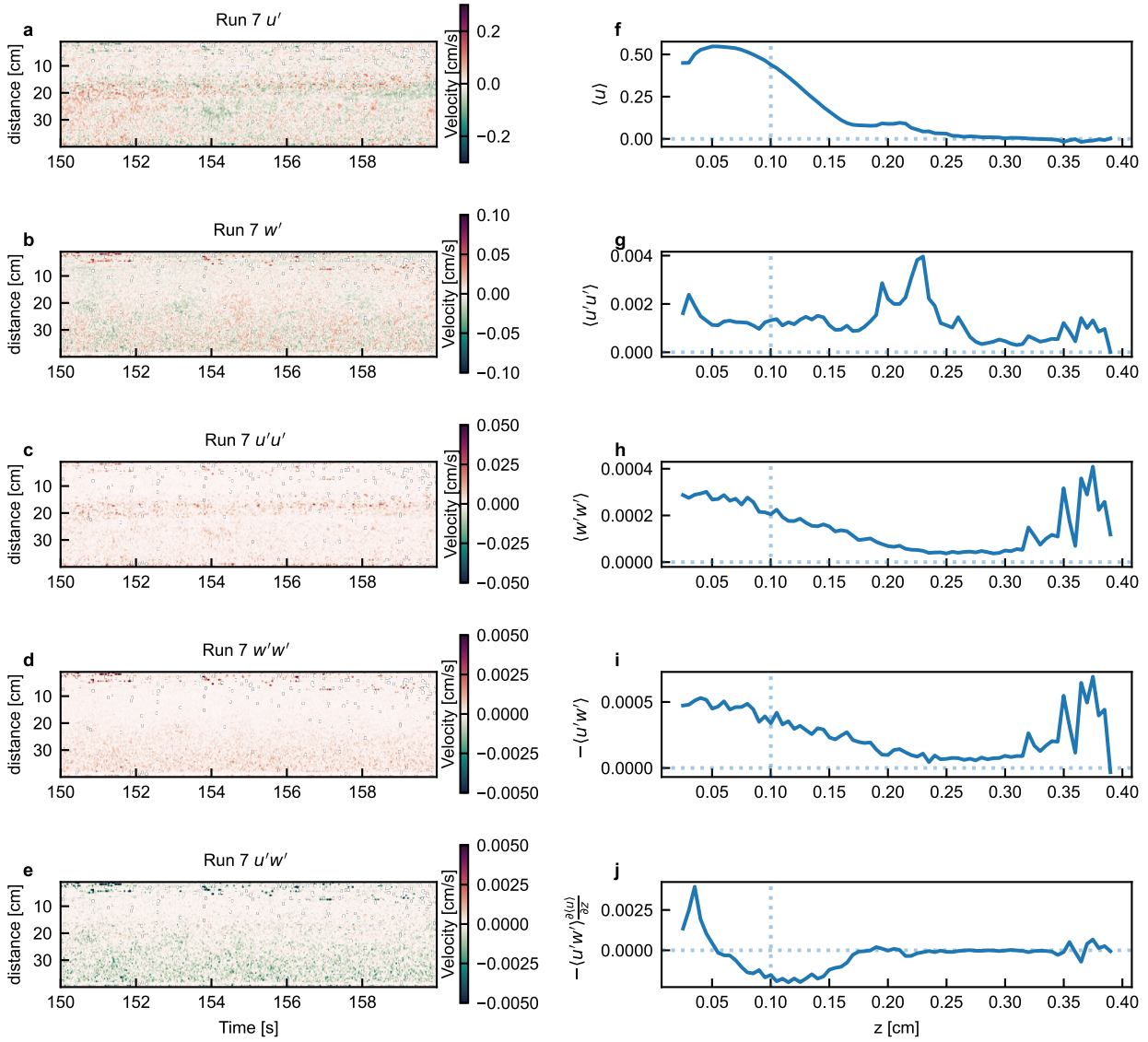


Figure 2.31: Turbulence analysis of Run 07. a) The time series of u' of the selected window. b) The time series of w' of the selected window. c) The time series of $u'u'$ of the selected window. d) The time series of $w'w'$ of the selected window. e) The time series of $u'w'$ of the selected window. f) time-averaged streamwise velocity profile. g) time-averaged Reynolds stress, $\langle u'u' \rangle$ profile. h) time-averaged Reynolds stress, $\langle w'w' \rangle$ profile. i) time-averaged Reynolds stress, $-\langle u'w' \rangle$ profile. j) Time-averaged TKE production rate at each height.

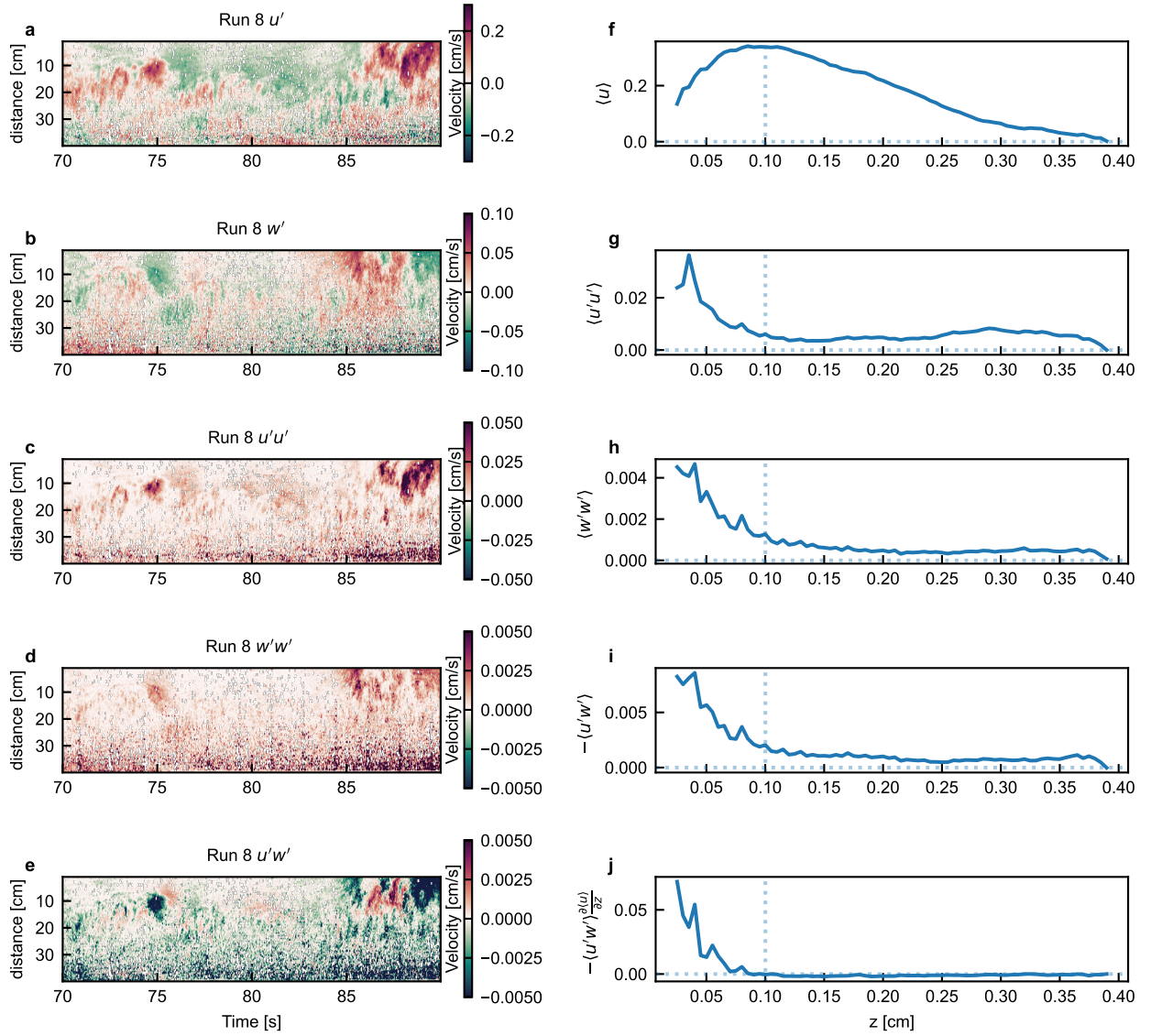


Figure 2.32: Turbulence analysis of Run 08. a) The time series of u' of the selected window. b) The time series of w' of the selected window. c) The time series of $u'u'$ of the selected window. d) The time series of $w'w'$ of the selected window. e) The time series of $u'w'$ of the selected window. f) time-averaged streamwise velocity profile. g) time-averaged Reynolds stress, $\langle u'u' \rangle$ profile. h) time-averaged Reynolds stress, $\langle w'w' \rangle$ profile. i) time-averaged Reynolds stress, $-\langle u'w' \rangle$ profile. j) Time-averaged TKE production rate at each height.

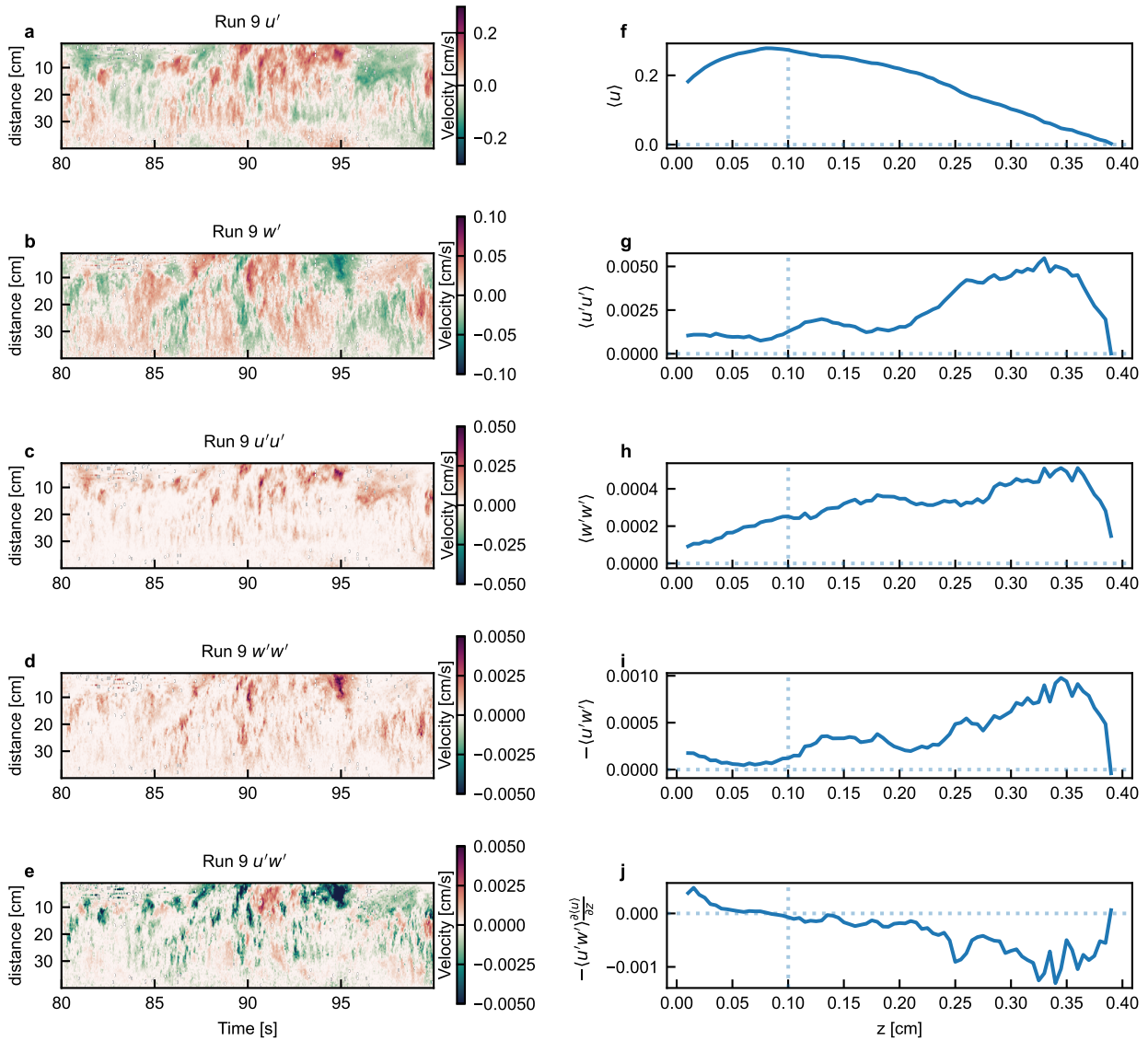


Figure 2.33: Turbulence analysis of Run 09. a) The time series of u' of the selected window. b) The time series of w' of the selected window. c) The time series of $u'u'$ of the selected window. d) The time series of $w'w'$ of the selected window. e) The time series of $u'w'$ of the selected window. f) time-averaged streamwise velocity profile. g) time-averaged Reynolds stress, $\langle u'u' \rangle$ profile. h) time-averaged Reynolds stress, $\langle w'w' \rangle$ profile. i) time-averaged Reynolds stress, $-\langle u'w' \rangle$ profile. j) Time-averaged TKE production rate at each height.

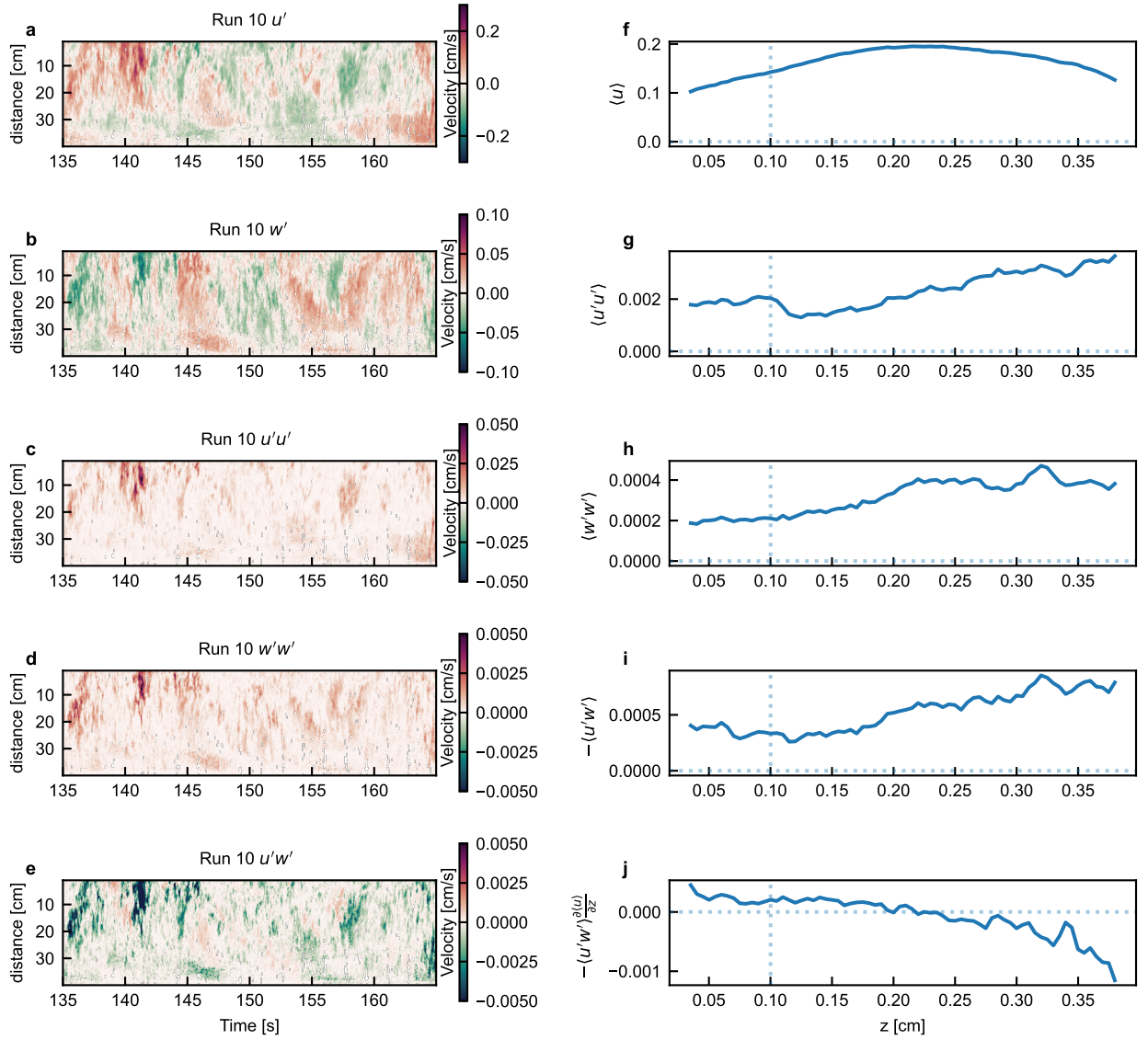


Figure 2.34: Turbulence analysis of Run 10. a) The time series of u' of the selected window. b) The time series of w' of the selected window. c) The time series of $u'u'$ of the selected window. d) The time series of $w'w'$ of the selected window. e) The time series of $u'w'$ of the selected window. f) time-averaged streamwise velocity profile. g) time-averaged Reynolds stress, $\langle u'u' \rangle$ profile. h) time-averaged Reynolds stress, $\langle w'w' \rangle$ profile. i) time-averaged Reynolds stress, $-\langle u'w' \rangle$ profile. j) Time-averaged TKE production rate at each height.

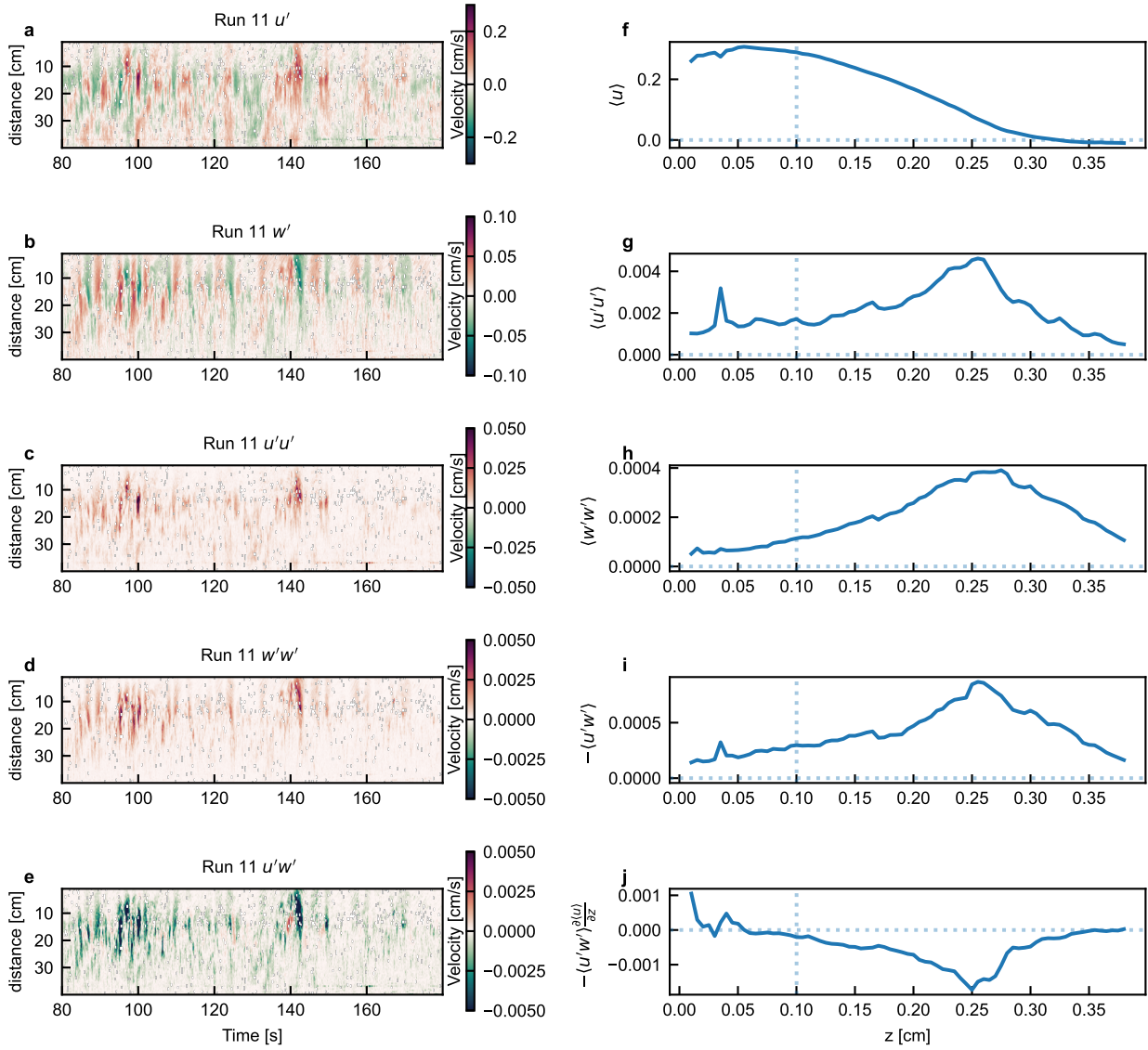


Figure 2.35: Turbulence analysis of Run 11. a) The time series of u' of the selected window. b) The time series of w' of the selected window. c) The time series of $u'u'$ of the selected window. d) The time series of $w'w'$ of the selected window. e) The time series of $u'w'$ of the selected window. f) time-averaged streamwise velocity profile. g) time-averaged Reynolds stress, $\langle u'u' \rangle$ profile. h) time-averaged Reynolds stress, $\langle w'w' \rangle$ profile. i) time-averaged Reynolds stress, $-\langle u'w' \rangle$ profile. j) Time-averaged TKE production rate at each height.

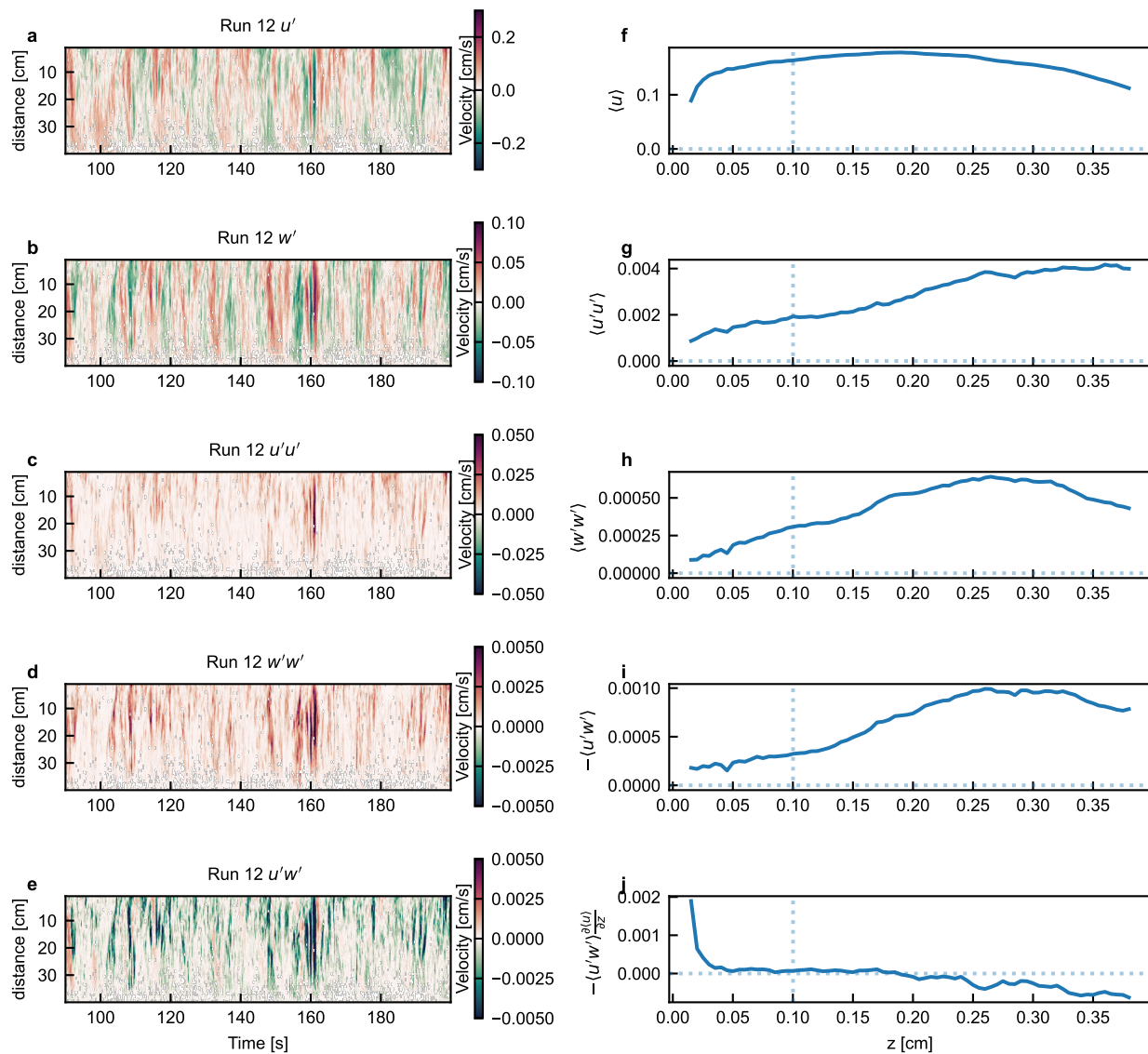


Figure 2.36: Turbulence analysis of Run 12. a) The time series of u' of the selected window. b) The time series of w' of the selected window. c) The time series of $u'u'$ of the selected window. d) The time series of $w'w'$ of the selected window. e) The time series of $u'w'$ of the selected window. f) time-averaged streamwise velocity profile. g) time-averaged Reynolds stress, $\langle u'u' \rangle$ profile. h) time-averaged Reynolds stress, $\langle w'w' \rangle$ profile. i) time-averaged Reynolds stress, $-\langle u'w' \rangle$ profile. j) Time-averaged TKE production rate at each height.

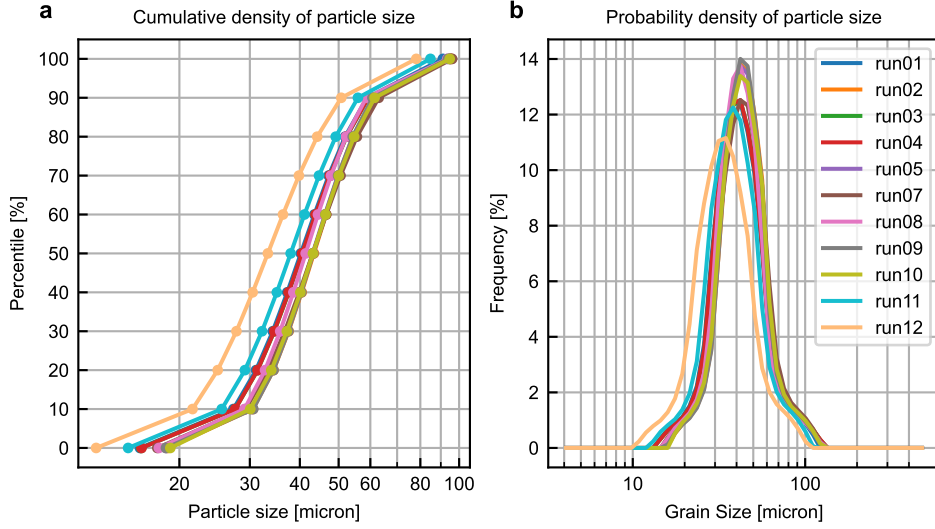


Figure 2.37: The particle-size distribution in the mixing tank was measured for each run. a) Cumulative density of particle size. b) Probability density of particle size.

sampling rate (21 ml s^{-1}). The benefit of the peristaltic pump is its constant suction rate; the precise management of the sampling duration and the amount of sample is possible. 1 mm ID silicon tubes are connected to a series of holes that are drilled on the sidewall of the channel (0.7, 2.8, 4.7, 6.8, 9.0, 11.0, 16.0, 21.0, 26.0, 30.5, 35.7, and 40.5 cm above the bed. See Fig. 2.11) to minimise the flow obstruction. Due to the limitation of the setting, peristaltic pump located roughly 3 meters away from the sampling location of the channel. The distance between the tubes and the peristaltic pump caused the adrapt decrease in suction rate. To increase the suction rate, Y-shape barbed connections are used between each 1mm ID tube and two of 2.79 mm ID manifold tubes (Fig. 2.39b,c). The manifold tubes are then attached to the 24 channels of the peristaltic pump (Fig. 2.39b,c). The discharge end of each manifold tube is attached to the custom board which is designed to fix the tubes at desired position (Fig. 2.39a,c). Beneath the custom board, there is a slidable tray on which 12 plastic pots are aligned.

The detailed procedures of flow sampling is summarised as follow. The aim of this flow sampling is to estimate the time-averaged flow concentration profile of near-equilibrium turbidity currents. Hence, the sampling is conducted from body part of each flow and first and last 45 (s) of each flow is disposed. Collected samples are sealed in plastic sample pots. Then, to minimise the error due to the evaporation of liquid inside the pots, the weight of each samples are measured right after the experiments. The volumetric concentration of each sample is estimated as follow.

$$\phi = \frac{\rho_a m_s}{\rho_s m_{\text{mix}}}, \quad (2.24)$$

where m_s and m_{mix} denote the weight of dry sediment particles in each pot and the weight of fluid and sediment mixture in each pot respectively. m_s and m_{mix} are estimated as follow. Firstly, the weight of each

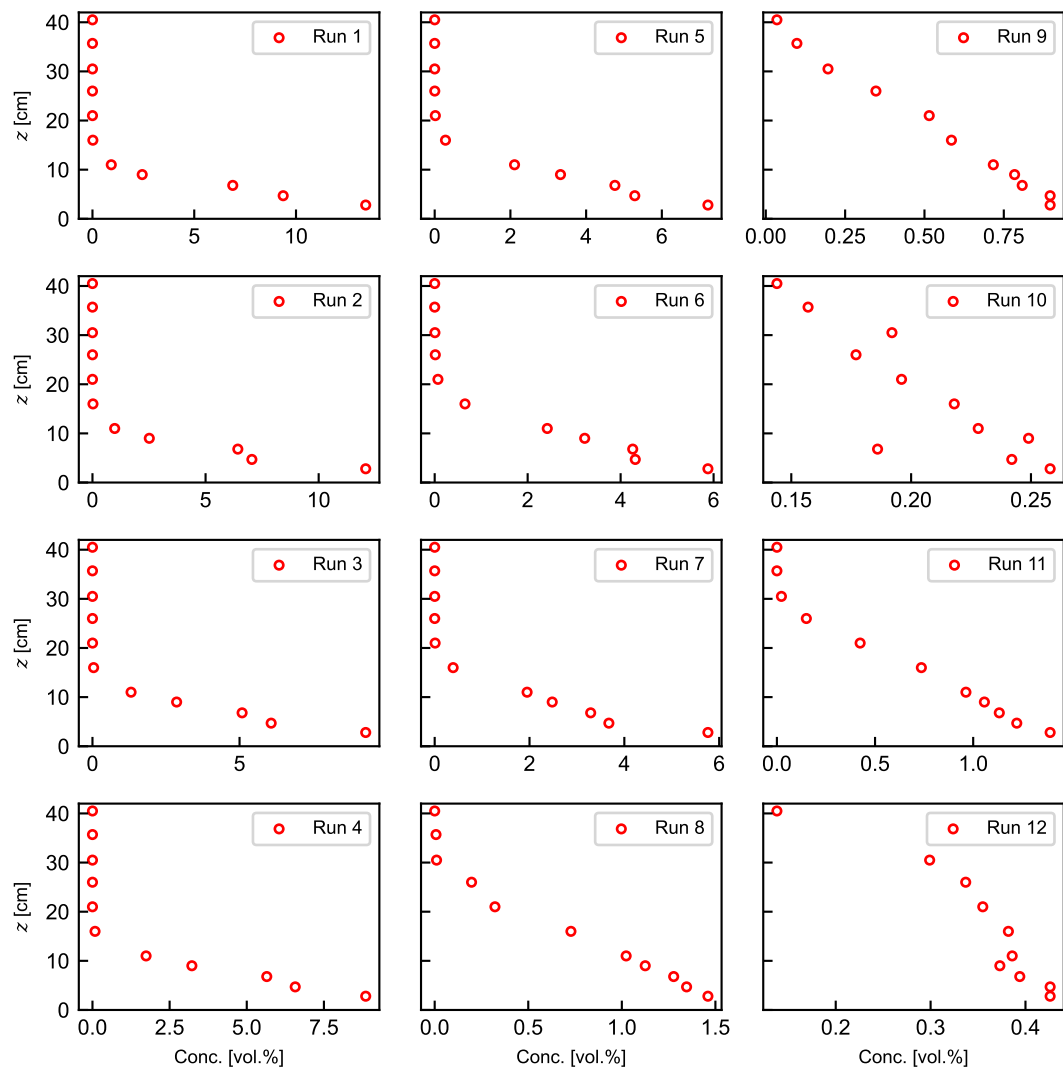


Figure 2.38: The volumetric concentration of each run calculated from the collected samples via the siphon array.

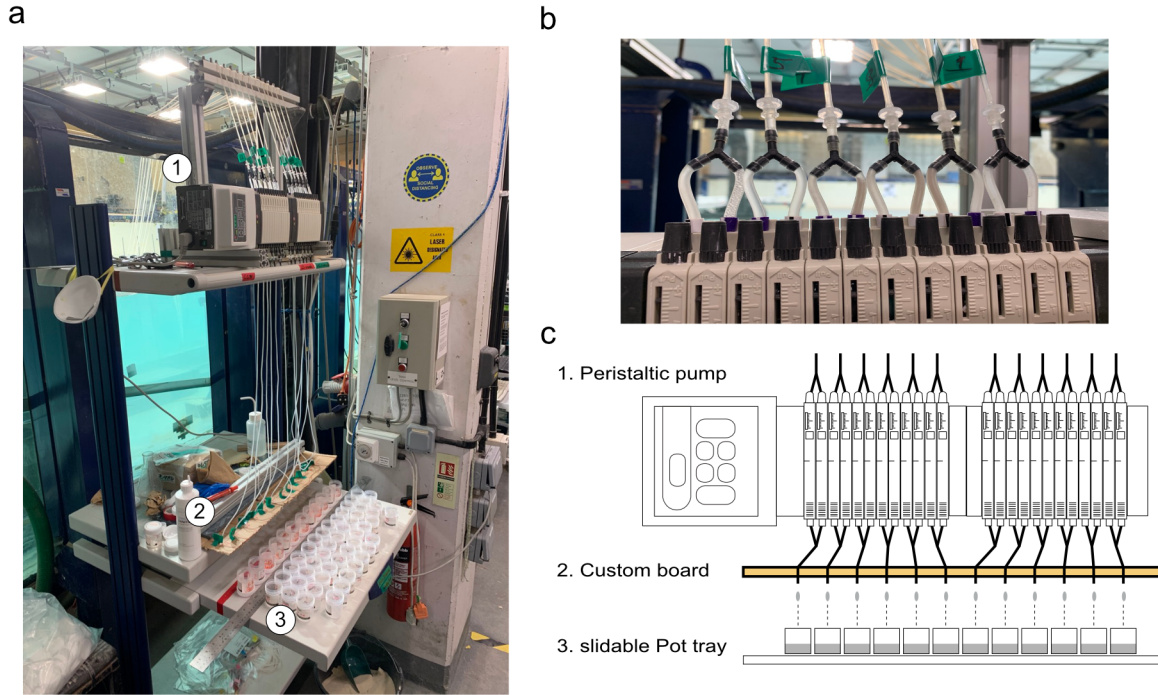


Figure 2.39: a) The photograph of the equipment of suspended sediment concentration. b) The picture of Y-shape barbed connections attached on the peristaltic pump. c) Schematic diagram of the peristaltic pump. The numbering corresponds to the number in (a).

pot, m_{pot} is measured before the experiments. Then, m_{mix} is estimated as,

$$m_{\text{mix}} = m_{\text{total}} - m_{\text{pot}} \quad (2.25)$$

where m_{total} is the total weight of sample which includes a pot and water-sediment mixture. m_{total} are measured by the high precision analytical scale (0.0001g accuracy) right after the each experiment to minimise the error due to the evaporation of fluid inside the pot. After dried the samples by using oven, m_s are estimated by

$$m_s = m_{\text{dry}} - m_{\text{pot}} \quad (2.26)$$

where m_{dry} is the measured weight of dried sample which include the weight of pot and dried particles.

The volumetric concentration of samples from the mixing tank is also measured in the same procedures above, then, the particle-size distribution is estimated using LDM (Laser Diffraction method) by Malvern MasterSize. (Fig. 2.37).

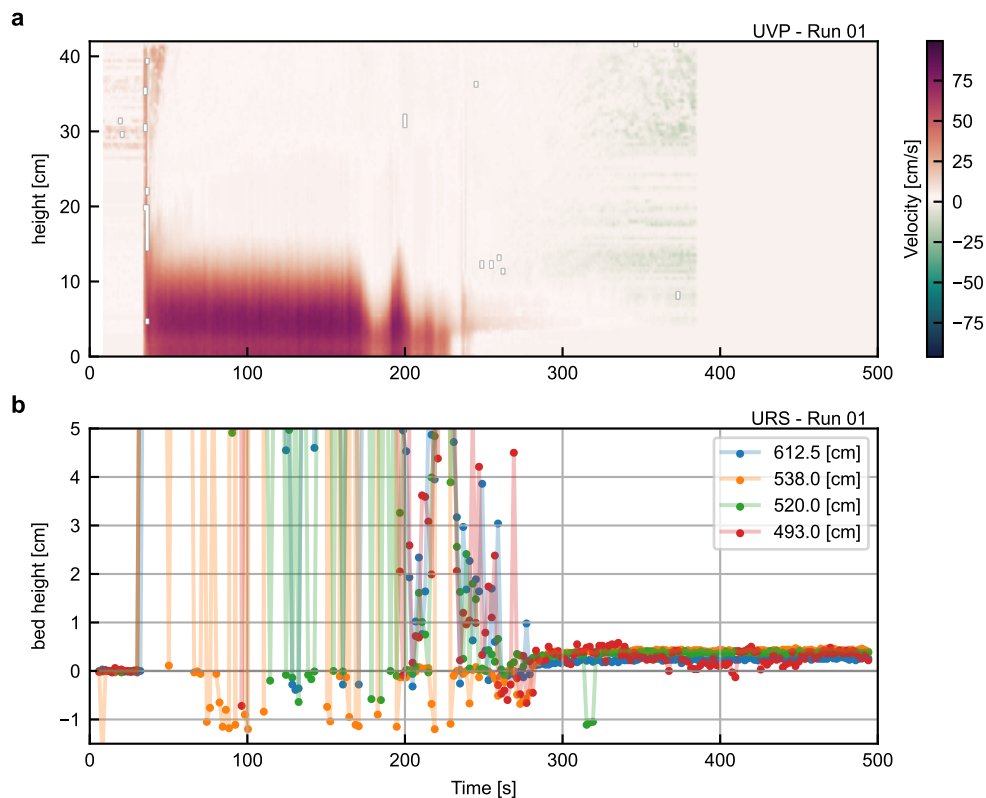


Figure 2.40: URS measurement of the aggradation rate of Run 01. a) Angled UVP data without cleaning for the reference of the flow duration. b) URS data at different locations. Figures in the legend represents the distant of each URS data from the upstream end of the channel. The URS data exhibited a great extent of noise during the flow event.

2.3.4 Monitoring of bed profile

Aggradation rate, for flow equilibrium, and bed depth is monitored by using the bed profiler from a single ADV (Acoustic Doppler Velocimeter) suspended above the flow. In addition to ADV, 4 ultrasonic sensors (URSS) to monitor the aggradation rate are mounted (Fig. 2.40–2.51). To reduce mobile bedload, and ADV measurement noise, experiments start with the unerodible bed of the Perspex channel. The maximum aggradation rate of the well-developed flow body observed in our experiments is 0.02 mm/s in run 11 (Fig. 2.50b). It should be noted that for all the runs but run 11, both ADV and URSS failed to monitor the bed height during the flow events. Even for the run 11, the three URSS failed to measure the bed profile. The URS mounted at 5.2 meters downstream from the upstream end exhibited relatively smaller noise. For those runs, the aggradation rate is monitored from the videos that were captured by high-resolution GoPro cameras. As a result, for those high concentration runs, deposition only occurred at the very end of the flow event (the tail of the flow) but we observed almost no deposition from the head and body of each flow where the velocity and density measurement are conducted.

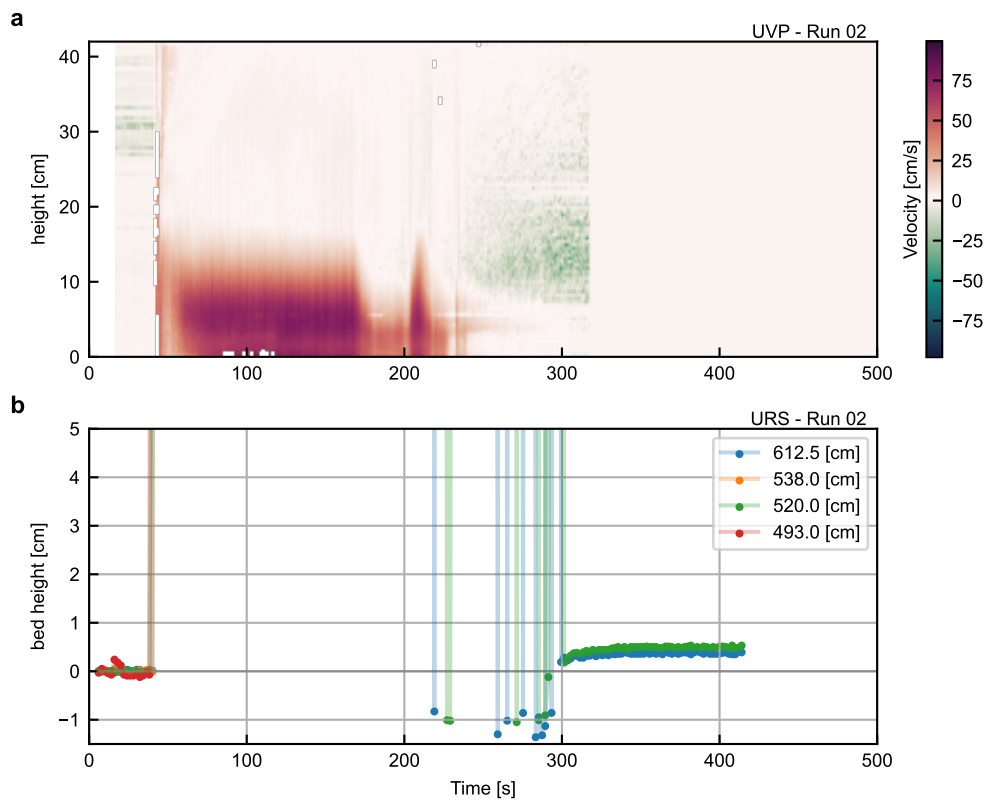


Figure 2.41: URS measurement of the aggradation rate of Run 02. a) Angled UVP data without cleaning for the reference of the flow duration. b) URS data at different locations. Figures in the legend represents the distant of each URS data from the upstream end of the channel. The URS data exhibited a great extent of noise during the flow event.

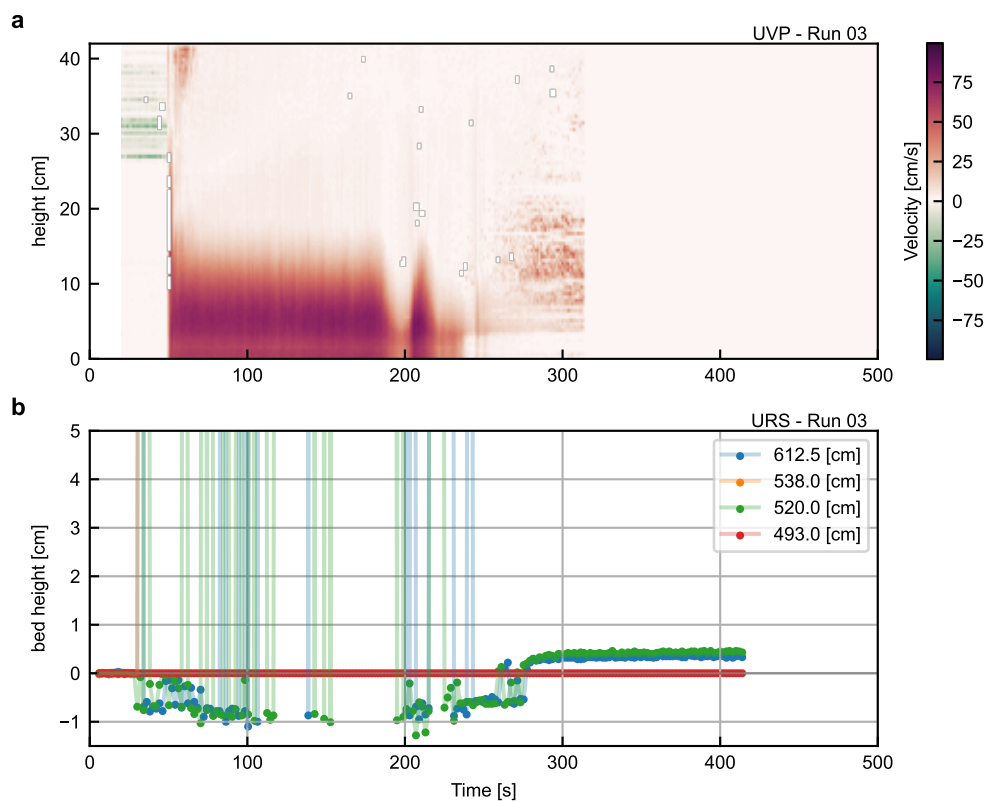


Figure 2.42: URS measurement of the aggradation rate of Run 03. a) Angled UVP data without cleaning for the reference of the flow duration. b) URS data at different locations. Figures in the legend represents the distant of each URS data from the upstream end of the channel. The URS data exhibited a great extent of noise during the flow event.

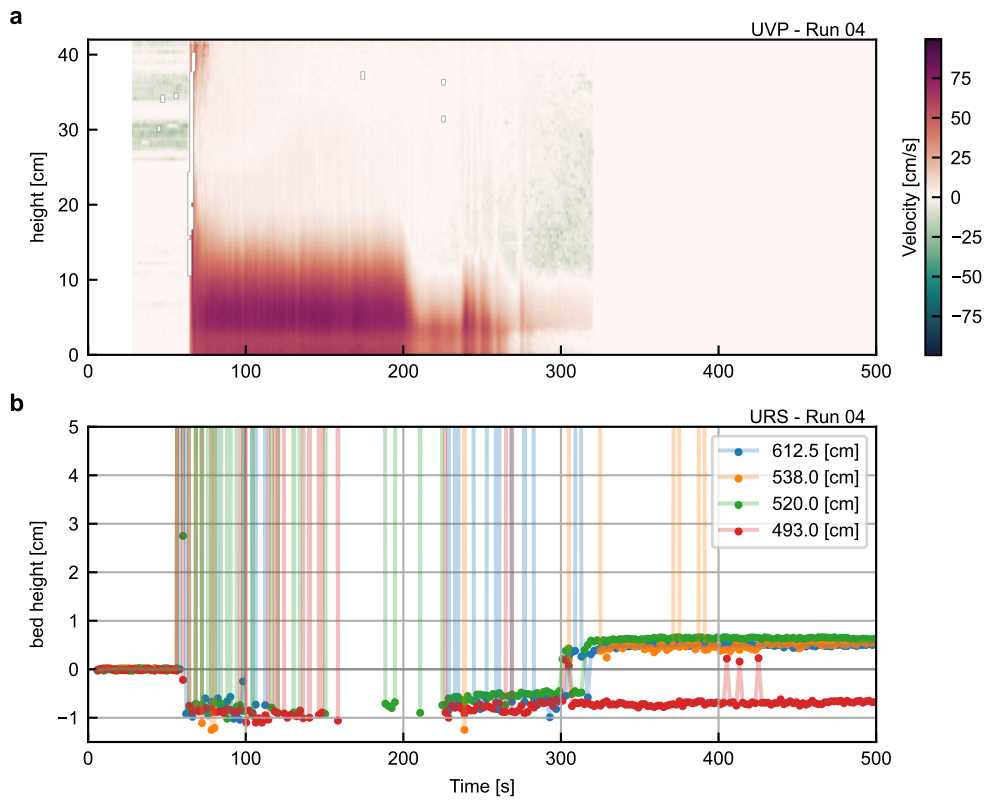


Figure 2.43: URS measurement of the aggradation rate of Run 04. a) Angled UVP data without cleaning for the reference of the flow duration. b) URS data at different locations. Figures in the legend represents the distant of each URS data from the upstream end of the channel. The URS data exhibited a great extent of noise during the flow event.

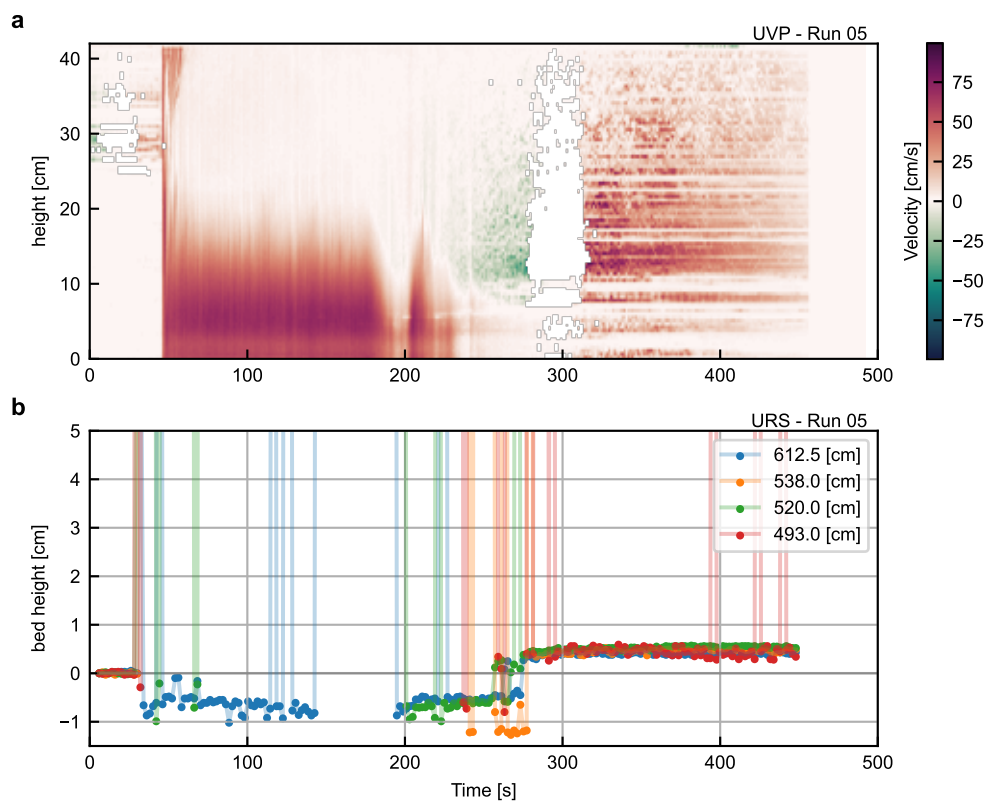


Figure 2.44: URS measurement of the aggradation rate of Run 05. a) Angled UVP data without cleaning for the reference of the flow duration. b) URS data at different locations. Figures in the legend represents the distant of each URS data from the upstream end of the channel. The URS data exhibited a great extent of noise during the flow event.

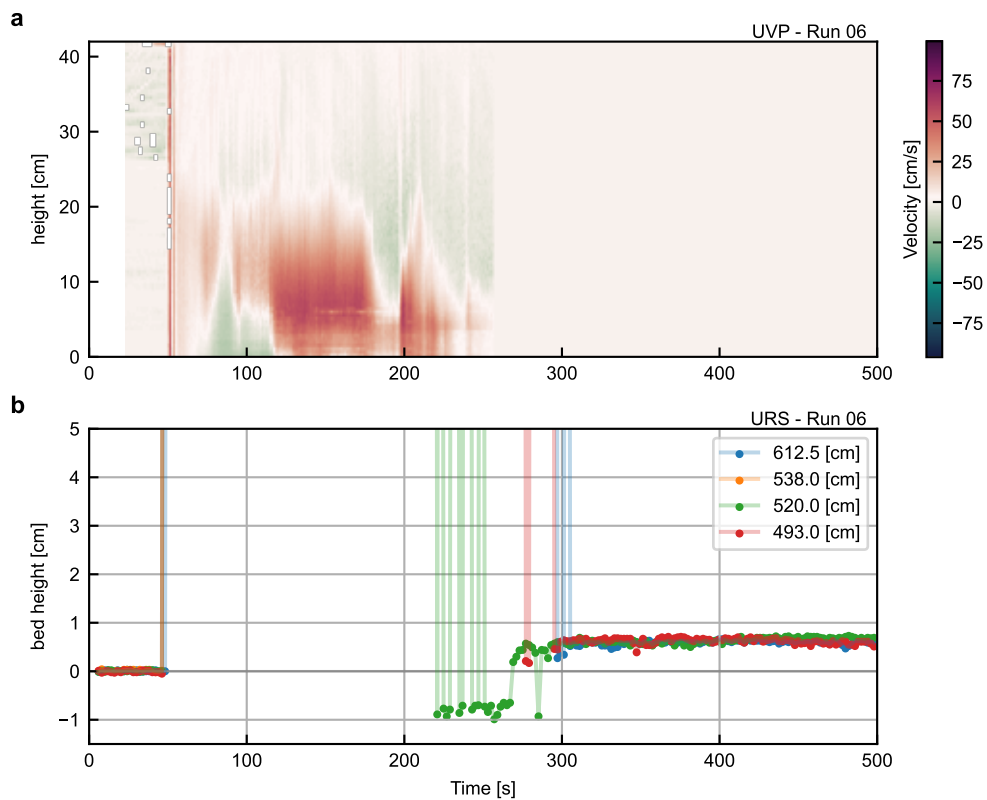


Figure 2.45: URS measurement of the aggradation rate of Run 06. a) Angled UVP data without cleaning for the reference of the flow duration. b) URS data at different locations. Figures in the legend represents the distant of each URS data from the upstream end of the channel. The URS data exhibited a great extent of noise during the flow event.

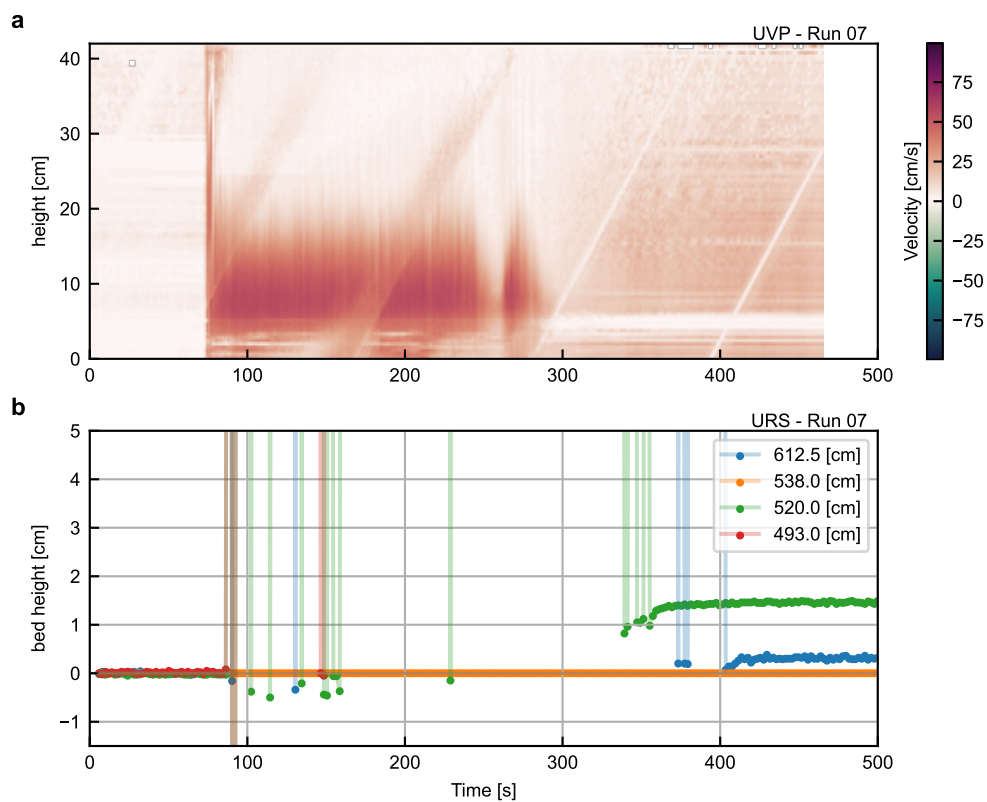


Figure 2.46: URS measurement of the aggradation rate of Run 07. a) Angled UVP data without cleaning for the reference of the flow duration. b) URS data at different locations. Figures in the legend represents the distant of each URS data from the upstream end of the channel. The URS data exhibited a great extent of noise during the flow event.

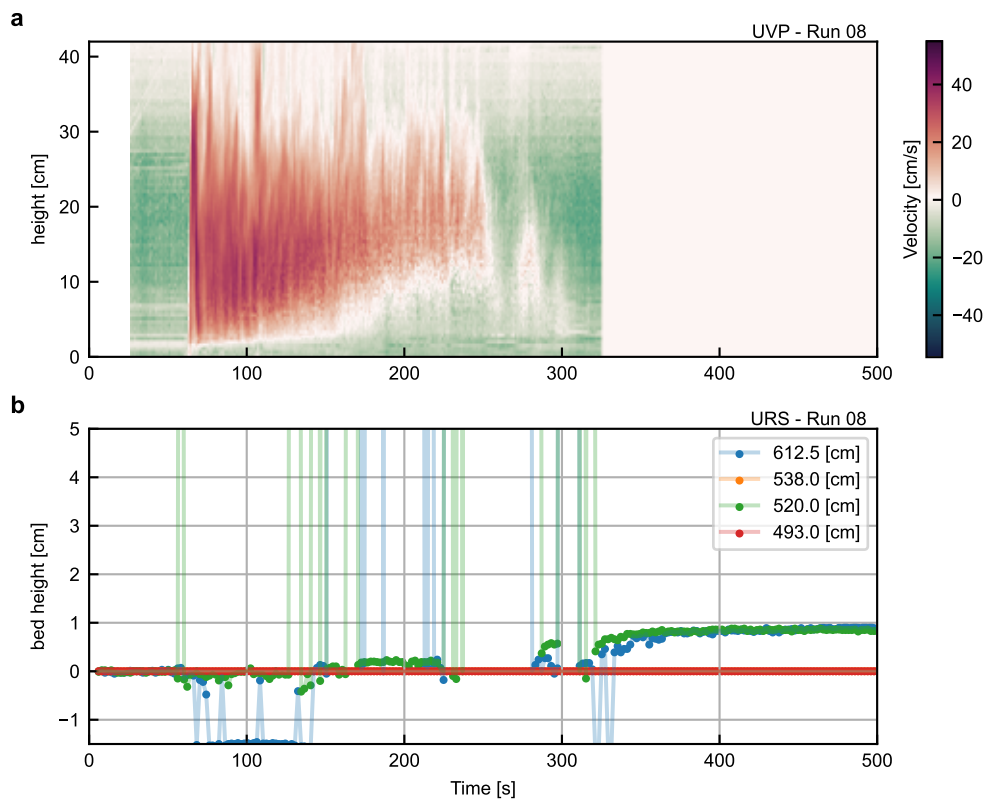


Figure 2.47: URS measurement of the aggradation rate of Run 08. a) Angled UVP data without cleaning for the reference of the flow duration. b) URS data at different locations. Figures in the legend represents the distant of each URS data from the upstream end of the channel. The URS data exhibited a great extent of noise during the flow event.

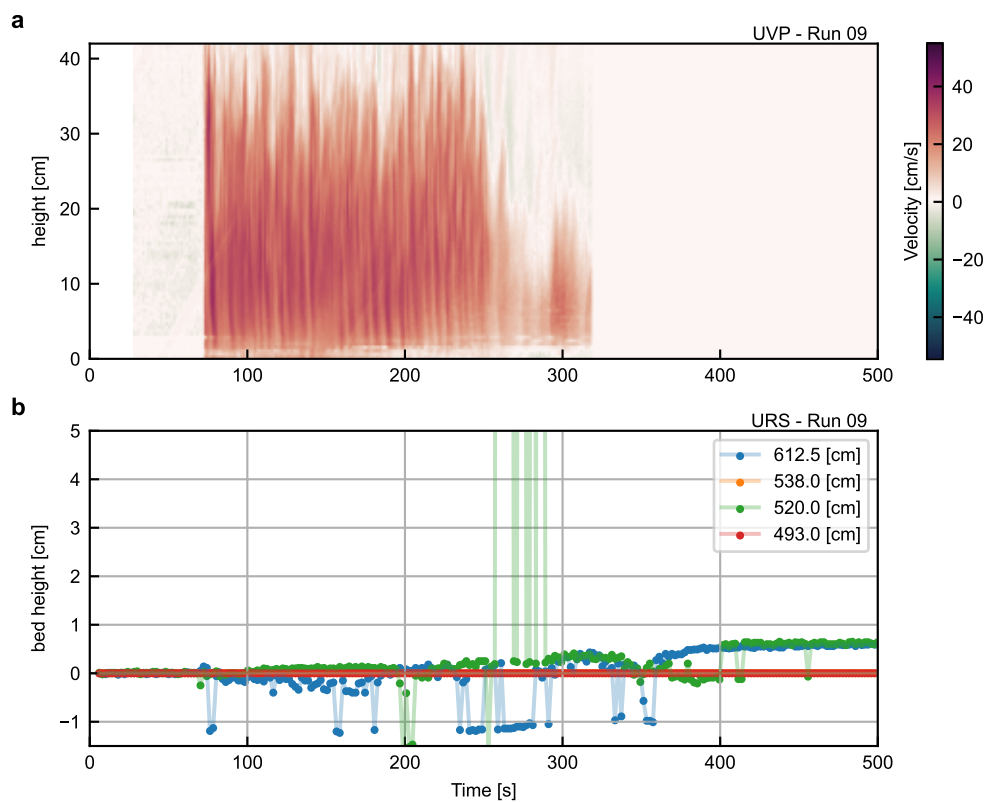


Figure 2.48: URS measurement of the aggradation rate of Run 09. a) Angled UVP data without cleaning for the reference of the flow duration. b) URS data at different locations. Figures in the legend represents the distant of each URS data from the upstream end of the channel. The URS data exhibited a great extent of noise during the flow event.

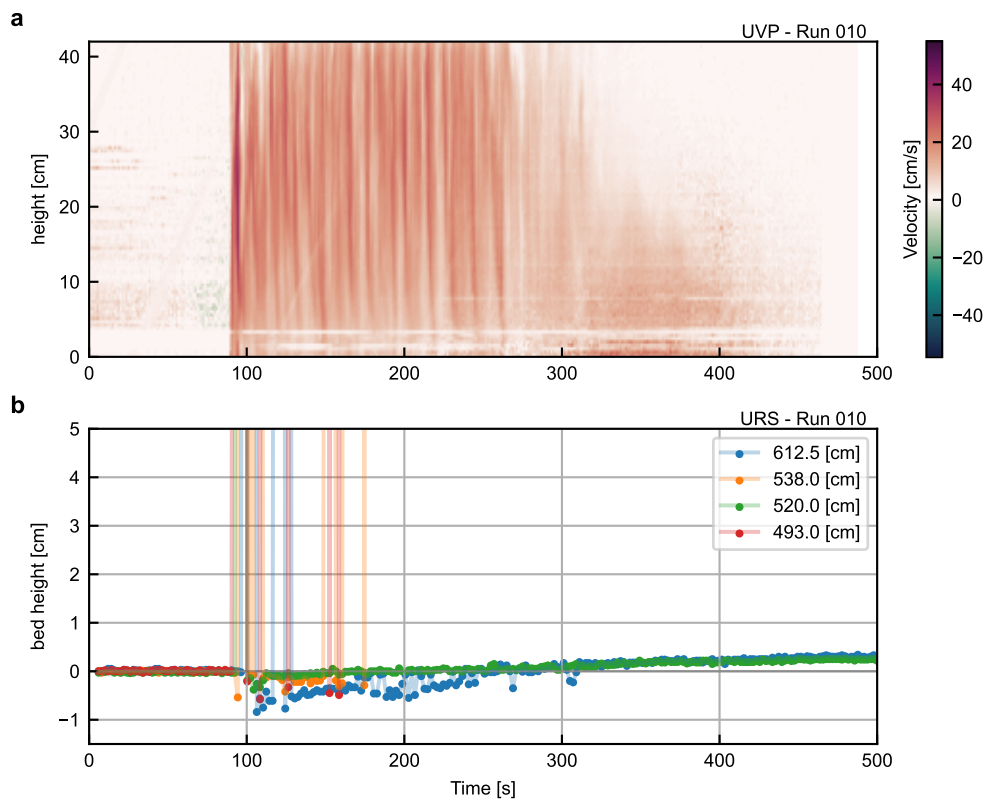


Figure 2.49: URS measurement of the aggradation rate of Run 10. a) Angled UVP data without cleaning for the reference of the flow duration. b) URS data at different locations. Figures in the legend represents the distant of each URS data from the upstream end of the channel. The URS data exhibited a great extent of noise during the flow event.

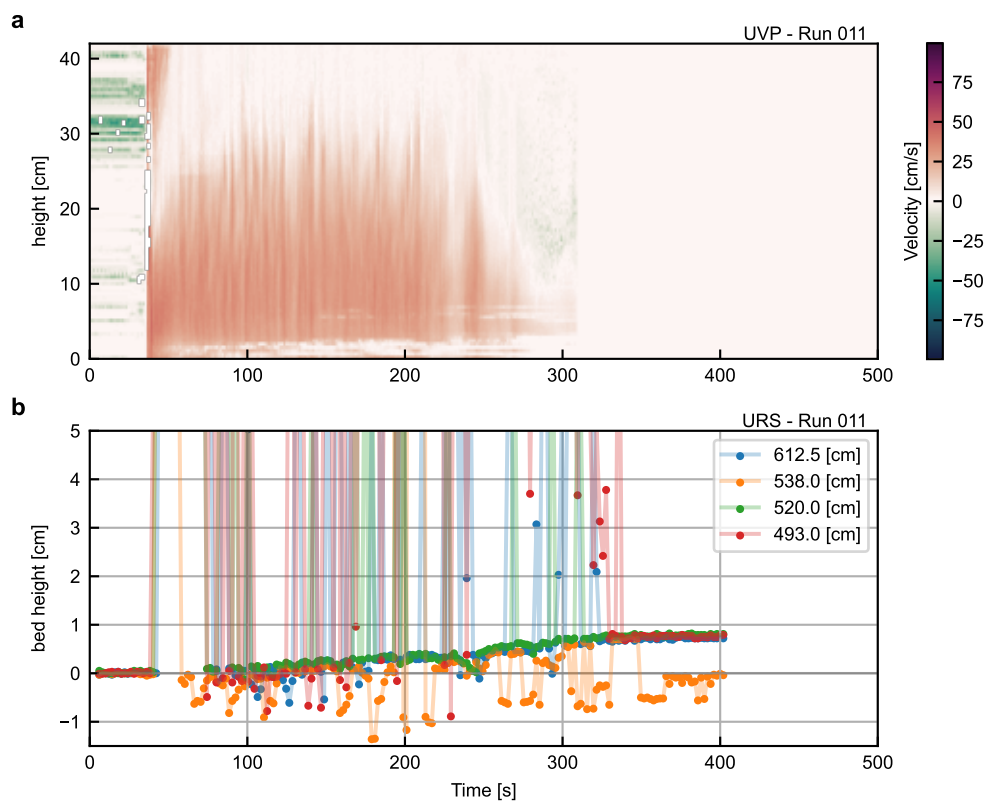


Figure 2.50: URS measurement of the aggradation rate of Run 11. a) Angled UVP data without cleaning for the reference of the flow duration. b) URS data at different locations. Figures in the legend represents the distant of each URS data from the upstream end of the channel. The URS data exhibited a great extent of noise during the flow event.

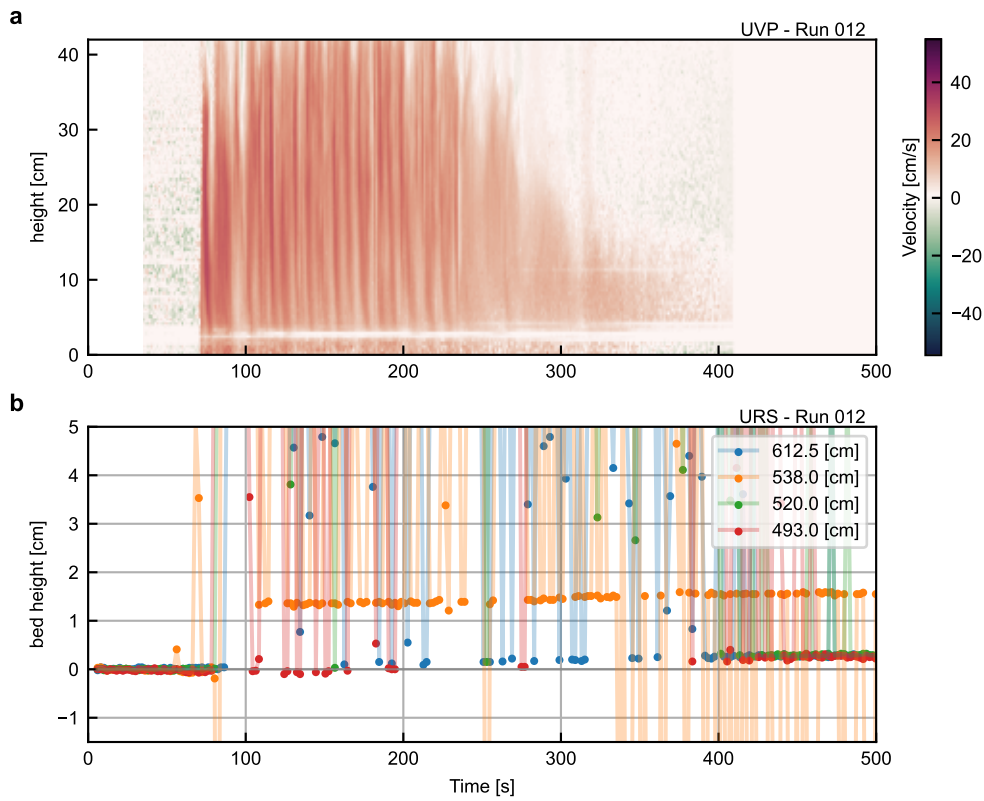


Figure 2.51: URS measurement of the aggradation rate of Run 12. a) Angled UVP data without cleaning for the reference of the flow duration. b) URS data at different locations. Figures in the legend represents the distant of each URS data from the upstream end of the channel. The URS data exhibited a great extent of noise during the flow event.

Chapter 3

Vertical Flow Structure

3.1 Introduction

In this chapter, I model the vertical shape of the velocity and concentration profiles using the sources gathered in Chapter 2. Better prediction of vertical stratification of turbidity currents is fundamental to understanding the flow dynamics of long-runout turbidity currents along sinuous submarine-channel networks (Stacey and Bowen, 1990; Abad et al., 2011; Dorrell et al., 2019; Wells and Dorrell, 2021). For instance, overspilling along sinuous meandering channels is a key process for both flow runout and the development of submarine channel network systems (Nakajima and Kneller, 2013; Dorrell et al., 2014; Dorrell et al., 2015; Miramontes et al., 2020). How a flow reduces/increases its density through overspilling requires high-accuracy vertical stratification models. Since the overspilled particles form the levee, the vertical flow structures are also a key control of the formation of leveed channels. Further, the frequency of avulsions, the abandonment of the current channel and the formation of a new channel are fundamental to understanding how the submarine fan system develops (Lopez, 2001; Kolla et al., 2007; Dorrell et al., 2015). The channel avulsion can occur due to external forces such as sea level change or channel occlusion by debrites (Kolla et al., 2007). However, avulsion can also occur without those allogenic factors (Dorrell et al., 2015). When a channel is under an aggradational condition, the channel is infilled quicker than levees are built, increasing the probability of avulsion to happen (Dorrell et al., 2015). This increase in channel instability depends on overspilling and, thus, the vertical flow structures.

Turbidity currents dynamics, their risks and sedimentary deposits have been traditionally simulated by depth average models (Parker et al., 1986). These reduced complexity models, such as depth-averaged models, are favoured as they lower computational cost, so real-world scale systems can be considered (Dorrell et al., 2014; Traer et al., 2015). However, depth-averaged models commonly assume the flow is vertically uniform, so-called “*top-hat*” models. As mentioned above, overspilling occurs at the very top layer of a flow, where the

flow concentration is relatively more dilute than the bottom layer. However, in the “*top-hat*” models, the flow concentration is vertically uniform and thus significantly overestimates the loss of the suspended sediment particles and the total kinetic energy due to overspilling. This overestimation makes it almost impossible for a flow to trace the meandering channels without dissipation, highlighting how vital the proper vertical structure models are.

Another problem of the “*top-hat*” models is their centre of mass. Compared to the stratified flows, “*top-hat*” models always overestimate the height of the centre of mass (section 1.2.6 and 1.3.5). Turbidity currents always entrain ambient fluid and dilute and thicken downstream. In the stratified flows, it is primarily the top of the flow, which is diluted by entrainment. Therefore, the centre of mass remains low in the current. On the other hand, in the “*top-hat*” models, the height of the centre of mass increases as a flow is thickened, forming a pressure gradient from downstream to upstream, which will decelerate the flow. Further, an increase in the centre of mass makes the entire flow unstable and less channelised, making it almost impossible for the flow to run out long distances.

To discuss how vertical structures impact flow dynamics, the conservation equations of sediment mass and momentum of a turbidity current in a straight channel are considered here. Depth-averaged models can be derived through the integration of the conservation equations (section 1.2.2 and 1.2.6). The mass of sediment and momentum conservations of a flow may be described as (e.g. Parker et al., 1986) (section 1.3.5),

$$\frac{\partial \langle \phi \rangle}{\partial t} + \frac{\partial \langle u \rangle \langle \phi \rangle}{\partial x} = -\frac{\partial}{\partial z} (\langle \phi' w' \rangle - w_s \langle \phi \rangle), \quad (3.1)$$

$$\frac{\partial \langle u \rangle}{\partial t} + \frac{\partial \langle u \rangle^2}{\partial x} + \frac{\partial \langle u \rangle \langle w \rangle}{\partial z} = -\frac{1}{\rho_f} \frac{\partial \langle p \rangle}{\partial x} + Rg \langle \phi \rangle \theta + \frac{\partial}{\partial z} (-\langle u' w' \rangle) \quad (3.2)$$

where $\langle u \rangle$, $\langle w \rangle$, $\langle \phi \rangle$, $\langle p \rangle$ denotes the Reynolds-averaged downstream velocity, bed-normal velocity, volumetric concentration of suspended particle, and hydrostatic pressure respectively. It should be noted that $\langle \rangle$ brackets and primes denote the Reynolds average and the fluctuating part of the parameters. ρ_f denotes the flow density. $R = (\rho_s - \rho_a)/\rho_a$ denotes the relative excess density of the sediment to fluid. θ denotes the slope. g denotes the gravitational acceleration. $\langle u' w' \rangle$ denotes the Reynolds stress term. The pressure term $\langle p \rangle$ can be described as,

$$\langle p \rangle = \rho_f Rg \int_z^\infty \langle \phi \rangle dz. \quad (3.3)$$

The vertical integration of the equations (3.1) and (3.2) with the aid of the equation (3.3) yields,

$$\frac{\partial}{\partial t} \int_0^\infty \langle \phi \rangle dz + \frac{\partial}{\partial x} \int_0^\infty \langle u \rangle \langle \phi \rangle dz = \langle \phi' w' \rangle|_{\text{bed}} - w_s \langle \phi \rangle|_{\text{bed}} \quad (3.4)$$

$$\frac{\partial}{\partial t} \int_0^\infty \langle u \rangle dz + \frac{\partial}{\partial x} \int_0^\infty \langle u \rangle^2 dz = -\frac{1}{\rho_f} \frac{\partial}{\partial x} \int_0^\infty \langle p \rangle dz + Rg\theta \int_0^\infty \langle \phi \rangle dz + \frac{\partial}{\partial z} \int_0^\infty -\langle u' w' \rangle dz. \quad (3.5)$$

The flow velocity and volumetric concentration can be described using the structure functions, $\xi_u(\hat{z})$ and $\xi_\phi(\hat{z})$ as,

$$\xi_u(\hat{z}) = \langle u \rangle / U, \quad \xi_\phi(\hat{z}) = \langle \phi \rangle / \Phi, \quad (3.6)$$

where $\hat{z} = z/h$ is the normalised distance from the bed. In the equation (3.4) and (3.5), when we consider the 1st-order integral terms of flow velocity and concentration respectively,

$$\int_0^\infty \langle u \rangle d\hat{z} = U, \quad \int_0^\infty \langle \phi \rangle d\hat{z} = \Phi. \quad (3.7)$$

The 2nd-order integral terms in the equation (3.4) and (3.5) will be

$$\int_0^\infty \langle u \rangle \langle \phi \rangle d\hat{z} = U\Phi \int_0^\infty \xi_u \xi_\phi d\hat{z}, \quad \int_0^\infty \langle u \rangle^2 d\hat{z} = U^2 \int_0^\infty \xi_u^2 d\hat{z}. \quad (3.8)$$

The integration of pressure term, $\langle p \rangle$ is given by

$$\begin{aligned} \int_0^\infty \langle p \rangle d\hat{z} &= \frac{\rho_f Rg}{h} \int_0^\infty \int_z^\infty \langle \phi \rangle dz' dz \\ &= \frac{\rho_f Rg}{h} \int_0^\infty z \langle \phi \rangle dz \\ &= (\rho_s - \rho_a)gh\Phi \int_0^\infty \hat{z} \xi_\phi d\hat{z}. \end{aligned} \quad (3.9)$$

In the equations (3.8) and (3.9), the following vertical-flow-structure-induced weighting terms (shape factors) can be found (section 1.2.6),

$$W_{u^2} \equiv \int_0^\infty \xi_u^2 d\hat{z}, \quad W_{u\phi} \equiv \int_0^\infty \xi_u \xi_\phi d\hat{z}, \quad W_P \equiv 2 \int_0^\infty \hat{z} \xi_\phi d\hat{z}. \quad (3.10)$$

$\langle u \rangle \langle \phi \rangle$ and $\langle u \rangle \langle u \rangle$ represent the material and momentum transport rate at a given height. Therefore, the depth-integrated values of them, thus, represent the total material and momentum transport rate of a flow. The last term of the equation 3.10 appears in the hydrostatic pressure gradient term of the shallow water equation (Parker et al., 1986; Dorrell et al., 2014). For the same depth-integrated concentration and velocity fields, those three terms are only dependent on the weighting terms, $W_{u\phi}$, W_{u^2} , and W_P each of which is a function of the structure functions, ξ_ϕ and/or ξ_u . Within the same $\int \langle u \rangle dz$ and $\int \langle \phi \rangle dz$, the unstratified model (top-hat) yields the minimum transport rate compared with other stratified models (Fig. 3.1). In stratified flows (Fig. 3.1), most of the material and momentum transport occur around the velocity maximum elevation, increasing the total depth-integrated transport rates.

In the unstratified flow model ($W_P = 1$), the pressure term (Eq. 3.10) increases towards the streamwise direction as the flow is thickened by water entrainment. This physically means that the entire suspended

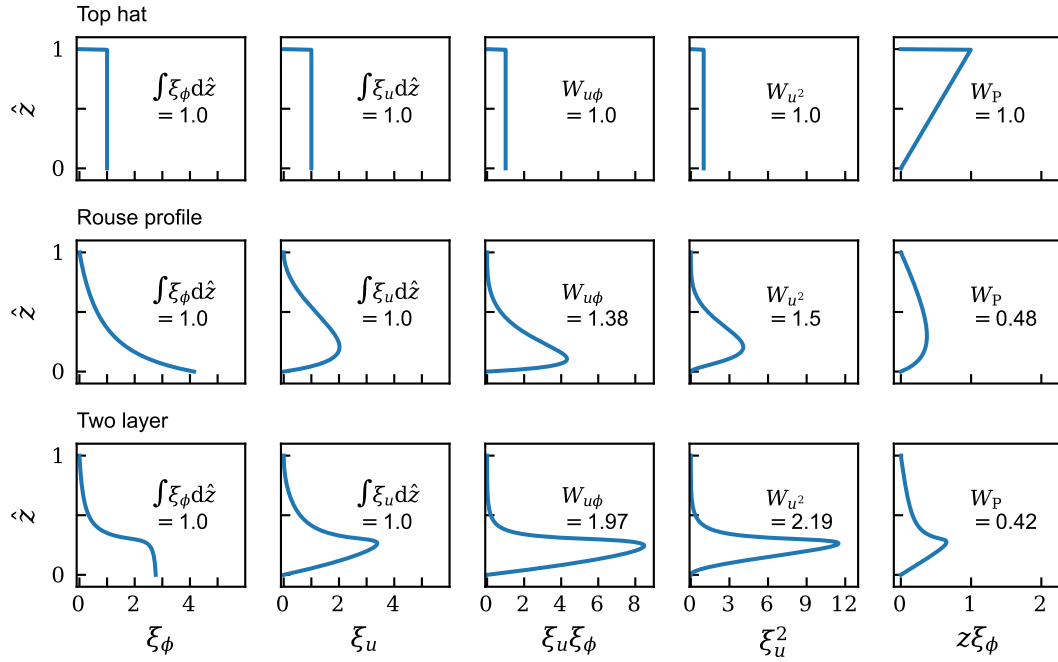


Figure 3.1: Comparison of flow profiles between 'top-hat' model (top row) and stratified flow models (Rouse-type stratified flow in the second column and stream-jet-type flow in the third column) with the same depth-averaged streamwise velocity and flow concentration values. From the left side, each column represents the vertical profile of idealised streamwise flow velocity, flow concentration, material transport term, momentum transport term, and pressure gradient term. The Y-axes are normalised by the flow height, h . Each axis of the right three X-axes is normalised by its depth-integrated value.

sediment will be lifted by the water entrainment so that the flow can maintain its unstratified flow profile. Even when there is no sediment exchange at the bed, the thickening of a flow immediately dilutes the entire flow in the case of an unstratified model. Then, the centre of mass is lifted as the flow is thickened, generating the positive pressure gradient downstream. The resultant pressure field slows the flow down. With increasing stratification, it is speculated that the sediment entrainment increases the near-bed concentration while the water entrainment dilutes the upper layer of the flow, which enhances the flow stratification downstream. Increasing flow stratification decreases the pressure term (Fig. 3.1). The negative downstream pressure gradient accelerates the flow. Therefore, a better understanding of flow stratification is fundamental for the better prediction of long-runout turbidity currents.

As introduced in the data collection section (Chapter 2), many flume experiments have been designed and conducted to analyse the detailed flow structures of turbidity currents and how they vary with the flow parameters (e.g. grain size, flow velocity). Yet, recent numerical models (Dorrell et al., 2014) used empirical vertical shape factors (Parker et al., 1986; Abad et al., 2011) but resulted in poor prediction of flow behaviour in natural-scale sinuous submarine channels. The previous failures in the prediction of flow structures can be attributed to the lack of direct measurement data of natural-scale turbidity currents and the lack of synthetic studies to connect the results of different flume experiments. The link between various flow parameters and the flow structures is still poorly understood. Although the link between the velocity profile and the concen-

tration profile has been speculated since more than 30 years ago (Stacey and Bowen, 1988a), how these two profiles constrain each other remains unclear. When we consider a near-equilibrium turbidity current, since the excess density provides the driving force for the flow, the velocity profile should scale with the density profile. Having said that, if the excessive mixing or shear that redistributes the material and momentum exists, the link between the two profiles may not work as speculated. To understand how density currents transport materials, it is essential to clarify these unsolved problems.

To this end, this study develops empirical vertical flow structure models of non-conservative density currents based on the recently reported direct observation data of natural-scale events (Simmons et al., 2020) and the gathered 70-years of laboratory-scale experiments (Chapter 2). Also included is the data from the newly conducted flume experiments in this study. Since the primary objective of this study is to predict the hydrodynamics of natural-scale turbidity currents, the validation of the model with direct measurements of turbidity currents is essential.

3.2 Existing models for flow concentration profile

The concentration profile of a turbidity current is key to understanding the depositional and erosional processes as well as the flow behaviour, as described above. Previous work has detailed how the profile is determined by the relationship between the turbulent mixing induced by the shear at the flow interfaces, particle exchange at the bed, particle settling, and particle-particle interaction (Wells and Dorrell, 2021).

In the case of conservative flows where the suspended sediment does not settle, the stratification of a flow occurs due to the entrainment of ambient fluid caused by the shear at the upper interface. The stability of the upper interface has been suggested to have a strong dependency on Fr_d (Sequeiros et al., 2010b; Kneller et al., 2016). The decreasing Fr_d stabilizes the flow interface and thus reduces the ambient water entrainment (Sequeiros et al., 2010b; Kneller et al., 2016). For such flows, the flow concentration profile is hypothesised to be described by a function of Fr_d (Abad et al., 2011).

Thus, the previous study (Abad et al., 2011) developed an empirical model of conservative salinity currents, assuming that both the velocity and concentration profiles are a function of Fr_d . The concentration profile of this model assumes the existence of a constant concentration layer in the lower part of the flow. In this lower layer of the flow, the flow concentration is assumed to be constant, and the ratio of the thickness of this uniform layer to the flow depth, \hat{h}_c is further assumed to be the exponential function of Fr_d as,

$$\hat{h}_c = \begin{cases} 1, & Fr_d < 0.38 \\ 2.59 \exp(-2.5 Fr_d), & Fr_d \geq 0.38 \end{cases} \quad (3.11)$$

Although this Fr_d -dependence function describes the density profiles of conservative flows relatively well,

it lacks the density stratification mechanics by the settling of suspended sediment, so it is not sufficient to predict the concentration profiles of the sediment-laden turbidity currents.

In the case of non-conservative flows, particle settling becomes one of the primary mechanics of flow stratification. The sediment concentration profile of the open channel flows is known to be well described by the Rouse equilibrium profile. Rouse (1939) assumed that the diffusion flux of the suspended sediment due to the turbulent mixing initiated at the lower boundary is balanced with the particle settling flux, deriving the well-known theoretical concentration profile for the open-channel flows. This balance may be expressed as,

$$\frac{d}{d\hat{z}} \left(\nu_t \frac{d\langle\phi\rangle}{d\hat{z}} + w_s \langle\phi\rangle \right) = 0, \quad (3.12)$$

where ν_t denotes the eddy viscosity. Assuming zero flux at boundaries, the following boundary conditions can be derived from the equation (3.12),

$$\nu_t \frac{d\langle\phi\rangle}{d\hat{z}} + w_s = 0|_{\hat{z}=0,1}. \quad (3.13)$$

Rouse models assume a parabolic eddy diffusivity as mixing decays towards boundaries, which can be expressed as,

$$\nu_t(\hat{z}) \sim \kappa u_* \hat{z}(1 - \hat{z}). \quad (3.14)$$

However, in the case of turbidity currents, the flows are likely to be highly sheared at both boundaries, resulting the relatively constant eddy viscosity throughout the flow ($\nu_t \sim \kappa u_* h$). Then, simplified form of the Rouse profile can be described as an exponential decay function of β for instance,

$$\langle\phi\rangle = \exp\left(-w_s \frac{z}{\nu_t}\right) \sim \exp(-\beta \hat{z}), \quad (3.15)$$

where the Rouse number $\beta = w_s/\kappa u_*$, describes the ratio of particle settling and the diffusivity due to the shear at the boundary.

However, when it comes to the sediment-laden turbidity currents, the shear at the upper interface is not negligible as it is in the fluvial rivers, so that the diffusivity of suspension is expected to be essentially different from the cases of open-channel flows. Since the Rouse profile cannot capture the stratification mechanics due to the shear at the upper interface, his model for the open-channel flows is not applicable to the turbidity currents.

There is also a theoretical vertical flow profile model of sediment-laden turbidity currents (Pittaluga and Imran, 2014). This model applies a traditional turbulence closure model (Mellor and Yamada, 1982) to

the RANS equation and derives the vertical stratification functions of a near equilibrium turbidity currents, assuming that there is no sediment exchange or entrainment of water through the flow interfaces. Pittaluga and Imran (2014) demonstrated that the developed model can reasonably predict the vertical velocity and density profiles of laboratory-scale salinity currents (Sequeiros et al., 2010b) and also the velocity profiles of natural-scale turbidity currents in Monterey and Hueneme Canyons (Xu et al., 2010). However, this model requires information on a reference concentration at the specific elevation to predict the vertical flow profiles, which is guessed by trial and error using an iterative procedure. Further, this is computationally expensive for the application of the numerical simulation of natural-scale turbidity currents. Although they used the natural-scale turbidity currents data for the validation of the velocity profile of their model, there is yet no validation of this model against the flow concentration profiles of natural-scale turbidity currents.

The ideal vertical concentration profile model of turbidity currents should capture the complex balance between particle settling and the diffusion due to the lower and upper shear of a flow. The theoretical model of Pittaluga and Imran (2014) has a turbulence closure problem, and they had to make some severe assumptions such as the no-material exchange through the flow interfaces. The empirical salinity flow model (Abad et al., 2011) is less complex than the theoretical model, but the applicability is limited to conservative flows.

3.3 Characterisation of the vertical flow concentration profile

3.3.1 Methods

Here, the concentration profiles of sediment-laden turbidity currents are investigated to parametrise flow stratification using the dimensionless flow properties including the Froude, Rouse, and Reynolds numbers. To summarise, we investigate the possible combinations of different flow parameters to describe the structure function, ξ_ϕ . To determine the best combination of flow parameters to describe the concentration profile, multiple regression analysis is conducted. Multiple regression analysis is a statistical technique to predict a single explained variable from the combination of multiple explanatory variables. Here, this technique is applied to predict each coefficient of the fit function (described below in this section). The procedures for the development of the empirical model using multiple regression analysis can be summarised as follows: i) The datasets were subdivided into the training and test sets based on the criteria described below. The profile models are trained by using training dataset. ii) The flow concentration profiles of the training datasets were fitted by the method of least squares. iii) Prepare all possible combinations of explanatory variables (If there are n explanatory variables, there are 2^n combinations). The different types of functions, both linear and non-linear, are considered. Thus, the number of candidate functions can be $m2^n$ in total, where m is the number of types of function. iii) In each candidate function, multiple regression analyses were conducted with the fit function parameters as the explained variables and the flow properties as the explanatory variables within the training set. This procedure optimises each candidate function within the given combination of

explanatory variables. iv) The statistical information criteria (AIC: Akaike Information Criteria and CV: Cross Validation score) are calculated for all regression models to select the best model. iv) To evaluate the generalisation performance, the selected model was validated using the test dataset independent of the training datasets (see the first step). The detailed methodology of each step is elaborated below.

Possible governing parameters for vertical concentration profile

Here, we consider the combination of parameters that may relate to the development of the flow concentration profile of turbidity currents. It is assumed that the vertical profile of a steady-state density current in a fully or partially confined channel can be fully described by the following nine parameters: flow depth, h [m], depth-averaged flow velocity, U [m/s], density of the flow, ρ_f [kg/m³], and density of the ambient fluid, ρ_a [kg/m³] (constant), the dynamic viscosity of the fluid, μ [kg/ms], shear velocity, u_* [m/s], settling velocity, w_s [m/s], hydraulic radius, r_h [m], gravitational acceleration, g [m/s²] (constant). The Buckingham Pi theorem (Buckingham, 1914) is used here to obtain a set of dimensionless variables that can fully describe the dimensionless shape factors of the sediment concentration profile. By applying the Buckingham Pi theorem, the above nine dimensional parameters with three primary dimensions ([s], [m], and [kg]) reduce to six dimensionless variables, which are assumed to determine the flow concentration profile:

$$\xi_\phi = f \left(Fr_d = \frac{U}{\sqrt{gR\Phi h}}, Re = \frac{\rho_f U h}{\mu}, \beta = \frac{w_s}{\kappa u_*}, C_D = \frac{u_*^2}{U^2}, \frac{r_h}{h}, \rho_\Delta = \frac{\rho_f - \rho_a}{\rho_a} \right). \quad (3.16)$$

where Fr_d and Re are the densimetric Froude and Reynolds numbers, respectively. The Rouse number β is the dimensionless settling velocity normalized by the Karman coefficient and the shear velocity. C_D is the basal drag coefficient, and $\frac{r_h}{h}$ is the ratio of the hydraulic radius to the flow depth. ρ_Δ denotes the dimensionless flow buoyancy.

Here, the relationships between dimensionless parameters are considered. For instance, since $\rho_\Delta = R\Phi$ and $\rho_f = (\rho_\Delta + 1)\rho_a$;

$$Fr_d = \frac{U}{\sqrt{g\rho_\Delta h}}, \quad Re = \frac{(\rho_\Delta + 1)\rho_a U h}{\mu}. \quad (3.17)$$

When ρ_Δ is fixed, Fr_d becomes a function of the depth-averaged flow velocity, U and flow height, h (g is constant). Likewise, if ρ_Δ is fixed, Re becomes a function of Uh , assuming that μ and ρ_a are constant. Also, drag coefficient, C_D may be a function of dimensionless hydraulic radius r_h/h . The total shear stress at boundaries τ can be described as (Hygelund and Manga, 2003)

$$\tau = \rho_f g r_h \theta_e \quad (3.18)$$

where θ_e is the energy slope, which describes the change in the hydraulic head divided by the distance over

which the change occurs. When the shear at the side wall is small enough, $u_* \simeq \sqrt{\tau/\rho}$. Therefore,

$$C_D \simeq \frac{gh\theta_e r_h}{U^2 h} \quad (3.19)$$

Furthermore, Rouse number, β can be described with the combination of Re and C_D ,

$$\beta = \frac{w_s \rho_a (\rho_\Delta - 1) h}{\kappa \mu \text{Re} \sqrt{C_D}} \quad (3.20)$$

Within the turbidity currents dataset, the dynamic viscosity of the fluid, μ and the Karman coefficient, κ can be assumed to be constant. Furthermore, within the laboratory-scale dataset, the variation of the flow height, h is small compared with the variation of other parameters such as flow velocity, U . Therefore, when we assume the constant values of ρ_Δ , Re and C_D , this equation indicates that when Rouse number β increases, it means the increase in particle settling velocity w_s . The developed models in this study will be the function of some of these dimensionless parameters which are interconnected with each other. Thus, the interpretation of the developed models are carefully considered.

Selection of datasets

The non-conservative flow data containing both the velocity and concentration profiles are used in this study, and the conservative flows are excluded (Table 3.1). This is because the flow stratification mechanics fundamentally differ between conservative and non-conservative flows. While the non-conservative flows have particle settling as one of the factors of flow stratification, conservative flows do not have this mechanics at all. For this reason, we focus on the non-conservative flows hereafter in this analysis. The selected dataset is further subdivided into training and test datasets. This is a common approach in machine learning to avoid the over-fitting. Commonly, test data are chosen randomly to avoid the training and test data from being biased. At the same time, the test data are expected to be independent of the training data. This is because the main aim of the validation with the test data is to evaluate the generalisation performance of the trained model. In terms of the vertical profile model trained by multiple sets of laboratory experiments, the over-fitting problem can occur even if the test data are chosen completely randomly. This is because the data from the same laboratory setting are similar to each other, and thus the model is likely to over-fit to each laboratory setting rather than an individual measurement. Over-fitting can occur in a way where the developed model can predict the new data from the same laboratory well, but poorly predict the new data from an unseen laboratory setting.

To avoid the risks of over-fitting mentioned above, all the data from three different laboratory experiments (García, 1993; Packman and Jerolmack, 2004; Eggenhuisen et al., 2020) are chosen as the test data (Table 3.1) so that they cover a wide range of channel slopes, median particle sizes, depth-averaged flow concentration,

Training data	Counts	Slope (%)	Material	d_{50} (μm)	Measurement tools
Michon et al. (1955)	64	0.3–3.6	Kaolinite	14.6	$\langle u \rangle$: MPCM $\langle \phi \rangle$: Siphon array (4–12)
Tesaker (1969)	33	5.0–12.5	Quartz Kaolinite	360–410 1.1–1.5* ²	$\langle u \rangle$: Velocity meters* ⁴ (3) $\langle \phi \rangle$: Siphon array (3)
Altinakar (1988)	46	1.0–2.96	Quartz	14 / 32	$\langle u \rangle$: MPCM $\langle \phi \rangle$: Siphon array (16)
Islam and Imran (2010)	4	0.0–8.0	Silt	25	$\langle u \rangle$: ADV $\langle \phi \rangle$: Siphon array (20)
Varjavand et al. (2015)	3	1.25	Kaolinite	13.4	$\langle u \rangle$: Angled UVP $\langle \phi \rangle$: Siphon array (14)
Leeuw et al. (2018a)	1	15.8–19.4	Sand	141	$\langle u \rangle$: Angled UVP $\langle \phi \rangle$: Siphon array (4)
Sequeiros et al. (2018)	8	9.0	Plastic	57	$\langle u \rangle$: Angled UVP $\langle \phi \rangle$: Siphon array (11)
Farizan et al. (2019)	6	1.0	Kaolinite	11	$\langle u \rangle$: ADV $\langle \phi \rangle$: ADV
Pohl et al. (2020)	1	14.1	Quartz	133	$\langle u \rangle$: Angled UVP $\langle \phi \rangle$: Siphon array (4)
Simmons et al. (2020)	5* ¹	0.7	Silt	9.9–11* ³	$\langle u \rangle$: ADCPs $\langle \phi \rangle$: ADCPs
This study	12 14	5 5	Glass beads Kaolinite	33–43 9	$\langle u \rangle$: UVPs $\langle \phi \rangle$: Siphon array (12)
Test data	Counts	Slope (%)	Material	d_{50} (μm)	Measurement tools
García (1993)	2	8	Silica	9	$\langle u \rangle$: MPCM $\langle \phi \rangle$: Optical probes
Packman and Jerolmack (2004)	4	1.0	Quartz Kaolinite	12 1.3	$\langle u \rangle$: ADV $\langle \phi \rangle$: Siphon array (6)
Eggenhuisen et al. (2020)	2	7.0–14.0	Sand	130	$\langle u \rangle$: Angled UVP $\langle \phi \rangle$: Siphon array (4)
Simmons et al. (2020)	8* ¹	0.7	Silt	9.9–11* ³	$\langle u \rangle$: ADCPs $\langle \phi \rangle$: ADCPs

MPCM: Micro-Propeller Current-Meter; UVP: Ultrasonic Velocity Profiler;
ADV: Acoustic Doppler Profiler; ADCPs: Acoustic Doppler Current Profilers

Table 3.1: Counts column displays the total number of the set of profiles (velocity and concentration) from each source. The figures in the parentheses represent the number of equipment in the array. *¹ The training data is from Event 5 and the test data is from Event 1 and Event 4. Event names are identical to Simmons et al. (2020). *² Original reported values of grain size from hydrometer analysis. *³ d_{50} from Event 1, 4, and 5 from the original source. *⁴ Velocity meters are special equipment that are designed for their particular study.

and the overall shape of the vertical concentration profile. The test dataset also includes two turbidity currents observed in Congo Canyon, corresponding to Events 1 and 4 in (Simmons et al., 2020). The test data from Congo Canyon are chosen by the following method so that the selected data represents the variation of near-bed concentration in the selected window of each Event (see Fig. 2.5 to 2.7 for the selected windows). Firstly, the data from the selected window are subdivided into four groups, each representing a distinct range of near-bed concentrations, varying from low to high. This stratification ensures that the concentrations in each group are clearly delineated. The test data are then selected to include one profile from each of the aforementioned groups. The rest of the datasets, including Event 5 of Congo Canyon and other experimental data, are used as the model-training dataset.

Further data selection was conducted with the following criteria to reduce the influence of the measurement noise and maximise the performance of multiple regression analysis. Firstly, the measurement data in Congo Canyon was removed from the training dataset when the highest reliable measurement point was below the normalized elevation $\hat{z} = 0.8$, because the estimation of the flow height can be erroneous when the measurements in the upper part of the flow are not available. The concentration profiles sometimes contained the artifact noise around the upper flow interface in the turbidity currents observed in Congo Canyon (Simmons et al., 2020). The concentration and velocity profiles in the upper part of the flow were judged to be unreliable in such cases. It is important to note that each laboratory dataset contains various types of errors, including measurement tool errors, graph-reading tool errors, and errors in interpolation/extrapolation methods. Accurately estimating each error source is challenging due to the variability in measurement tools across different sources. It is assumed that these errors are correlated and tend to cancel each other out. Therefore, although it is a stringent assumption, it is posited that these potential errors in the training data are negligible for the subsequent analysis.

Fit function for flow concentration profiles

The empirical modelling of the concentration profiles requires the formulation of a function to which the original measurement data are fitted. The fit function should be able to exhibit the range of possible vertical profiles of turbidity currents appropriately with the minimum number of fit parameters. The advantage of fewer parameters in the model is that it prevents over-fitting and aids interpretation.

This study employs the following function based on the generalized Schlick's bias and gain function (Barron, 2020) to describes $\tilde{\phi}$, which denotes the ratio of the sediment concentration $\langle\phi\rangle$ to the near-bed concentration $\langle\phi_b\rangle$. Schlick's bias and gain functions are a type of easing functions, which are commonly used in computer games and animation for a visually smooth movement. The input value of this function is the percentage of time that has passed since the start of the animation. The output value is the percentage of the movement that has taken place. Here, the original function is modified so that it can take the range of concentration-profile

shapes as below:

$$\frac{\langle \phi \rangle}{\langle \phi_b \rangle} = \tilde{\phi}(\hat{z}, s_1, s_2) = \begin{cases} \frac{s_2(1-\hat{z})}{1-\hat{z}+s_1(s_2-1+\hat{z})+\zeta} & \text{if } 1-\hat{z} < s_2 \\ \frac{(s_2-1)\hat{z}}{\hat{z}-s_1(s_2-1+\hat{z})+\zeta} + 1 & \text{if } 1-\hat{z} \geq s_2 \end{cases}, \quad \text{where } 1 < s_1 \quad \text{and} \quad 0 \leq s_2 \leq 1 \quad (3.21)$$

where $\hat{z} = z/h$. This function has two parameters, s_1 and s_2 , and employs two different curves for the lower and upper parts of the profiles. The parameter s_1 determines the curvature of curves, and s_2 is the height of the inflection point of the function. The parameter ζ is the small constant value to avoid the denominator from becoming zero. In this study, $\zeta = 10^{-10}$ is set as constant. It should be noted that $\tilde{\phi}|_{\hat{z}=0} = 1$ and $\tilde{\phi}|_{\hat{z}=1} = 0$ regardless of the values of s_1 and s_2 .

From Equation (3.21), the shape factor of flow concentration ξ_ϕ can be described as:

$$\xi_\phi(\hat{z}, s_1, s_2) = \frac{\langle \phi \rangle}{\Phi} = \frac{\tilde{\phi}}{\int_0^1 \tilde{\phi}(\hat{z}) d\hat{z}} = \frac{\tilde{\phi}(\hat{z}, s_1, s_2)}{(2s_2 - 1)P_s + (1 - s_2)}, \quad (3.22)$$

where

$$P_s = \frac{(1 - s_1) + s_1 \log s_1}{(1 - s_1)^2}. \quad (3.23)$$

Thus, the shape of the concentration profile only depends on two parameters, s_1 and s_2 (Fig. 3.2). From Equation (3.22), r_0 , the ratio of near-bed concentration $\langle \phi_b \rangle$ to the depth-averaged concentration Φ , can be described as,

$$r_0 = \frac{\langle \phi_b \rangle}{\Phi} = \frac{1}{(2s_2 - 1)P_s + (1 - s_2)}. \quad (3.24)$$

The threshold parameter s_2 , controls the height of the inflection point ($\hat{z} = 1 - s_2$) of the profile (Barron, 2020). The profiles in the upper layer above the inflection point exhibit a large negative gradient, while those in the lower layer tend to be less stratified (Fig. 3.2). Physically, this inflection point can be regarded as a potential boundary between the upper dilute and the lower dense layer of a density current.

As described in the section 3.2, gravity currents may take the shape of concentration profiles different from open channel flows. Open-channel flows exhibit Rouse-type profiles where the concentration decreases exponentially upward. In contrast, as an end-member, the density flows may also take the sigmoidal profiles where the lower part of the flow shows nearly uniform concentration. The parameter s_2 describes which of two end-member profiles the actual profile is close to. The profile approximates well the Rouse-type profile

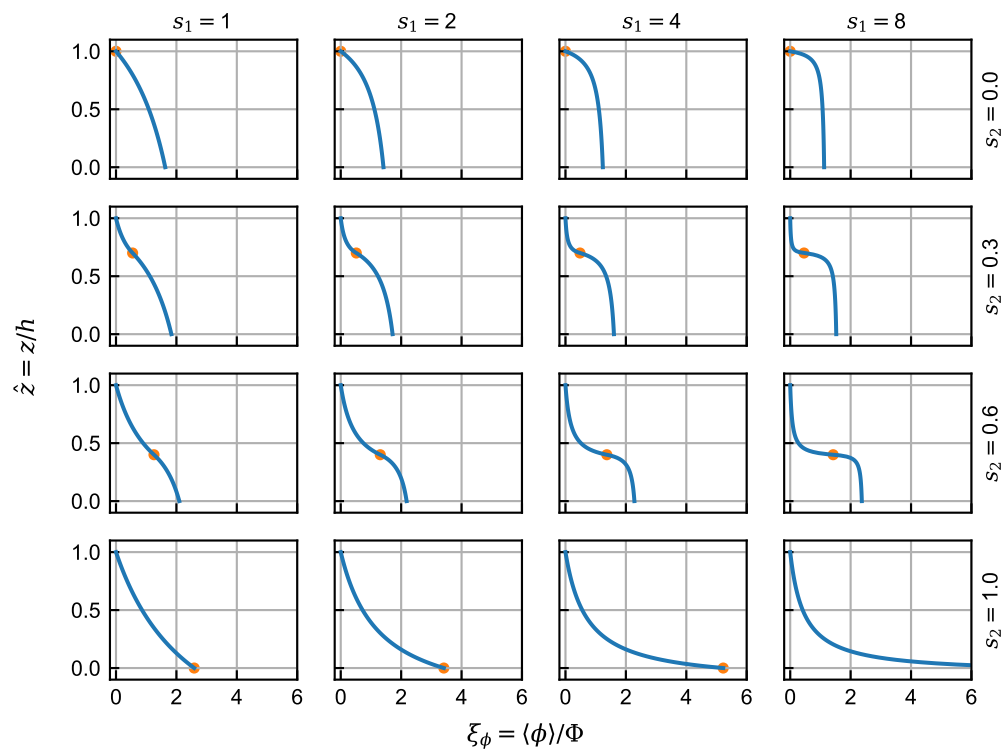


Figure 3.2: The visualisation of the shape factor ξ_ϕ based on the generalised Schlick's bias and gain function Barron, 2020. Y axis is normalised by flow height and X axis is normalised by depth-averaged flow concentration. s and t denote the slope and threshold parameter in the equation (3.21)

when s_2 is set to unity. As s_2 decreases, the profile exhibits the sigmoidal form, becoming homogeneous at $s_2 = 0$.

The slope parameter, s_1 , denotes the slope of the curve at the inflection point (Barron, 2020), controlling the curvature of the profiles of both the upper and lower layers. When s_1 is close to unity, the gradient becomes almost constant throughout the profile, and thus transition from the lower to the upper layers appears to be obscure and gradual (Fig. 3.2). As s_1 increases, the concentration profile tends to be intensely stratified at the boundary between the lower and upper layers (Fig. 3.2).

To examine the fitness of the function used in this study, it was compared with the following functions (Fig. 3.5).

$$\xi_\phi(\hat{z}) = a_1 \exp(a_2 \hat{z}) \quad (3.25)$$

$$\xi_\phi(\hat{z}) = \sum_{i=0}^5 a_i \hat{z}^i \quad (3.26)$$

$$\xi_\phi(\hat{z}) = \frac{a_1 \hat{z} + a_2}{a_3 \hat{z} + a_4 \exp a_5 \hat{z}} + a_6 \quad (3.27)$$

where a represents the fitting parameter. From the top, they are the Rouse-type profile (Eq. 3.25), 5th-order polynomial (Eq. 3.26), and a sigmoidal function (Eq. 3.27). The Rouse-type function (3.25) requires two fitting parameters, while the other functions require six parameters. Equation (3.25) is based on the Rouse model where the diffusion flux due to the bed shear balances with the particle settling flux. Equation (3.27) is also able to take the Rouse-type equation when the fitting parameters a_1 , a_3 , and a_6 are close to zero. The fitting parameters a_1 , a_3 , and a_6 enables the function to take the range of different shapes. The equation (3.26) is a simple polynomial function and fitting parameters do not have any physical explanation. The least-square method is used to acquire the best-fit values of coefficients of each fitting parameter, including s_1 and s_2 of the equation (3.22).

Multiple linear regression

In the previous subsection, the shape factor ξ_ϕ representing the normalised vertical flow concentration profile was described as the function with the model parameters s_1 and s_2 . Multiple regression analyses were conducted to investigate which flow parameters determine the vertical profile of flow sediment concentration. There are six dimensionless parameters, densimetric Froude number Fr_d , Rouse number, β , Reynolds number, Re , drag coefficient C_D , normalised hydraulic radius, r_h/h , and relative density, ρ_Δ . The scatter plots (Fig. 3.3) imply that the normalised hydraulic radius, r_h shows almost no correlation between fit parameters, s_1 and s_2 , so in this study, r_h is excluded from the multiple regression analysis. Assuming s_1 and s_2 are independent

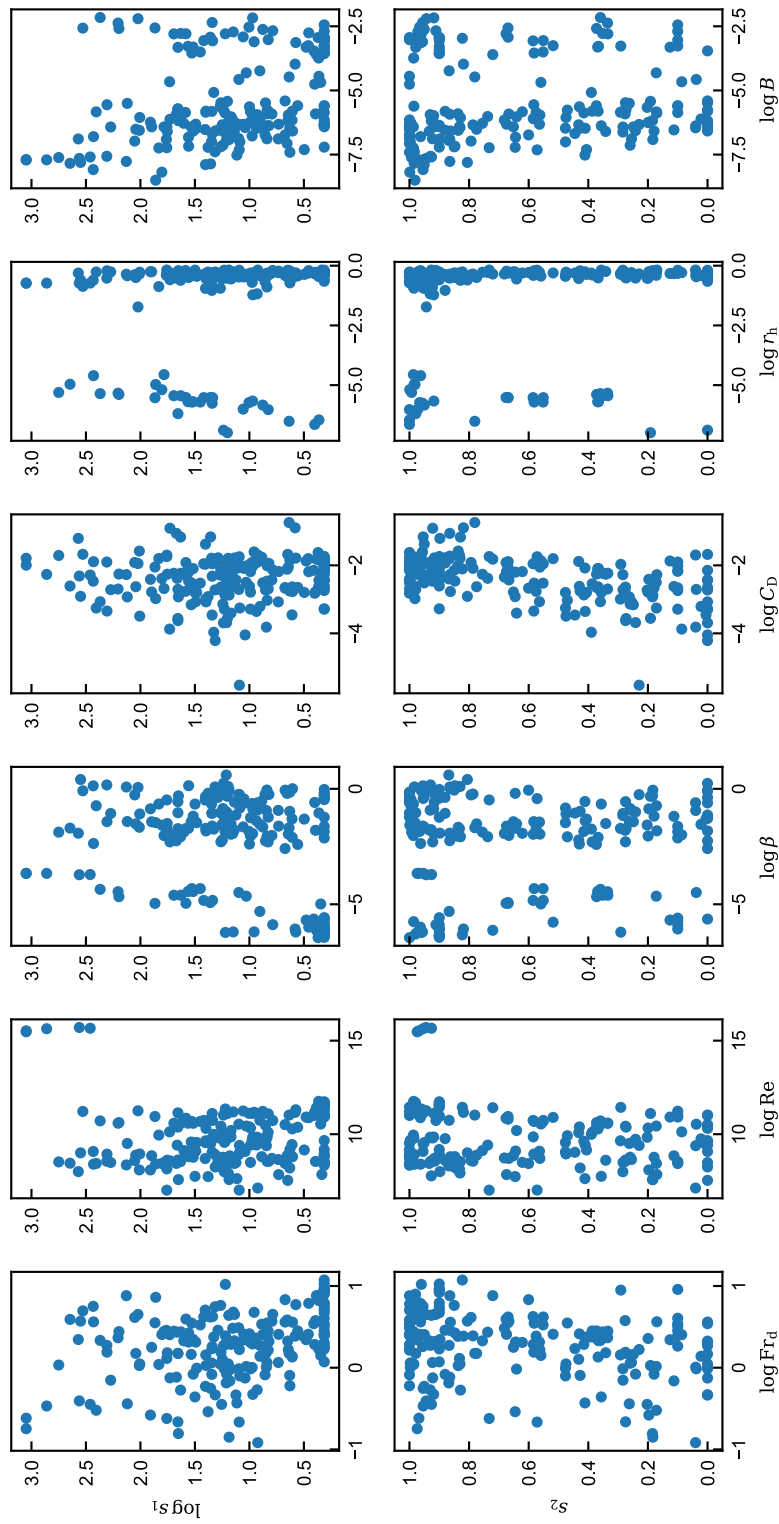


Figure 3.3: Scatter plots of each dimensionless parameter against s_1 and s_2 of the training data. The best-fit values of s_1 and s_2 of each data are estimated by the least-square method.

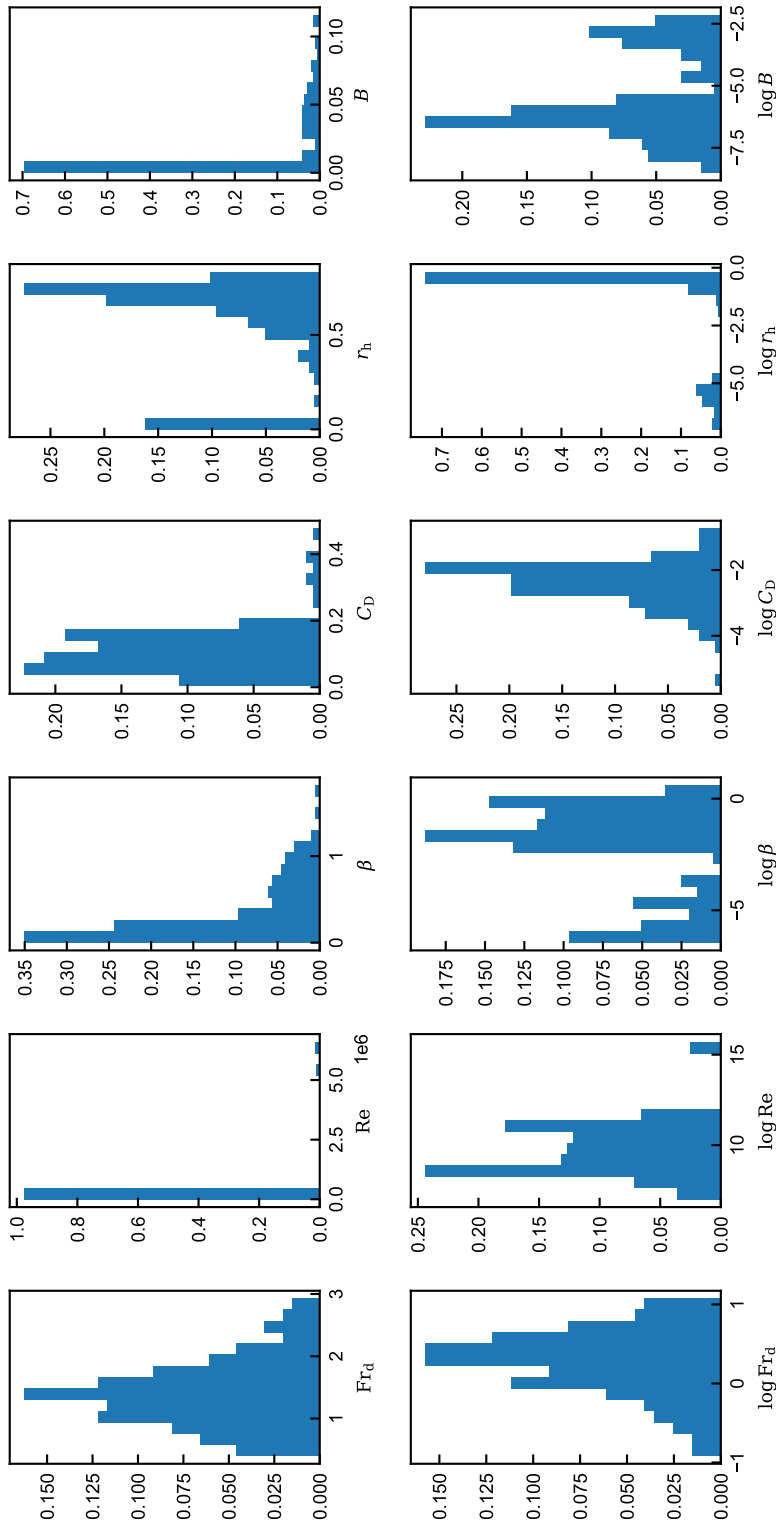


Figure 3.4: Histograms of each dimensionless parameter. Top row displays original values, and the bottom row displays the logarithmic values. Y axes denote the frequency of each parameter.

of each other, equation (3.22) may be closed using

$$s_1 = f_1(\text{Fr}_d, \text{Re}, \beta, C_D, \rho_\Delta) \quad \text{and} \quad s_2 = f_2(\text{Fr}_d, \text{Re}, \beta, C_D, \rho_\Delta). \quad (3.28)$$

The dependence on some parameters can be neglected if the remaining parameters are sufficient to predict ξ_ϕ . In the equation (3.28), it is not necessary to include all parameters in the model if some of them are enough to predict ξ_ϕ . To investigate which set of parameters are the best for describing ξ_ϕ , the following procedures are conducted. Firstly, assuming some basic formulae of model functions, all possible models are listed with every combination of dimensionless parameters. Multiple regression analysis is then conducted to determine the fit parameters of each model. Finally, the best model is chosen statistically from the developed models.

As first step, some assumptions need to be made to formulate the relation between explained variables (s_1 and s_2) and explanatory variables (Fr_d , Re , β , C_D , and ρ_Δ). The distribution of selected dimensionless parameters (Fig. 3.4) show normal-like distributions for the logarithmic values. From the observation (Fig. 3.3 and 3.4), log-log relationship between the explanatory variables and s_1 and log-normal relationship between the explanatory variables and s_2 are assumed. For s_1 , to force the boundary condition $1 < s_1$, the following form is assumed:

$$s_1 = f_1(Q_1, \dots, Q_n) = \begin{cases} \alpha_1 & (n = 0) \\ 1 + \exp(\alpha_{1,0} + \sum_{i=1}^n \alpha_{1,i} \log Q_i) & (1 \leq n) \end{cases}. \quad (3.29)$$

For s_2 ($0 \leq s_2 \leq 1$),

$$s_2 = f_2(Q_1, \dots, Q_n) = \begin{cases} \alpha_2 & (n = 0) \\ \text{Max}(0, \min(1, \alpha_{2,0} + \sum_{i=1}^n \alpha_{2,i} \log Q_i)) & (1 \leq n) \end{cases}, \quad (3.30)$$

where Q_i denotes the i th dimensionless variable and $\alpha_{1,i}$ and $\alpha_{2,i}$ are the exponent for Q_i . The $\alpha_{1,0}$ and $\alpha_{2,0}$ are empirical coefficients for s_1 and s_2 , respectively. n denotes the number of selected dimensionless parameters. In this study, there are five dimensionless parameters to be considered (Eq. 3.28), so $0 \leq n \leq 5$. There are ${}_5C_n$ possible combinations of dimensionless parameters (Q_i) for each n , so the total number of the candidates of model functions becomes $\sum_n {}_5C_n = 32$ each for f_1 , and f_2 .

For the estimation of the best fit parameters α and a_i of each model, k -fold Cross Validation method (KCV) is conducted (Anthony and Holden, 1998). The KCV method splits a dataset into “ k ” independent folds and trains the model with all but one subset. Then, the method evaluates the generalisation error of the model prediction from the remaining fold. These procedures are iterated k times, changing the subset for calculating the mean squared error, resulting in all subsets being used for both training and calculating the error. In each iteration, the Python package, `scipy.optimize.curve_fit` is used for the non-linear least squares to estimate the

best fit values, standard deviations, and p-values of each parameter. The best fit values of each parameter are estimated as the mean values of k times iteration. The advantage of KCV method is the model can learn the data efficiently without over-fitting.

Model selection

The models determined by multiple linear regression were evaluated by two metrics: the Akaike Information Criterion (AIC) and the k -folds Cross-Validation (KCV). For predicting the sediment concentration profiles, this study selected the model exhibiting smaller values in these metrics, indicating a higher generalisation ability.

AIC is a measure used in statistical modeling and model selection. The primary purpose of AIC is to balance the goodness of fit of a statistical model with its complexity, penalizing models that are too complex. AIC is defined as (Akaike, 1998):

$$\text{AIC} = -2l_{\max} + 2(n + 1) \quad (3.31)$$

where n is the number of parameters in the model and l_{\max} is the maximum log-likelihood function. The likelihood function represents the probability of observing the given data under a particular set of parameter values. The probability density function for the regression residual Υ is assumed to be a normal distribution with zero mean and the variance σ^2 ,

$$f(\Upsilon|\sigma) = \frac{1}{\sqrt{2\pi\sigma^2}} \exp\left(-\frac{\Upsilon^2}{2\sigma^2}\right) \quad (3.32)$$

The joint probability density of the observed residuals $\Upsilon_1, \Upsilon_2, \dots, \Upsilon_\chi$ is

$$f(\Upsilon_1, \Upsilon_2, \dots, \Upsilon_\chi | \alpha_0, \alpha_1, \dots, \alpha_n) = \prod_{i=1}^{\chi} f(\varepsilon_i | \sigma), \quad (3.33)$$

where χ is the total number of observed data. The likelihood function, L , is

$$L(\alpha_0, \alpha_1, \dots, \alpha_n | \Upsilon_1, \Upsilon_2, \dots, \Upsilon_\chi) = f(\Upsilon_1, \Upsilon_2, \dots, \Upsilon_\chi | \alpha_0, \alpha_1, \dots, \alpha_n) \quad (3.34)$$

$$= \prod_{i=1}^{\chi} \frac{1}{\sqrt{2\pi\sigma^2}} \exp\left(-\frac{\Upsilon_i^2}{2\sigma^2}\right) \quad (3.35)$$

$$= (2\pi\sigma^2)^{-\chi/2} \exp\left(-\frac{1}{2\sigma^2} \sum_{i=1}^{\chi} \Upsilon_i^2\right) \quad (3.36)$$

The log-likelihood function, l , becomes,

$$l(\alpha_0, \alpha_1, \dots, \alpha_n | \Upsilon_1, \Upsilon_2, \dots, \Upsilon_\chi) = \ln(L(\alpha_0, \alpha_1, \dots, \alpha_n | \Upsilon_1, \Upsilon_2, \dots, \Upsilon_\chi)) \quad (3.37)$$

$$= -\frac{n}{2} \ln(2\pi\sigma^2) - \frac{1}{2\sigma^2} \sum_{i=1}^{\chi} \Upsilon_i^2 \quad (3.38)$$

The set of the parameters α and $a_1 \dots a_k$ are estimated by non-linear least squares so that it maximises the log-likelihood function (l_{\max}), which is equivalent to maximizing the likelihood function since the log function is a strictly increasing function.

In addition to the AIC described above, this study employed the cross-validation score (CV) defined as:

$$CV = \frac{1}{\chi k} \sum_{j=1}^k \sum_{i=1}^{\chi} (y_{ij} - \hat{y}_{ij})^2 \quad (3.39)$$

where y_{ij} is i th observed data in the j th fold in KCV and \hat{y}_{ij} denotes i th predicted value by the model trained by the j th fold. The variable χ denotes the number of data in the fold. This CV value was used to select the model showing the best generalisation ability. In this study, the value k was set to 10. Other values for k from 5 to 20 were tested, and it was confirmed that the resultant CV scores did not vary significantly depending on the choice of the k value.

After calculating these two metrics, the p-values for each model's exponents of the dimensionless flow parameters were obtained. The models containing the exponents with an averaged p-value higher than the 0.05 significance level were not considered in selecting the best model in this study. The cross-validation results were also used for estimating the confidence intervals of the model predictions (Barber et al., 2021).

3.3.2 Results

Evaluation of fitting function

The modified Schlick's function (Eq. 3.21) provides a good fit for the sediment concentration profiles observed in the gathered dataset without overfitting. As previously articulated (Dorrell et al., 2019; Wells and Dorrell, 2021), the Rouse-type function is not able to describe the conservative flow concentration profile (e.g. Fig. 3.5d–f). While the polynomial (Eq. 3.26) is more flexible capturing a variety of concentration profiles, they tend to cause overfitting (Fig. 3.5b–f). Although the functions approximate the data points, they exhibited irregularities in profile shapes that were not physically plausible. The same problem also happened in the cases of the sigmoid-type function (Eq. 3.27 and Fig. 3.5e).

Model	AIC	CV	ρ_{Δ}			β			Fr _d			Re			C _b			$\alpha_{1,0}$				
			coef	p	error	coef	p	error	coef	p	error	coef	p	error	coef	p	error	coef	p	error		
β, Fr_d	482	0.902	-	-	-	0.088	0.044	0.018	-0.8	0.0	0.072	-	-	-	-	-	-	-	-	1.077	0.039	0.0
Fr _d	486	0.909	-	-	-	-	-	-	-0.994	0.0	0.044	-	-	-	-	-	-	-	-	0.933	0.018	0.0
ρ_{Δ}, β, Re	487	0.927	-0.161	0.02	0.025	0.143	0.019	0.018	-	-	-	0.175	0.008	0.017	-	-	-	-	-	-1.603	0.264	0.044
β	497	0.976	-	-	-	0.159	0.0	0.014	-	-	-	-	-	-	-	-	-	-	-	1.023	0.042	0.0

Table 3.2: The candidate models of s_1 of Congo-included model selected by k -fold Cross Validation. Models are sorted by AIC and CV in descending order, and thus the top model is the best performance model. Models with p -values > 0.05 are excluded from this table. The decimals of AIC are floored. Other figures are rounded to 3 decimal places.

Model	AIC	CV	ρ_{Δ}			β			Fr _d			Re			C _b			$\alpha_{2,0}$			
			coef	p	error	coef	p	error	coef	p	error	coef	p	error	coef	p	error	coef	p	error	
β, Fr_d, Re, C_b	24	0.067	-	-	-	0.092	0.0	0.004	0.305	0.0	0.017	0.087	0.0	0.004	0.309	0.0	0.01	0.63	0.044	0.0	0.0
β, Fr_d, C_b	49	0.078	-	-	-	0.047	0.0	0.004	0.26	0.0	0.023	-	-	-	0.293	0.0	0.01	1.348	0.025	0.0	0.0
ρ_{Δ}, Fr_d, C_b	51	0.078	-0.052	0.001	0.005	-	-	-	0.261	0.0	0.022	-	-	-	0.274	0.0	0.009	0.91	0.044	0.0	0.0
β, Re, C_b	53	0.079	-	-	-	0.058	0.0	0.004	-	-	-	0.072	0.0	0.003	0.31	0.0	0.013	0.783	0.029	0.0	0.0
ρ_{Δ}, Re, C_b	62	0.082	-0.045	0.005	0.005	-	-	-	-	-	-	0.049	0.004	0.003	0.282	0.0	0.012	0.569	0.055	0.017	0.0
Fr _{d}, C_b}	62	0.083	-	-	-	-	-	-	0.164	0.004	0.018	-	-	-	0.26	0.0	0.01	1.191	0.026	0.0	0.0
β, C_b	67	0.086	-	-	-	0.024	0.049	0.004	-	-	-	-	-	-	0.296	0.0	0.012	1.373	0.031	0.0	0.0
C _b	70	0.087	-	-	-	-	-	-	-	-	-	-	-	-	0.275	0.0	0.012	1.27	0.027	0.0	0.0
ρ_{Δ}, Fr_d	111	0.109	-0.039	0.03	0.005	-	-	-	0.297	0.0	0.023	-	-	-	-	-	-	0.321	0.031	0.004	0.004
Fr _d	114	0.111	-	-	-	-	-	-	0.223	0.001	0.021	-	-	-	-	-	-	0.552	0.009	0.0	0.0

Table 3.3: The candidate models of s_2 of Congo-included model selected by k -fold Cross Validation. Models are sorted by AIC and CV in descending order, and thus the top model is the best performance model. Models with p -values > 0.05 are excluded from this table. The decimals of AIC are floored. Other figures are rounded to 3 decimal places.

Model	AIC	CV	ρ_{Δ}		β		Fr _d		Re		C _D		$\alpha_{1,0}$			
			coef	p	error	coef	p	error	coef	p	error	coef	p	error	p	
β, Fr_d	459	0.852	-	-	0.136	0.001	0.011	-0.453	0.043	0.086	-	-	-	1.044	0.043	0.0
β	462	0.861	-	-	0.181	0.0	0.009	-	-	-	-	-	-	1.01	0.045	0.0
Fr _d , Re	462	0.874	-	-	-	-	-0.534	0.019	0.093	-0.19	0.008	0.022	-	2.599	0.215	0.0
Re	467	0.89	-	-	-	-	-	-	-	-0.275	0.0	0.018	-	3.259	0.178	0.0
Fr _d	468	0.906	-	-	-	-	-0.815	0.0	0.079	-	-	-	-	0.849	0.032	0.0

Table 3.4: The candidate models of s_1 of lab-based model selected by k -fold Cross Validation. Models are sorted by AIC and CV in descending order, and thus the top model is the best performance model. Models with p -values > 0.05 are excluded from this table. The decimals of AIC are floored. Other figures are rounded to 3 decimal places.

Model	AIC	CV	ρ_{Δ}		β		Fr _d		Re		C _D		$\alpha_{2,0}$							
			coef	p	error	coef	p	error	coef	p	error	coef	p	error	p					
$\beta, \text{Fr}_d, \text{Re}, C_D$	25	0.069	-	-	-	0.085	0.0	0.005	0.349	0.0	0.02	0.057	0.034	0.011	0.3	0.0	0.012	0.865	0.105	0.0
β, Fr_d, C_D	29	0.069	-	-	-	0.063	0.0	0.003	0.379	0.0	0.016	-	-	-	0.286	0.0	0.012	1.319	0.031	0.0
$\rho_{\Delta}, \text{Fr}_d, C_D$	45	0.076	-0.048	0.002	0.005	-	-	0.307	0.0	0.02	-	-	-	-	0.261	0.0	0.011	0.879	0.025	0.0
Fr _d , C _D	54	0.081	-	-	-	-	-	0.223	0.0	0.018	-	-	-	-	0.248	0.0	0.01	1.134	0.022	0.0
β, Re, C_D	55	0.082	-	-	-	0.064	0.0	0.004	-	-	-	0.087	0.002	0.008	0.314	0.0	0.013	0.666	0.093	0.007
β, C_D	65	0.086	-	-	-	0.026	0.026	0.004	-	-	-	-	-	-	0.294	0.0	0.013	1.366	0.036	0.0
C _D	68	0.087	-	-	-	-	-	-	-	-	-	-	-	-	0.271	0.0	0.01	1.253	0.023	0.0
β, Fr_d	97	0.102	-	-	-	0.039	0.008	0.004	0.399	0.0	0.023	-	-	-	-	-	-	0.573	0.01	0.0
$\rho_{\Delta}, \text{Fr}_d$	100	0.105	-0.034	0.048	0.005	-	-	0.359	0.0	0.023	-	-	-	-	-	-	-	0.313	0.027	0.004
Fr _d	103	0.107	-	-	-	-	-	0.297	0.0	0.02	-	-	-	-	-	-	-	0.518	0.009	0.0

Table 3.5: The candidate models of s_2 of lab-based model selected by k -fold Cross Validation. Models are sorted by AIC and CV in descending order, and thus the top model is the best performance model. Models with p -values > 0.05 are excluded from this table. The decimals of AIC are floored. Other figures are rounded to 3 decimal places.

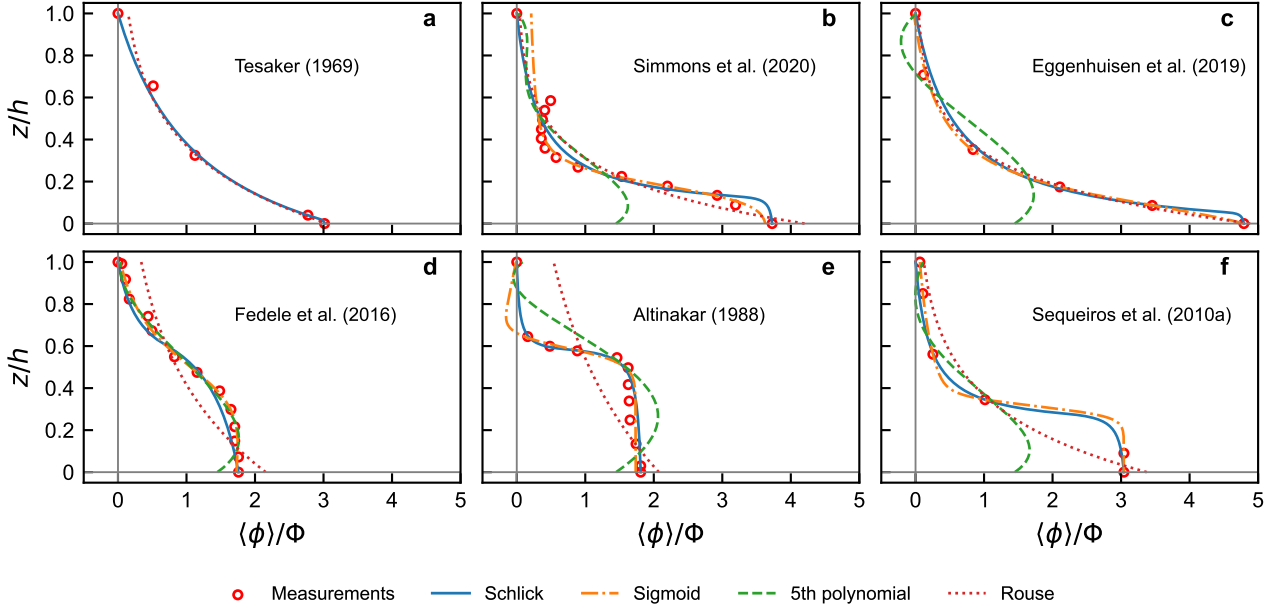


Figure 3.5: Example of curve fitting of different types of fitting functions. The dotted data is the original measurement data

Results of multiple regression and model selection

Two groups of multiple linear regression models were constructed: Congo-included models are trained by all the training data (Table 3.1) which include measurement data from both natural- and laboratory-scale flows, and lab-based models are trained by a part of the training data (Table 3.1) where natural-scale flows (Simmons et al., 2020) are excluded and only contain the measurements from the laboratory-scale flows. The best model is then selected for each group based on the CV and AIC scores (Table 3.2–3.5).

After the k -fold Cross Validation, the models that contain any parameter with higher p -values than 0.05 are excluded. Here, the dimensionless parameters chosen by the models exhibiting lower CV and AIC scores are described.

For the slope parameter s_1 , 4 models out of 32 in Congo-included group (Table 3.2) and 5 models out of 32 in lab-based group (Table 3.4) survived from the model selection based on the significance level check by p -values. Within the surviving Congo-included models, Rouse number, β appears in 3 models out of 4 (Table 3.2). Froude number, Fr_d appears in 2 models out of 4. Reynolds number, Re and flow buoyancy, ρ_Δ appear in 1 model out of 4. There are no surviving models with drag coefficient, C_D in the Congo-included group. When it comes to the surviving models of lab-based group (Table 3.4), Fr_d appears in 3 models out of 5, β and Re appears in two models out of 5, while there are no models with the other parameters ρ_Δ and C_D .

For the threshold parameter s_2 , 10 models out of 32 in the Congo-included group and also 10 models out of 32 in the lab-based group passed the significance level check by p -values (Table 3.3–3.5). Fr_d and C_D appears in majority of the models both in Congo-included and lab-based groups. While the Re and ρ_Δ only appears

in 2–3 models. β appears in 4–5 models out of 10. The remained models in Congo-included and lab-based groups are almost identical to each others in terms of the combination of dimensionless parameters. The minor difference is that Congo-included models are slightly more likely to adopt ρ_Δ and Re compared to the lab-based models.

The best model of s_1 and s_2 in Congo-included group adopted four dimensionless parameters: the densimetric Froude number Fr_d , Rouse number β , Reynolds number Re , and drag coefficient C_D . Formulations for the coefficients s_1 and s_2 take the form:

$$\begin{aligned} s_1 &= f_1(Fr_d, \beta) \simeq 1 + \exp(1.08 + \log Fr_d^{-0.80} \beta^{0.088}) \\ s_2 &= f_2(Fr_d, \beta, Re, C_D) \simeq \text{Max}(0, \min(1, 0.63 + \log Fr_d^{0.31} \beta^{0.092} Re^{0.087} C_D^{0.31})). \end{aligned} \quad (3.40)$$

This model's CV and AIC scores (482 and 0.902 for s_1 and 24 and 0.067 for s_2 , respectively) were consistently the smallest in the models of Congo-included group, and the p-values of all parameters are below the significance level (5 %). Hereafter, this best model is called the Congo-included Model.

The best model in the models of lab-based group adopted four dimensionless parameters: the densimetric Froude number Fr_d , Rouse number β , Reynolds number Re , and drag coefficient C_D . The formulations of the coefficients s_1 and s_2 take the form:

$$\begin{aligned} s_1 &= f_1(Fr_d, \beta) \simeq 1 + \exp(1.04 + \log Fr_d^{-0.45} \beta^{0.14}) \\ s_2 &= f_2(Fr_d, \beta, Re, C_D) \simeq \text{Max}(0, \min(1, 0.87 + \log Fr_d^{0.35} \beta^{0.085} Re^{0.057} C_D^{0.30})). \end{aligned} \quad (3.41)$$

This model's CV and AIC scores (459 and 0.852 for s_1 and 25 and 0.069 for s_2 , respectively) were consistently the smallest in the lab-based group, and the p-values of all parameters are below the significance level (5 %). Hereafter, this model is called the lab-based Model.

Test of the models

Here, Congo-included and lab-based models obtained in the above section are validated with the test dataset (Table 3.1) to investigate the performance of the obtained models against unseen data. Neither of these laboratory- and natural-scale test datasets are used in the training datasets.

Firstly, each model was validated with the laboratory-scale test dataset (Fig. 3.6). The laboratory-scale flows in the test data are composed of three different sources: i) two measurements with fine sand particles from Eggenhuisen et al. (2020), ii) two measurements with fine-silt-sized silica from Garcìa (1993) and iii) four measurements with fine-silt-sized quarts and Kaolinite from Packman and Jerolmack (2004).

(i) Regarding the test data of Eggenhuisen et al. (2020), the shapes of the sediment concentration profiles exhibit the typical Rouse-type profiles. Both models' predictions exhibited almost same shape and show very

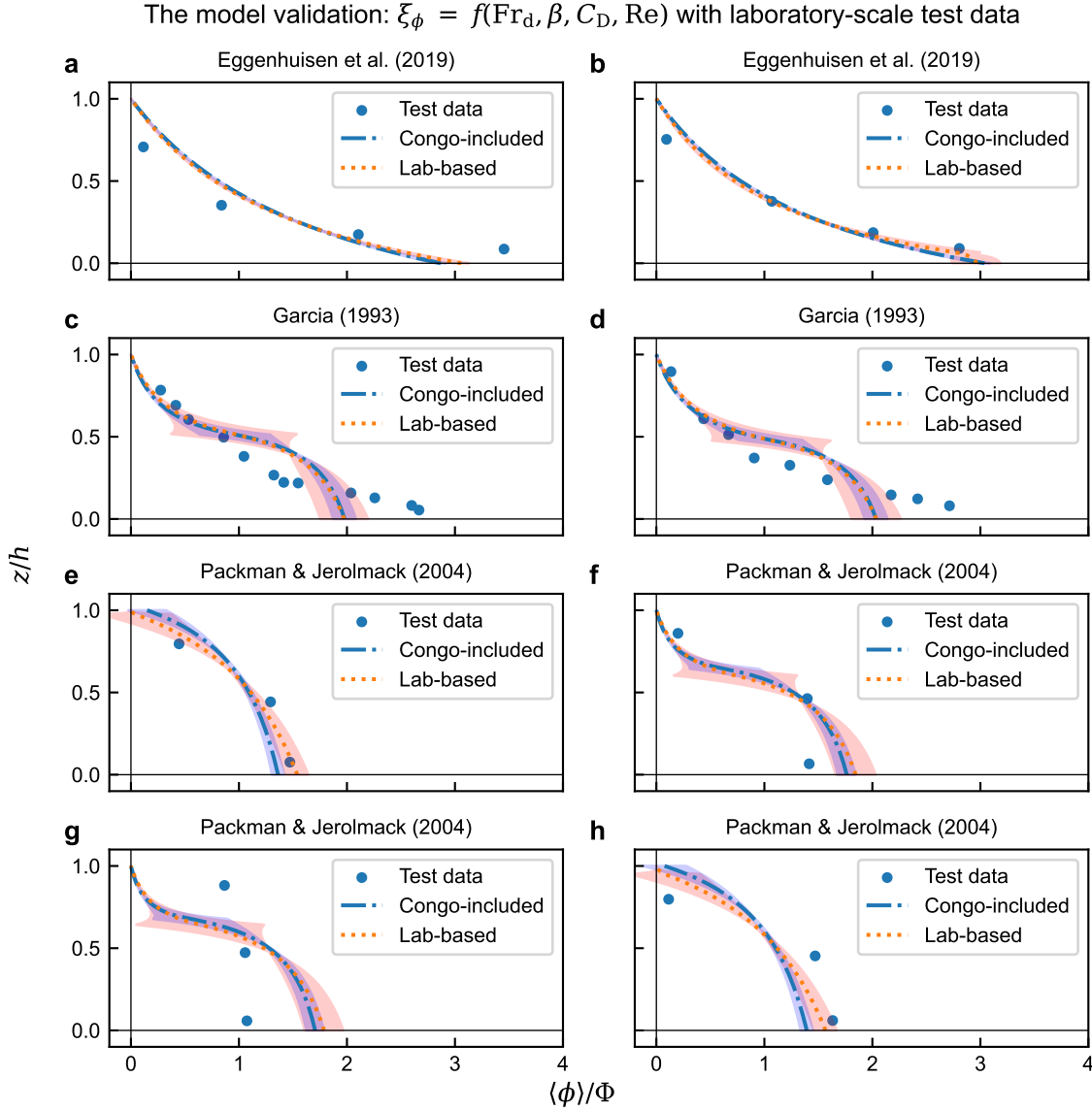


Figure 3.6: Validation of the models with the selected laboratory-scale data. The original measurements are indicated by blue dots. The range of uncertainties at each height are depicted by shaded area. a,b) Test data from Eggenhuisen et al. (2020). Slope, S , differs between the runs: a) $S = 0.14$, b) $S = 0.07$. c,d) Test data from Garcia (1993). Initial concentration differs between the runs: c) $\Phi_0 = 0.143$ vol.%, d) $\Phi_0 = 0.133$ vol.%. e,f,g,h) Test data from Packman and Jerolmack (2004). For each figure, the material of suspended particles are e,h) Kaolinite and f,g) Silica, type of salt in the ambient fluid is e,h) CaCl_2 and g,f) NaCl , salt concentration is e,h) 50 mM (millimolar) and g,f) 10 mM, and the measurement locations are e,g) 140 cm and f,h) 40 cm downstream from the inlet.

good agreement with the two measurements (Fig. 3.6a and b).

(ii) The two measurements from Garcia (1993) exhibit relatively sigmoidal shape compared with the measurements of Eggenhuisen et al. (2020) (Fig. 3.6c and d). Both model's predictions almost capture the sigmoidal feature of the measurement dataset although it slightly underestimate the near-bed flow concentration.

(ii) The four measurements from Packman and Jerolmack (2004) exhibit conservative-flow type profile where lower half of the flow shows almost uniform flow concentration (Fig. 3.6e–h). Both model's predictions reasonably capture the overall trend. Especially, Figure 3.6e, f and h shows better agreements with the models than Figure 3.6g, h. Given that this analysis does not account for salinity differences, salt types, or the distance from the inlet as parameters in model development, these factors may potentially reduce the model's performance as depicted in Figure 3.6g, h. To summarise, both models exhibit almost identical and reasonable performance in all laboratory-scale training data. The minor difference is that the lab-scale model tends to show wider uncertainty for sigmoidal profiles.

As mentioned above, the potential effects of certain parameters, such as salinity, which are not included in the multivariate analysis, remain an open question. It is also possible that the some of the laboratory-scale test data are not fully developed due to the lack of flow duration or distance from the inlet. To verify the dependency of flow structures on these factors, additional experiments and observations across a broader range of settings are crucial.

Secondly, the predictive performances of Congo-included and lab-based models are tested with the natural-scale datasets. Figure 3.7 shows the validation results of each model with datasets of the natural-scale turbidity currents in Congo Canyon, which are Events 1 and 4 in Simmons et al. (2020). These natural-scale flows were quite dilute in concentration ($< 0.04\%$ in the layer-averaged concentration), and the measured profiles were strongly stratified compared to the laboratory-scale flows.

Congo-included model (which is trained with Event 5 of Congo events) exhibited a better performance than the lab-based model especially for the prediction in near-bed concentration. When it comes to the lab-based model trained only by the laboratory-scale dataset, it also outputs reasonable results although it tends to underestimate the near-bed concentration compared with Congo-included models.

3.4 Parameterisation of streamwise velocity profile

3.4.1 Correlation between the velocity and sediment concentration profiles

Previous work has modelled the vertical velocity and concentration profiles of turbidity currents independently (Abad et al., 2011). How strongly a concentration profile constrains the velocity profile or vice versa was poorly understood. However, density stratification caused by gradients of sediment concentration induces the vertical

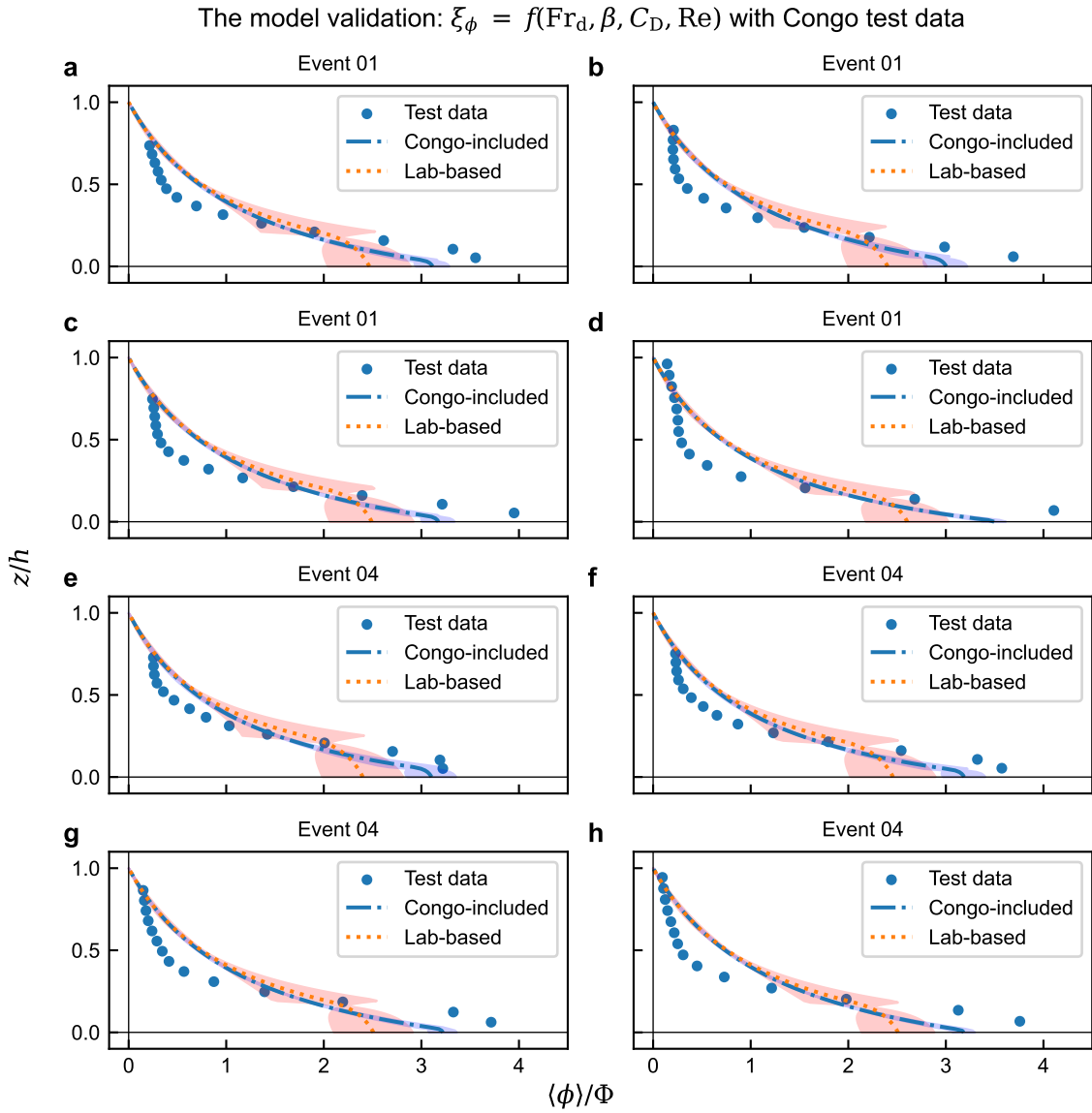


Figure 3.7: Validation of the models with the TYPE I data. The original measurements are indicated by blue dots. The range of uncertainties at each height are depicted by shaded area. Test data from a,b,c,d) Event 01 and e,f,g,h) Event 04. Although the profiles are similar each other, the four test data from each Event were chosen so that they cover the wide variation in near-bed concentration within the Event.

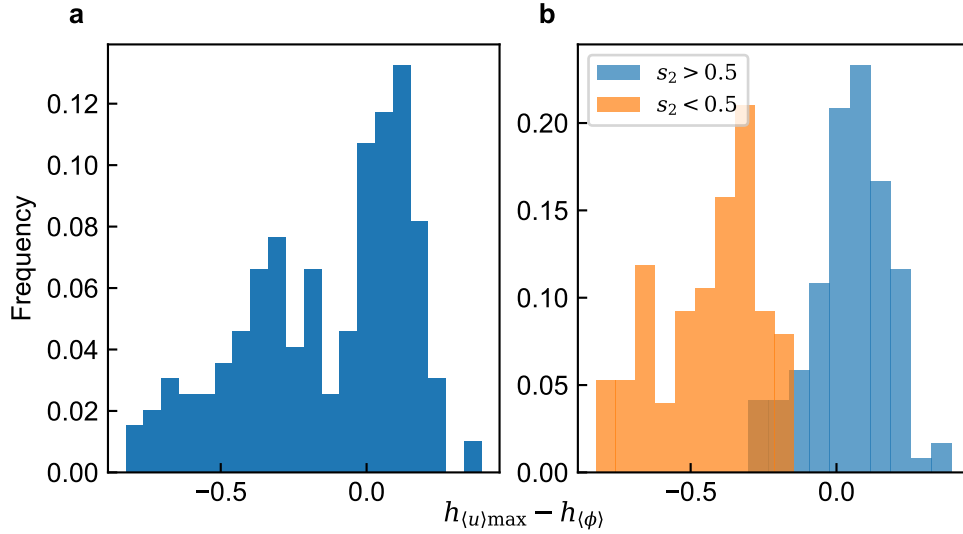


Figure 3.8: Histograms of the difference between the velocity-maximum height, $h_{(u)\max}$ and the maximum height in the gradient of flow concentration, $h_{(\phi)}$. a) All training data included. b) The data is subdivided into two groups based on s_2 .

variation in the flow's driving force and is thus hypothesised to dictate velocity profiles. In addition, a highly stratified velocity profile is associated with intense bed shear stress, which increases the near-bed concentration and thus makes the vertical flow concentration profile stratified (Wells and Dorrell, 2021). Similarly, strong shear at the upper interface and entrainment of the ambient fluid diffuse both suspended sediment particles and the momentum of the flow upward. The velocity and concentration profiles interact, and thus, those profiles should be examined simultaneously.

Stacey and Bowen (1988a) stated that a maximum in the gradient of the concentration profile at or close to the height of the velocity maximum is one noticeable feature of the turbidity current structure. Thus, velocity and concentration may not be independent. Abad et al. (2011) assumed that velocity and concentration profiles are the function of Fr_d . Thus, they also supposed the implicit correlation between velocity and concentration.

When we split the profile of a turbidity current at the elevation of the velocity maximum point, the lower layer experiences shear from the bed, forming a logarithmic vertically increasing velocity profile. This lower layer is relatively high in concentration, making it denser than the upper layer. The shear at the flow's upper interface decelerates the upper dilute layer, caused by the ambient water's friction and entrainment. The shear between the current and the ambient results in a monotonically decreasing velocity in the upper layer. Several studies approximated the velocity profile in the upper layer with a modified Gaussian profile (Altinakar et al., 1996).

If the transition between the lower dense and upper dilute layers is distinct, the velocity profile may show a sharpened profile around the velocity maximum elevation (Dorrell et al., 2019; Lloyd et al., 2022). On the other hand, when the transition between the two layers is gradual, the elevations of the maximum velocity

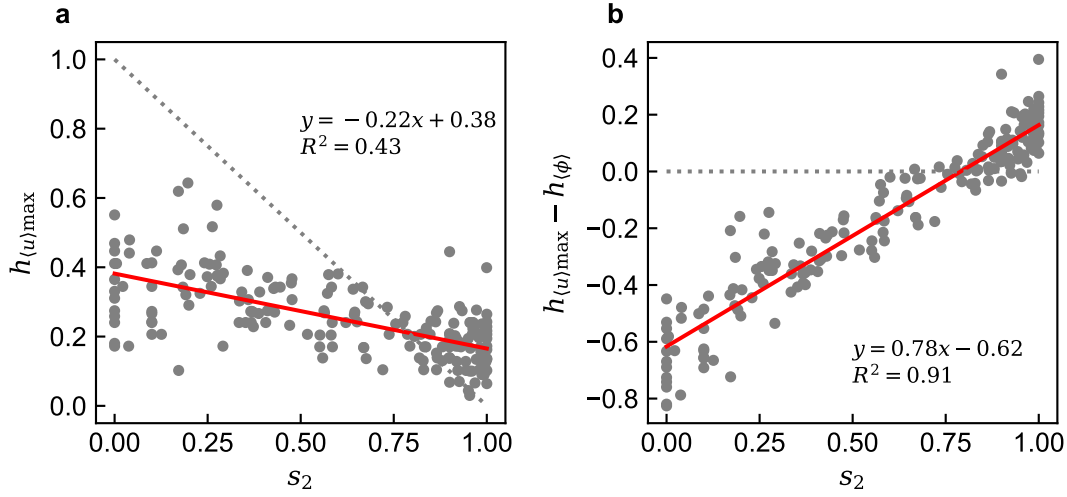


Figure 3.9: Scatter plots between the velocity maximum height and the inflection point of flow concentration. The gray dotted lines are the traditional assumption, $h_{(u)\max} = h_{(\phi)} = 1 - s_2$ (Stacey and Bowen, 1988a). a) The velocity maximum heights of all training data are plotted against s_2 . b) height differences between the velocity maximum and the maximum in the concentration gradient are plotted against s_2 . The red solid lines represent the regression lines estimated by the least-squared method.

and the maximum in the concentration gradient may be different.

Although the link between velocity and concentration profiles has been argued for more than 30 years (Stacey and Bowen, 1988a; Kneller and Buckee, 2000; Felix, 2002; Abad et al., 2011; Migeon et al., 2012; Dorrell et al., 2019), these speculations are not yet theoretically or empirically established due to the lack of a synthetic study of the link between velocity and concentration profiles. The link between velocity and concentration profiles may be described by the following relationship:

$$\xi_u(\hat{z}, s, t) = F_{u\phi}\xi_\phi(\hat{z}, s, t), \quad (3.42)$$

where $F_{u\phi}$ is the function which describes the link between the velocity and concentration profiles ξ_u to ξ_ϕ . The shape of this function is unknown. This section aims to develop an empirical model of $F_{u\phi}$.

Here, the correlation between the velocity and sediment concentration profiles is examined. Firstly, the claim of Stacey and Bowen (1988a) is investigated using the compiled profiles. In the compiled profiles, the height difference between the velocity maximum, $h_{(u)\max}$ and the maximum in the gradient of the concentration $h_{(\phi)}$ shows a bimodal distribution (Fig. 3.8a). This bimodal distribution can be distinguished based on the threshold parameter of Schlick function, s_2 which corresponds to the distance from the top to the maximum in the gradient of the concentration (Fig. 3.8b). The relation between s_2 and $h_{(\phi)}$ is

$$h_{(\phi)} = 1 - s_2. \quad (3.43)$$

For the profile with $s_2 > 0.5$, the speculation of Stacey and Bowen (1988a) holds relatively well, while for the profile with $s_2 < 0.5$, the velocity maximum height $h_{\langle u \rangle_{\max}}$ tends to be much lower than $h_{\langle \phi \rangle}$. The height difference $h_{\langle u \rangle_{\max}} - h_{\langle \phi \rangle}$ shows excellent linear correlation with s_2 (Fig. 3.9). The best-fit line by least-square method yields the following relationship ($R^2 = 0.91$)

$$h_{\langle u \rangle_{\max}} - h_{\langle \phi \rangle} = 0.78s_2 - 0.62. \quad (3.44)$$

From the equations (3.43) and (3.44),

$$h_{\langle u \rangle_{\max}} = 0.38 - 0.22s_2. \quad (3.45)$$

In the above, the empirical relationship between the velocity maximum height and the maximum in the gradient of concentration profile is obtained. Yet, this model is only able to predict the height of the velocity maximum and not able to predict the full velocity profile from the concentration profile. As a next step, the prediction of a full profile of streamwise velocity of a turbidity current is considered. To this end, the ratio of the flow velocity to concentration in the vertical profile $r_{u\phi}(\hat{z})$ is introduced as:

$$r_{u\phi}(\hat{z}) = \frac{\xi_u}{\xi_\phi} = \frac{\langle u \rangle / U}{\langle \phi \rangle / \Phi} \quad (3.46)$$

where \hat{z} is the elevation from the bed normalised by the flow height h . Zero slip condition implies that $\langle u \rangle = 0$ at $\hat{z} = 0$ and $\hat{z} = 1$, $r_{u\phi}(\hat{z}) = 0$ at $\hat{z} = 0$ and $\hat{z} = 1$. A higher $r_{u\phi}$ value means a relatively high flow velocity with a low concentration.

In this analysis, both measured values of velocity and concentration were interpolated by the cubic spline function, and 500 points equally distributed from the bottom to the top of the flows were chosen to obtain the values for calculating $r_{u\phi}(\hat{z})$. This aims to reveal the primary factors which control the link between velocity and concentration profiles. As a result, it was indicated that the shapes of both profiles strongly depended on each other in the lower part of the flows. Figure 3.10 exhibited the variation of $r_{u\phi}$ at different heights \hat{z} . The lower half (i.e., $\hat{z} < 0.5$) of the profiles exhibited small variation in the values of $r_{u\phi}$ for all datasets (Fig. 3.10), although the upper half ($\hat{z} > 0.5$) showed large variation. Overall, the median profiles of $r_{u\phi}$ showed similar parabola shapes (Fig. 3.10a–d).

The data with $s_2 > 0.5$ tends to exhibit slightly higher $r_{u\phi}$ values at the upper part of the flow (Fig. 3.10b), while the data with $s_2 < 0.5$ show slightly smaller $r_{u\phi}$ values at the upper part of the flow (Fig. 3.10c). Nevertheless, regardless of s_2 values, almost all data showed similar $r_{u\phi}$ profiles.

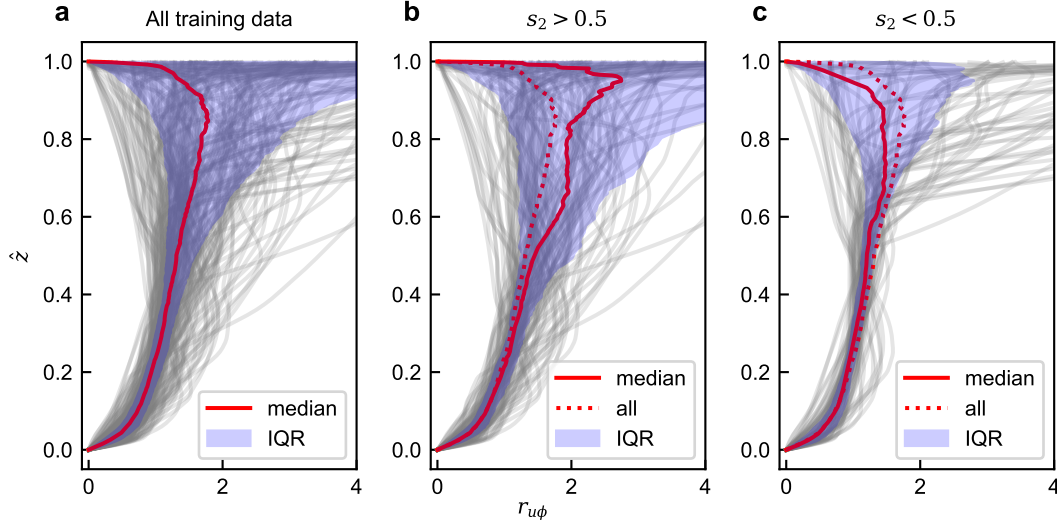


Figure 3.10: The ratio of the velocity ξ_u to the concentration ξ_ϕ profiles of density flows. All profiles are plotted by grey line, and the median profile is depicted by the red solid line. The blue region indicates the interquartile range at each height. a) All training data. b) Training data with $s_2 > 0.5$. c) Training data with $s_2 < 0.5$. The red dotted line represents the median profile of (a)

3.4.2 Prediction of velocity profiles

The $r_{u\phi}$ within the data in Figure 3.10 shows almost constant values in lower part of the flow. The direct implication is that $r_{u\phi}$ is only dependent on \hat{z} . For the upper layer, $r_{u\phi}$ varies in a wider range. The primary cause of this variation may be the error of original measurements and extrapolation. In the upper layer, both velocity and concentration are small. A small error in the measurements of $\langle u \rangle$ and $\langle \phi \rangle$ could result in a significant difference in $r_{u\phi}$. On top of that, most of the flume experiments in the compiled sources have fewer measurement points in the upper layer compared with the bottom layer, which exacerbates the uncertainty of $r_{u\phi}$ in the upper layer. From this observation, this study proposes the following relation for estimating the shape factor of the velocity profiles ξ_u :

$$\xi_u(\hat{z}, s_1, s_2) = \frac{F_{u\phi}(\hat{z})\xi_\phi(\hat{z}, s_1, s_2)}{\int_0^1 F_{u\phi}(\hat{z})\xi_\phi(\hat{z}, s, t)d\hat{z}} \quad (3.47)$$

where $F_{u\phi}$ denotes the ratio of the shape factor ξ_u to ξ_ϕ and is assumed to be the function of only \hat{z} . The shape factor ξ_ϕ for the concentration profiles can be predicted from lab-based or Congo-included models constructed from the training data described in the previous section. In addition, considering that the relation between the velocity and sediment concentration depends only on the height (Fig. 3.10), this study estimated $F_{u\phi}(\hat{z})$ as the 7-point moving average of the median values of $r_{u\phi}(\hat{z})$ in Figure 3.10a. Hereafter, this model is referred to as the ξ_u model.

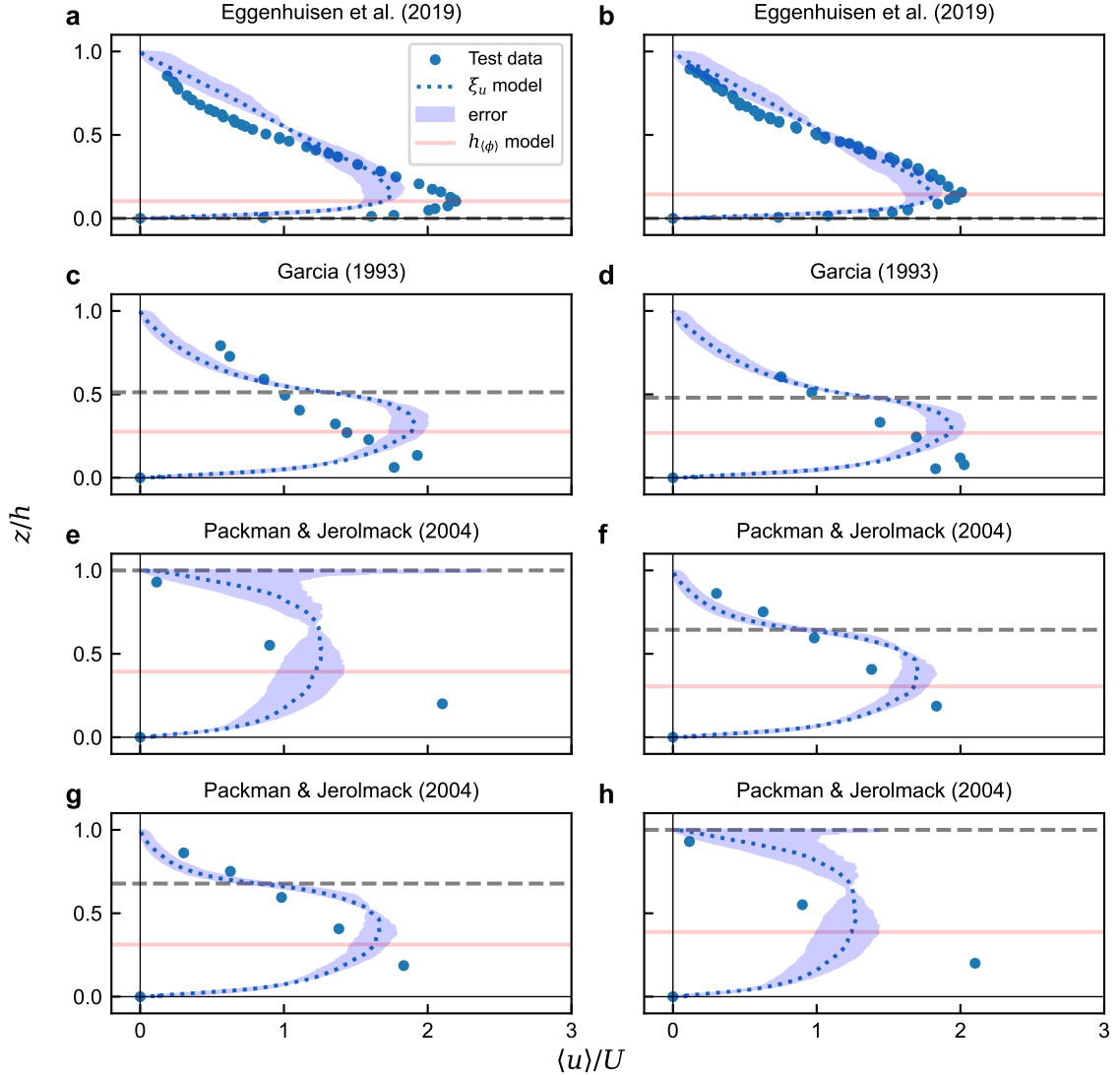


Figure 3.11: Velocity profiles which are predicted from the product of the profile of Congo-included ξ_ϕ model and $F_{u\phi}$. Blue dots represent the original measurements from each laboratory-scale test data. The blue shaded area represents the error of velocity profile, estimated from IQR of the $r_{u\phi}$ values in Figure 3.10a. The red solid line is the velocity maximum height estimated by the equation (3.45). Gray dashed lines are the height of maximum in gradient of concentration profile which Stacey and Bowen (1988a) assumed to coincide with the velocity maximum height. a,b) Test data from Eggenhuisen et al. (2020). Slope, S , differs between the runs: a) $S = 0.14$, b) $S = 0.07$. c,d) Test data from Garcia (1993). Initial concentration differs between the runs: c) $\Phi_0 = 0.143$ vol.%, d) $\Phi_0 = 0.133$ vol.%. e,f,g,h) Test data from Packman and Jerolmack (2004). For each figure, the material of suspended particles are e,h) Kaolinite and f,g) Silica, type of salt in the ambient fluid is e,h) CaCl_2 and g,f) NaCl , salt concentration is e,h) 50 mM (millimolar) and g,f) 10 mM, and the measurement locations are e,g) 140 cm and f,h) 40 cm downstream from the inlet.

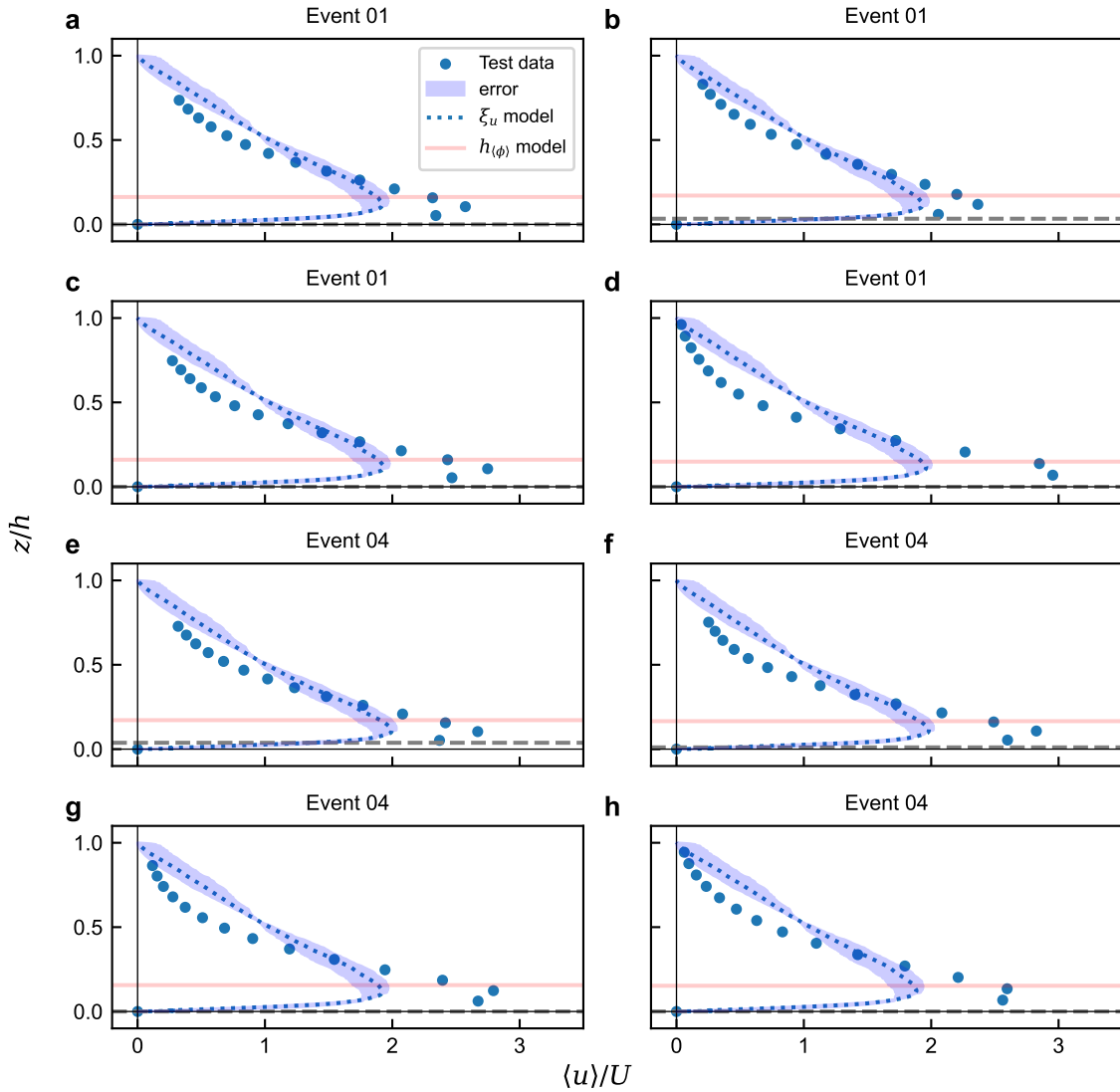


Figure 3.12: Velocity profiles which are predicted from the product of the profile of Congo-included ξ_{ϕ} model and $F_{u\phi}$. Blue dots represent the original measurements from each Congo test data. The blue shaded area represents the error of velocity profile, estimated from IQR of the $r_{u\phi}$ values in Figure 3.10a. The red solid line is the velocity maximum height estimated by the equation (3.45). Gray dashed lines are the height of maximum in gradient of concentration profile, which Stacey and Bowen (1988a) assumed to coincide with the velocity maximum height. Test data from a,b,c,d) Event 01 and e,f,g,h) Event 04. Each velocity profile corresponds to the concentration profile in Figure 3.7

3.4.3 Validation of the prediction of the velocity profiles

The ξ_u model (Eq. 3.47) for predicting ξ_u was validated using the test datasets chosen from the laboratory datasets (Eggenhuisen et al., 2020; García, 1993; Packman and Jerolmack, 2004) and natural-scale datasets (Simmons et al., 2020) (Fig. 3.11 and 3.12; also see Table 3.1). As mentioned above, the relatively large uncertainty of $r_{u\phi}$ may result in poor prediction in ξ_u in the upper layer of the flow. To evaluate the sensitivity of ξ_u against the deviation of $F_{u\phi}(\hat{z})$ in the upper region of the flow, the 25 and 75 percentile lines are also used as comparison (Fig. 3.11 and 3.12).

As a result, the velocity profiles predicted by the model fit well with both the laboratory-scale (Fig. 3.11) and natural-scale test datasets (Fig. 3.12), although they showed relatively large deviations from the profiles of a part of the laboratory-scale data (Fig. 3.11e, h). Despite the large uncertainty of $r_{u\phi}$ in the upper part of the flow (Fig. 3.10a), the uncertainty of the upper layer of the predicted ξ_u shows a relatively smaller range apart from Figure (3.11e, h). In addition, the ξ_u model captures the velocity maximum height of the original measurement very well. The performance of ξ_u model is as good as the empirical $h_{\langle\phi\rangle}$ model (Eq. 3.45) and shows excellent agreement with the $h_{\langle\phi\rangle}$ model (Eq. 3.45, and red lines in Fig. 3.11 and 3.12). On the other hand, the traditional assumption that the velocity maximum height coincides with the height of the maximum in the gradient of the flow concentration (Stacey and Bowen, 1988a) does not hold for test data as well as the training data (Grey dashed lines in Fig. 3.11 and 3.12).

3.5 Discussion

3.5.1 Significance of the natural-scale datasets for understanding velocity and concentration profiles of turbidity currents

The results of this study implied that lab-based and Congo-included models can predict laboratory-scale and natural-scale turbidity currents with reasonable accuracy. The Congo-included model performs slightly better than the lab-based model regarding the Natural-scale test data, especially around the near-bed concentration (Fig. 3.7).

This implies that the model trained by the natural-scale data outperforms other models. The potential limitation of the Congo-included models is their applicability to other natural-scale settings. Since the Congo-included model is only validated with two events in Congo, whether this model can predict the natural-scale turbidity currents in other submarine-fan systems is unknown. Having said that, since the lab-based model already shows reasonable performance in Congo test data, those models are likely to have excellent generalisation performance. Thus, it is also expected to show good predictions in other settings. Improvements in technologies of direct observation may eventually make it possible to establish many local high-accuracy models specialised to each submarine-fan system.

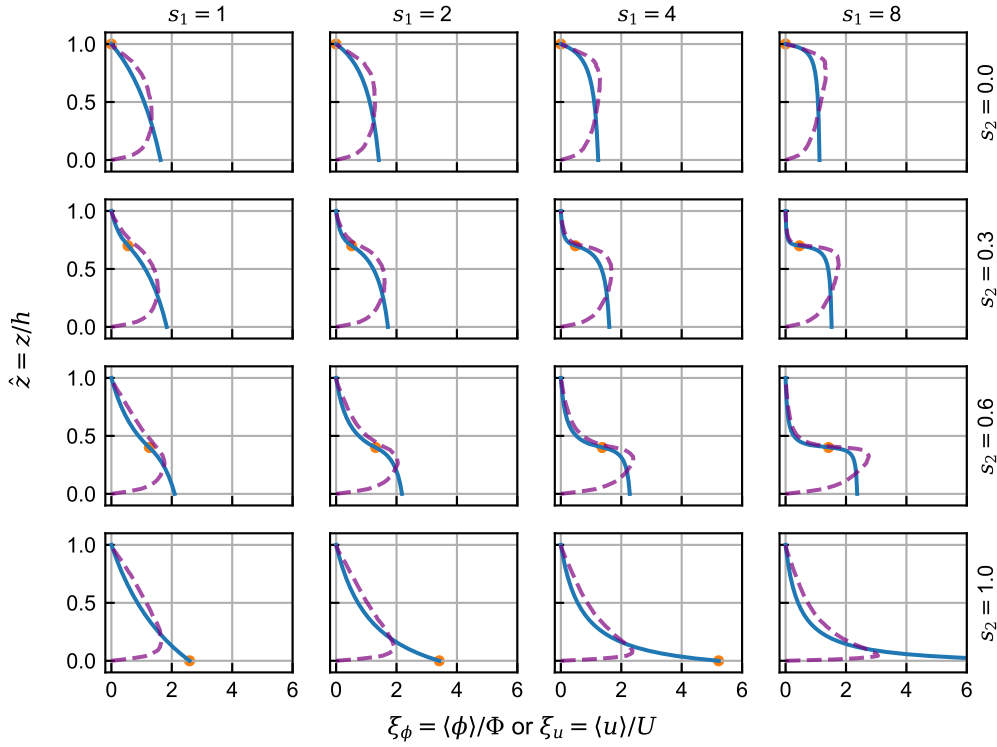


Figure 3.13: The visualisation of the shape factor ξ_ϕ and ξ_u based on the fit function parameters s_1 and s_2 . Blue solid curves denote ξ_ϕ . Purple dashed curves denote ξ_u .

3.5.2 Correlation between velocity and concentration profiles

This study revealed that the shape of the velocity profiles of turbidity currents is correlated with that of their concentration profiles, which implies that the velocity profiles can be modelled as the subordinate function of the concentration profiles.

Previously, Stacey and Bowen (1988a) stated that the velocity maximum coincides with the maximum in the gradient of flow concentration. However, the compiled data revealed that this is only applicable to the data with high s_2 values (Fig. 3.9b). The concentration profiles with high s_2 show relatively well stratified Rouse-profile-like shape (The bottom row in Fig. 3.13). This type of flow profiles are typically reported in supercritical flows (Sequeiros et al., 2010a). A supercritical flow exhibits a low stability in upper flow interface, resulting in gradual transition to ambient fluid (profiles with high s_2 in Fig. 3.13), while the flow interface of a subcritical flow tends to be steady and thus show a relatively distinct interface (profiles with low s_2 in Fig. 3.13).

Further analysis revealed that there is a linear correlation between s_2 and the height difference between velocity maximum and the maximum in the gradient of flow concentration (Fig. 3.9b and Eq. 3.45). The physics behind this linear correlation remains unknown, but the height of the velocity maximum does not increase as expected with the increase in the inflection point of the flow concentration profile. This is presumably because

the shear between the ambient fluid suppresses the increase in velocity-maximum height. On the other hand, shear between the ambient fluid enhances the diffusion of suspended material over the velocity maxima. The higher inflection point of flow concentration than the velocity maxima indicates that the suspended sediment is well mixed through the velocity maxima.

Interestingly, the ξ_u model developed in this study performs almost the same as the empirical $h_{(\phi)}$ model in terms of predicting velocity-maximum height. On top of that, the ξ_u model can also predict the full profile with reasonable accuracy. This result implies that the velocity profiles are dependent on the concentration profile. More intensive validation and training of the model with additional experiments and direct observations is expected to improve the model.

3.5.3 Governing parameters for velocity and concentration profiles

The results of the model developed in this study lead to the following questions: (i) which flow parameters play a critical role in determining the shape of concentration and velocity profiles? (ii) What physical processes are involved in the governing dimensionless parameters? To answer these questions, the flow profile dependence on flow parameters were investigated using the Congo-included model of ξ_ϕ and the ξ_u model.

Both the lab-based and Congo-included models employed four flow parameters as descriptors of the shape factor of flow concentration

$$\xi_\phi(s_1, s_2) = f \left(\text{Fr}_d = \frac{U}{\sqrt{g\rho_\Delta h}}, \beta = \frac{w_s}{\kappa u_*}, C_D = \frac{u_*^2}{U^2}, \text{Re} = \frac{(\rho_\Delta + 1)\rho_a U h}{\mu} \right) \quad (3.48)$$

$$\xi_u(\hat{z}) = \frac{F_{u\phi}(\hat{z})\xi_\phi(\hat{z}, s_1, s_2)}{\int_0^1 F_{u\phi}(\hat{z})\xi_\phi(\hat{z}, s_1, s_2)d\hat{z}} \quad (3.49)$$

A near-equilibrium dilute turbidity current ($\rho_\Delta \ll 1$) in a submarine channel is considered. The viscosity μ , the density of ambient water, ρ_a , von Karman coefficient, κ , and gravitational acceleration, g are considered constant in this analysis. Further, since $\rho_\Delta \ll 1$ is assumed, $\rho_\Delta + 1 \simeq 1$. Then, each dimensionless parameter is correlated with the following expressions,

$$\text{Fr}_d \propto \frac{U}{\sqrt{\rho_\Delta h}}, \quad (3.50)$$

$$\beta \propto \frac{w_s}{u_*}, \quad (3.51)$$

$$C_D \propto \frac{u_*^2}{U^2}, \quad (3.52)$$

$$\text{Re} \propto U h. \quad (3.53)$$

The densimetric Froude number Fr_d and Rouse number β have been considered important the results of KCV (Table 3.2–3.5) and the careful comparison of the models (Fig. 3.6, 3.7, 3.18 and 3.19) imply that the four

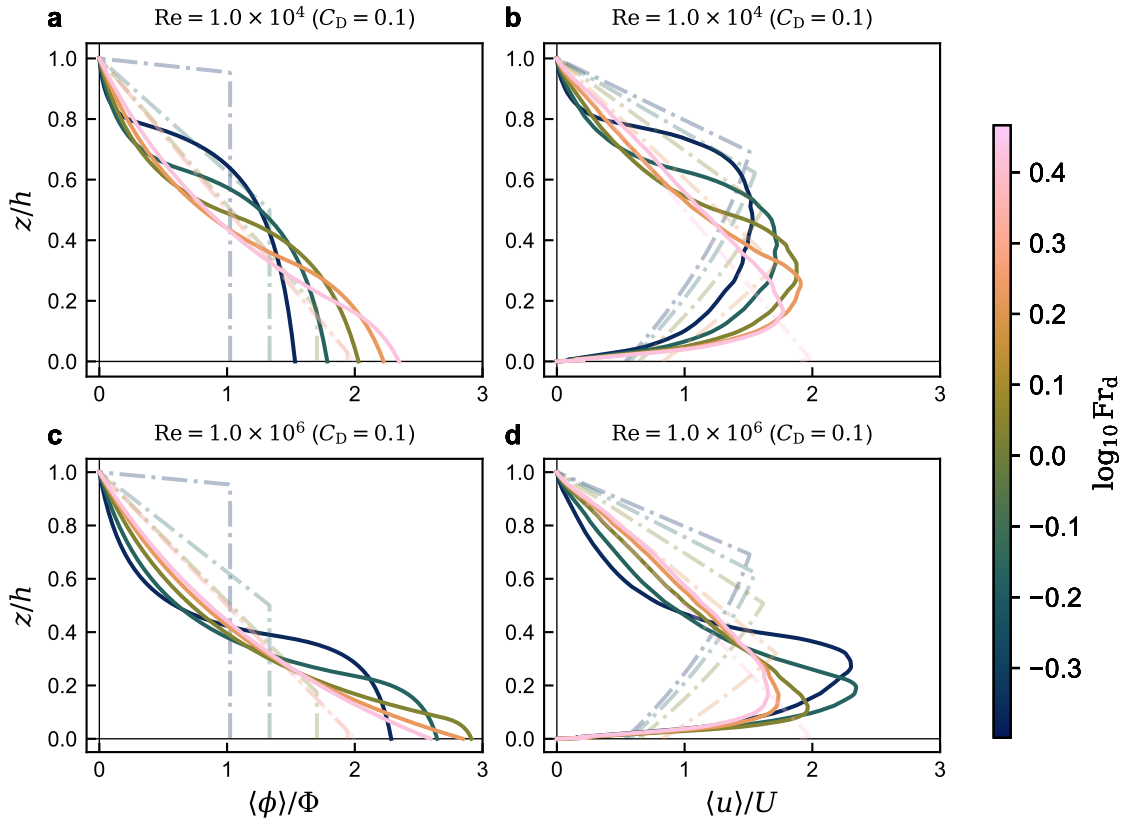


Figure 3.14: Fr_d dependency of the velocity and concentration profiles under different Re conditions. The Congo-included model is used for ξ_ϕ . The drag coefficient and the Rouse number are fixed ($C_D = 0.1$ and $\beta = 0.091$). The faint coloured dashed lines for comparison show the profiles predicted by Abad et al. (2011) with the same flow parameters. (a) Concentration profiles predicted by the Congo-included model ($Re = 1.0 \times 10^4$). The profiles are highly stratified as Fr_d increases. (b) The velocity profiles predicted by the ξ_u model ($Re = 1.0 \times 10^4$). The height of the maximum flow velocity point lowers as Fr_d increases. (c) The concentration profiles predicted by the Congo-included Model ($Re = 1.0 \times 10^6$). (d) The velocity profiles predicted by the ξ_u model ($Re = 1.0 \times 10^6$). The ratio of the maximum velocities to the layer-averaged velocities tends to be larger than those predicted by the Lab-based Model.

dimensionless parameters Fr_d , β , C_D , and Re are vital to predict the flow profiles.

As mentioned in the section 3.2, Fr_d relates to the stability of the upper interface of a flow. Abad et al. (2011) developed the Fr_d -dependent flow profile models for saline flows β is the vital factor determining the vertical flow concentration profile in open-channel flows (Rouse profile, see Eq. 3.15). The models developed in this study fill the research gap. The vertical structure of turbidity currents is considered with the Froude and the Rouse numbers Fr_d and β .

Here, the response of the flow profile against Fr_d and β with fixed values of other parameters (Re and C_D) is considered.

densimetric Froude number

Firstly, the influence of the densimetric Froude number Fr_d on the variations in concentration and velocity profiles ξ_ϕ and ξ_u is examined (Fig. 3.14 and 3.15). Previous studies have suggested that the elevation of the

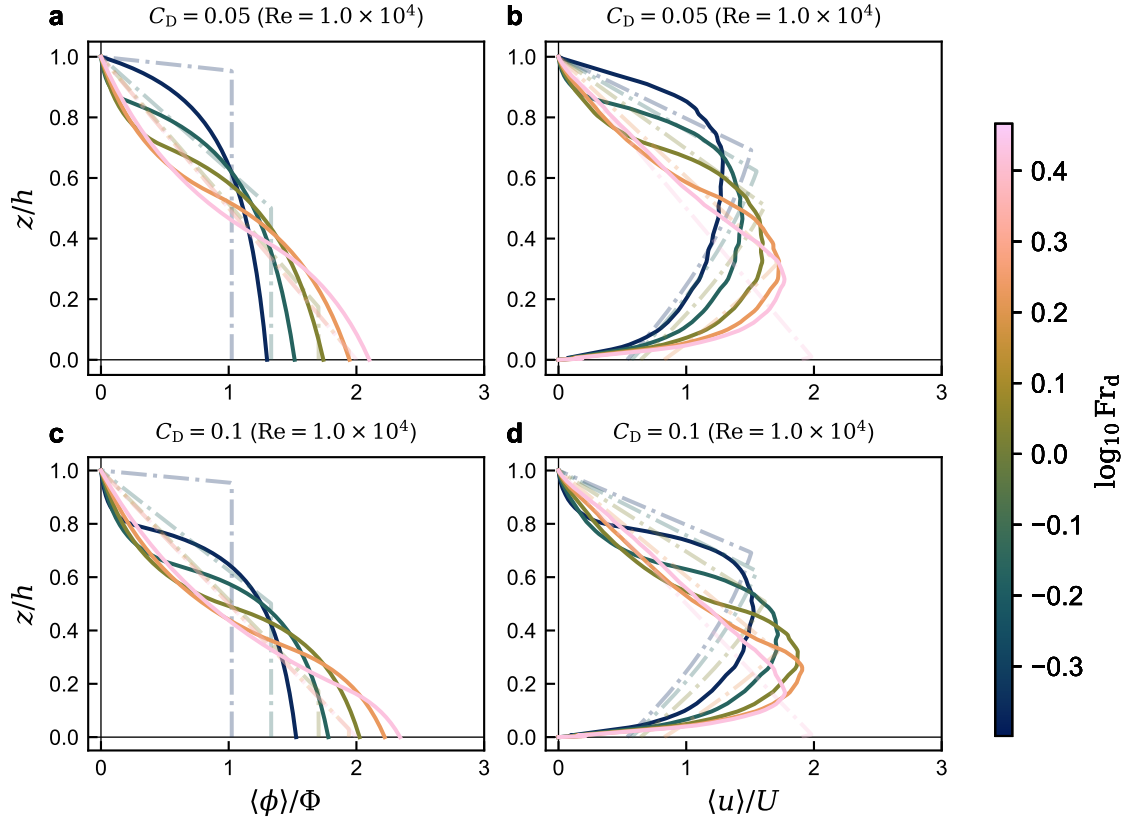


Figure 3.15: Fr_d dependency of the velocity and concentration profiles under different C_D conditions. The Congo-included model is used for ξ_ϕ . The Re and the Rouse number are fixed ($Re = 10 \times 10^4$ and $\beta = 0.091$). The faint coloured dashed lines for comparison show the profiles predicted by Abad et al. (2011) with the same flow parameters. (a) Concentration profiles predicted by the Congo-included model ($C_D = 0.05$). The profiles are highly stratified as Fr_d increases. (b) The velocity profiles predicted by the ξ_u model ($C_D = 0.05$). The height of the maximum flow velocity point lowers as Fr_d increases. (c) The concentration profiles predicted by the Congo-included Model ($C_D = 0.1$). (d) The velocity profiles predicted by the ξ_u model ($C_D = 0.1$). The ratio of the maximum velocities to the layer-averaged velocities tends to be larger than those predicted by the Lab-based Model.

velocity maximum point increases and concentration profiles are less stratified as Fr_d decreases (Sequeiros et al., 2010b). This is because increasing the Froude number means more mixing at the flow interface, which thickens and dilutes the upper layer of the flow. Overall, the results of both models demonstrated this trend well in velocity and concentration profiles (Fig. 3.14 and 3.15).

Compared with the laboratory-scale setting ($Re \sim 10^4$), natural-scale setting ($Re \sim 10^6$) shows more stratified profiles with the same Fr_d values (Fig. 3.14). While the reason why natural-scale turbidity currents tend to stratify more remains to be solved, one potential factor is the water depth. Usually, the water depth in the flume is less than $\sim 10h$, whereas it reaches $\sim 100h$ in cases of natural-scale turbidity currents. The laboratory flume's shallow water depth may suppress the evolution of the upper dilute layer of the flow due to the relatively strong counterflow. However, the potential effects of water depth on flow stratification remain to be solved as areas for useful numerical and experimental research in the future.

The vertical flow profile model proposed by Abad et al. (2011) only considered the effect of the Froude number Fr_d . From Figures (3.15a, b), the models of Abad et al. (2011) predicted relatively similar profiles to the models in this study when C_D and Re were small. However, for the setting with the high values of Re or C_D , the model predictions of this study significantly deviate from those of the model of Abad et al. (2011). They exhibited strong stratifications in both velocity and concentration profiles (3.14c, d and 3.15c, d).

Rouse number

Secondly, the influence of the Rouse number β on the variations in concentration and velocity profiles ξ_ϕ and ξ_u is examined (Fig. 3.16 and 3.17) is considered. As β increases, the particle settling flux dominates the flow, making the suspended particles concentrate on the near-bed region. In contrast, as β decreases, the turbulent diffusion becomes dominant, dispersing the suspended particles and making the concentration profile vertically uniform. Overall, the models in this study capture these fundamental trends very well (Fig. 3.16 and 3.17). The stratification trends for different Re and C_D are also similar to the trends observed in a range of Fr_d . In the high Re setting (i.e., natural-scale flows), the flow exhibits more stratified profiles with the same β values. Likewise, the flow becomes more stratified in a high C_D setting.

Compared to the Froude and Rouse numbers, the physical significance of C_D and Re to the vertical flow structure is challenging to interpret. C_D relates to the roughness of the bed, whose role in determining the flow vertical structure is unknown. The Reynolds number Re describes the ratio between inertia and viscosity forces in the flows. All laboratory-scale data have a similar order of $Re \sim 10^4$, while the natural-scale data show $Re \sim 10^6$. It has been claimed that if $Re \gtrsim 10^4$, the flows have similar turbulent dynamics (Peltier and Caulfield, 2003).

To investigate the effect of Re , the second-best model of s_2 was tested against the test data (Fig. 3.18 and

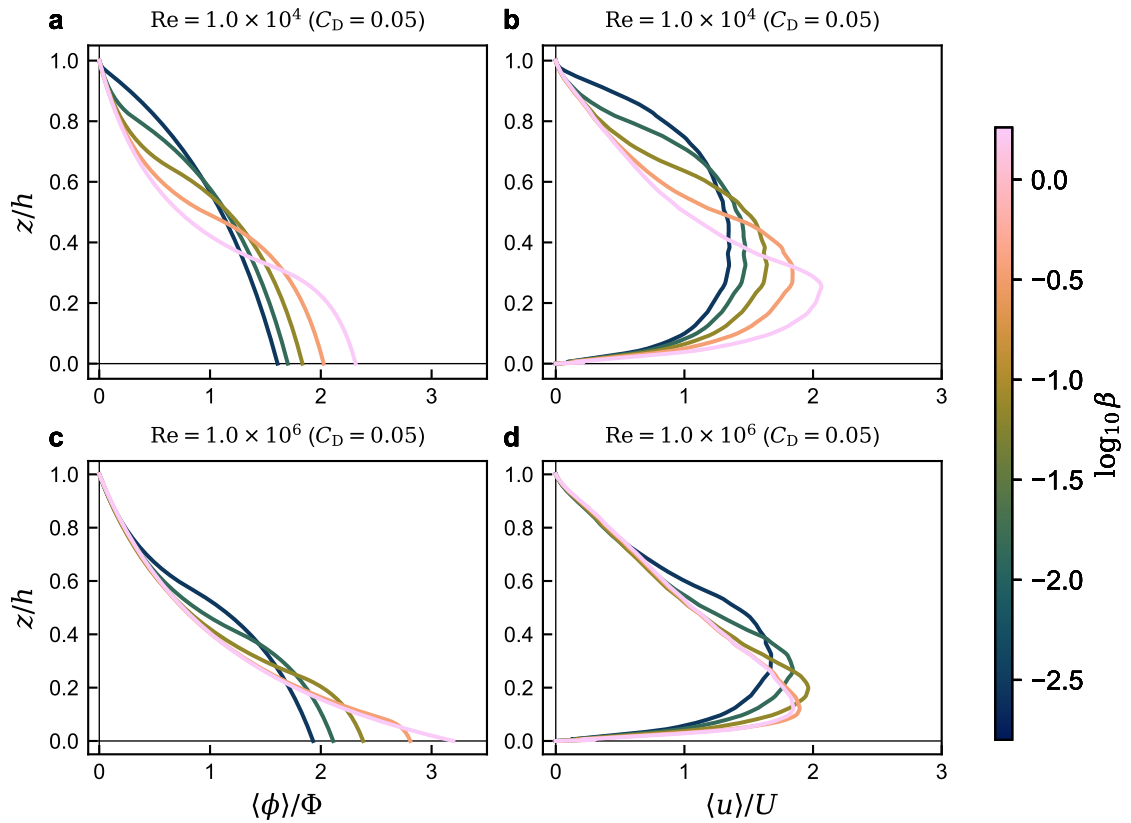


Figure 3.16: β dependency of the velocity and concentration profiles under different Re conditions. The Congo-included model is used for ξ_ϕ . The drag coefficient and the Rouse number are fixed ($C_D = 0.05$ and $\beta = 0.091$). (a) Concentration profiles predicted by the Congo-included model ($Re = 1.0 \times 10^4$). The profiles are highly stratified as β increases. (b) The velocity profiles predicted by the ξ_u model ($Re = 1.0 \times 10^4$). The height of the maximum flow velocity point lowers as Fr_d increases. (c) The concentration profiles predicted by the Congo-included Model ($Re = 1.0 \times 10^6$). (d) The velocity profiles predicted by the ξ_u model ($Re = 1.0 \times 10^4$).

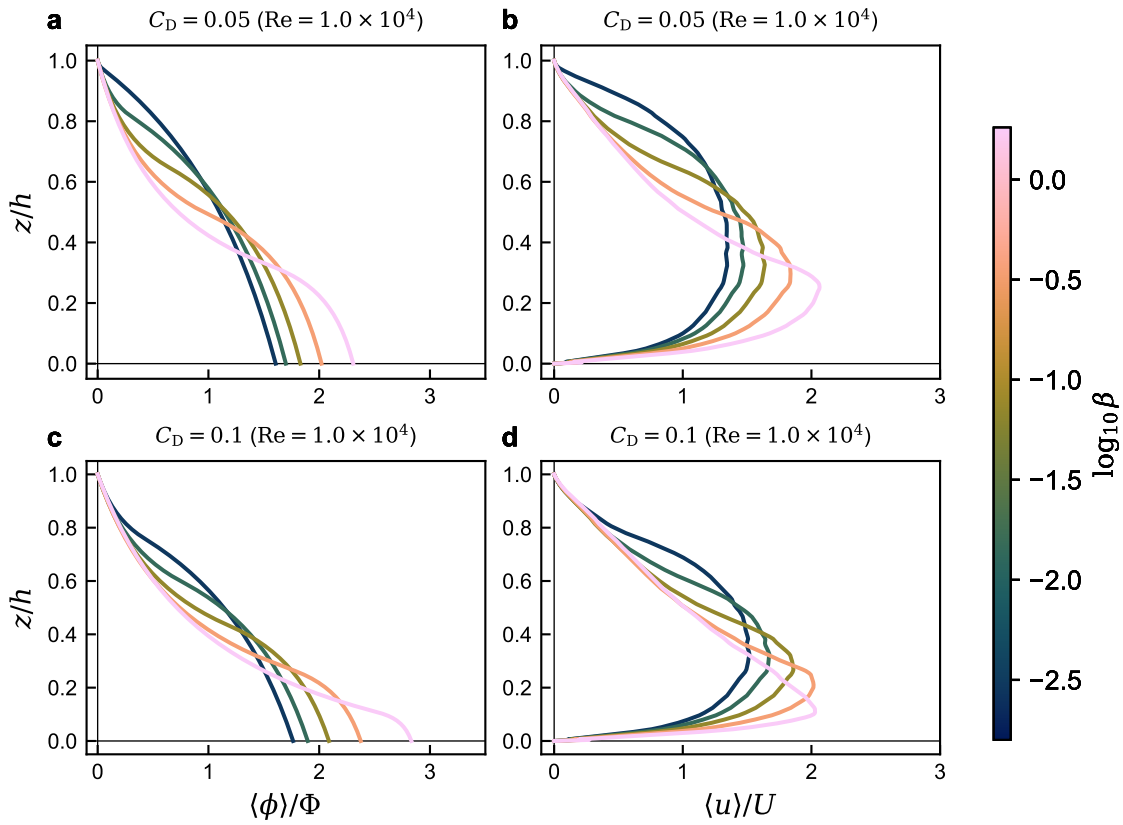


Figure 3.17: β dependency of the velocity and concentration profiles under different C_D conditions. The Congo-included model is used for ξ_ϕ . The Re and the Rouse number are fixed (Re = 10×10^4 and $\beta = 0.091$). (a) Concentration profiles predicted by the Congo-included model ($C_D = 0.05$). The profiles become more stratified as β increases. (b) The velocity profiles predicted by the ξ_u model ($C_D = 0.05$). The height of the maximum flow velocity point lowers as β increases. (c) The concentration profiles predicted by the Congo-included Model ($C_D = 0.1$). (d) The velocity profiles predicted by the ξ_u model ($C_D = 0.1$).

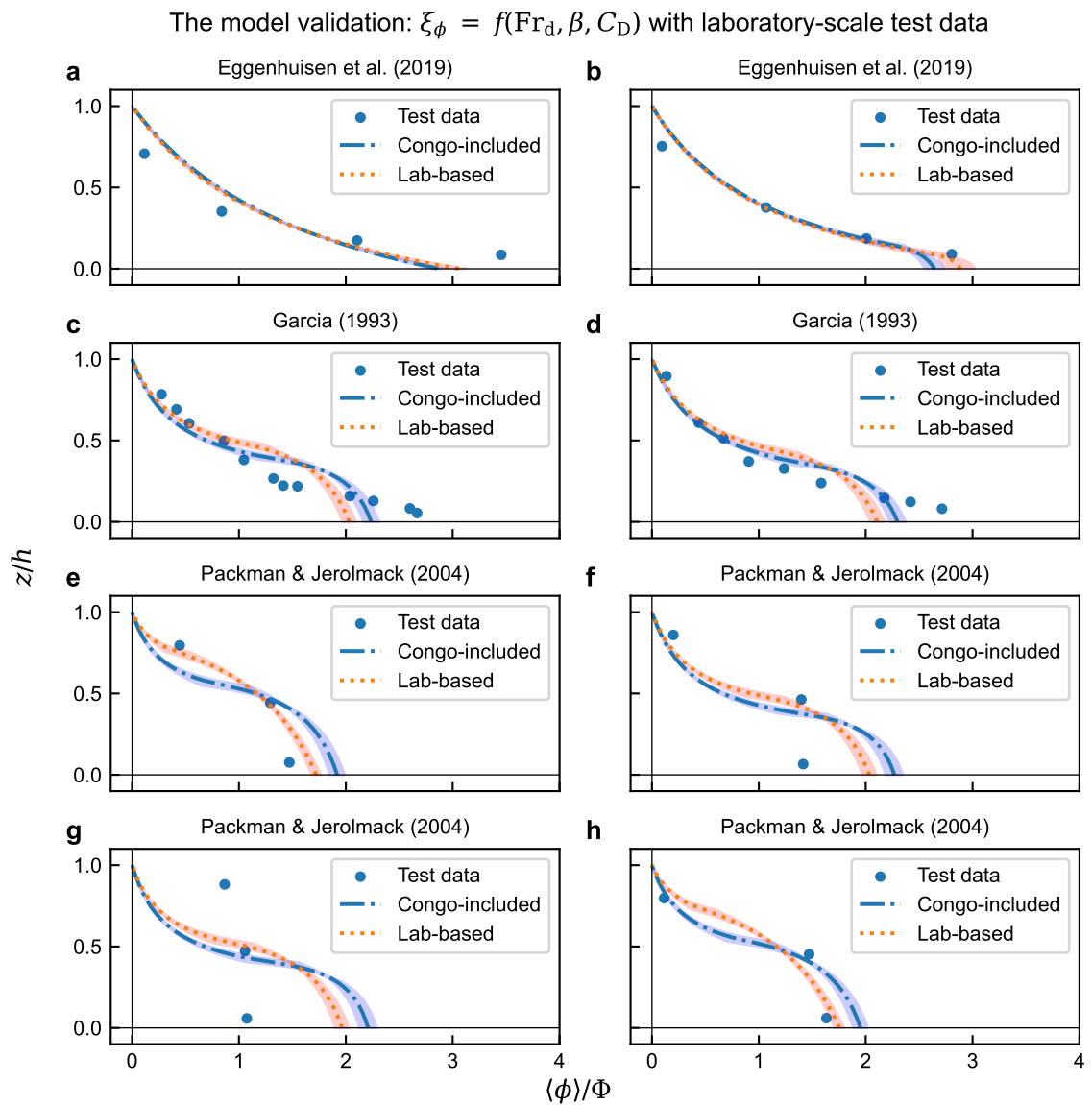


Figure 3.18: Validation of the models with the selected laboratory-scale data. The original measurements are indicated by blue dots. The range of uncertainties at each height is depicted by the shaded area.

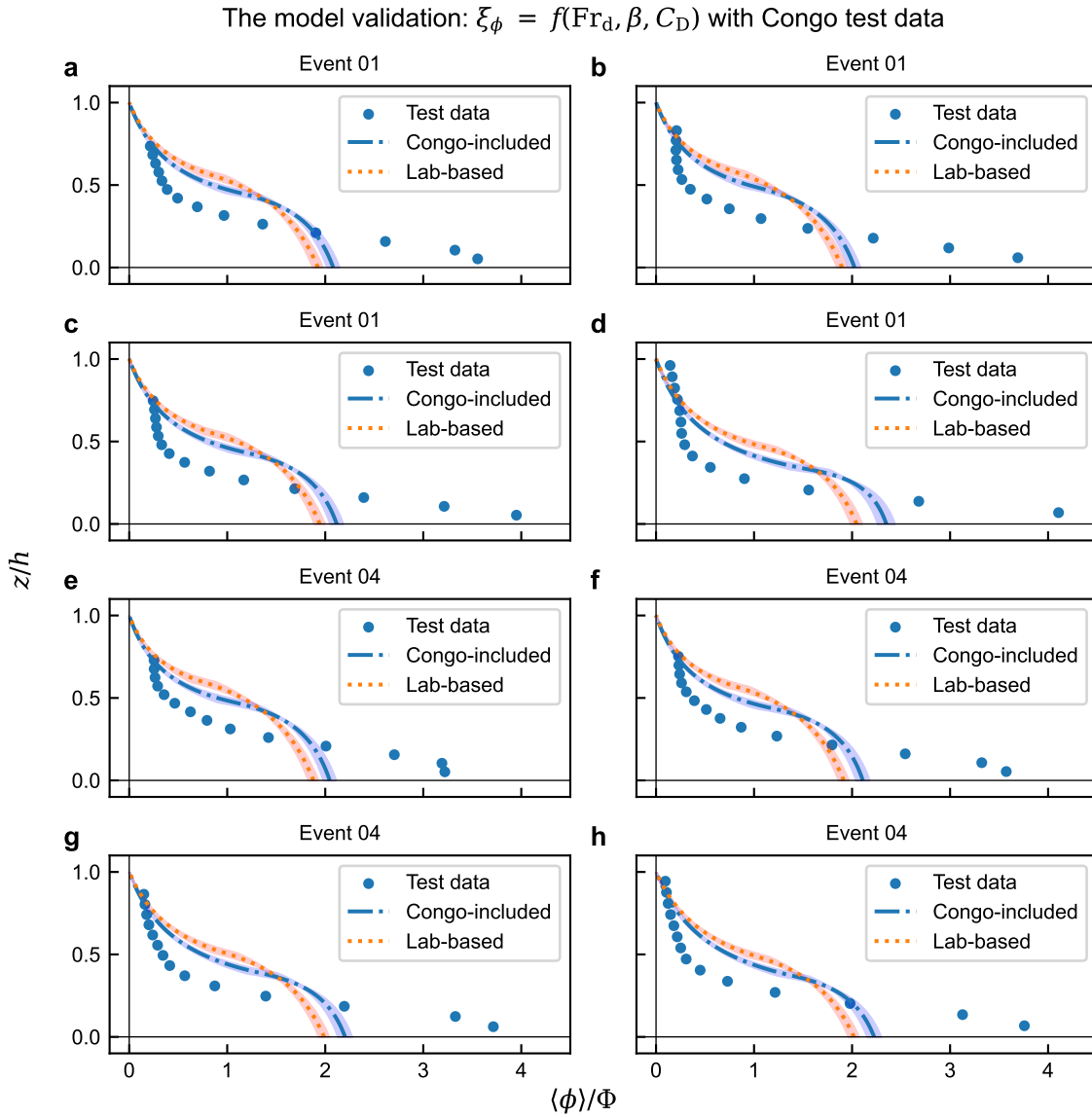


Figure 3.19: Validation of the models with the Congo test data. The original measurements are indicated by blue dots. The ranges of uncertainties at each height are depicted by the shaded area.

3.19). The second-best model of s_2 is,

$$\begin{aligned} s_2 &= f_2(\text{Fr}_d, \beta, C_D) \simeq \text{Max} \left(0, \min \left(1, 1.35 + \log \text{Fr}_d^{0.26} \beta^{0.047} C_D^{0.29} \right) \right) \quad (\text{Congo-included}) \\ s_2 &= f_2(\text{Fr}_d, \beta, C_D) \simeq \text{Max} \left(0, \min \left(1, 1.32 + \log \text{Fr}_d^{0.38} \beta^{0.063} C_D^{0.29} \right) \right) \quad (\text{Lab-based}) \end{aligned} \quad (3.54)$$

For s_1 , the same models in the equations (3.40) and (3.41) were used.

The simpler models without Re exhibited similar performance against the laboratory-scale test data (Fig. 3.18). However, both lab-based and Congo-included models excluding Re showed poor predictions for the natural-scale test data, implying that this parameter is related to some phenomenon caused by the difference in the scale of turbidity currents (Fig. 3.19).

Considering that the model without Re performs well in lab-scale test data (Fig. 3.18), it should be considered the possibility that the Reynolds number is not the scale of turbulence itself in this case but an effect of some unknown parameter related to the entire scale of the flow, such as the shape of submarine-channels, how close the flows are to equilibrium state, or depth of the ambient water, rather than the difference in dynamics of turbulence. For example, the limited height of the experimental facility to the water surface may cause a weak reversal flow in the ambient fluid in the opposite direction to that of the turbidity current generated in the experiment. The presence of this reversal flow would affect the flow vertical structure of the turbidity current. In contrast, the submarine channel offshore Congo is roughly 2 km deep, so the influence of the reversal flow above the turbidity current can be negligible. Assessing how closely flows approach equilibrium is challenging, particularly when comparing laboratory-scale and natural-scale data. However, the laboratory-scale experiments compiled in this study are reported to exhibit temporal steady-state conditions. Water entrainment influences the downstream flow evolution, leading to spatial variations. Nevertheless, these downstream changes due to water entrainment progress very slowly in the compiled dataset. Similar arguments apply to natural-scale turbidity currents. Given the extended flow duration (days to weeks) from the source and the nearly constant slope around the measurement location Simmons et al., 2020, the flow is likely in a temporal steady-state with minimal downstream spatial evolution. Therefore, it is unlikely that Re reflects differences in either temporal or spatial evolution.

In summary, the Froude and Rouse numbers Fr_d and β describe essential factors of the equilibrium flow stratification. On the other hand, the physical processes represented by the roughness and Reynolds numbers C_D and Re are unknown. It is speculated that they are related to the flow magnitudes, suggesting that further parametric examination is needed to solve this problem.

3.5.4 Implications for material transport efficiency of turbidity currents

In the previous section, the response of the flow structures against the dimensionless parameters is investigated. This section considers the implications of the dynamics of flow structures predicted in the developed models

to the flow dynamics in a natural-scale submarine channel. As mentioned in the section 3.1 (see Eq. 3.1 and 3.2; also see Eq. 1.58 in the section 1.3.5), when we consider the integrated conservation equations of sediment and momentum, the structure functions ξ_u and ξ_ϕ appears as some shape factors :

$$\frac{\partial}{\partial t} \Phi h + \frac{\partial}{\partial x} U \Phi h W_{u\phi} = \langle \phi' w' \rangle|_{\text{bed}} - w_s \langle \phi_b \rangle = w_s (e_s - r_0 \Phi) \quad (3.55)$$

$$\frac{\partial}{\partial t} U h + \frac{\partial}{\partial x} U^2 W_{u^2} = -\frac{(\rho_s - \rho_a)}{\rho_f} \frac{\partial}{\partial x} \frac{1}{2} g h \Phi W_P + R g h \theta \Phi + \langle u' w' \rangle|_{z=0} - \langle u' w' \rangle|_{z \rightarrow \infty} \quad (3.56)$$

where

$$W_{u^2} \equiv \int_0^\infty \xi_u^2 d\hat{z}, \quad W_{u\phi} \equiv \int_0^\infty \xi_u \xi_\phi d\hat{z}, \quad W_P \equiv 2 \int_0^\infty \hat{z} \xi_\phi d\hat{z}. \quad (3.57)$$

The shape factor W_{u^2} appears in the advection term of momentum conservation equation (3.56). Likewise, $W_{u\phi}$ appears in the advection term of the mass conservation equation of sediment particles (Eq. 3.55). W_P appears in the pressure term in the momentum conservation equation (Eq. 3.56). A high W_{u^2} value means that the amount of advection of momentum will be enhanced due to the flow stratification. Similarly, a high $W_{u\phi}$ value means that the amount of advection of suspended particles will be enhanced due to the flow stratification. $W_{u\phi}$ increases when the velocity and concentration profiles are stratified in a way that the velocity maximum region coincides with the high-concentration bottom layer (Fig. 3.1). The high W_P indicates the less stratified flow concentration (close to ‘top-hat’ model, see Fig. 3.1). As W_P decreases, more suspended particles gather in the centre of the channel, which enables the flow to traverse meandering submarine-channel suppressing the loss of suspended materials due to overspilling (Dorrell et al., 2014). The near-bed to depth-averaged concentration ratio r_0 in the equation (3.55) also depends on ξ_ϕ and can be estimated with the developed model by the equation (3.24). The near-bed concentration plays a vital role in sediment deposition and erosion (Clare et al., 2015; Talling et al., 2015). Despite its importance, there is no practical model for predicting near-bed concentration of turbidity currents. In the previous studies, r_0 has often been assumed constant between 1.5 and 2.0 (Parker et al., 1986; Garcia, 1993; Altinakar et al., 1996; Kubo and Nakajima, 2002; Kostic and Parker, 2006). Parker et al. (1986) also incorporated the empirical model for open-channel flows (Eq. 1.70), but Parker et al. (1986) reported that this open-channel model provides acceptable values only within a narrow range of Rouse number ($0.05 < \beta < 0.5$), and also speculated that a fixed value $r_0 = 1.6$ performs well in the model.

Efficiency of material transport of turbidity currents

Here, based on the three shape factors and r_0 described above, the mechanics of material transport of turbidity currents are discussed. The previous Fr_d -based model of structure functions (Abad et al., 2011) increases W_{u^2} and $W_{u\phi}$ as Fr_d increases (Fig. 3.20a, b). This change will enhance the efficiency of material and momentum transport rate of the flow. Similarly, as Fr_d increases, W_P decreases (Fig. 3.20g). The change in W_P is

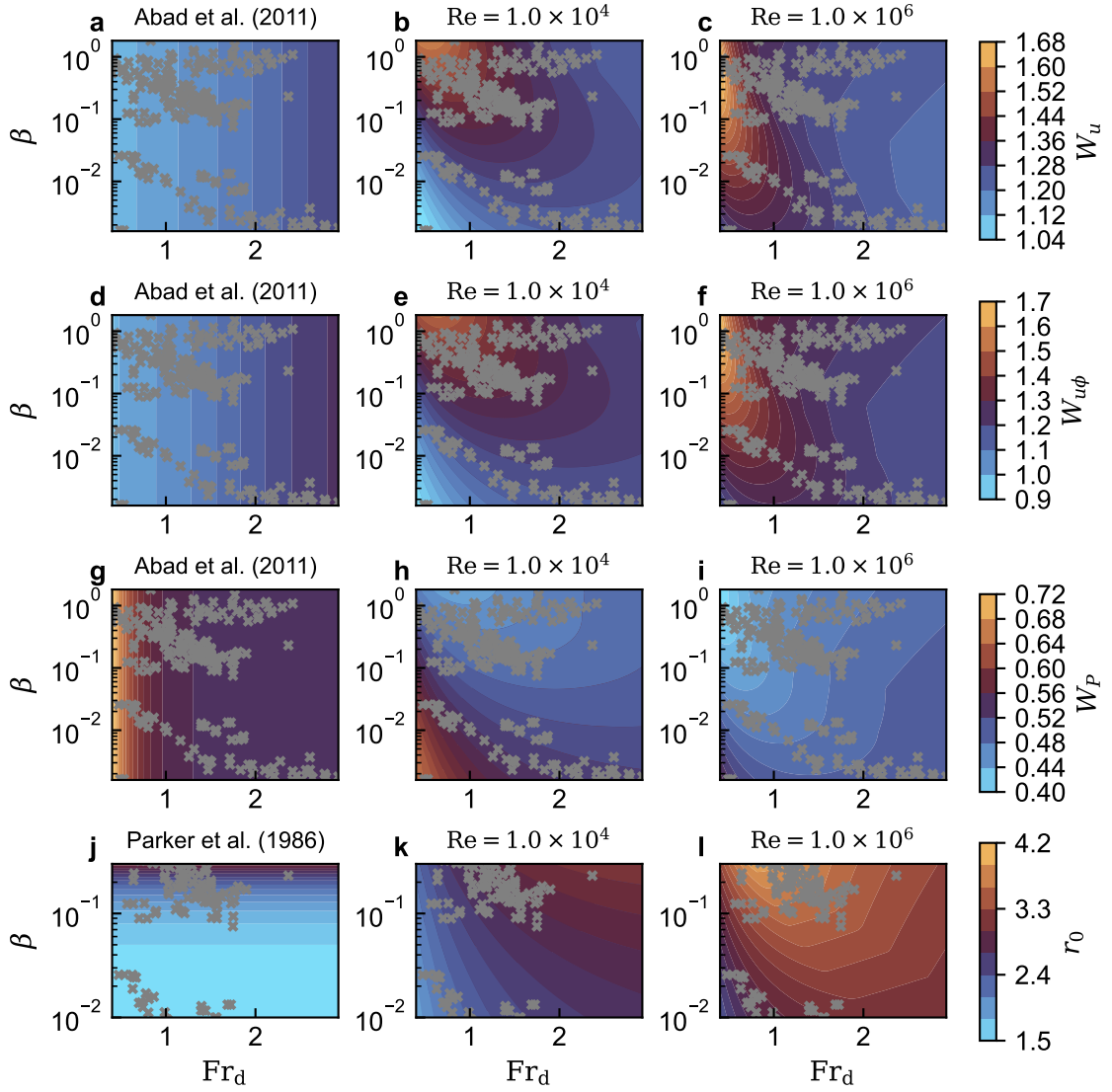


Figure 3.20: Froude and Rouse number dependency of weighting terms of modified hydrostatic pressure W_P (blue curve), density flux, $W_{u\phi}$, fluid acceleration, W_{u^2} , and the near-bed to depth-averaged concentration ratio, r_0 under different models: a,d,g) The models from Abad et al. (2011), j) The model from Parker et al. (1986), b,e,h,k) The developed models in this study with $Re = 1.0 \times 10^4$ (Laboratory-scale), c,f,i,l) The developed models in this study with $Re = 1.0 \times 10^6$ (Natural-scale). a,b,c) variation of W_{u^2} in Fr_d - β space, d,e,f) variation of $W_{u\phi}$ in Fr_d - β space, h,g,i) variation of W_P in Fr_d - β space, j,k,l) variation of r_0 in Fr_d - β space. Throughout, Gray cross markers represent the training and test data in this study. The drag coefficient, C_D is fixed as 0.1.

relatively large in low Fr_d state ($Fr_d < 1$), while for the high Fr_d state ($Fr_d > 1$), the W_P is almost constant ($W_P \sim 0.6$). These trends imply that when flows decelerate and Fr_d decrease, the efficiencies of material and momentum transport rates decrease. Once Fr_d decreases below unity, the W_P rapidly increases, making the flow concentration profile almost vertically uniform. In a submarine channel, this will cause a significant loss of driving force due to the sediment loss by overspilling, which makes it almost impossible for the flow to traverse a long distance.

On the other hand, the models developed in this study exhibit different trends (Fig. 3.20b,c,e,f,h,i). The model with low Re setting (Laboratory-scale: $Re \sim 1.0 \times 10^4$), W_{u^2} and $W_{u\phi}$ are more sensitive to the change in β rather than in Fr_d (Fig. 3.20b, e). Furthermore, in the case of high- β flows ($\beta \gtrsim 0.1$), W_{u^2} increases as Fr_d decreases, which is the opposite trend compared with the model of Abad et al. (2011). The intensity of the shape factors is also different from the model of Abad et al. (2011). The previous model shows $W_{u^2} < 1.3$ and $W_{u\phi} < 1.3$ within $0.5 < Fr_d < 3$, while in the developed models in this study, both W_{u^2} and $W_{u\phi}$ can exceed 1.5 depending on Fr_d and β values (Fig. 3.20a, b, d, e). When it comes to W_P , the model in this study predicts far smaller values compared with the model of Abad et al. (2011) with the same Fr_d values, implying the stronger stratification of flow concentration (Fig. 3.20g). The value of W_P is less sensitive to Fr_d and shows almost constant values for the same β value (Fig. 3.20g).

When it comes to the high Re setting (Natural-scale: $Re \sim 1.0 \times 10^6$), W_{u^2} and $W_{u\phi}$ exhibit high values even for the low Fr_d flows (Fig. 3.20c, f). In addition, unlike the low Re setting, W_{u^2} and $W_{u\phi}$ are more sensitive to Fr_d rather than β (Fig. 3.20c, f). Regardless of the value of β , the flow increases the efficiency of momentum and material transport rate as Fr_d decreases. Overall, the flows in high Re setting tend to show higher efficiency in both material and momentum transport compared with low-Re model or the previous model of Abad et al. (2011). When it comes to W_P , it also shows the opposite trend (Fig. 3.20i). For the high- β flows, as Fr_d decreases, W_P also decreases. The value of W_P is even less than the model of low Re. While the W_P is less sensitive to Fr_d in the case of low Re case, the model with high Re shows higher sensitivity to β . Having said that, the value of W_P is always small regardless of Fr_d and β values ($W_P \lesssim 0.5$).

In terms of the r_0 , contrary to the previous works, the model developed in this study predicts a wider variation of r_0 dependent on both Fr_d and β (Fig. 3.20j,k,l). Firstly, even from the observation of laboratory and natural-scale events, it is clear that r_0 can often exceed 2.0 (Fig. 3.6 and 3.7). Having said that, this relatively large r_0 is partially because the height scale used in this study is different from previous works. In Ellison and Turner's integral height scale, the r_0 is expected to take relatively smaller values. Nonetheless, the developed model implies that a fixed r_0 is clearly a poor assumption since r_0 can take a wider range ($1.5 < r_0 < 4$). Also, the open-channel model used in Parker et al. (1986) significantly underestimates r_0 , especially for the low β or high Fr_d flows. The predicted r_0 in the high Re setting is extremely high $3 < r_0 < 4$ due to the well-developed upper dilute layer.

3.6 Conclusion

The implications of the developed structure function ξ_ϕ and ξ_u can be summarised as follows. Firstly, both particle settling (relates to β) and shear between ambient fluid (relates to Fr_d) play a vital role in the vertical flow structure of velocity and concentration. On top of that, the bed roughness (relates to C_D) and turbulent intensity (relates to Re) are also important. Having said that, Re plays a vital role mainly in distinguishing the laboratory-scale from natural-scale data. The model without Re also performs well in terms of the laboratory-scale test data. Therefore, it is more plausible to say that there are other important factors that characterise the strong stratification of natural-scale flows, which cannot be captured by the selected dimensionless parameters in this study. Since the analysis in this study could not include those factors as dimensionless parameters in the multiple regression analysis; those unknown factors only appear as the difference in Re values. To overcome this limitation, more data of direct observations of natural-scale data are essential to clarify the difference between laboratory-scale and natural-scale events.

The flow velocity profiles of turbidity currents are found to be strongly correlated with the flow concentration profiles rather than other depth-averaged flow parameters. The implication of this strong bond between velocity and concentration is that the prediction of velocity or concentration may be possible from the other profile.

All models in this study imply the existence of flow mechanics which enhances the material and momentum transport when the flow decelerates as if the flow is trying to avoid being dissipated, maximising the transport efficiency by themselves (Fig. 3.20). Also, the flow thickening is likely to thicken only the upper dilute layer by which W_P decreases as Fr_d decreases. These unexpected dynamics of the internal flow structures may be the primary reason why turbidity currents can traverse ultra-long distances over shallow slopes without dissipation.

Implementing the developed models into system-scale numerical models (Dorrell et al., 2014) is expected to improve our understanding of the flow behaviour of long-runout turbidity currents along a sinuous submarine channel, as well as the evolution of submarine channel networks.

Chapter 4

Sediment Transport Capacity of Long-runout Turbidity Currents

4.1 Statement and author contributions

The work in this chapter has been published in *Nature Communications* (Fukuda et al., 2023). The data used in this study are the same data compiled in Chapter 2. A part of the supplementary data of Fukuda et al. (2023) are already shown in Chapter 2, and the rest of the supplementary data are available in the appendix (see A.1–A.3) I undertook the data compilation and the statistical analyses in this chapter. The co-authors in Fukuda et al. (2023) supported the interpretation of the results of the data compilations and the statistical analyses. The iterative least squares method against the fluvial data in Figure 4.3 was co-developed with myself and Edward W. G. Skevington (co-author). The detailed methodology of the curve fitting method is elaborated in the appendix (section A.3). The schematic illustration of the internal energetics figure (Fig. 4.6) was also co-developed with myself, Edward W. G. Skevington and Robert M. Dorrell. Other authors helped with the data collection and improving the draft.

4.2 Introduction

Gravity currents are a broad class of flows with a wide range of environmental applications, including terrestrial cold fronts and submarine thermohaline currents (Simpson, 1997). Of particular interest are particle-driven gravity currents, such as powder snow avalanches, pyroclastic density, and turbidity currents. Turbidity currents have received significant attention due to: their capacity to travel long distances, 100s-1,000s of kilometres, along sinuous submarine canyon-channel systems (Meiburg and Kneller, 2010a; Wells and Dorrell, 2021); their importance to the deep marine environment (Weimer et al., 2007; Picot et al., 2019); the de-

positional record of paleoenvironments (Goldfinger, 2011); and for geohazard risk management (Heezen and Ewing, 1952b; Bruschi et al., 2006; Hsu et al., 2008).

Turbidity currents are generated by the presence of suspended sediment, meaning they have a higher density than ambient water. This density difference generates a downslope gravitational force. The resulting flow produces turbulent mixing, keeping sediment in suspension (Parker et al., 1986). This suspension-flow feedback loop is referred to as autosuspension, the minimal requirement for long runout (Knapp, 1938; Bagnold et al., 1962) in all particle-driven gravity currents. Accurate prediction of autosuspension is essential to quantify gravity current propagation, natural hazard risk, and, for turbidity currents, deep marine biogeochemical cycling and anthropogenic environmental impact. However, despite its importance, the mechanisms that enable autosuspension are poorly understood because the kinetic energy of the flow is consumed to maintain the particles in suspension, and uplift them during turbulent mixing with the environment (Wells and Dorrell, 2021), which ultimately stalls the flow.

Historically, autosuspension has been explained by the positive feedback whereby sediment entrainment increases the turbulence, referred to as self-acceleration (Parker et al., 1986). Where the slope is steep, such as in the proximal regions of submarine canyons or on volcanic slopes, gravitational forcing (proportional to the slope) is relatively large and thus gravity currents are predominantly net-erosional. Entrainment of sediment provides the flow with additional mass and driving force, increasing the momentum and the basal drag, which in turn increases the turbulent energy, further enhancing sediment entrainment and accelerating the flow (Parker et al., 1986). However, turbidity currents can propagate for extensive distances and, in distal reaches, they can traverse near-zero slopes ($< 10^{-4}$ m/m) (Konsoer et al., 2013). In these regions, the gravitational forcing, proportional to slope, is small. Consequently, the velocity is reduced and the flow is, at best, only weakly erosional, if not net-depositional. Without net-sediment erosion, the work done due to the entrainment of the ambient fluid decelerates the flow (Parker et al., 1986), and ultimately causes sediment deposition. The loss of sediment reduces the driving force and decelerates the flow. This negative feedback loop stalls the flow, precluding self-acceleration as an explanation of autosuspension. For partially confined flows, including channel-levee systems, this is exacerbated by the loss of mass and momentum due to overspill (Dorrell et al., 2014).

The turbulent kinetic energy (TKE) of a flow is often taken as a measure of its capability to suspend sediment (Knapp, 1938; Bagnold et al., 1962; Velikanov et al., 1954). While there may be local regions where the TKE is dissipated by the flow dynamics, over the total length of the flow the TKE generated and dissipated is vastly greater than the amount stored at any one location. Consequently, the net advection of TKE is negligible (Caulfield, 2021), and a necessary condition for autosuspension is that the energy loss of the mean flow integrated over the bed-normal direction, P_{loss} , must exceed the integrated buoyancy production required to maintain the sediment in suspension, B_{gain} , and the integrated viscous dissipation, ϵ . This yields the famed

Knapp-Bagnold (K-B) autosuspension criterion (Knapp, 1938; Bagnold et al., 1962)

$$P_{\text{loss}} > B_{\text{gain}} + \epsilon. \quad (4.1)$$

Bagnold (Bagnold et al., 1962) proposed that energy is lost by the mean flow through the shear production of turbulence, and gained by the sediment through turbulent uplift, and this assumption has been widely adopted by subsequent authors (Parker, 1982; Parker et al., 1986; Pratson et al., 2000; Kostic and Parker, 2006; Hu and Cao, 2009; Pantin and Franklin, 2009; Dorrell et al., 2018a; Amy and Dorrell, 2022). Explicitly, the assumption is that, to leading order,

$$P_{\text{loss}} \simeq P_{\text{shear}} \equiv \int_0^h -\langle u'w' \rangle \frac{\partial \langle u \rangle}{\partial z} dz, \quad \text{and} \quad B_{\text{gain}} \simeq B_{\text{turb}} \equiv \int_0^h gR \langle w'\phi' \rangle dz. \quad (4.2)$$

Here and throughout, ϕ and Φ denote local and depth-averaged volumetric sediment concentration respectively; u and U denote the local and depth-averaged fluid velocity; g denotes gravitational acceleration; $R = \rho_s/\rho - 1$ denotes reduced density; w_s denotes particle settling velocity; h is the extent of the current in the bed normal direction z , i.e. flow depth. Primes and angled brackets denote the Reynolds fluctuations and time-averaged values respectively.

For equilibrium fluvial flows, $\langle w'\phi' \rangle = \phi w_s$ (Dorrell et al., 2011), such that $B_{\text{gain}} \simeq B_f \equiv gR\Phi h w_s$. Moreover, assuming a logarithmic velocity profile, the energy loss in fluvial flow is estimated as $P_{\text{loss}} \simeq P_f \equiv u_*^2 U$, where u_* is the shear velocity (Bagnold et al., 1962; Parker et al., 1986; Pope et al., 2006; Andersen et al., 2007; Amy and Dorrell, 2022). Indeed, equilibrium fluvial flow models for suspended sediment transport, based on the same physical arguments as the K-B criterion (Velikanov et al., 1954; Bagnold, 1966), provide an extensively validated linear proportionality between the concentration of suspended sediment and the dimensionless flow power (Wan and Wang, 1994a; Van Maren et al., 2009; Hu and Cao, 2009; Dorrell et al., 2018a),

$$\Phi \propto \frac{P_f}{N_f} = \frac{u_*^2 U}{gR h w_s}, \quad (4.3)$$

where $N_f = B_f/\Phi$ is the normalised buoyancy production term (the energy required to suspend a unit volume of sediment).

A common class of closures for flows are ‘top-hat’ models, where there is no vertical variation in flow structure. However, via basal shear, these models do capture log-law production energetics to leading order, and the two approaches are equivalent for fluvial systems (Rastogi and Rodi, 1978). Such models have been extended to gravity currents (Ellison and Turner, 1959), including turbidity currents (Parker et al., 1986), and form the basis of contemporary system scale models (Parker et al., 1986; Pantin and Franklin, 2009; Kostic and Parker, 2006; Dorrell et al., 2014). The dimensionless flow power inherent to top-hat models of gravity currents can

be derived from the kinetic energy conservation equation of the mean flow, which is only modified by the presence of entrainment

$$\frac{P_{\text{th}}}{N_{\text{th}}} = \frac{u_*^2 U + \frac{1}{2} e_w U^3}{gRh \left(w_s + \frac{1}{2} e_w U \right)}. \quad (4.4)$$

Here P_{th} is derived from the ‘top-hat’ gravity current model as the energy loss of a mean flow, P_{loss} , and it is assumed that all energy lost is attributed to the shear production of TKE. Moreover, $B_{\text{th}} = \Phi N_{\text{th}} = \Phi gRh \left(w_s + \frac{1}{2} e_w U \right)$ is the buoyancy production in the model, where e_w is the water entrainment rate, calculated as the energy required for the sediment to remain uplifted, B_{gain} , and assumed equal to the turbulent uplift. If there is no entrainment, $P_{\text{th}} = P_{\text{f}}$ and $B_{\text{th}} = B_{\text{f}}$, thus these are the minimal adjustments to fluvial theory to include entrainment. Consequently, for top-hat models to be valid, it is required that the turbulence in gravity currents is essentially the same as in fluvial systems, despite the substantial differences in the flow structure. This implicit assumption is the target of the present analysis.

In this work, the correlation between the total energy loss of a mean flow, P_{loss} , and the energy required to keep sediment in suspension, B_{gain} , is reviewed for near-equilibrium flows, to investigate whether idealised flow power theory is an appropriate predictor for autosuspension. While the total energy loss of a mean flow in gravity currents is unknown, it has previously been assumed (Bagnold et al., 1962; Parker et al., 1986; Pope et al., 2006; Andersen et al., 2007; Amy and Dorrell, 2022) proportional to the log-law total-shear TKE production, P_{f} or the mean-flow energy loss predicted in the top-hat model, P_{th} . This study reviews experimental and direct observation of gravity currents available in the literature, adding new experiments to directly address data gaps. Crucially, data shows that the total energy loss of the mean flow, P_{th} , has a non-linear dependence on the work required to keep sediment in suspension, B_{th} . A review of the energy deficit implies that particulate transport in gravity currents is driven by mixing at scales larger than that of TKE.

4.3 Data reduction

To parameterize autosuspension of gravity currents 70-years of research, including empirical and observational data, were compiled (Fig. 4.1; also see appendix A.1). These data include the first-ever complete observations of natural-scale turbidity currents (Simmons et al., 2020). Also included are all laboratory-scale studies of constant-discharge sediment-laden turbidity currents in straight channels (see Table 2.1 and Chapter 2 for detail methodology of data compilation). These are separated into data that have both velocity and concentration profiles (TYPE I) and data that only have velocity profiles (TYPE II).

Equilibrium sediment transport, implying no net sediment deposition or net erosion and no flow acceleration or deceleration, here defines the requirements for autosuspension in long runout flows.

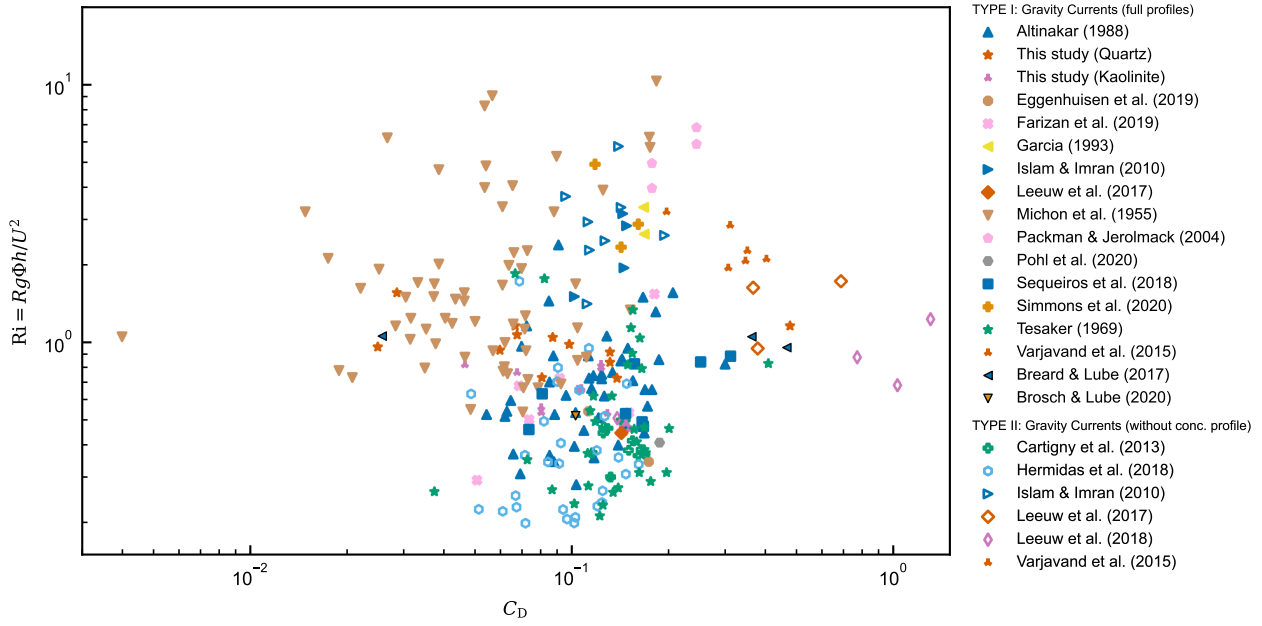


Figure 4.1: Symbols depict field observations and experimental studies of sediment-laden turbidity currents (See Table 2.1 for the detailed reference and settings of experiments of each literature).

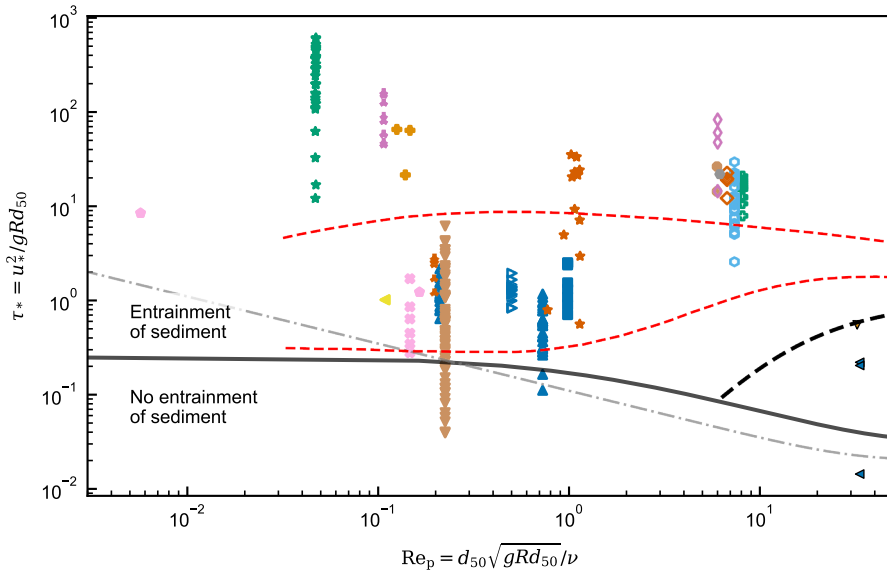


Figure 4.2: Shields diagram. Shields number, τ_* , versus the particle Reynolds number, Re_p , of experimental and observational gravity current data (Fig. 4.1). Here, ν denotes the kinematic fluid viscosity. Solid (Guo, 2020) and dash-dot (Parker et al., 2003) curves depict the criteria of incipient motion. The black dashed line depicts the $w_s = u_*$ criterion for suspended load (Bagnold, 1966). Equilibrium sediment suspension criteria for monodisperse and poorly-sorted suspensions are depicted by the lower and upper red dashed curves respectively (Dorrell et al., 2018a). The symbols and colours are as per Figure 4.1.

When the bed shear stress, described by the dimensionless Shields number, is less than the threshold needed for incipient sediment motion no sediment can be maintained in suspension: the flow is depositional. Therefore, data below Guo’s empirical Shields number criterion for incipient motion (Guo, 2020) are not considered representative of autosuspension and are removed from further analysis. Accordingly, none of the TYPE II data and 19% of TYPE I data (38 out of 203 points) are excluded as belonging to strictly dispositional flow. The remaining turbidity current data lies within the suspended load regime for dilute flows (Bagnold, 1966).

4.4 Turbidity current capacity

	Flow type	Subsets	Figure	Curve fit	R^2
i)	Fluvial flows	Dilute (P_f , linear fit)	4.3a	$1.1 \times 10^{-2} \left(\frac{P_f}{N_f} \right)^{1.0^*}$	0.76
ii)	Gravity currents	Dilute (P_f)	4.3b	$5.6 \times 10^{-3} \left(\frac{P_f}{N_f} \right)^{0.36}$	0.65
iii)		Dilute (P_{th} , linear fit)	-	$1.0 \times 10^{-1} \left(\frac{P_{th}}{N_{th}} \right)^{1.0^*}$	0.34
iv)		Dilute (P_{th})	4.3c	$1.1 \times 10^{-2} \left(\frac{P_{th}}{N_{th}} \right)^{0.49}$	0.72

*The power of correlation is fixed as unity for the linear fits.

Table 4.1: Fitted power-law correlation results and the coefficient of determination, R^2 , of the subsets of data points (Fig. 4.3), using orthogonal distance regression (see Methods).

In equilibrium flows, the total kinetic energy loss of the mean flow, P_{loss} , is assumed to be well approximated by simplified ‘top-hat’ models. The energy loss balances both the work done to keep sediment in suspension and viscous dissipation, Equation (4.1). When TKE production is dominated by the effects of basal drag then the energy available to uplift sediment is given by the log-law of the wall, $P_{loss} \simeq P_f$. Thereby, a linear correlation is implied between the volumetric concentration and dimensionless flow power, P_f/N_f , where $N_f = gRhw_s$. This flow-power balance is tested against compiled near-equilibrium laboratory- and natural-scale gravity currents (Fig. 4.3 and appendix A.2). For comparison, the recent laboratory experiments (Breard and Lube, 2017; Brosch and Lube, 2020) of pyroclastic density currents (PDCs) are also gathered (see Table. 2.1).

From the fluvial flow data (Fig. 4.3a), three regimes of concentration are identified: dilute, transitional, and hyperconcentrated flow. Dilute flows, $\Phi \lesssim 10^{-2}$, are characterised by a linear increase in concentration with dimensionless flow power, P_f/N_f (Fig. 4.3a and Table 4.1 i). With increasing concentration, $10^{-2} \lesssim \Phi \lesssim 10^{-1}$, transitional flows exhibit a change in correlation from increasing to decreasing dimensionless flow power as concentration increases. This transition may be explained by the onset of turbulence dampening and particle-particle interactions dominating the sediment transport mechanics (Van Maren et al., 2009). Hyperconcentrated flows, $\Phi \gtrsim 10^{-1}$, are characterised by a non-linear decrease in dimensionless flow power with increasing concentration. As concentration continues to rise, dimensionless flow power decreases by at least two orders

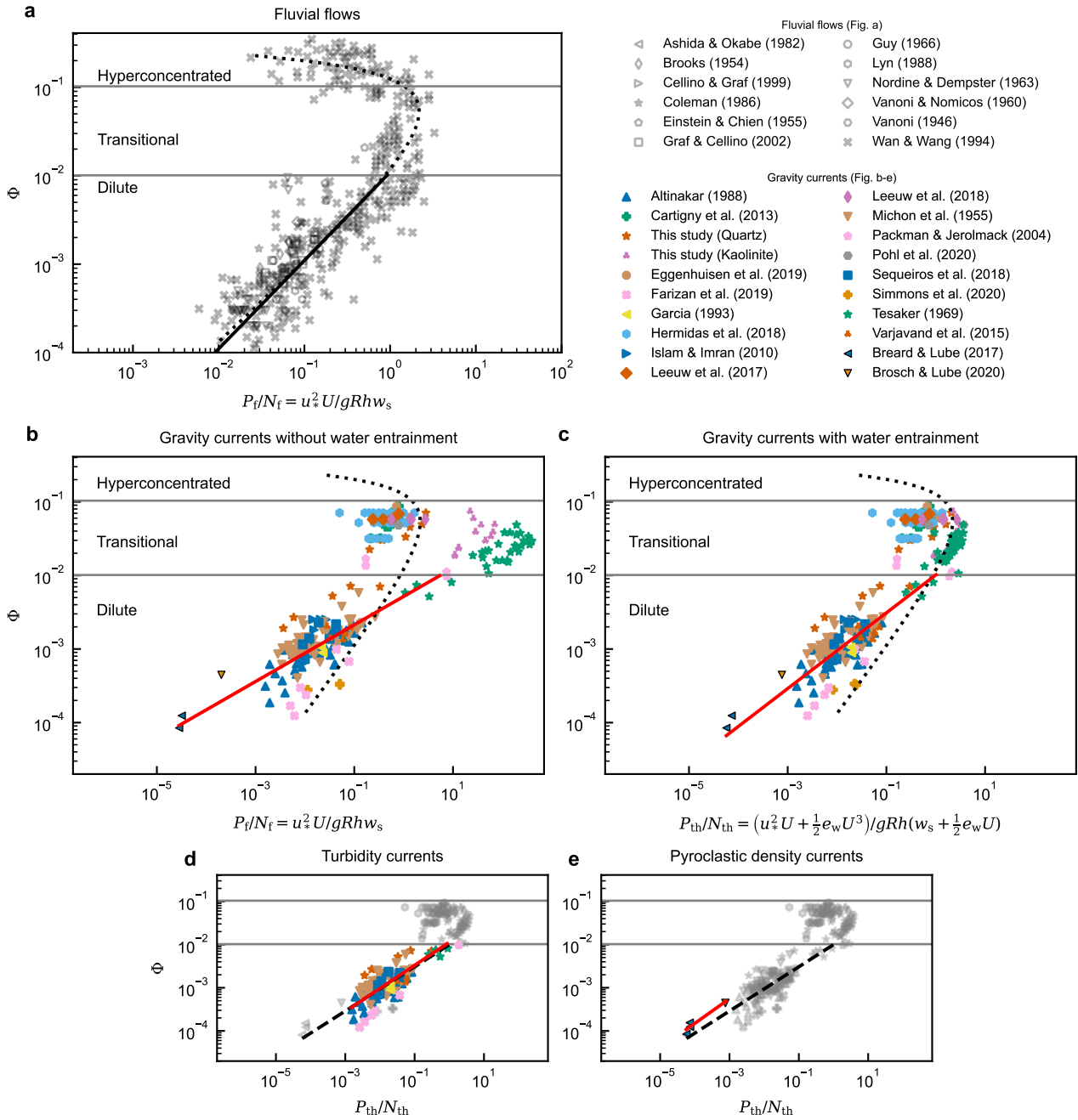


Figure 4.3: Sediment concentration, Φ , versus dimensionless flow power, P_{\sim}/N_{\sim} for: a) fluvial data with the log-law model, P_f/N_f ; b) all gravity current data with the log-law model; c) all gravity current data with the top-hat, entrainment based, model, P_{th}/N_{th} ; d) turbidity current concentration with the top-hat model; and e) pyroclastic density current concentration with the top-hat model. Dilute, transitional and hyperconcentrated regimes are separated by grey solid lines. The parametric correlation of concentration and dimensionless flow power in fluvial systems (fitted using an iterative least squares method, see appendix A.3 for the detailed methodology) is depicted by a black dotted curve. Power-law correlations (Table 4.1) in dilute regimes of each subset are depicted by black (a) and red (b–e) solid lines. Black dashed lines (d–e) represent the power-law correlation of dilute gravity currents (red solid line in Fig. c).

of magnitude.

The gravity current data (Fig. 4.3b–e) also exhibit three similar regimes of concentration; the threshold concentrations between regimes are approximately equal to those of fluvial systems. However, the correlation of concentration with dimensionless flow power is remarkably different. The dimensionless flow power, based on both the log-law energy production model P_f (Fig. 4.3b), and the top-hat model, P_{th} (Fig. 4.3c), have a strongly non-linear correlation with sediment concentration, Φ . The fit of both models is good, but shows an improvement when using the top-hat-based correlation, see Table 4.1 ii) and iv). However, a linear model provides a poor best fit in comparison, contrast Table 4.1 iii) and iv). Moreover, the turbidity current data (Fig. 4.3d) show almost identical non-linear dependency to the pyroclastic density current data (Fig. 4.3e), suggesting that the non-linear dependency is universal to all types of gravity currents.

Critically, the non-linear relationship results in dilute gravity currents being able to maintain a higher suspended sediment concentration versus fluvial flows of an equivalent dimensionless flow power (Fig. 4.3c). Previously unrecognised, this has the potential to explain autosuspension in long-runout systems. The correlation suggests that when a dilute gravity current accelerates, it is not as erosive as a fluvial system, and similarly, when a gravity current decelerates, deposition is more limited. This implies that the suspended-load of gravity currents is significantly underestimated, i.e. providing more motive force on shallower slopes, and is less sensitive to changes in flow power than has previously been assumed based on the use of fluvial analogues (Parker, 1982; Parker et al., 1986; Pratson et al., 2000; Kostic and Parker, 2006; Hu and Cao, 2009; Pantin and Franklin, 2009; Dorrell et al., 2018a; Amy and Dorrell, 2022). Since the limited super-dilute pyroclastic density current dataset also exhibits a similar non-linear trend to turbidity currents (Fig. 4.3e), it is likely that the fluvial-based or top-hat gravity current models are a poor approximation not only for turbidity currents but also for particle-driven gravity currents in general.

It is noted that a limited proportion of the data (see Table 2.1) use cohesive material (kaolinite). It is plausible that flocculation of cohesive particles may occur, increasing particle settling velocity, and decreasing dimensionless flow power. However, the growth of flocs is limited by shear rates and their size decreases as the flow increases (Jarvis et al., 2005). Therefore, in strongly sheared gravity current experiments, the development of flocs and resulting underestimation of settling velocity is expected to be limited. Further, it would not change the observation that the relationship between concentration and dimensionless flow power is non-linear, see Fig. 4.3b–e, Table 4.1 ii) and iv). Moreover, whilst the increase in P_{th}/N_{th} of gravity currents (Fig. 4.3c) follows the trend of fluvial data in the transitional regime it is based on an empirical water entrainment function, e_w . The empirical water entrainment function has been developed for dilute currents, thus it is expected the values of P_{th}/N_{th} in the transitional regime have some inherent error. However, this does not impact the primary findings of the non-linear correlation in the dilute regime.

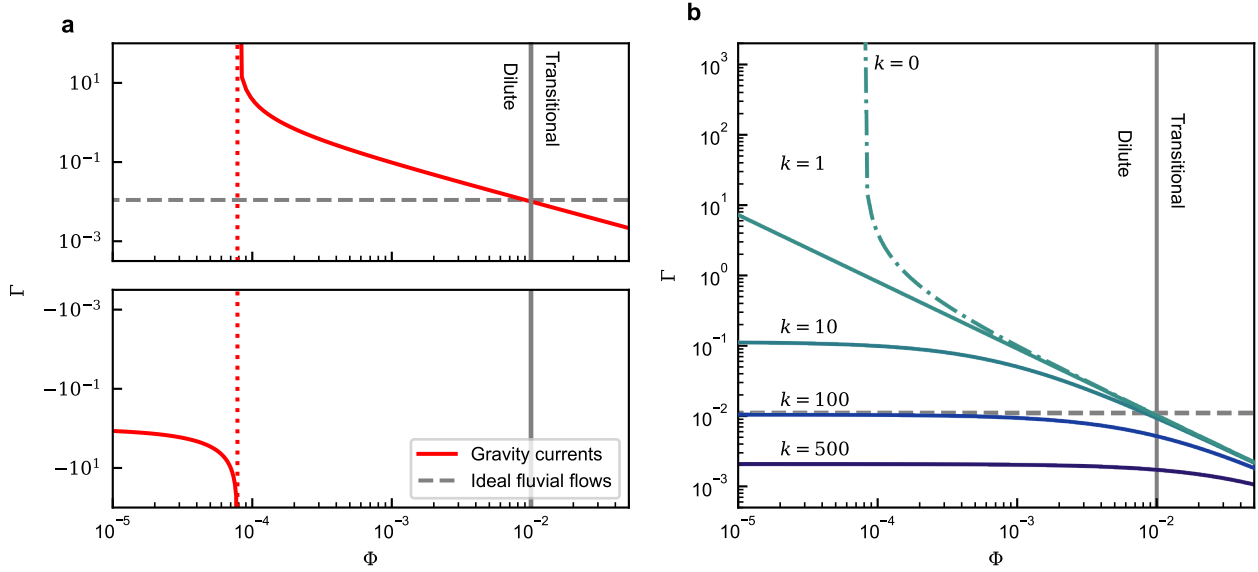


Figure 4.4: Predicted turbulent flux coefficient. The turbulent flux coefficient, Γ , as a function of concentration, Φ . a) Computed Γ , assuming $P = P_{th}$ and $S = 0$. The red dotted line indicates the vertical asymptote for the gravity current curve (red solid). b) Computed Γ , assuming $P = P_{th} + S$, where the additional energy is parameterised in terms of the buoyancy production $S = kB_{th}$. The dotted-dashed curve has $k < 1$, for which Γ diverges to infinity for some values of Φ . Throughout, the Dilute/Transitional regime threshold and the ideal fluvial flow curve is depicted by gray solid and gray dashed lines respectively.

4.5 Discussion

4.5.1 Energy balance of TKE

The fundamental differences between fluvial flows and dilute gravity currents (turbidity currents and pyroclastic density currents) documented above raise the following questions: Do the top-hat mean-flow energy loss, buoyancy production and dissipation balance? What are the implications for autosuspension models?

In top-hat gravity current models (Parker et al., 1986), P_{th} is the energy released by the mean-flow and available for the suspension of particles, which requires energy B_{th} . Additionally, the flow experiences viscous dissipation of energy ϵ . However, as will be shown, there is insufficient energy in this model to suspend the sediment. For the present analysis, the missing energy will be denoted by S , so that the energy balance is

$$P = P_{th} + S \simeq B_{th} + \epsilon_{th} = \left(1 + \frac{1}{\Gamma}\right) B_{th}, \quad (4.5)$$

where the total turbulent flux coefficient, $\Gamma = B_{th}/\epsilon_{th}$, denotes the ratio of top-hat buoyancy production, B_{th} , to dissipation, ϵ_{th} . Using Equation (4.5) and the curve fitting results, see Table 4.1 i) and iv), Γ can be

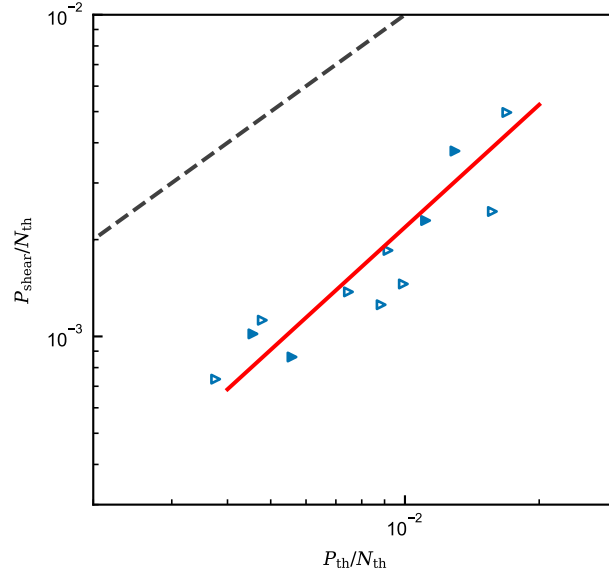


Figure 4.5: Power-law correlation (Eq. 4.7, Table 4.1) is depicted by a red solid line. Gray dashed line indicates the line of equality ($y = x$). Data are calculated from the empirical measurements reported by Islam and Imran (Islam and Imran, 2010). Symbols as per Figure 4.1.

expressed as:

$$\Gamma = \left(\frac{P_{\sim}}{B_{\sim}} + \frac{S}{B_{\sim}} - 1 \right)^{-1} \simeq \begin{cases} 1.1 \times 10^{-2} & : \text{Fluvial flows } (S = 0, \quad B_{\sim} = B_f, \quad P_{\sim} = P_f) \\ (9 \times 10^3 \Phi^{1.0} + k - 1)^{-1} & : \text{Gravity currents } (B_{\sim} = B_{th}, \quad P_{\sim} = P_{th}) \end{cases} \quad (4.6)$$

where $k = S/B_{th}$ denotes the ratio of missing energy to the top-hat buoyancy production, B_{th} . The fluvial data (Fig. 4.3a) and Equation (4.6) implies that, for fluvial flows, Γ is constant. Only $\sim 1.1\%$ of the energy production is consumed by buoyancy production, while the rest is consumed by dissipation. For gravity currents in contrast Γ depends on Φ (Fig. 4.4a). Assuming that the extra energy source, $S = 0$ and thus $k = 0$, Γ grows with decreasing flow concentration, diverging at $\Phi = 1.4 \times 10^{-4}$, before becoming negative. However, ϵ_{\sim} and B_{\sim} are strictly positive, thus Γ must also always be positive.

Clearly, $S = 0$ is a poor approximation. Equation (4.6) implies that the energy balance of near-equilibrium gravity currents can only be satisfied with a non-zero energy source/sink, S . To satisfy the minimum requirement, $\Gamma > 0$ for all Φ , the additional energy source term is constrained by $k > 1$. A hypothesized upper limit for the turbulent flux coefficient (Osborn, 1980; Caulfield, 2021) is $\Gamma \leq 0.2$, this is broken for $\Phi < 6 \times 10^{-4}$. To satisfy this limit a value of $k \sim 10$ would be required. However, it is unlikely that turbidity currents reach this maximum mixing efficiency, and a larger value of k is likely required. Previously, it has been assumed that the amount of TKE consumed by buoyancy production in gravity currents is similar to that in fluvial flows (Pantin, 1979). To satisfy $\Gamma \sim 10^{-2}$, Equation (4.6), then $k \sim 100$ (Fig. 4.4b). Thus, K-B type criteria

and top-hat gravity current models (Bagnold et al., 1962; Parker, 1982; Parker et al., 1986; Pratson et al., 2000; Kostic and Parker, 2006; Hu and Cao, 2009; Pantin and Franklin, 2009; Dorrell et al., 2018a; Amy and Dorrell, 2022) fail to explain the energy balance of gravity currents.

Autosuspension mechanisms The TKE balance of turbidity currents required for autosuspension cannot be explained without additional TKE production (i.e. $S > 0$ in Eq. 4.5; Fig. 4.4). If TKE production mechanisms were the same for turbidity currents and open-channel flows, then greater open-channel flow suspended-loads would be observed (cf. Fig. 4.3). Therefore, to explain the TKE required for autosuspension in turbidity currents, mechanisms for additional TKE production must disproportionately affect turbidity currents compared to open-channel flows. In the self-acceleration model (Parker et al., 1986), it is implicitly assumed that the TKE is generated by entrainment of sediment from the bed into suspension, which consequently increase the shear rate of the flow, generating more turbulence. However, as highlighted, this mechanism does not work over shallow slopes or the distal region of submarine channel systems. Whilst the shortfall in the energy budget is known, $S \sim 100B$ (Fig. 4.4), the mechanism to produce TKE is unknown. Potential candidates of additional TKE production are classified into two distinct types: (i) self-induced TKE production, i.e. induced by the internal flow structure; and (ii) environment-induced TKE production, i.e. by external forcing. Here, a variety of such mechanisms are discussed.

Firstly, self-induced TKE production is considered. The near-equilibrium assumption in Equation (4.5) means that the material derivative of the local TKE is negligible. Although the data selection of near-equilibrium flows was conducted carefully, there is no reliable direct measurement to support a zero material derivative of TKE in either natural-scale events or laboratory-scale experiments. A non-zero material derivative results in a local accumulation of TKE and is inherent to all transient flows. Further, unlike open channel flows, the dynamics of turbidity currents are controlled by the flow density, relative to ambient water. Recent research has demonstrated (Dorrell et al., 2019; Marshall et al., 2021b) that density stratification results in internal gravity waves, causing mixing at flow scale. Flow scale mixing, unlike local turbulent mixing which is well approximated as diffusion and characterised by TKE, results in the non-local redistribution of momentum and scalar transport fields (Dorrell et al., 2019). Such flow scale mixing, and associated sediment suspension, would not scale with shear production of TKE.

Secondly, potential external forcings which may generate/enhance the TKE production are considered. These include secondary flow circulation at channel bends (Abad et al., 2011; Dorrell et al., 2013; Azpiroz-Zabala et al., 2017a), Coriolis force effects (Dorrell et al., 2013; Davarpanah Jazi et al., 2020), continuous bottom currents (Miramontes et al., 2020), and return flows (Sumner et al., 2014; Toniolo et al., 2007; Patacci et al., 2015). Due to the density difference between turbidity currents and ambient fluid, the superelevation of flow around sinuous channel bends (a consequence of the balance of centrifugal, hydrostatic pressure, and shear forces) is much larger in turbidity currents than in open-channel flows (Dorrell et al., 2013). This means that

the magnitude, and therefore the impact, of secondary flow on mixing and suspending particulate materials is enhanced in sinuous submarine channel systems. Although enhanced mixing by secondary flow may account for additional TKE production in sinuous channels, it does not explain long runout in relatively straight channels or in unconfined systems. However, turbidity current systems can be so large that Coriolis forces can enable secondary flow formation and enhance its magnitude in both straight and sinuous channels (Davaranah Jazi et al., 2020). In marine environments, continuous, relatively low-density, cross-slope directed bottom currents, may interact with downslope propagating turbidity currents (Miramontes et al., 2020). Locally, this may introduce additional shear and mixing in the upper part of a turbidity current. However, this local interaction cannot explain the additional TKE production required across the entirety of turbidity current runout lengths. Return flows generate additional shear at the upper boundary of turbidity currents, potentially enhancing the TKE production in both natural-scale and laboratory-scale flows. This mechanism is likely only important in shallow water environments, including scaled-laboratory experiments, reservoirs (Kostaschuk et al., 2018a), fjords (Clare et al., 2016), and in exchange flows (Marmoush et al., 1984); additionally it may be important in tidally-dominated (Hage et al., 2019) or ponded deep-water environments systems (Patacci et al., 2015).

For long runout flows, an additional TKE source, S , is needed to enable the suspension of particulate material and to balance energy sinks through buoyancy production, B , and dissipation, ϵ : as a minimum $S = B$. If $B \ll \epsilon$, as in open channel flows, the additional energy source is much larger, $S \sim 100B$. Similar non-linear relationships between suspended sediment concentration and dimensionless flow power exist for near equilibrium natural-scale and laboratory-scale turbidity currents (Fig. 4.3, Table 4.1). Most likely this suggests that processes resulting in production of additional TKE are similar between laboratory scale experiments and natural-scale flows. Further research, providing extended (volumetric) spatial and temporal flow velocity and density data, is required to fully understand energy balance models, Eq. 4.5, of turbulent gravity currents. However, high Reynolds numbers gravity current dynamics are prohibitively expensive to study computationally, especially where the ratio of momentum to mass diffusion is large (as in the particulate laden turbidity currents (Marshall et al., 2021a)). Thus, there is a continued need to develop measurement methodology for, and take measurements from, natural-scale and laboratory-scale empirical data. Where it is seen here that laboratory-scale turbidity currents provide a justifiable analogue to natural scale flows.

The energy balance of gravity currents required for autosuspension cannot be explained without an additional energy source, i.e. $S > 0$ in Equation (4.5) and Figure 4.4. Crucially, if the energetic mechanisms were the same for gravity currents and fluvial flows, then gravity currents would be substantially more dilute, cf. Figure 4.3b–e. Therefore, to explain autosuspension, mechanisms for particle uplift must be present that are absent, or of negligible importance, in fluvial flows. It is plausible that the shear production, Equation (4.2), predicted by top-hat models is less than the actual production in real flows, and this possibility is addressed

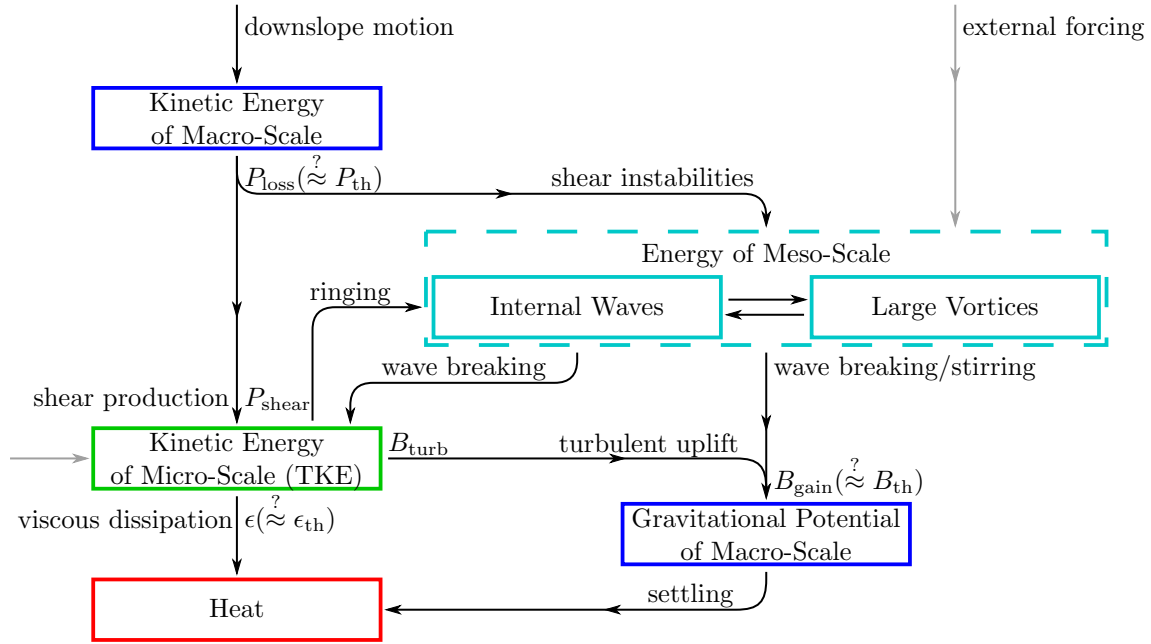


Figure 4.6: Proposed internal energetics of gravity currents. The internal stores of energy are shown by boxes, and the transfer of energy by black arrows: the energy lost at the tail of each arrow is equal to the energy gained at its tip. Grey arrows represent the input of energy from external forcing (energy could also be lost to these forces).

first. The shear production is calculated from empirical data (Islam and Imran, 2010), and plotted in Figure 4.5. However, the limited data available suggest that the directly computed shear production term, P_{shear} , is substantially lower than the ‘top-hat’ energy loss term, P_{th} ,

$$\frac{P_{\text{shear}}}{N_{\text{th}}} = 0.74 \left(\frac{P_{\text{th}}}{N_{\text{th}}} \right)^{1.27} \quad (R^2 = 0.92). \quad (4.7)$$

Consequently, if shear production represents all available energy, the size of the missing energy source is substantially larger. To understand the origin of these shortcomings, the energetic dynamics within a gravity current will be broken down and explored conceptually; a schematic of these dynamics is provided in Figure 4.6. The dynamics of the flow occur on three distinct length-scales: the macro-scale flow on the scale of the length of the current, which is the scale of the top-hat model; the meso-scale flow on the scale of the depth of the current, which is able to support internal waves (Lefauve et al., 2018; Kostaschuk et al., 2018b; Dorrell et al., 2019; Marshall et al., 2021b; Salinas et al., 2021) and the largest vortices (Peakall and Sumner, 2015; Dorrell et al., 2018b); and the micro-scale flow, which supports the turbulent vortices (TKE). In Figure 4.6 the gravitational potential of the sediment is split between the macro-scale contribution, the vertical distribution of the sediment is (on average) slowly varying, and the meso-scale contribution due to the rise and fall of internal waves, for example.

In simplified models of gravity currents, such as top-hat models, it is the macro-scale kinetic energy that is captured, and on shallow slopes it is this macro-scale flow which is energised by the down-slope component of

gravity. As the longitudinal flow accelerates/decelerates, the flow thins/thickens, exchanging the macro-scale energy between the kinetic and gravitational potential (not included in Figure 4.6). This kinetic energy is lost at a rate P_{loss} . Large scale internal shear can generate flow instabilities, such as the Kelvin-Helmholtz or Holmboe instabilities, resulting in internal waves (Lefauve et al., 2018; Kostaschuk et al., 2018b; Dorrell et al., 2019; Marshall et al., 2021b; Salinas et al., 2021), which can be seeded at flow initiation (Best et al., 2005; Kostaschuk et al., 2018b). Alternatively, the mean flow energy may be used to stimulate large vortices, for example, secondary flow circulation (Straub et al., 2011; Peakall and Sumner, 2015; Dorrell et al., 2018b). The internal shear generated by the macro-scale flow also directly energises turbulent vortices through shear production. The meso-scale flow structures are able to generate gravitational potential directly, by stirring the flow (Straub et al., 2011), and through wave breaking which also generates TKE. The turbulence is, in turn, able to ‘ring’ density interfaces generating internal waves (Dorrell et al., 2019; Marshall et al., 2021b; Lloyd et al., 2022), or uplift particles through the diffusive effect of vortices. The TKE and gravitational potential are slowly lost to heat through viscous effects.

In addition to these internal processes, in many currents external forcing directly drives the flow, also depicted in Figure 4.6. Examples include the Coriolis force (Dorrell et al., 2013; Davarpanah Jazi et al., 2020), bottom currents (Miramontes et al., 2020), tidal forcing, return flows (Sumner et al., 2014; Toniolo et al., 2007; Patacci et al., 2015), and thermal effects in pyroclastic density currents (Andrews and Manga, 2012; Shimizu et al., 2019). However, these effects are not equally featured in the flows in our dataset, and are expected to result in quite different internal dynamics. Thus, the trend in Figure 4.3(c) and the derived missing energy cannot be explained by these external forces, and instead they generate the scatter about the trend.

It is worth pausing to reconsider what the top-hat model represents. The production, P_{th} , is derived as approximating the energy loss from the mean flow P_{loss} , and B_{th} as approximating the energy gain by the sediment B_{gain} . However, it is clear from Figure 4.3 and the implied missing energy that at least one of these approximations is inaccurate, most likely both. Through Figure 4.5 we see that P_{th} does not approximate the shear production. Consequently, the top-hat production does not represent *any* of the indicated production terms on Figure 4.6.

Therefore, a likely explanation (indeed the only one that remains) is that the top-hat model is wrong: the dynamics of the flow are not well represented if the information about the vertical variation of density and velocity are neglected. The origins of the top-hat model are in fluvial systems, where the log-law of the wall holds across a large portion of the flow. In this context, it is possible to calculate the shear production P_{shear} exactly (Bagnold et al., 1962; Parker et al., 1986; Pope et al., 2006; Andersen et al., 2007; Amy and Dorrell, 2022), and the result is here denoted by $P_{\text{f}} = u_*^2 U$. A consequence of the driving density being uniform over the depth of the flow is that the top-hat model, in fluvial systems, gives exactly the same energy loss from the kinetic energy of the mean flow (Rastogi and Rodi, 1978), which enables the top-hat models to

accurately capture the flow energetics (up to internal waves and large-scale vortices). There is no reason to believe that the energetics of gravity currents are similarly well represented by top-hat models because the driving density varies over the depth. Experiments have shown that the shape factors resulting from the depth variation of density and velocity in laboratory currents differ from top-hat models by up to 40% (Islam and Imran, 2010). In other settings, a strong density interface is generated around the maximum velocity, which is maintained through locally negative turbulent production driven by radiation stresses (Dorrell et al., 2019; Marshall et al., 2021b; Salinas et al., 2021) analogous to atmospheric jets (Dritschel and Scott, 2011). In either case, the loss of energy from the mean flow will be substantially different to the top-hat model. It is possible that $P_{\text{loss}} > P_{\text{th}}$, a large portion of this energy loss would need to go into the meso-scale structures because the mean-flow energy loss would be substantially larger than the shear production. In addition, the buoyancy production required by top-hat models is an upper bound, the sediment is assumed to be as high up as possible, and including the vertical variation of density would reduce this requirement so that $B_{\text{gain}} < B_{\text{th}}$. The reduction in the expected amount of energy passing through the TKE budget reduces the expected amount of energy loss to dissipation, meaning that a larger portion of the energy loss by the mean flow goes into particle uplift.

While investigations into the vertical structure of gravity currents have been conducted (Parker et al., 1987; Islam and Imran, 2010), the implications for the energetics remains an open problem. The momentum balance and sediment transport models may also need to be updated. Here, the vertical structure has already been incorporated in models, (Parker et al., 1987), though it is not clear if this is sufficient to capture the effective force generated during the production of meso-scale structures, and the resulting dissipation-free uplift of particles.

The explanations can be summarised by writing

$$S = (P_{\text{loss}} - P_{\text{th}}) + (B_{\text{th}} - B_{\text{gain}}) + (\epsilon_{\text{th}} - \epsilon), \quad (4.8)$$

which summarises the effective extra energy available in a real current compared to the modelled current. Here, $P_{\text{loss}} > P_{\text{th}}$ due to the additional macro-scale kinetic energy lost to meso-scale internal waves and large vortices. This invalidates the long-standing Knapp-Bagnold hypothesis that all the energy lost by the macro-scale flow drives turbulence through shear production, and that turbulence is the only means of particle uplift. Note that the additional energy loss does not necessarily imply an energy depletion, real gravity currents may have a larger macro-scale kinetic energy budget than top-hat models due to the vertical variation of velocity. Additionally, $B_{\text{gain}} < B_{\text{th}}$, due to the lowering of the centre of mass when the vertical structure of density is captured (Dorrell et al., 2014), which reduces the gravitational potential that must be maintained. Finally, $\epsilon < \epsilon_{\text{th}}$ because the TKE budget is lower, a large portion of the energy instead stored in the meso-scale structures. Thus, the presence of meso-scale structures increases the energetic efficiency of

autosuspension.

To address the apparent missing energy in the models, future work must move beyond the approximations appropriate for open-channel and fluvial systems, and capture the complexity present in the structure and internal dynamics of gravity currents. The resulting additional capacity to support particles, that is the increased autosuspension capability, has numerous implications for environmental currents. The long run-out of turbidity currents has been a long standing enigma, and the results presented here show that the current is able to maintain a much higher sediment load than previously believed. This gives significantly more driving force on shallow slopes, and a much slower deposition rate of particles, which facilitates the transport of sediment to the distal parts of submarine systems. More broadly, particle-driven gravity currents are known to be highly destructive, with flows capable of causing immense damage. For the accurate prediction of gravity currents, this work shows that research focus is required on the dynamics of meso-scale energy exchange and balances, to be captured by the next generation of reduced order models.

Chapter 5

Conclusion

5.1 Achievements

5.1.1 Flume experiments and data compilation

In this thesis, I have made substantive advances to our understanding of turbidity currents by undertaking the first-ever comprehensive compilation of 70 years of laboratory-scale turbidity current data (see Table 2.1 in Chapter 2). This compilation includes a diverse range of experimental conditions, as well as the direct observation of natural-scale turbidity currents from Simmons et al. (2020). By consolidating and analysing this extensive dataset, I have gained valuable insights into the complex dynamics and behaviours of turbidity currents under various settings.

Moreover, to enhance the scope and depth of the investigations, I conducted a series of newly designed large-scale flume experiments. These experiments were designed to provide high-resolution vertical flow profile data, offering details on the internal structure and characteristics of turbidity currents. The incorporation of advanced measurement techniques and instrumentation facilitated the acquisition of precise and reliable data, enabling a deeper understanding of the near-equilibrium state of turbidity currents.

The synergy between the historical laboratory-scale data compilation and the contemporary large-scale flume experiments has allowed me to draw robust conclusions about the key factors influencing turbidity current dynamics. This combined approach has significantly advanced our understanding of gravity currents, contributing to the broader body of knowledge in sediment transport dynamics.

In terms of data compilation, I believe my study stands out for its innovative approaches, particularly in the estimation of the full turbidity current profile from raw measurements. Two key methodologies played a pivotal role in this process:

- **Original Interpolation and Extrapolation Methods:** To derive a comprehensive profile from the experimental measurements, I developed and applied original interpolation and extrapolation methods (section 2.2.2). These techniques not only facilitated the integration of disparate data but also allowed me to construct a continuous and detailed representation of the turbidity current's vertical flow structure.
- **Redefined Flow Height Criteria:** Unlike traditional approaches that rely on the Ellison and Turner's height scale, this study rigorously justifies a different criterion for the flow height. In the methodology (section 2.2.2), the flow height is precisely determined as the level at which both velocity and concentration reach zero (or at the same level of the ambient). By aligning the flow height with the cessation of flow properties, this approach captures the true boundary of the current, offering a more insightful understanding of its behaviour.

These innovative data compilation methods enhance the reliability and accuracy of the obtained profiles, elevating the quality of the findings and the broader implications for sediment transport research summarised below.

5.1.2 Time-averaged vertical flow concentration profile of turbidity currents

Using the compiled dataset, I developed an empirical model which predicts the time-averaged concentration profile of turbidity currents (Chapter 3). The key findings and developments in this domain are encapsulated in the following points:

- **High-Accuracy Empirical Model Development:** A major milestone in Chapter 3 involves the development of a high-accuracy empirical model designed to predict the concentration profile of both laboratory-scale and natural-scale turbidity currents. By incorporating dimensionless parameters, notably the Froude number (Fr_d) and the Rouse number β , the developed model successfully approximates the intricate balances between the diffusion induced by shear at the interfaces and particle settling. The developed model exhibited an excellent generalisation performance both in laboratory-scale and natural-scale test data.
- **Significance of C_D and Re as Parameters:** An important revelation from my model selection is the recognition of the critical role played by the drag coefficient (C_D) and the Reynolds number Re in describing the flow concentration profiles. Especially, it is shown that incorporating Re greatly increases the performance in prediction of natural-scale turbidity currents.
- **Challenges in Natural-Scale Predictions:** While my model exhibits high accuracy in predicting both in laboratory-scale and natural-scale turbidity currents, its current limitation lies in predicting the profile of natural-scale data without the aid of Reynolds number (Re). The model without Re cannot predict the highly stratified natural-scale test data, despite the high accuracy in the prediction

of laboratory-scale test data. Considering the order of Re in the data ($\gtrsim 10^4$), the large scale dynamics are expected to be independent of the Reynolds number, there being a separation between the mean flow scale and the Kolmogorov scale. Thus, it is more plausible that differences in Re are not directly related to flow stratification. This intriguing result implies the existence of another factor, yet to be identified, that characterises the differences between laboratory-scale and natural-scale flows.

These developments mark a significant leap forward in our ability to model and understand the complex dynamics of turbidity currents, opening avenues for future research and refinement of flow structure models. The better prediction of flow structures are fundamental to understand the flow dynamics of turbidity currents traversing through the sinuous submarine-channel networks and the evolution of resultant sedimentary architectures.

5.1.3 Time-averaged vertical flow velocity profile of turbidity currents

In the Chapter 3, this study successfully formulated the strong correlation between the flow structures of velocity and concentration of pseudo-steady turbidity currents (section 3.4) and developed the empirical model of velocity profile prediction. The key findings and advancements are encapsulated in the following points:

- **Correlation between Inflection Point and Velocity Characteristics:** A significant discovery in my research is the identification of a robust linear correlation between the height of the maximum in the gradient of the flow concentration profile (inflection height) and the velocity maximum. This correlation underscores the intricate relationship between the concentration dynamics and velocity characteristics, providing a valuable link that enhances our ability to predict and understand turbidity current behaviour.
- **Constant Correlation Across Entire Profiles:** Building upon the initial correlation discovery, this study further revealed a strong correlation between the entire velocity (ξ_u) and concentration profiles (ξ_ϕ). Remarkably, this correlation remains independent of other flow parameters, suggesting a universal relationship governing the interplay of velocity and concentration throughout the vertical extent of turbidity currents.
- **Accuracy of Correlation-Based Model:** Utilising the identified correlations, I formulated a model that accurately predicts the velocity profile of test data. This model shows a very good performance with the both laboratory-scale and natural-scale turbidity currents test data, and also show an excellent agreement with the linear correlation I found between the height of velocity maximum and inflection point.
- **Novel Flow Dynamics for Material-Transport Efficiency:** The integration of vertical concentra-

tion and velocity models developed in this study unravels novel flow dynamics, particularly in scenarios characterised by low Froude numbers (Fr_d), such as the decelerated flow in a distal seabed with a shallow slope. In the depth-integrated conservation equations, the weighting terms of material transport $W_{u\phi}$ and momentum transport W_{u^2} increase as Fr_d decreases, implying that the efficiency of material transport will be enhanced in the low- Fr_d state. Also, the weighting term of the pressure term W_P decreases as Fr_d decreases. Contrary to the previous models, this decreasing W_P will channelise the flow and suppress the loss of suspended sediment due to overspilling as Fr_d decreases.

These findings contribute to a deeper understanding of the material-transport dynamics of turbidity currents.

5.1.4 The energetics of turbidity currents

The investigation into the energetics of turbidity currents has unveiled a significant underestimation of sediment-load capacity of turbidity currents, challenging the applicability of traditional fluvial energetics theory. Key insights and revelations from this study are summarised in the following points:

- Deviation from Traditional Energetics Theory:** This analysis demonstrates that the energetics of turbidity currents defy description by traditional fluvial energetics based on the ‘top-hat’ model, showing the significant underestimation of the sediment-load capacity of turbidity currents (Fig. 4.3). Not only turbidity currents but also the limited data of pyroclastic density currents (PDCs) exhibit the similar energy dynamics that significantly deviate from the established principles governing fluvial flows. The direct implication of the results is that not only turbidity currents but also the sediment-laden gravity currents are fundamentally different from the fluvial flows in their energetics. This result highlights the importance of better understanding of gravity currents’ energetics, which may explain the long-standing enigma of long-runout feature of gravity currents.
- Unexplained Energy Shortage:** The observed energy shortage in turbidity currents cannot be fully explained by conventional theories which only describe the energetics between energy loss of the mean flow and the micro-scale shear production of TKE. The direct implication of the results is that conventional micro-scale shear production of turbulent kinetic energy (P_{th}) does not represent the energetics of gravity currents. This discrepancy underscores the need for a more comprehensive understanding of the various contributors to the mixing mechanism in turbidity currents.
- Energy Transfer to Meso-Scale Structures:** This analysis suggests that a substantial amount of energy loss in the mean flow is transferred to the formation of meso-scale flow structures such as internal waves and large vorticities by shear instabilities. These meso-scale features contribute to the mixing of the turbidity current, adding a layer of complexity to the energetics of these sediment-laden flows.

This work has been published in *Nature Communications* (Fukuda et al., 2023)

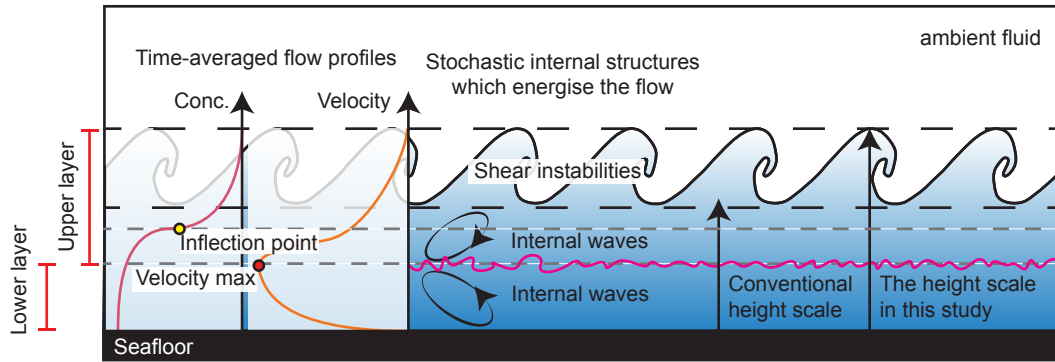


Figure 5.1: Schematic diagram of internal flow structures of turbidity currents. The developed vertical structure models in Chapter 3 demonstrated the correlation between concentration and velocity profiles (on the left side of the figure). Also, Chapter 4 highlighted the importance of the meso-scale flow structures such as the shear instabilities in material transport capacity of turbidity currents (illustration in the middle of the figure). All of those findings depend on the new flow height definition contrary to the traditional assumption of Ellison and Turner’s flow height (right side of the figure).

5.2 Implication of the results

The Literature Review (section 1.6) posed the following research questions.

- What controls the vertical structure of turbidity currents and how does this affect flow dynamics?
- Is the energetics of turbidity currents similar to the rivers?

The careful analysis in this thesis provides insight into these key questions. The analysis of vertical structure of the flow (Chapter 3) indicates that the velocity and concentration profiles are strongly correlated and play a vital role in the material-transport efficiency of turbidity currents. Further, the validation of the conventional fluvial energetics theory in Chapter 4 reveals that the energetics of gravity currents are fundamentally different from the fluvial open-channel flows. Here, based on these results obtained in this thesis, the long-runout and material-transport mechanics of turbidity currents are discussed.

5.2.1 Long-runout of turbidity currents

In a shallow slope submarine channel on the distal seafloor, the streamwise component of gravitational forcing is very small. Thus, the flow is speculated to be depositional or, at best, near-equilibrium (Parker et al., 1986; Tilston et al., 2015). Subsequently, flow deceleration thickens and dilutes the flow in the conventional ‘top-hat’ model with uniform velocity and concentration profiles. Consequently, the flow becomes unstable as the height of the centre of mass increases. In a partially confined submarine-channel, this process makes it almost impossible for the flow to traverse a long distance along the sinuous channel due to the significant amount of suspended-material loss in overspilling. In the real world, the flow is well confined in the channel and traverse more than 1000 km without dissipation, and the mechanics which enable this remains as an enigma. This knowledge gap necessitates the better understanding of the dynamics of vertical flow structure

of near-equilibrium turbidity currents.

Chapter 3 focuses on the time-averaged internal structure of the flow, and unraveled the internal flow mechanics which maximise the material-transport efficiency of flows in a low- Fr_d state (Fig. 3.20 in Chapter 3). These mechanics are represented by the strong correlation between concentration and velocity profiles (Fig. 3.10). Historically, the height of the velocity maximum has been speculated to coincide with the inflection point of flow concentration (Stacey and Bowen, 1988a). Although this trend has been recognised as a rule of thumb, the detailed correlation between these two heights has been not quantitatively investigated. The linear correlation between $h_{\langle u \rangle_{\max}}$ and $h_{\langle u \rangle_{\max}} - h_{\langle \phi \rangle}$ means that the velocity maximum locates in the lower highly-concentrated layer of the flow, increasing the material-transport efficiency $W_{u\phi}$. This is the key factor for the flow to maintain the high material-transport efficiency even in the low- Fr_d state (see Fig. 3.9, 3.13 and 3.20). Further, comparing with the previous model (Abad et al., 2011), the flow shows more stratification and channelisation (more mass concentrates in the centre of the channel). Stratification will significantly reduce the loss of suspended material due to the overspilling compared with the conventional models. On top of that, in Chapter 4, we demonstrated that the conventional Knapp-Bagnold autosuspension criteria significantly underestimate the sediment-load capacity of turbidity currents (Fig. 4.3). For the dilute turbidity currents ($\Phi \sim 10^{-3}$), a flow can maintain the same amount of suspended sediment with ~ 0.01 times smaller dimensionless flow power P_{th}/N_{th} . An additional energy source is required to explain this significant discrepancy between the conventional energetics model and the observations. The direct implication of this shortfall in energy is that the meso-scale internal waves and large vortices generated by the shear instabilities play a vital role in particle uplift.

5.2.2 Material transport mechanics of turbidity currents

As discussed above, the novel flow dynamics in the time-averaged flow structures elaborated in Chapter 3 enables the stable and efficient material transport of turbidity currents. This is presumably one of the key factors enabling the long-runout of turbidity currents. Further, in Chapter 4, it has been suggested that the shortfall in energy presumably comes from the meso-scale internal waves and large vortices generated by the shear instabilities, which play a vital role in particle uplift.

For instance, the shear instabilities such as Kelvin-Helmholtz instabilities can be observed at the upper flow interface of turbidity currents. The stability of the upper interface depends on Fr_d . A high- Fr_d flow has a more unstable interface, due to the strong shear. These shear instabilities at the top of the flow act to push down both the inflection point of the flow concentration and the height of the velocity maximum. However, when Fr_d is small (subcritical), the interface becomes relatively stable, and thus the shear instabilities may not develop. The upper dilute layer becomes thinner, and the lower dense layer occupies the flow. Therefore, the contribution of internal waves and vortices in subcritical and supercritical flows should be different and

may have some correlation between Fr_d . In Chapter 3, we found the strong correlation between velocity and concentration profiles (Fig. 3.10). This correlation is expected to provide a constraint to the development of shear instability layers at the upper interface (Fig. 5.1). Having said that, how the time-averaged vertical flow structures relate to the spatial and temporal development of internal waves and large vortices requires more intensive investigation and observations.

5.3 Future works

This study has provided new insights into sediment transport mechanics of turbidity currents. Simultaneously, the novel findings revenue for the new research to investigate. Here, further areas of research which could build upon the findings of this study are highlighted.

In Chapter 3, I developed the empirical models which can predict the full vertical profiles of streamwise velocity and concentration of turbidity currents at high accuracy (ξ_u and ξ_ϕ). These structure functions provided the empirical formula for the weighting terms of shallow water equations (W_{u^2} , $W_{u\phi}$, and W_P). Further, using these weights in system-scale numerical simulations would enable the better understanding of the evolution of sedimentary architectures. For instance, implementing the developed model to the shallow water model (Dorrell et al., 2014) can improve the accuracy of the prediction of overspilling. A better prediction of overspilling facilitates a more accurate prediction of the evolution of submarine channel networks, which is essential to predicting the dispersion of nutrients, sediments and pollutants in deep marine systems. The structure models of this study are expected to enable more accurate predictions of natural-scale flows, providing valuable insights to the evolution of sinuous submarine-channel networks. However, further improvements could still be made in these empirical models. One of the limitations of the developed models is the shortage of natural-scale training data. Currently, only one event from the Congo canyon (Simmons et al., 2020) is included in the training dataset. As discussed in section 3.5, the limited performance of the trained model without Re against the natural-scale test data suggests that there are some unknown factors which differentiate the flow behaviours in laboratory-scale and natural-scale turbidity currents. It is possible that the developed models in Chapter 3 overfitted to Congo's data causing poor performance in other natural-scale settings. To address this limitation of the models, more data from direct observations of natural-scale settings are required. Also, the height-scale used in this study could be improved. In this study, the flow height is defined that the height where the velocity and concentration vanish. If there is no counterflow, this flow height may correspond to the very top of the shear-instability layer 5.1. However, it is also possible that the top of the shear-instability layer has a negative velocity and a non-zero sediment concentration, especially in the laboratory-scale settings where the counterflow may not be negligible. This is also raised as one of the potential causes of the model's limited prediction of natural-scale data in Chapter 3. In such cases, it is questionable if the height-scale used in this study is appropriate. Further investigations are required to address this height-scale issue, which is

expected to improve the models in this study. Increasing the amount of data from experiments and simulation may also help improve the models. Furthermore, currently the velocity profile model ξ_u is dependent on the correlation between the interpolated and extrapolated velocity and concentration profiles. The uncertainty in the upper region of the ratio ξ_u/ξ_ϕ makes the model less reliable in the area near the upper interface. Thus, the intensive high resolution observations of the upper boundary of turbidity currents would enable a better understanding of the correlation between velocity and concentration profiles. The intensive observations of the upper layer are also important for the better understanding of the shear instabilities. As hypothesised in Chapter 4, internal waves and large vortices may play a vital role in terms of the energetics of gravity currents. To understand how those meso-scale flow structures energise the flow, intensive spatio-temporal simulations and observations of the turbulent field of gravity currents are required, which enables investigation of the meso-scale structures in turbidity currents.

In summary, this thesis has significantly advanced our understanding of turbidity currents, providing valuable insights into sediment transport mechanics. The compilation of 70 years of laboratory-scale data with newly conducted large-scale flume experiments, has provided valuable insights into the complex dynamics of turbidity currents. Innovative data compilation methods, including original interpolation and extrapolation techniques, have enhanced the reliability of obtained profiles. The analysis on the flow stratification of compiled turbidity currents data revealed a strong correlation between velocity and concentration profiles, leading to the formulation of an accurate correlation-based empirical stratification model. The identified correlation across entire profiles suggests a universal relationship governing the interplay of velocity and concentration in turbidity currents, contributing to a deeper understanding of material-transport dynamics. Further analysis based on the developed empirical models for predicting vertical profiles of streamwise velocity (ξ_u) and concentration (ξ_ϕ) revealed the flow dynamics of gravity currents which enables the flow to enhance the material and momentum transport efficiency especially in distal region where the slope is extremely shallow. The investigation into the energetics of turbidity currents challenges traditional fluvial energetics theory, highlighting a significant underestimation of sediment-load capacity. The observed energy shortage cannot be fully explained by conventional theories, emphasizing the need for a more comprehensive understanding of contributors to mixing mechanisms in turbidity currents. However, this work has identified a need for the better understanding of the strong stratification mechanics, and the flow mixing dynamics of natural-scale turbidity currents. Stratification mechanics of natural-scale turbidity currents may be addressed by intensive observations of natural-scale turbidity currents in various settings. As it hypothesised in Chapter 4, the meso-scale flow structures such as internal waves may play a vital role in terms of the material transport of turbidity currents. However, the contribution of those flow structures to the sediment-load capacity of turbidity currents is still poorly understood. Instantaneous measurements of three-dimensional turbulent fields and buoyancy perturbation may provide valuable insights into the better understanding of the meso-scale structures such as the internal waves. Yet, the current available measurement techniques of flow concentration are

mostly designed to measure time-averaged values. Therefore, technical advances in measurement techniques are also required. As highlighted in the introduction 1, such advances in understanding turbidity currents are essential to a better understanding of material transport mechanics from shallow to deep ocean and the evolution of sedimentary architectures in which 100-1000s year-scale environmental events are expected to be recorded.

Appendix A

Appendix Chapter

A.1 Drag coefficient

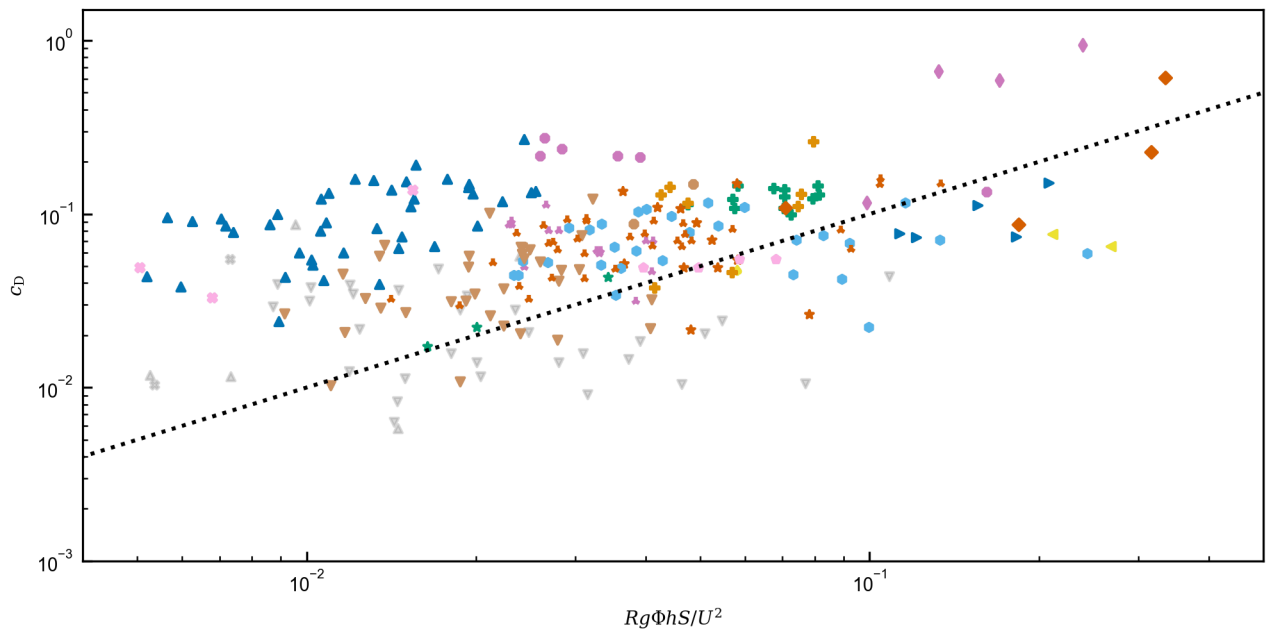


Figure A.1: Log-log plot of the estimated drag coefficient (Eq. 1.62) versus the top-hat drag coefficient (Parker et al., 1986) (Eq. A.1). The black dotted line represents the ideal linear line ($C_D = Rg\Phi hS/U^2$). The gray points indicate that those data points are excluded by the near-equilibrium criteria (Fig. 2 in the main text).

In this study the drag coefficient, C_D is estimated from the velocity gradient (Eq. 1.62). On the other hand, when a flow is in equilibrium, top-hat (unstratified) shallow water models (Parker et al., 1986) give

$$C_D = \frac{Rg\Phi hS}{U^2}, \quad (\text{A.1})$$

where S denotes the energy slope. Here, we compare the drag coefficient values estimated from the velocity gradient (Eq. 1.62) and those values based on the top-hat equilibrium assumption (Eq. A.1), see Figure A.1. The top-hat drag coefficient shows relatively better correlation with velocity-profile-based drag coefficient in the relatively large drag coefficient region ($Rg\Phi hS/U^2 \gtrsim 0.05$). While the flows with the low top-hat drag coefficient ($Rg\Phi hS/U^2 \lesssim 0.05$) show a relatively poor correlation with the velocity-profile-based drag coefficient. This serves to further stress the main conclusion, that the top-hat model does not accurately capture the dynamics of gravity currents.

A.2 Flow power plot

From the flow power theory (Velikanov et al., 1954; Bagnold, 1966) and the autosuspension criteria (Bagnold et al., 1962), the following proportionality is assumed

$$P_{\text{shear}} \propto B_{\text{turb}}, \quad \text{where} \quad P_{\text{shear}} = - \int_0^\infty \langle u'w' \rangle \frac{\langle u \rangle}{z} dz \quad \text{and} \quad B_{\text{turb}} = \int_0^\infty \tilde{B} dz = \int_0^\infty Rg \langle w' \phi' \rangle dz, \quad (\text{A.2})$$

where P denotes the shear production of the mean flow, and the buoyancy production term, B , denotes the work done by turbulence to keep sediment in suspension. For the fluvial flows, assuming $B_f = \Phi N_f = Rg\Phi h w_s$ and the direct proportionality between total production, P_{loss} and the log-law production, $P_f = u_*^2 U$,

$$\Phi \propto \frac{P_f}{N_f} = \frac{u_*^2 U}{Rg h w_s}, \quad (\text{A.3})$$

is obtained.

Laboratory-scale turbidity currents data There are few data points in the dilute regime around $10^{-1} < P_f/B_f < 10^0$. This is not because the data is excluded due to the introduced equilibrium criteria (Fig. 2 in the main text) but simply the long-duration experiments of turbidity currents with flow concentration, $\Phi \sim 0.5\%$ are limited (Supplementary Fig. A.2). Our flume experiments partially fill this data gap by adding three runs within the target concentration range.

Pyroclastic density currents The recent laboratory experiments (Breard and Lube, 2017; Brosch and Lube, 2020) of pyroclastic density currents (PDCs) are gathered (see Table. 2.1). The same methodology of data compilation for turbidity currents is applied for PDCs. For the entrainment rate of air of pyroclastic density currents, the empirical equation (Dellino et al., 2019)

$$e_w = 0.21 \text{Ri}_o^{-1.1} \quad (\text{A.4})$$

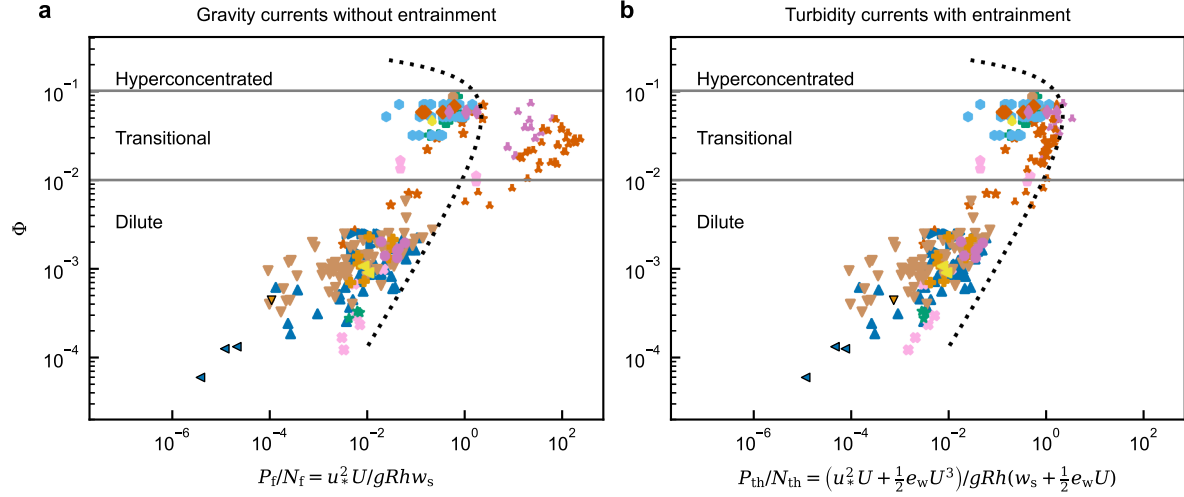


Figure A.2: Sediment transport capacity for gravity currents without data reduction. Sediment concentration, Φ , versus dimensionless flow power, P_f/N_f for: a) all gravity current data with the log-law production term, P_f ; b) all gravity current data with the top-hat production term, P_{th} . Throughout, dilute, transitional and hyperconcentrated regimes are separated by gray solid lines. Parametric correlations of concentration and dimensionless flow power are depicted by black dotted curves. Symbol shapes as per Figure 1 in the main text.

is used, where $Ri_o = g'h \cos \theta / U^2$ is the overall Richardson number, g' is the reduced gravity, and θ denotes the angle of slope.

Fluvial flows The fluvial data from natural-scale rivers (Nordin and Dempster, 1963; Wan and Wang, 1994a) and laboratory-scale experiments (Guy et al., 1966; Ashida and Okabe, 1982; Cellino and Graf, 1999; Graf and Cellino, 2002; Einstein and Chien, 1955; Coleman, 1986; Lyn, 1988; Vanoni, 1946; Vanoni and Nomicos, 1960; Brooks, 1954) are gathered (Fig. 3 in the main text and Supplementary Fig. A.2a). The Yellow river data (Wan and Wang, 1994a) are gathered from the figure from (van Maren, 2007), using a graph reading software. Since the shear velocity values and raw velocity profiles of Yellow River data points are not available in the original source, the average skin drag coefficient, C_D of Yellow River data is estimated from the recent velocity measurement data (Moodie et al., 2022). The reported flow parameters from each source such as flow velocity, volumetric flow concentration, and median particle size are directly used for the calculation. For the detailed data compilation methodology for the rest of the data, see Dorrell et al. (2018a).

source	site
Vanoni (1946)	Laboratory exp.
Brooks (1954)	Laboratory exp.
Einstein and Chien (1955)	Laboratory exp.
Vanoni and Nomicos (1960)	Laboratory exp.
Nordin and Dempster (1963)	Rio Grande
Guy et al. (1966)	Laboratory exp.

Coleman (1986)	Laboratory exp.
Lyn (1988)	Laboratory exp.
Wan and Wang (1994a)	Yellow River
Ashida and Okabe (1982)	Laboratory exp.
Cellino and Graf (1999)	Laboratory exp.
Graf and Cellino (2002)	Laboratory exp.

Table A.1: Summary of the compiled fluvial source.

A.3 Curve Fitting

In Chapter 4, two types of regression analyses are conducted. For the simple linear regression, the Orthogonal Distance Regression (ODR) method (Boggs and Rogers, 1990) is used. While Ordinary Least Squares (OLS) treat the data for explanatory variables (x -axis) as without error, minimising the distance from the response variable (y -axis) to the fitted curve, ODR accounts equally for errors of both explanatory and response variables, minimising the orthogonal distance between each data point and the fitted curve. All explanatory variables in the linear regressions in this study are expected to exhibit error due to (for example) the limitation of measurement tools such as UVP or siphon arrays. Thus, ODR is considered as more suitable than OLS. To infer the goodness of fit of ODR, the coefficient of determination, R^2 is introduced. R^2 is calculated from the sum of squares of residuals, RSS and the total sum of squares, TSS as,

$$R^2 = 1 - \frac{\text{RSS}}{\text{TSS}}, \quad (\text{A.5})$$

where RSS and TSS for ODR is calculated as,

$$\text{RSS} = \sum_i d(x_i, y_i, f(\beta))^2 \quad (\text{A.6})$$

$$\text{TSS} = \sum_i (y_i - \bar{y})^2, \quad (\text{A.7})$$

where (x_i, y_i) denotes the coordinate of the i^{th} observed data, $d(x_i, y_i, f)^2$ denotes the squared orthogonal distance between (x_i, y_i) and the fitted curve f , and \bar{y} denotes the mean value of y_i .

Iterative least squares method To fit a curve to the fluvial data set (black dotted curve in Fig. 4.3a–c), we use the least squares fit for a parametric curve fitting. To simplify notation, here we will use the notation $x = \log_{10}(P_f/Rghw_s)$, $y = \log_{10}(\Phi)$, so that the goal is to fit a curve $(x(t), y(t))$ to the given set of data points (x_i, y_i) . The curves are written as polynomials in the parameter t , and we choose to take x as a quadratic in

t and y as a cubic in t , so that

$$x = \sum_{n=0}^2 a_n t^n, \quad y = \sum_{m=0}^3 b_m t^m. \quad (\text{A.8})$$

This parametrization in the variable t has a symmetry of the form $t \mapsto c_0 + c_1 t$, which has corresponding transformations for the coefficients a_n, b_n , that keeps the curve in the x - y plane unchanged. To remove this symmetry, we select two of the coefficients by choosing $t = 0$ to correspond to the extremal value of x , $a_1 = 0$, and the rate of change of y around this point to be unity, $b_1 = 1$.

To fit the curve to the data (x_i, y_i) , we recognise that we must not only determine the coefficients a_n, b_n , but also a set of values t_i which are the parameter values for the closest point on the curve to the data point. We do this employing the residuals

$$\epsilon_i(\boldsymbol{\beta}) = x_i - f_i(\boldsymbol{\beta}) \quad \text{where} \quad f_i(\boldsymbol{\beta}) = \sum_{n=0}^2 a_n t_i^n, \quad (\text{A.9})$$

and

$$\delta_i(\boldsymbol{\beta}) = y_i - g_i(\boldsymbol{\beta}) \quad \text{where} \quad g_i(\boldsymbol{\beta}) = \sum_{m=0}^3 b_m t_i^m, \quad (\text{A.10})$$

where bold characters denote column vectors or matrices, and $\boldsymbol{\beta}$ will be defined later. For now we simply state it is the value to be optimised. The sum of squared residuals is then

$$S(\boldsymbol{\beta}) = \sum_i (\epsilon_i(\boldsymbol{\beta})^2 + \delta_i(\boldsymbol{\beta})^2). \quad (\text{A.11})$$

and we employ the method of least squares, seeking a local minimum of $S(\boldsymbol{\beta})$. Following the standard deviation for the method of least squares, we can find a local minimum by iterating from one value, $\boldsymbol{\beta}^k$, to the next, $\boldsymbol{\beta}^{k+1}$, using

$$(\mathbf{F}^T \mathbf{F} + \mathbf{G}^T \mathbf{G}) \Delta \boldsymbol{\beta} = \mathbf{F}^T \boldsymbol{\epsilon} + \mathbf{G}^T \boldsymbol{\delta} \quad (\text{A.12})$$

where $\boldsymbol{\beta}^{k+1} = \boldsymbol{\beta}^k + \Delta \boldsymbol{\beta}$ and

$$F_{ij} = \frac{\partial f_i}{\partial \beta_j}(\boldsymbol{\beta}^k), \quad G_{ij} = \frac{\partial g_i}{\partial \beta_j}(\boldsymbol{\beta}^k). \quad (\text{A.13})$$

The algorithm we use proceeds as follows, where $\|\boldsymbol{\beta}\| = \frac{1}{M} \sum_{m=1}^M \beta_m$.

1. Initialise the values of t_i to $t_i = 1$ for $x_i < 1$, $y_i > -2$; to $t_i = 0$ for $x_i \geq 1$; and to $t_i = -1$ otherwise. Add to these t_i a random amount between -0.05 and 0.05 to desingularize what follows.

2. Initialise a_n and b_m to random values between 0 and 1, except for $a_1 = 0$ and $b_1 = 1$.
3. Apply the iteration (A.12) with $\boldsymbol{\beta} = (a_0, a_2, b_0)^T$ until $\|\Delta\boldsymbol{\beta}\| < 10^{-4}$, which is equivalent to fitting x as a quadratic in y ,
4. Apply the iteration (A.12) with $\boldsymbol{\beta} = (a_0, a_2, b_0, b_2, b_3, t_0, t_1, \dots)^T$ and $\boldsymbol{\beta}^{k+1} = \boldsymbol{\beta}^k + \frac{1}{10}\Delta\boldsymbol{\beta}$ until $\|\Delta\boldsymbol{\beta}\| < 10^{-4}$, which is the full fitting of the curve
5. For each point, search over values of t to find a t_i that is the global minimizer of $\epsilon_i^2 + \delta_i^2$, to ensure that all data points are identified with the correct points on the curve
6. Apply step 4 again

At this stage the optimal values of a_n and b_m are known, and can be used to plot the best fit curve. For both cases $a_1 = 0$ and $b_1 = 1$. For the fluvial case

$$\begin{aligned}
 a_0 &= 0.332, & a_1 &= 0, & a_2 &= -1.412, \\
 b_0 &= -1.281, & b_1 &= 1, & b_2 &= -0.583, & b_3 &= 0.1621, \\
 & & & & & & & -1.282 < t < 1.179.
 \end{aligned}
 \tag{A.14}$$

References

- Abad, Jorge D., Sequeiros, Octavio E., Spinewine, Benoit, Pirmez, Carlos, Garcia, Marcelo H., and Parker, Gary (2011). “Secondary current of saline underflow in a highly meandering channel: Experiments and theory”. In: *Journal of Sedimentary Research* 81.11, pp. 787–813. DOI: 10.2110/jsr.2011.61.
- Akaike, Hirotogu (1998). “Information Theory and an Extension of the Maximum Likelihood Principle”. In: *Selected Papers of Hirotogu Akaike*. Ed. by Emanuel Parzen, Kunio Tanabe, and Genshiro Kitagawa. New York, NY: Springer New York, pp. 199–213. DOI: 10.1007/978-1-4612-1694-0_15.
- Alexander, Jan and Mulder, Thierry (2002). “Experimental quasi-steady density currents”. In: *Marine Geology* 186.3, pp. 195–210. DOI: 10.1016/S0025-3227(02)00313-4.
- Allen, J. R. L. (1971). “Mixing at turbidity current heads, and its geological implications”. In: *Journal of Sedimentary Research* 41.1, pp. 97–113. DOI: 10.1306/74D721F8-2B21-11D7-8648000102C1865D.
- (1991). “The Bouma division A and the possible duration of turbidity currents”. In: *Journal of Sedimentary Research* 61.2, pp. 291–295. DOI: 10.1306/D42676F4-2B26-11D7-8648000102C1865D.
- Altinakar, M. S. (1988). “Weakly Depositing Turbidity Currents on Small Slopes”. PhD dissertation. EPF Lausanne, CH.
- Altinakar, M.S., Graf, W.H., and Hopfinger, E.J. (1996). “Flow structure in turbidity currents”. In: *Journal of Hydraulic Research* 34.5, pp. 713–718. DOI: 10.1080/00221689609498467.
- Amy, L.A., Peakall, J., and Talling, P.J. (2005). “Density- and viscosity-stratified gravity currents: Insight from laboratory experiments and implications for submarine flow deposits”. In: *Sedimentary Geology* 179.1, pp. 5–29. DOI: 10.1016/j.sedgeo.2005.04.009.
- Amy, Lawrence and Dorrell, Robert (2022). “Equilibrium sediment transport by dilute turbidity currents: Comparison of competence-based and capacity-based models”. In: *Sedimentology* 69.2, pp. 624–650. DOI: 10.1111/sed.12921.

- Andersen, T.J., Fredsoe, J., and Pejrup, M. (2007). “In situ estimation of erosion and deposition thresholds by Acoustic Doppler Velocimeter (ADV)”. In: *Estuarine, Coastal and Shelf Science* 75.3, pp. 327–336. DOI: 10.1016/j.ecss.2007.04.039.
- Andrews, Benjamin J. and Manga, Michael (2012). “Experimental study of turbulence, sedimentation, and coignimbrite mass partitioning in dilute pyroclastic density currents”. In: *Journal of Volcanology and Geothermal Research* 225-226, pp. 30–44. DOI: 10.1016/j.jvolgeores.2012.02.011.
- Anthony, Martin and Holden, Sean B (1998). “Cross-validation for binary classification by real-valued functions: theoretical analysis”. In: *Proceedings of the eleventh annual conference on Computational learning theory*, pp. 218–229.
- Arai, Kazuno, Naruse, Hajime, Miura, Ryo, Kawamura, Kiichiro, Hino, Ryota, Ito, Yoshihiro, Inazu, Daisuke, Yokokawa, Miwa, Izumi, Norihiro, Murayama, Masafumi, et al. (2013). “Tsunami-generated turbidity current of the 2011 Tohoku-Oki earthquake”. In: *Geology* 41.11, pp. 1195–1198. DOI: 10.1130/G34777.1.
- Argyropoulos, C.D. and Markatos, N.C. (2015). “Recent advances on the numerical modelling of turbulent flows”. In: *Applied Mathematical Modelling* 39.2, pp. 693–732. DOI: 10.1016/j.apm.2014.07.001.
- Ashida, K. and Okabe, T. (1982). “On the Calculation Method of the Concentration of Suspended Sediment under Non-equilibrium Condition”. In: *Proceedings of the Japanese conference on hydraulics* 26, pp. 153–158. DOI: 10.2208/prohe1975.26.153.
- Azpiroz-Zabala, M., Cartigny, M. J. B., Sumner, E. J., Clare, M. A., Talling, P. J., Parsons, D. R., and Cooper, C. (2017a). “A General Model for the Helical Structure of Geophysical Flows in Channel Bends”. In: *Geophysical Research Letters* 44.23, pp. 11, 932–11, 941. DOI: 10.1002/2017GL075721.
- Azpiroz-Zabala, Maria, Cartigny, Matthieu J. B., Talling, Peter J., Parsons, Daniel R., Sumner, Esther J., Clare, Michael A., Simmons, Stephen M., Cooper, Cortis, and Pope, Ed L. (2017b). “Newly recognized turbidity current structure can explain prolonged flushing of submarine canyons”. In: *Science Advances* 3.10, e1700200. DOI: 10.1126/sciadv.1700200.
- Baas, Jaco H, McCaffrey, William D, Haughton, Peter DW, and Choux, Caroline (2005). “Coupling between suspended sediment distribution and turbulence structure in a laboratory turbidity current”. In: *Journal of Geophysical Research: Oceans* 110.C11. DOI: 10.1029/2004JC002668, 2005.
- Babonneau, Nathalie, Savoye, Bruno, Cremer, Michel, and Bez, Martine (2010). “Sedimentary architecture in meanders of a submarine channel: detailed study of the present Congo turbidite channel (Zaiango project)”. In: *Journal of Sedimentary Research* 80.10, pp. 852–866. DOI: 10.2110/j.sr.2010.078.

- Bagnold, Ralph Alger (1954). “Experiments on a gravity-free dispersion of large solid spheres in a Newtonian fluid under shear”. In: *Proceedings of the Royal Society of London. Series A. Mathematical and Physical Sciences* 225.1160, pp. 49–63. DOI: 10.1098/rspa.1954.0186.
- (1966). *An approach to the sediment transport problem from general physics*. Vol. 422. U.S. Geol. Surv. Prof. Paper, pp. I1–I37.
- Bagnold, Ralph Alger, Deacon, George Edward Raven, and Russell, Frederick Stratten (1962). “Auto-suspension of transported sediment; turbidity currents”. In: *Proceedings of the Royal Society of London. Series A. Mathematical and Physical Sciences* 265.1322, pp. 315–319. DOI: 10.1098/rspa.1962.0012.
- Bah, Abdul R., Kravchuk, Olena, and Kirchhof, Gunnar (2009). “Fitting Performance of Particle-size Distribution Models on Data Derived by Conventional and Laser Diffraction Techniques”. In: *Soil Science Society of America Journal* 73.4, pp. 1101–1107. DOI: 10.2136/sssaj2007.0433.
- Baines, Peter G (1998). *Topographic effects in stratified flows*. Cambridge university press.
- Barber, Rina Foygel, Candès, Emmanuel J., Ramdas, Aaditya, and Tibshirani, Ryan J. (2021). “Predictive inference with the jackknife+”. In: *The Annals of Statistics* 49.1, pp. 486–507. DOI: 10.1214/20-AOS1965.
- Barron, Jonathan T. (2020). *A Convenient Generalization of Schlick’s Bias and Gain Functions*. DOI: 10.48550/ARXIV.2010.09714.
- Bates, Charles C (1953). “Rational theory of delta formation”. In: *Aapg Bulletin* 37.9, pp. 2119–2162.
- Bell, Hugh Stevens (1942). “Studies for Students: Density Currents as Agents for Transporting Sediments”. In: *The Journal of Geology* 50.5, pp. 512–547. DOI: 10.1086/625070.
- Benjamin, T. Brooke (1968). “Gravity currents and related phenomena”. In: *Journal of Fluid Mechanics* 31.2, pp. 209–248. DOI: 10.1017/S0022112068000133.
- Best, J. L., Kirkbride, A. D., and Peakall, J. (2001). “Mean Flow and Turbulence Structure of Sediment-Laden Gravity Currents: New Insights using Ultrasonic Doppler Velocity Profiling”. In: *Particulate Gravity Currents*. John Wiley & Sons, Ltd, pp. 157–172. DOI: 10.1002/9781444304275.ch12.
- Best, James L., Kostaschuk, Ray A., Peakall, Jeffrey, Villard, Paul V., and Franklin, Mark (2005). “Whole flow field dynamics and velocity pulsing within natural sediment-laden underflows”. In: *Geology* 33.10, pp. 765–768. DOI: 10.1130/G21516.1.
- Birman, V. K., Meiburg, E., and Kneller, B. (2009). “The shape of submarine levees: exponential or power law?” In: *Journal of Fluid Mechanics* 619, pp. 367–376. DOI: 10.1017/S0022112008004862.

- Bo Pedersen, Flemming (1980). *A monograph on turbulent entrainment and friction in two-layer stratified flow*. Institute of Hydrodynamics and Hydraulic Engineering, Technical University of Denmark.
- Boggs, Paul T and Rogers, Janet E (1990). “Orthogonal distance regression”. In: pp. 183–194.
- Borden, Zachary and Meiburg, Eckart (2013). “Circulation based models for Boussinesq gravity currents”. In: *Physics of Fluids* 25.10, p. 101301. DOI: 10.1063/1.4825035.
- Bouma, Arnold H (1962). *Sedimentology of Some Flysch Deposits: A Graphic Approach to Facies Interpretation*. Amsterdam: Elsevier, 168p.
- Bouma, Arnold H., Normark, William R., and Normark, Neal E. Barnes William R. (1985). *Submarine Fans and Related Turbidite Systems*. Springer-Verlag New York, p. 222.
- Boussinesq, J. V. (1877). “Essai sur la Théorie des Eaux Courantes.(‘Essay on the Theory of Water Flow’)”. In: *Mémoires présentés par divers savants à l’Académie des Sciences*. 3rd ser. 23.1, pp. 1–680.
- (1903). “Theorie Analytique de la Chaleur vol 2 (Paris: Gauthier-Villars)”. In: p. 657.
- Breard, Eric C.P. and Lube, Gert (2017). “Inside pyroclastic density currents – uncovering the enigmatic flow structure and transport behaviour in large-scale experiments”. In: *Earth and Planetary Science Letters* 458, pp. 22–36. DOI: 10.1016/j.epsl.2016.10.016.
- Britter, R. E. and Simpson, J. E. (1978). “Experiments on the dynamics of a gravity current head”. In: *Journal of Fluid Mechanics* 88.2, pp. 223–240. DOI: 10.1017/S0022112078002074.
- Brooks, Norman H (1954). “Laboratory studies of the mechanics of streams flowing over a movable bed of fine sand”. PhD thesis. California Institute of Technology. DOI: 10.7907/JB2P-1H91.
- Brosch, Ermanno and Lube, Gert (2020). “Spatiotemporal sediment transport and deposition processes in experimental dilute pyroclastic density currents”. In: *Journal of Volcanology and Geothermal Research* 401, p. 106946. DOI: 10.1016/j.jvolgeores.2020.106946.
- Bruschi, Roberto, Bughi, Sabrina, Spinazzè, Maurizio, Torselletti, Enrico, and Vitali, Luigino (2006). “Impact of debris flows and turbidity currents on seafloor structures.” In: *Norwegian Journal of Geology/Norsk Geologisk Forening* 86.3, pp. 317–337.
- Buckee, C., Kneller, B., and Peakall, J. (2001). “Turbulence Structure in Steady, Solute-Driven Gravity Currents”. In: *Particulate Gravity Currents*. John Wiley & Sons, Ltd, pp. 173–187. DOI: 10.1002/9781444304275.ch13.

- Buckingham, E. (1914). “On Physically Similar Systems; Illustrations of the Use of Dimensional Equations”. In: *Phys. Rev.* 4 (4), pp. 345–376. DOI: 10.1103/PhysRev.4.345.
- Cala, Isabel de, Ohata, Koji, Dorrell, Robert, Naruse, Hajime, Patacci, Marco, Amy, Lawrence A., Simmons, Steve, McLelland, Stuart J., and McCaffrey, William D. (2020). “Relating the Flow Processes and Bedforms of Steady-State and Waning Density Currents”. In: *Frontiers in Earth Science* 8, p. 409. DOI: 10.3389/feart.2020.535743.
- Cantero, Mariano I, Cantelli, Alessandro, Pirmez, Carlos, Balachandar, S, Mohrig, David, Hickson, Thomas A, Yeh, Tzu-hao, Naruse, Hajime, and Parker, Gary (2012). “Emplacement of massive turbidites linked to extinction of turbulence in turbidity currents”. In: *Nature Geoscience* 5.1, p. 42. DOI: 10.1038/ngeo1320.
- Cantero, Mariano I., Balachandar, S., Cantelli, Alessandro, Pirmez, Carlos, and Parker, Gary (2009). “Turbidity current with a roof: Direct numerical simulation of self-stratified turbulent channel flow driven by suspended sediment”. In: *Journal of Geophysical Research: Oceans* 114.C3. DOI: 10.1029/2008JC004978.
- Cantero, Mariano I., Balachandar, S., García, Marcelo H., and Bock, David (2008). “Turbulent structures in planar gravity currents and their influence on the flow dynamics”. In: *Journal of Geophysical Research: Oceans* 113.C8. DOI: 10.1029/2007JC004645.
- Cartigny, Matthieu J.B., Postma, George, Berg, Jan H. van den, and Mastbergen, Dick R. (2011). “A comparative study of sediment waves and cyclic steps based on geometries, internal structures and numerical modeling”. In: *Marine Geology* 280.1, pp. 40–56.
- Cartigny, Matthieu JB, Eggenhuisen, Joris T, Hansen, Ernst WM, and Postma, George (2013). “Concentration-dependent flow stratification in experimental high-density turbidity currents and their relevance to turbidite facies models”. In: *Journal of Sedimentary Research* 83.12, pp. 1047–1065. DOI: 10.2110/jsr.2013.71.
- Caulfield, C.P. (2021). “Layering, Instabilities, and Mixing in Turbulent Stratified Flows”. In: *Annual Review of Fluid Mechanics* 53.1, pp. 113–145. DOI: 10.1146/annurev-fluid-042320-100458.
- Celik, Ismail and Rodi, Wolfgang (1991). “Suspended Sediment-Transport Capacity for Open Channel Flow”. In: *Journal of Hydraulic Engineering* 117.2, pp. 191–204. DOI: 10.1061/(ASCE)0733-9429(1991)117:2(191).
- Cellino, M. and Graf, W. H. (1999). “Sediment-Laden Flow in Open-Channels under Noncapacity and Capacity Conditions”. In: *Journal of Hydraulic Engineering* 125.5, pp. 455–462. DOI: 10.1061/(ASCE)0733-9429(1999)125:5(455).

- Chiang, Cheng-Shing, Yu, Ho-Shing, Noda, Atsushi, TuZino, Taqumi, and Su, Chih-Chieh (2012). “Avulsion of the Fangliao submarine canyon off southwestern Taiwan as revealed by morphological analysis and numerical simulation”. In: *Geomorphology* 177-178, pp. 26–37. DOI: 10.1016/j.geomorph.2012.07.011.
- Chikita, Kazuhisa (1989). “A field study on turbidity currents initiated from spring runoffs”. In: *Water Resources Research* 25.2, pp. 257–271. DOI: 10.1029/WR025i002p00257.
- Clare, M.A., Hughes Clarke, J.E., Talling, P.J., Cartigny, M.J.B., and Pratomo, D.G. (2016). “Preconditioning and triggering of offshore slope failures and turbidity currents revealed by most detailed monitoring yet at a fjord-head delta”. In: *Earth and Planetary Science Letters* 450, pp. 208–220. DOI: 10.1016/j.epsl.2016.06.021.
- Clare, MA, Cartigny, MJB, North, LJ, Talling, PJ, Vardy, ME, Hizzett, JL, Sumner, EJ, Hughes Clarke, John E, Spinewine, B, et al. (2015). “Quantification of near-bed dense layers and implications for seafloor structures: new insights into the most hazardous aspects of turbidity currents”. In: *Offshore Technology Conference*. Offshore Technology Conference. Offshore Technology Conference. DOI: 10.4043/25705-MS.
- Clark, Ian R. and Cartwright, Joseph A. (2011). “Key controls on submarine channel development in structurally active settings”. In: *Marine and Petroleum Geology* 28.7, pp. 1333–1349. DOI: 10.1016/j.marpetgeo.2011.02.001.
- Coleman, Neil L. (1986). “Effects of Suspended Sediment on the Open-Channel Velocity Distribution”. In: *Water Resources Research* 22.10, pp. 1377–1384. DOI: <https://doi.org/10.1029/WR022i010p01377>.
- Covault, JA (2011). “Submarine fans and canyon-channel systems: a review of processes, products, and models”. In: *Nature Education Knowledge* 3.10, p. 4.
- Covault, Jacob A, Sylvester, Zoltan, Hubbard, Stephen M, Jobe, Zane R, and Sech, Richard P (2016). “The stratigraphic record of submarine-channel evolution”. In: *The Sedimentary Record* 14.3, pp. 4–11.
- Covault, Jacob A., Kostic, Svetlana, Paull, Charles K., Ryan, Holly F., and Fildani, Andrea (2014a). “Submarine channel initiation, filling and maintenance from sea-floor geomorphology and morphodynamic modelling of cyclic steps”. In: *Sedimentology* 61.4, pp. 1031–1054. DOI: 10.1111/sed.12084.
- (2014b). “Submarine channel initiation, filling and maintenance from sea-floor geomorphology and morphodynamic modelling of cyclic steps”. In: *Sedimentology* 61.4, pp. 1031–1054. DOI: 10.1111/sed.12084.
- Covault, Jacob A., Kostic, Svetlana, Paull, Charles K., Sylvester, Zoltan, and Fildani, Andrea (2017). “Cyclic steps and related supercritical bedforms: Building blocks of deep-water depositional systems, western North America”. In: *Marine Geology* 393, pp. 4–20. DOI: 10.1016/j.margeo.2016.12.009.

- Curray, Joseph R, Emmel, Frans J, and Moore, David G (2002). “The Bengal Fan: morphology, geometry, stratigraphy, history and processes”. In: *Marine and Petroleum Geology* 19.10, pp. 1191–1223. DOI: 10.1016/S0264-8172(03)00035-7.
- Davarpanah Jazi, S., Wells, M. G., Peakall, J., Dorrell, R. M., Thomas, R. E., Keevil, G. M., Darby, S. E., Sommeria, J., Viboud, S., and Valran, T. (2020). “Influence of Coriolis Force Upon Bottom Boundary Layers in a Large-Scale Gravity Current Experiment: Implications for Evolution of Sinuous Deep-Water Channel Systems”. In: *Journal of Geophysical Research: Oceans* 125.3. DOI: 10.1029/2019JC015284.
- Dellino, P., Dioguardi, F., Doronzo, D. M., and Mele, D. (2019). “The Entrainment Rate of Non-Boussinesq Hazardous Geophysical Gas-Particle Flows: An Experimental Model With Application to Pyroclastic Density Currents”. In: *Geophysical Research Letters* 46.22, pp. 12851–12861. DOI: 10.1029/2019GL084776.
- Di Stefano, C., Ferro, V., and Mirabile, S. (2010). “Comparison between grain-size analyses using laser diffraction and sedimentation methods”. In: *Biosystems Engineering* 106.2, pp. 205–215. DOI: 10.1016/j.biosystemseng.2010.03.013.
- Dorrell, R. M., Amy, L. A., Peakall, J., and McCaffrey, W. D. (2018a). “Particle Size Distribution Controls the Threshold Between Net Sediment Erosion and Deposition in Suspended Load Dominated Flows”. In: *Geophysical Research Letters* 45.3, pp. 1443–1452. DOI: 10.1002/2017GL076489.
- Dorrell, R. M., Darby, S. E., Peakall, J., Sumner, E. J., Parsons, D. R., and Wynn, R. B. (2013). “Super-elevation and overspill control secondary flow dynamics in submarine channels”. In: *Journal of Geophysical Research: Oceans* 118.8, pp. 3895–3915. DOI: 10.1002/jgrc.20277.
- (2014). “The critical role of stratification in submarine channels: Implications for channelization and long runout of flows”. In: *Journal of Geophysical Research: Oceans* 119.4, pp. 2620–2641. DOI: 10.1002/2014JC009807.
- Dorrell, R. M., Hogg, A. J., Sumner, E. J., and Talling, P. J. (2011). “The structure of the deposit produced by sedimentation of polydisperse suspensions”. In: *Journal of Geophysical Research: Earth Surface* 116.F1. DOI: 10.1029/2010JF001718.
- Dorrell, R. M., Peakall, J., Darby, S. E., Parsons, D. R., Johnson, J., Sumner, E. J., Wynn, R. B., Özsoy, E., and Tezcan, D. (2019). “Self-sharpening induces jet-like structure in seafloor gravity currents”. In: *Nature Communications* 10.1, p. 1381. DOI: 10.1038/s41467-019-09254-2.
- Dorrell, R.M., Peakall, J., Burns, C., and Keevil, G.M. (2018b). “A novel mixing mechanism in sinuous seafloor channels: Implications for submarine channel evolution”. In: *Geomorphology* 303, pp. 1–12. DOI: 10.1016/j.geomorph.2017.11.008.

- Dorrell, R.M., Peakall, J., Sumner, E.J., Parsons, D.R., Darby, S.E., Wynn, R.B., Özsoy, E., and Tezcan, D. (2016). “Flow dynamics and mixing processes in hydraulic jump arrays: Implications for channel-lobe transition zones”. In: *Marine Geology* 381, pp. 181–193. DOI: 10.1016/j.margeo.2016.09.009.
- Dorrell, Robert M., Burns, Alan D., and McCaffrey, William D. (2015). “The inherent instability of leveed seafloor channels”. In: *Geophysical Research Letters* 42.10, pp. 4023–4031. DOI: 10.1002/2015GL063809.
- Dritschel, D. G. and Scott, R. K. (2011). “Jet sharpening by turbulent mixing”. In: *Philosophical Transactions of the Royal Society A: Mathematical, Physical and Engineering Sciences* 369.1937, pp. 754–770. DOI: 10.1098/rsta.2010.0306.
- Egashira, S (1980). “Basic research on the flow and mechanism of mixing of density-stratified fields”. In: *Ph. D. thesis* 132.
- Eggenhuisen, Joris T., Tilston, Mike C., Leeuw, Jan de, Pohl, Florian, and Cartigny, Matthieu J. B. (2020). “Turbulent diffusion modelling of sediment in turbidity currents: An experimental validation of the Rouse approach”. In: *The Depositional Record* 6.1, pp. 203–216. DOI: 10.1002/dep2.86.
- Einstein, HA and Chien, Ning (1955). “Effects of heavy sediment concentration near the bed on velocity and sediment distribution. MRD Sediment Series No. 8”. In: *Univ of California, Berkeley, US Army Corps of Engineers, Missouri Div.*
- Eisma, D and Kalf, J (1984). “Dispersal of Zaire river suspended matter in the estuary and the Angola Basin”. In: *Netherlands Journal of Sea Research* 17.2, pp. 385–411. DOI: 10.1016/0077-7579(84)90057-7.
- Ellison, T. H. and Turner, J. S. (1959). “Turbulent entrainment in stratified flows”. In: *Journal of Fluid Mechanics* 6.3, pp. 423–448. DOI: 10.1017/S0022112059000738.
- Elmore, R. Douglas, Pilkey, Orrin H., Cleary, William J., and Curran, H. Allen (1979). “Black Shell turbidite, Hatteras Abyssal Plain, western Atlantic Ocean”. In: *GSA Bulletin* 90.12, pp. 1165–1176.
- Eshel, G., Levy, G. J., Mingelgrin, U., and Singer, M. J. (2004). “Critical Evaluation of the Use of Laser Diffraction for Particle-Size Distribution Analysis”. In: *Soil Science Society of America Journal* 68.3, pp. 736–743. DOI: 10.2136/sssaj2004.7360.
- Ettema, Robert, Arndt, R, Roberts, P, and Wahl, T (2000). *Hydraulic modeling: Concepts and practice*. ASCE manuals and reports on engineering practice.
- Euler, L. (1755). “Principes généraux du mouvement des fluides”. In: *Mémoires de L’Académie Royale des Sciences et des Belles-Lettres de Berlin* 11, pp. 217–273.

- Farizan, Ahmadreza, Yaghoubi, Sina, Firoozabadi, Bahar, and Afshin, Hossein (2019). “Effect of an obstacle on the depositional behaviour of turbidity currents”. In: *Journal of Hydraulic Research* 57.1, pp. 75–89. DOI: 10.1080/00221686.2018.1459891.
- Fedele, Juan J., Hoyal, David, Barnaal, Zachary, Tulenko, Joseph, and Awalt, Shane (2016). “Bedforms created by gravity flows”. In: *Autogenic Dynamics and Self-Organization in Sedimentary Systems*. SEPM Society for Sedimentary Geology, pp. 95–121. DOI: 10.2110/sepmsp.106.12.
- Felix, M. (2002). “Flow structure of turbidity currents”. In: *Sedimentology* 49.3, pp. 397–419. DOI: <https://doi.org/10.1046/j.1365-3091.2002.00449.x>.
- Fildani, Andrea, Normark, William R., Kostic, Svetlana, and Parker, Gary (2006). “Channel formation by flow stripping: large-scale scour features along the Monterey East Channel and their relation to sediment waves”. In: *Sedimentology* 53.6, pp. 1265–1287. DOI: 10.1111/j.1365-3091.2006.00812.x.
- Fisher, Peter, Aumann, Colin, Chia, Kohleth, O’Halloran, Nick, and Chandra, Subhash (2017). “Adequacy of laser diffraction for soil particle size analysis”. In: *PLOS ONE* 12.5, pp. 1–20. DOI: 10.1371/journal.pone.0176510.
- Fisher, Richard V. (1983). “Flow transformations in sediment gravity flows”. In: *Geology* 11.5, pp. 273–274. DOI: 10.1130/0091-7613(1983)11<273:FTISGF>2.0.CO;2.
- Fiske, Richard S (1963). “Subaqueous pyroclastic flows in the Ohanapecosh Formation, Washington”. In: *Geological Society of America Bulletin* 74.4, pp. 391–406. DOI: "10.1130/0016-7606(1963)74[391:SPFITO]2.0.CO;2".
- Fiske, Richard S., Cashman, Katharine V., Shibata, Atsushi, and Watanabe, Kazuki (1998). “Tephra dispersal from Myojinsho, Japan, during its shallow submarine eruption of 1952–1953”. In: *Bulletin of Volcanology* 59.4, pp. 262–275. DOI: 10.1007/s004450050190.
- Fritsch, F. N. and Butland, J. (1984). “A Method for Constructing Local Monotone Piecewise Cubic Interpolants”. In: *SIAM Journal on Scientific and Statistical Computing* 5.2, pp. 300–304. DOI: 10.1137/0905021.
- Fukuda, Sojiro, Vet, Marijke G. W. de, Skevington, Edward W. G., Bastianon, Elena, Fernández, Roberto, Wu, Xuxu, McCaffrey, William D., Naruse, Hajime, Parsons, Daniel R., and Dorrell, Robert M. (2023). “Inadequacy of fluvial energetics for describing gravity current autosuspension”. In: *Nature Communications* 14.1, p. 2288. DOI: 10.1038/s41467-023-37724-1.

- Garcia, Marcelo and Parker, Gary (1989). “Experiments on Hydraulic Jumps in Turbidity Currents Near a Canyon-Fan Transition”. In: *Science* 245.4916, pp. 393–396. DOI: 10.1126/science.245.4916.393.
- (1991). “Entrainment of Bed Sediment into Suspension”. In: *Journal of Hydraulic Engineering* 117.4, pp. 414–435. DOI: 10.1061/(ASCE)0733-9429(1991)117:4(414).
- Garcia, Marcelo H. (1993). “Hydraulic Jumps in Sediment-Driven Bottom Currents”. In: *Journal of Hydraulic Engineering* 119.10, pp. 1094–1117. DOI: 10.1061/(ASCE)0733-9429(1993)119:10(1094).
- García, Marcelo H. (2008). “Sediment Transport and Morphodynamics”. In: *Sedimentation Engineering*. Chap. Chapter 2, pp. 21–163. DOI: 10.1061/9780784408148.ch02.
- García, Marcelo H. (1993). “Hydraulic Jumps in Sediment-Driven Bottom Currents”. In: *Journal of Hydraulic Engineering* 119.10, pp. 1094–1117. DOI: 10.1061/(ASCE)0733-9429(1993)119:10(1094).
- Geyer, W. Rockwell and Kineke, Gail C. (1995). “Observations of currents and water properties in the Amazon Frontal Zone”. In: *Journal of Geophysical Research: Oceans* 100.C2, pp. 2321–2339. DOI: 10.1029/94JC02657.
- Girardclos, Stéphanie, Schmidt, Oliver T., Sturm, Mike, Ariztegui, Daniel, Pugin, André©, and Anselmetti, Flavio S. (2007). “The 1996 AD delta collapse and large turbidite in Lake Brienz”. In: *Marine Geology* 241.1, pp. 137–154. DOI: 10.1016/j.margeo.2007.03.011.
- Goldfinger, Chris (2011). “Submarine Paleoseismology Based on Turbidite Records”. In: *Annual Review of Marine Science* 3.1, pp. 35–66. DOI: 10.1146/annurev-marine-120709-142852.
- Goldfinger, Chris, Morey, Ann E., Nelson, C. Hans, Gutiérrez-Pastor, Julia, Johnson, Joel E., Karabanov, Eugene, Chaytor, Jason, and Eriksson, Andrew (2007). “Rupture lengths and temporal history of significant earthquakes on the offshore and north coast segments of the Northern San Andreas Fault based on turbidite stratigraphy”. In: *Earth and Planetary Science Letters* 254.1, pp. 9–27. DOI: 10.1016/j.epsl.2006.11.017.
- Goossens, Dirk (n.d.). “Techniques to measure grain-size distributions of loamy sediments: a comparative study of ten instruments for wet analysis”. In: *Sedimentology* 55.1 (), pp. 65–96. DOI: 10.1111/j.1365-3091.2007.00893.x.
- Gorsline, D.S, Diego, T De, and Nava-Sanchez, E.H (2000). “Seismically triggered turbidites in small margin basins: Alfonso Basin, Western Gulf of California and Santa Monica Basin, California Borderland”. In: *Sedimentary Geology* 135.1, pp. 21–35. DOI: 10.1016/S0037-0738(00)00060-9.
- Graf, W.H. and Cellino, M. (2002). “Suspension flows in open channels; experimental study”. In: *Journal of Hydraulic Research* 40.4, pp. 435–447. DOI: 10.1080/00221680209499886.

- Gray, Thomas E., Alexander, Jan, and Leeder, Mike R. (2005). “Quantifying velocity and turbulence structure in depositing sustained turbidity currents across breaks in slope”. In: *Sedimentology* 52.3, pp. 467–488. DOI: 10.1111/j.1365-3091.2005.00705.x.
- Guo, Junke (2020). “Empirical Model for Shields Diagram and Its Applications”. In: *Journal of Hydraulic Engineering* 146.6, p. 04020038. DOI: 10.1061/(ASCE)HY.1943-7900.0001739.
- Gutiérrez-Pastor, JULIA, Nelson, C HANS, Goldfinger, CHRIS, Johnson, JOEL E, Escutia, CARLOTA, Eriksson, ANDREW, Morey, AE, and Kneller, B (2009). “Earthquake control of Holocene turbidite frequency confirmed by hemipelagic sedimentation chronology on the Cascadia and northern California active continental margins”. In: *External controls of deep-water depositional systems: Society for Sedimentary Geology (SEPM) Special Publication* 92, pp. 179–197.
- Guy, HP, Simons, DB, and Richardson, EV (1966). “Summary of alluvial channel data from flume experiments, 1956-61: US Geol”. In: *Survey Prof. Paper* 462.1, pp. 11–196.
- Hage, Sophie, Cartigny, Matthieu J.B., Sumner, Esther J., Clare, Michael A., Hughes Clarke, John E., Talling, Peter J., Lintern, D. Gwyn, Simmons, Stephen M., Silva Jacinto, Ricardo, Vellinga, Age J., Allin, Joshua R., Azpiroz-Zabala, Maria, Gales, Jenny A., Hizzett, Jamie L., Hunt, James E., Mozzato, Alessandro, Parsons, Daniel R., Pope, Ed L., Stacey, Cooper D., Symons, William O., Vardy, Mark E., and Watts, Camilla (2019). “Direct Monitoring Reveals Initiation of Turbidity Currents From Extremely Dilute River Plumes”. In: *Geophysical Research Letters* 46.20, pp. 11310–11320. DOI: 10.1029/2019GL084526.
- Hage, Sophie, Cartigny, Matthieu JB, Clare, Michael A, Sumner, Esther J, Vendettuoli, Daniela, Hughes Clarke, John E, Hubbard, Stephen M, Talling, Peter J, Lintern, D Gwyn, Stacey, Cooper D, et al. (2018). “How to recognize crescentic bedforms formed by supercritical turbidity currents in the geologic record: Insights from active submarine channels”. In: *Geology* 46.6, pp. 563–566. DOI: 10.1130/G40095.1.
- Hampton, Monty A. (1972). “The role of subaqueous debris flow in generating turbidity currents”. In: *Journal of Sedimentary Petrology* 42.4, pp. 775–793.
- Al-Hashemi, Hamzah M. Beakawi, Al-Amoudi, Omar S. Baghabra, Yamani, Zain H., Mustafa, Yassir M., and Ahmed, Habib-ur-Rehman (2021). “The validity of laser diffraction system to reproduce hydrometer results for grain size analysis in geotechnical applications”. In: *PLOS ONE* 16.1, pp. 1–18. DOI: 10.1371/journal.pone.0245452.
- Haughton, Peter, Davis, Christopher, McCaffrey, William, and Barker, Simon (2009). “Hybrid sediment gravity flow deposits – Classification, origin and significance”. In: *Marine and Petroleum Geology* 26.10, pp. 1900–1918. DOI: 10.1016/j.marpetgeo.2009.02.012.

- Heezen, Bruce C and Ewing, Maurice (1952a). "Turbidity currents and submarine slumps, and the 1929 Grand Banks earthquake". In: *American journal of Science* 250.12, pp. 849–873. DOI: 10.2475/ajs.250.12.849.
- Heezen, Bruce Charles and Ewing, William Maurice (1952b). "Turbidity currents and submarine slumps, and the 1929 Grand Banks earthquake". In: *American Journal of Science* 250 (12), pp. 849–873. DOI: 10.2475/ajs.250.12.849.
- Hermidas, Navid, Eggenhuisen, Joris T., Jacinto, Ricardo Silva, Luthi, Stefan M., Toth, Ferenc, and Pohl, Florian (2018). "A Classification of Clay-Rich Subaqueous Density Flow Structures". In: *Journal of Geophysical Research: Earth Surface* 123.5, pp. 945–966. DOI: 10.1002/2017JF004386.
- Hsu, Shu-Kun, Kuo, Jackie, Lo, Chung-Liang, Tsai, Ching-Hui, Doo, Wen-Bin, Ku, Chia-Yen, and Sibuet, Jean-Claude (2008). "Turbidity Currents, Submarine Landslides and the 2006 Pingtung Earthquake off SW Taiwan". In: *Terrestrial, Atmospheric, and Oceanic Sciences Journal* 19, pp. 767–772. DOI: 10.3319/TA0.2008.19.6.767(PT).
- Hu, Peng and Cao, Zhixian (2009). "Fully coupled mathematical modeling of turbidity currents over erodible bed". In: *Advances in Water Resources* 32.1, pp. 1–15. DOI: 10.1016/j.advwatres.2008.07.018.
- Hughes Clarke, John E. (2016). "First wide-angle view of channelized turbidity currents links migrating cyclic steps to flow characteristics". In: *Nature Communications* 7, p. 11896. DOI: 10.1038/ncomms11896.
- Hygelund, Bretagne and Manga, Michael (2003). "Field measurements of drag coefficients for model large woody debris". In: *Geomorphology* 51.1, pp. 175–185. DOI: 10.1016/S0169-555X(02)00335-5.
- Iatrou, M., Ferentinis, G., Papatheodorou, G., Piper, David J. W., and Tripsanas, E. (2007). "Anthropogenic Turbidity Current Deposits In A Seismically Active Graben, The Gulf Of Corinth, Greece: A Useful Tool For Studying Turbidity Current Transport Processes". In: *Submarine Mass Movements and Their Consequences: 3 International Symposium*. Ed. by Vasilis Lykousis, Dimitris Sakellariou, and Jacques Locat. Dordrecht: Springer Netherlands, pp. 149–157.
- Inman, Douglas L, Nordstrom, Charles E, and Flick, Reinhard E (1976). "Currents in submarine canyons: An air-sea-land interaction". In: *Annual Review of Fluid Mechanics* 8.1, pp. 275–310.
- Islam, M. Ashraful and Imran, Jasim (2010). "Vertical structure of continuous release saline and turbidity currents". In: *Journal of Geophysical Research: Oceans* 115.C8. DOI: 10.1029/2009JC005365.
- Jarvis, P, Jefferson, B, Gregory, J, and Parsons, S A (2005). "A review of floc strength and breakage." In: *Water Res* 39.14, pp. 3121–3137. DOI: 10.1016/j.watres.2005.05.022.

- Jobe, Zane R, Howes, Nick C, and Auchter, Neal C (2016). “Comparing submarine and fluvial channel kinematics: Implications for stratigraphic architecture”. In: *Geology* 44.11, pp. 931–934. DOI: 10.1130/G38158.1.
- Kane, Ian A., Kneller, Benjamin C., Dykstra, Mason, Kassem, Ahmed, and McCaffrey, William D. (2007). “Anatomy of a submarine channel–levee: An example from Upper Cretaceous slope sediments, Rosario Formation, Baja California, Mexico”. In: *Marine and Petroleum Geology* 24.6, pp. 540–563. DOI: 10.1016/j.marpetgeo.2007.01.003.
- Kane, Ian A., Pontén, Anna S. M., Vangdal, Brita, Eggenhuisen, Joris T., Hodgson, David M., and Spychala, Yvonne T. (2017). “The stratigraphic record and processes of turbidity current transformation across deep-marine lobes”. In: *Sedimentology* 64.5, pp. 1236–1273. DOI: 10.1111/sed.12346.
- Kassem, Ahmed and Imran, Jasim (2001). “Simulation of turbid underflows generated by the plunging of a river”. In: *Geology* 29.7, pp. 655–658. DOI: 10.1130/0091-7613(2001)029<0655:SOTUGB>2.0.CO;2.
- Katayama, H. (1997). “Comparison between a laser diffraction-scattering method and a hydrometer method in the grain size analysis for fine-grained sediments”. In: *Journal of the Sedimentological Society of Japan* 46.46, pp. 23–30. DOI: 10.4096/jssj1995.46.23.
- Keevil, Gareth M., Peakall, Jeff, Best, James L., and Amos, Kathryn J. (2006). “Flow structure in sinuous submarine channels: Velocity and turbulence structure of an experimental submarine channel”. In: *Marine Geology* 229.3, pp. 241–257. DOI: 10.1016/j.margeo.2006.03.010.
- Kelly, R. W., Dorrell, R. M., Burns, A. D., and McCaffrey, W. D. (2019). “The Structure and Entrainment Characteristics of Partially Confined Gravity Currents”. In: *Journal of Geophysical Research: Oceans* 124.3, pp. 2110–2125. DOI: 10.1029/2018JC014042.
- Khripounoff, A., Crassous, P., Bue, N. Lo, Dennielou, B., and Jacinto, R. Silva (2012). “Different types of sediment gravity flows detected in the Var submarine canyon (northwestern Mediterranean Sea)”. In: *Progress in Oceanography* 106, pp. 138–153. DOI: 10.1016/j.pocean.2012.09.001.
- Kineke, G.C, Woolfe, K.J, Kuehl, S.A, Milliman, J.D, Dellapenna, T.M, and Purdon, R.G (2000). “Sediment export from the Sepik River, Papua New Guinea: evidence for a divergent sediment plume”. In: *Continental Shelf Research* 20.16, pp. 2239–2266. DOI: 10.1016/S0278-4343(00)00069-8.
- Knapp, Robert T. (1938). “Energy-balance in stream-flows carrying suspended load”. In: *Eos, Transactions American Geophysical Union* 19.1, pp. 501–505. DOI: 10.1029/TR019i001p00501.

- Kneller, B.C., Bennett, S.J., and McCaffrey, W.D. (1997). “Velocity and turbulence structure of density currents and internal solitary waves: potential sediment transport and the formation of wave ripples in deep water”. In: *Sedimentary Geology* 112.3, pp. 235–250.
- Kneller, Ben (1995). “Beyond the turbidite paradigm: physical models for deposition of turbidites and their implications for reservoir prediction”. In: *Geological Society, London, Special Publications* 94.1, pp. 31–49. DOI: 10.1144/GSL.SP.1995.094.01.04.
- (2003). “The influence of flow parameters on turbidite slope channel architecture”. In: *Marine and Petroleum Geology* 20.6, pp. 901–910. DOI: 10.1016/j.marpetgeo.2003.03.001.
- Kneller, Ben and Buckee, Clare (2000). “The structure and fluid mechanics of turbidity currents: a review of some recent studies and their geological implications”. In: *Sedimentology* 47.s1, pp. 62–94. DOI: 10.1046/j.1365-3091.2000.047s1062.x.
- Kneller, Benjamin, Nasr-Azadani, Mohamad M., Radhakrishnan, Senthil, and Meiburg, Eckart (2016). “Long-range sediment transport in the world’s oceans by stably stratified turbidity currents”. In: *Journal of Geophysical Research: Oceans* 121.12, pp. 8608–8620. DOI: 10.1002/2016JC011978.
- Kneller, Benjamin C., Bennett, Sean J., and McCaffrey, William D. (1999). “Velocity structure, turbulence and fluid stresses in experimental gravity currents”. In: *Journal of Geophysical Research: Oceans* 104.C3, pp. 5381–5391. DOI: 10.1029/1998JC900077.
- Kolla, V., Posamentier, H.W., and Wood, L.J. (2007). “Deep-water and fluvial sinuous channels—Characteristics, similarities and dissimilarities, and modes of formation”. In: *Marine and Petroleum Geology* 24.6, pp. 388–405. DOI: 10.1016/j.marpetgeo.2007.01.007.
- Koller, Debora, Manica, Rafael, Borges, Ana de Oliveira, and Fedele, Juan (2019). “Experimental bedforms by saline density currents”. In: *Brazilian Journal of Geology* 49. DOI: 10.1590/2317-4889201920180118.
- Komar, Paul D. (1985). “The hydraulic interpretation of turbidites from their grain sizes and sedimentary structures”. In: *Sedimentology* 32.3, pp. 395–407. DOI: 10.1111/j.1365-3091.1985.tb00519.x.
- Konert, Martin and Vandenberghe, Jef (1997). “Comparison of laser grain size analysis with pipette and sieve analysis: a solution for the underestimation of the clay fraction”. In: *Sedimentology* 44.3, pp. 523–535. DOI: 10.1046/j.1365-3091.1997.d01-38.x.
- Konsoer, Kory, Zinger, Jessica, and Parker, Gary (2013). “Bankfull hydraulic geometry of submarine channels created by turbidity currents: Relations between bankfull channel characteristics and formative flow discharge”. In: *Journal of Geophysical Research: Earth Surface* 118.1, pp. 216–228. DOI: 10.1029/2012JF002422.

- Kostaschuk, Ray, Nasr-Azadani, Mohamad M., Meiburg, Eckart, Wei, Taoyuan, Chen, Zhongyuan, Negretti, Maria Eletta, Best, Jim, Peakall, Jeff, and Parsons, Daniel R. (2018a). “On the Causes of Pulsing in Continuous Turbidity Currents”. In: *Journal of Geophysical Research: Earth Surface* 123.11, pp. 2827–2843. DOI: 10.1029/2018JF004719.
- (2018b). “On the Causes of Pulsing in Continuous Turbidity Currents”. In: *Journal of Geophysical Research: Earth Surface* 123.11, pp. 2827–2843. DOI: 10.1029/2018JF004719.
- Kostic, Svetlana (2011a). “Modeling of submarine cyclic steps: Controls on their formation, migration, and architecture”. In: *Geosphere* 7.2, pp. 294–304. DOI: 10.1130/GES00601.1.
- (2011b). “Modeling of submarine cyclic steps: Controls on their formation, migration, and architecture”. In: *Geosphere* 7.2, pp. 294–304. DOI: 10.1130/GES00601.1.
- Kostic, Svetlana and Parker, Gary (2006). “The response of turbidity currents to a canyon-fan transition: internal hydraulic jumps and depositional signatures”. In: *Journal of Hydraulic Research* 44.5, pp. 631–653. DOI: 10.1080/00221686.2006.9521713.
- Kostic, Svetlana, Sequeiros, Octavio, Spinewine, Benoit, and Parker, Gary (2010). “Cyclic steps: A phenomenon of supercritical shallow flow from the high mountains to the bottom of the ocean”. In: *Journal of Hydro-environment Research* 3.4, pp. 167–172. DOI: 10.1016/j.jher.2009.10.002.
- Kubo, Yu’suke, Syvitski, James P.M., Hutton, Eric W.H., and Paola, Chris (2005). “Advance and application of the stratigraphic simulation model 2D-SedFlux: From tank experiment to geological scale simulation”. In: *Sedimentary Geology* 178.3, pp. 187–195. DOI: 10.1016/j.sedgeo.2005.04.005.
- Kubo, Yu’suke and Nakajima, Takeshi (2002). “Laboratory experiments and numerical simulation of sediment-wave formation by turbidity currents”. In: *Marine Geology* 192.1, pp. 105–121. DOI: 10.1016/S0025-3227(02)00551-0.
- Lauder, Brian Edward and Sharma, BI (1974). “Application of the energy-dissipation model of turbulence to the calculation of flow near a spinning disc”. In: *Letters in heat and mass transfer* 1.2, pp. 131–137.
- Lavery, Andone C., Schmitt, Raymond W., and Stanton, Timothy K. (2003). “High-frequency acoustic scattering from turbulent oceanic microstructure: The importance of density fluctuations”. In: *The Journal of the Acoustical Society of America* 114.5, pp. 2685–2697. DOI: 10.1121/1.1614258.
- Leeuw, Jan de, Eggenhuisen, Joris T., and Cartigny, Matthieu J. B. (2018a). “Linking submarine channel-levee facies and architecture to flow structure of turbidity currents: insights from flume tank experiments”. In: *Sedimentology* 65.3, pp. 931–951. DOI: 10.1111/sed.12411.

- Leeuw, Jan de, Eggenhuisen, Joris T., Spychala, Yvonne T., Heijnen, Maarten S., Pohl, Florian, and Cartigny, Matthieu J.B. (2018b). “Sediment Volume and Grain-Size Partitioning Between Submarine Channel-Levee Systems and Lobes: An Experimental Study”. In: *Journal of Sedimentary Research* 88.7, pp. 777–794. DOI: 10.2110/jsr.2018.46.
- Lefauve, Adrien, Partridge, J. L., Zhou, Qi, Dalziel, S. B., Caulfield, C. P., and Linden, P. F. (2018). “The structure and origin of confined Holmboe waves”. In: *Journal of Fluid Mechanics* 848, pp. 508–544. DOI: 10.1017/jfm.2018.324.
- Liu, James T., Wang, Yu-Huai, Yang, Rick J., Hsu, Ray T., Kao, Shuh-Ji, Lin, Hui-Ling, and Kuo, Fang Hsu (2012). “Cyclone-induced hyperpycnal turbidity currents in a submarine canyon”. In: *Journal of Geophysical Research: Oceans* 117.C4. DOI: 10.1029/2011JC007630.
- Lloyd, C.J., Dorrell, R.M., and Caulfield, C.P. (2022). “The coupled dynamics of internal waves and hairpin vortices in stratified plane Poiseuille flow”. In: *Journal of Fluid Mechanics* 934, A10. DOI: 10.1017/jfm.2021.1007.
- Lopez, A, Gustavsson, H, and Korkiala-Tanttu, L (2021). “Comparison between hydrometer and laser diffraction methods in the determination of clay content in fine-grained soils”. In: *IOP Conference Series: Earth and Environmental Science* 710.1, p. 012012. DOI: 10.1088/1755-1315/710/1/012012.
- Lopez, M. (2001). “Architecture and depositional pattern of the Quaternary deep-sea fan of the Amazon”. In: *Marine and Petroleum Geology* 18.4, pp. 479–486. DOI: 10.1016/S0264-8172(00)00071-4.
- Lowe, Donald R (1982). “Sediment gravity flows; II, Depositional models with special reference to the deposits of high-density turbidity currents”. In: *Journal of sedimentary research* 52.1, pp. 279–297. DOI: 10.1306/212F7F31-2B24-11D7-8648000102C1865D.
- Lu, Ning, Ristow, Gerald H, and Likos, William J (2000). “The accuracy of hydrometer analysis for fine-grained clay particles”. In: *Geotechnical Testing Journal* 23.4, pp. 487–495.
- Luchi, R., Balachandar, S., Seminara, G., and Parker, G. (2018). “Turbidity Currents With Equilibrium Basal Driving Layers: A Mechanism for Long Runout”. In: *Geophysical Research Letters* 45.3, pp. 1518–1526. DOI: 10.1002/2017GL075608.
- Luchi, Rossella, Parker, Gary, Balachandar, S, and Naito, Kensuke (2015). “Mechanism Governing Continuous Long-Runout Turbidity Currents”. In: *Journal of Japan Society of Civil Engineers, Ser. B1 (Hydraulic Engineering)* 71. DOI: 10.2208/jscejhe.71.I_619.

- Lyn, D. A. (1988). “A similarity approach to turbulent sediment-laden flows in open channels”. In: *Journal of Fluid Mechanics* 193, pp. 1–26. DOI: 10.1017/S0022112088002034.
- Lynds, Ranie M., Mohrig, David, Hajek, Elizabeth A., and Heller, Paul L. (2014). “Paleoslope Reconstruction In Sandy Suspended-Load-Dominant Rivers”. In: *Journal of Sedimentary Research* 84.10, pp. 825–836. DOI: 10.2110/jsr.2014.60.
- Mansour, N., Kim, J., and Moin, P. (1989). “Near-wall k-epsilon turbulence modeling”. In: *AIAA Journal* 27.8, pp. 1068–1073. DOI: 10.2514/3.10222.
- Maren, D. S. van, Winterwerp, J. C., Wang, Z. Y., and Pu, Q. (2009). “Suspended sediment dynamics and morphodynamics in the Yellow River, China”. In: *Sedimentology* 56.3, pp. 785–806. DOI: 10.1111/j.1365-3091.2008.00997.x.
- Markatos, N.C. (1986). “The mathematical modelling of turbulent flows”. In: *Applied Mathematical Modelling* 10.3, pp. 190–220. DOI: 10.1016/0307-904X(86)90045-4.
- Marmoush, Yehia R., Smith, Alan A., and Hamblin, Paul F. (1984). “Pilot Experiments on Thermal Bar in Lock Exchange Flow”. In: *Journal of Energy Engineering* 110.3, pp. 215–227. DOI: 10.1061/(ASCE)0733-9402(1984)110:3(215).
- Marshall, C. R., Dorrell, R. M., Dutta, S., Keevil, G. M., Peakall, J., and Tobias, S. M. (2021a). “The effect of Schmidt number on gravity current flows: The formation of large-scale three-dimensional structures”. In: *Physics of Fluids* 33.10, p. 106601. DOI: 10.1063/5.0064386.
- Marshall, C. R., Dorrell, R. M., Keevil, G. M., Peakall, J., and Tobias, S. M. (2021b). “Observations of large-scale coherent structures in gravity currents: implications for flow dynamics”. In: *Experiments in Fluids* 62.6, p. 120. DOI: 10.1007/s00348-021-03217-4.
- Maslin, Mark, Knutz, Paul C., and Ramsay, Tony (2006). “Millennial-scale sea-level control on avulsion events on the Amazon Fan”. In: *Quaternary Science Reviews* 25.23, pp. 3338–3345. DOI: 10.1016/j.quascirev.2006.10.012.
- Mastbergen, Dick R. and Van Den Berg, Jan H. (2003). “Breaching in fine sands and the generation of sustained turbidity currents in submarine canyons”. In: *Sedimentology* 50.4, pp. 625–637. DOI: 10.1046/j.1365-3091.2003.00554.x.
- McCool, Wayne W. and Parsons, Jeffrey D. (2004). “Sedimentation from buoyant fine-grained suspensions”. In: *Continental Shelf Research* 24.10, pp. 1129–1142. DOI: 10.1016/j.csr.2004.03.009.

- Meiburg, Eckart and Kneller, Ben (2010a). “Turbidity Currents and Their Deposits”. In: *Annual Review of Fluid Mechanics* 42.1, pp. 135–156. DOI: 10.1146/annurev-fluid-121108-145618.
- (2010b). “Turbidity currents and their deposits”. In: *Annual Review of Fluid Mechanics* 42.1, pp. 135–156. DOI: 10.1146/annurev-fluid-121108-145618.
- Meiburg, Eckart, Radhakrishnan, Senthil, and Nasr-Azadani, Mohamad (2015). “Modeling Gravity and Turbidity Currents: Computational Approaches and Challenges”. In: *Applied Mechanics Reviews* 67.4, p. 040802. DOI: 10.1115/1.4031040.
- Mellor, George L. and Yamada, Tetsuji (1982). “Development of a turbulence closure model for geophysical fluid problems”. In: *Reviews of Geophysics* 20.4, pp. 851–875. DOI: 10.1029/RG020i004p00851.
- Menter, F. (1993). “Zonal Two Equation k-w Turbulence Models For Aerodynamic Flows”. In: *23rd Fluid Dynamics, Plasmadynamics, and Lasers Conference*. DOI: 10.2514/6.1993-2906.
- Menter, F. R. (1994). “Two-equation eddy-viscosity turbulence models for engineering applications”. In: *AIAA Journal* 32.8, pp. 1598–1605. DOI: 10.2514/3.12149.
- Menter, Florian R. (2009). “Review of the shear-stress transport turbulence model experience from an industrial perspective”. In: *International Journal of Computational Fluid Dynamics* 23.4, pp. 305–316. DOI: 10.1080/10618560902773387.
- Merzkirch, Wolfgang (1987). *Flow visualization*. Academic Press, New York.
- Michon, X., Goddet, J., and Bonnefille, R. (1955). *Etude theorique et experimentale des courants de densite*. Laboratoire national d’hydraulique.
- Middleton, G. V. (1966a). “Small-scale models of turbidity currents and the criterion for auto-suspension”. In: *Journal of Sedimentary Research* 36.1, pp. 202–208. DOI: 10.1306/74D71442-2B21-11D7-8648000102C1865D.
- Middleton, Gerard V. (1966b). “Experiments on density and turbidity currents: I. Motion of the head”. In: *Canadian Journal of Earth Sciences* 3.4, pp. 523–546. DOI: 10.1139/e66-038.
- (1966c). “Experiments on density and turbidity currents: II. Uniform flow of density currents”. In: *Canadian Journal of Earth Sciences* 3.5, pp. 627–637. DOI: 10.1139/e66-044.
- (1967). “Experiments on density and turbidity currents: III. Deposition of sediment”. In: *Canadian Journal of Earth Sciences* 4.3, pp. 475–505. DOI: 10.1139/e67-025.
- Migeon, Sébastien, Mulder, Thierry, Savoye, Bruno, and Sage, Françoise (2012). “Hydrodynamic processes, velocity structure and stratification in natural turbidity currents: Results inferred from field data in the

- Var Turbidite System”. In: *Sedimentary Geology* 245-246, pp. 48–62. DOI: <https://doi.org/10.1016/j.sedgeo.2011.12.007>.
- Miramontes, Elda, Eggenhuisen, Joris T., Jacinto, Ricardo Silva, Poneti, Giovanni, Pohl, Florian, Normandeau, Alexandre, Campbell, D. Calvin, and Hernández-Molina, F. Javier (2020). “Channel-levee evolution in combined contour current–turbidity current flows from flume-tank experiments”. In: *Geology* 48.4, pp. 353–357. DOI: 10.1130/G47111.1.
- Mohrig, David and Buttle, James (2007). “Deep turbidity currents in shallow channels”. In: *Geology* 35.2, pp. 155–158. DOI: 10.1130/G22716A.1.
- Moodie, Andrew J., Nittrouer, Jeffrey A., Ma, Hongbo, Carlson, Brandee N., Wang, Yuanjian, Lamb, Michael P., and Parker, Gary (2022). “Suspended Sediment-Induced Stratification Inferred From Concentration and Velocity Profile Measurements in the Lower Yellow River, China”. In: *Water Resources Research* 58.5, e2020WR027192. DOI: <https://doi.org/10.1029/2020WR027192>.
- Mueller, W.U., Garde, A.A., and Stendal, H. (2000). “Shallow-water, eruption-fed, mafic pyroclastic deposits along a Paleoproterozoic coastline: Kangerluluk volcano-sedimentary sequence, southeast Greenland”. In: *Precambrian Research* 101.2, pp. 163–192. DOI: 10.1016/S0301-9268(99)00087-X.
- Mueller, Wulf and White, James D.L. (1992). “Felsic fire-fountaining beneath Archean seas: pyroclastic deposits of the 2730 Ma Hunter Mine Group, Quebec, Canada”. In: *Journal of Volcanology and Geothermal Research* 54.1, pp. 117–134. DOI: 10.1016/0377-0273(92)90118-W.
- Mulder, T., Savoye, B., and Syvitski, J. P. M. (1997). “Numerical modelling of a mid-sized gravity flow: the 1979 Nice turbidity current (dynamics, processes, sediment budget and seafloor impact)”. In: *Sedimentology* 44.2, pp. 305–326. DOI: 10.1111/j.1365-3091.1997.tb01526.x.
- Mulder, Thierry and Alexander, Jan (2001). “The physical character of subaqueous sedimentary density flows and their deposits”. In: *Sedimentology* 48.2, pp. 269–299. DOI: 10.1046/j.1365-3091.2001.00360.x.
- Mulder, Thierry and Hüeneke, Heiko (2016). “Bouma Sequence”. In: *Encyclopedia of Marine Geosciences*, pp. 68–69. DOI: 10.1007/978-94-007-6238-1_135.
- Mulder, Thierry and Syvitski, James P. M. (1995). “Turbidity Currents Generated at River Mouths during Exceptional Discharges to the World Oceans”. In: *The Journal of Geology* 103.3, pp. 285–299. DOI: 10.1086/629747.

- Mulder, Thierry, Syvitski, James P.M., Migeon, Sébastien, Faugères, Jean-Claude, and Savoye, Bruno (2003). “Marine hyperpycnal flows: initiation, behavior and related deposits. A review”. In: *Marine and Petroleum Geology* 20.6, pp. 861–882. DOI: 10.1016/j.marpetgeo.2003.01.003.
- Mulder, Thierry, Syvitski, James PM, and Skene, Kenneth I (1998). “Modeling of erosion and deposition by turbidity currents generated at river mouths”. In: *Journal of Sedimentary Research* 68.1, pp. 124–137. DOI: 10.2110/jsr.68.124.
- Nakajima, Takeshi and Kneller, Benjamin C. (2013). “Quantitative analysis of the geometry of submarine external levées”. In: *Sedimentology* 60.4, pp. 877–910. DOI: 10.1111/j.1365-3091.2012.01366.x.
- Nakajima, Takeshi, Peakall, Jeffrey, McCaffrey, William D., Paton, Douglas A., and Thompson, Philip J. P. (2009). “Outer-Bank Bars: A New Intra-Channel Architectural Element within Sinuous Submarine Slope Channels”. In: *Journal of Sedimentary Research* 79.12, pp. 872–886. DOI: 10.2110/jsr.2009.094.
- Navier, C. L. M. H. (1823). “Mémoire sur les lois du mouvement des fluides”. In: *Mém. Acad. R. Sci. Inst. Fr.* VI, p. 389.
- Necker, F., Hartel, C., Kleiser, L., and Meiburg, E. (2005). “Mixing and dissipation in particle-driven gravity currents”. In: *Journal of Fluid Mechanics* 545, pp. 339–372. DOI: 10.1017/S0022112005006932.
- Necker, F., Härtel, C., Kleiser, L., and Meiburg, E. (2002). “High-resolution simulations of particle-driven gravity currents”. In: *International Journal of Multiphase Flow* 28.2, pp. 279–300.
- Nilsen, Tor Helge (2007). *Atlas of deep-water outcrops*. AAPG The American Association of Petroleum Geologists, p. 504.
- Nogueira, Helena I. S., Adduce, Claudia, Alves, Elsa, and Franca, Mario J. (2014). “Dynamics of the head of gravity currents”. In: *Environmental Fluid Mechanics* 14.2, pp. 519–540. DOI: 10.1007/s10652-013-9315-2.
- Nordin, Carl F and Dempster, George R (1963). *Vertical distribution of velocity and suspended sediment, Middle Rio Grande, New Mexico*. 462-B. US Government Printing Office. DOI: 10.3133/pp462B.
- Normark, William R and Piper, David JW (1991). “Initiation processes and flow evolution of turbidity currents: implications for the depositional record”. In: *SEPM Special Publication* 46, pp. 207–230.
- Osborn, T. R. (1980). “Estimates of the Local Rate of Vertical Diffusion from Dissipation Measurements”. In: *Journal of Physical Oceanography* 10.1, pp. 83–89. DOI: 10.1175/1520-0485(1980)010<0083:EOTLRO>2.0.CO;2.

- Packman, A.I. and Jerolmack, D. (2004). "The role of physicochemical processes in controlling sediment transport and deposition in turbidity currents". In: *Marine Geology* 204.1, pp. 1–9. DOI: 10.1016/S0025-3227(03)00359-1.
- Pantin, H.M. (1979). "Interaction between velocity and effective density in turbidity flow: Phase-plane analysis, with criteria for autosuspension". In: *Marine Geology* 31.1, pp. 59–99. DOI: 10.1016/0025-3227(79)90057-4.
- Pantin, Henry M. and Franklin, Mark C. (2009). "Predicting autosuspension in steady turbidity flow: Ignition points and their relation to Richardson numbers". In: *Journal of Sedimentary Research* 79.12, pp. 862–871. DOI: 10.2110/jsr.2009.095.
- Parker, G, Ashworth, PJ, Bennett, JL, Best, JL, and McLelland, SJ (1996). "Some speculations on the relation between channel morphology and channel-scale flow structures". In: *Coherent flow structures in open channels* 423.
- Parker, G., Garcia, M., Fukushima, Y., and Yu, W. (1987). "Experiments on turbidity currents over an erodible bed". In: *Journal of Hydraulic Research* 25.1, pp. 123–147. DOI: 10.1080/00221688709499292.
- Parker, Gary (1982). "Conditions for the ignition of catastrophically erosive turbidity currents". In: *Marine Geology* 46.3, pp. 307–327. DOI: 10.1016/0025-3227(82)90086-X.
- Parker, Gary, Fukushima, Yusuke, and Pantin, Henry M. (1986). "Self-accelerating turbidity currents". In: *Journal of Fluid Mechanics* 171, pp. 145–181. DOI: 10.1017/S0022112086001404.
- Parker, Gary, Seminara, Giovanni, and Solari, Luca (2003). "Bed load at low Shields stress on arbitrarily sloping beds: Alternative entrainment formulation". In: *Water Resources Research* 39.7. DOI: 10.1029/2001WR001253.
- Parsons, Jeffrey D., Bush, John W. M., and Syvitski, James P. M. (2001). "Hyperpycnal plume formation from riverine outflows with small sediment concentrations". In: *Sedimentology* 48.2, pp. 465–478. DOI: 10.1046/j.1365-3091.2001.00384.x.
- Parsons, Jeffrey D., Friedrichs, Carl T., Traykovski, Peter A., Mohrig, David, Imran, Jasim, Syvitski, James P. M., Parker, Gary, Puig, Pere, Buttle, James L., and García, Marcelo H. (2007). "The Mechanics of Marine Sediment Gravity Flows". In: *Continental Margin Sedimentation*. John Wiley & Sons, Ltd, pp. 275–337. DOI: 10.1002/9781444304398.ch6.
- Patacci, Marco, Houghton, Peter D.W., and Mccaffrey, William D. (2015). "Flow Behavior of Ponded Turbidity Currents". In: *Journal of Sedimentary Research* 85.8, pp. 885–902. DOI: 10.2110/jsr.2015.59.

- Patel, V. C., Rodi, W., and Scheuerer, G. (1985). "Turbulence models for near-wall and low Reynolds number flows - A review". In: *AIAA Journal* 23.9, pp. 1308–1319. DOI: 10.2514/3.9086.
- Paull, C.K., Caress, D.W., Lundsten, E., Gwiazda, R., Anderson, K., McGann, M., Conrad, J., Edwards, B., and Sumner, E.J. (2013). "Anatomy of the La Jolla Submarine Canyon system; offshore southern California". In: *Marine Geology* 335, pp. 16–34. DOI: 10.1016/j.margeo.2012.10.003.
- Paull, Charles K, Caress, David W, Ussler, William, Lundsten, Eve, and Meiner-Johnson, Melissa (2011). "High-resolution bathymetry of the axial channels within Monterey and Soquel submarine canyons, offshore central California". In: *Geosphere* 7.5, pp. 1077–1101. DOI: 10.1130/GES00636.1.
- Paull, Charles K, Ussler III, William, Caress, David W, Lundsten, Eve, Covault, Jacob A, Maier, Katherine L, Xu, Jingping, and Augenstein, Sean (2010). "Origins of large crescent-shaped bedforms within the axial channel of Monterey Canyon, offshore California". In: *Geology* 6.6, pp. 755–774. DOI: 10.1130/GES00527.1.
- Peakall, Jeff, McCaffrey, Bill, and Kneller, Ben (2000). "A process model for the evolution, morphology, and architecture of sinuous submarine channels". In: *Journal of Sedimentary Research* 70.3, p. 434. DOI: 10.1306/2DC4091C-0E47-11D7-8643000102C1865D.
- Peakall, Jeff and Sumner, Esther J. (2015). "Submarine channel flow processes and deposits: A process-product perspective". In: *Geomorphology* 244, pp. 95–120. DOI: 10.1016/j.geomorph.2015.03.005.
- Peltier, W. R. and Caulfield, C. P. (2003). "Mixing efficiency in stratified shear flows". In: *Annual Review of Fluid Mechanics* 35.1, pp. 135–167. DOI: 10.1146/annurev.fluid.35.101101.161144.
- Picot, M., Droz, L., Marsset, T., Dennielou, B., and Bez, M. (2016). "Controls on turbidite sedimentation: Insights from a quantitative approach of submarine channel and lobe architecture (Late Quaternary Congo Fan)". In: *Marine and Petroleum Geology* 72, pp. 423–446. DOI: 10.1016/j.marpetgeo.2016.02.004.
- Picot, M., Marsset, T., Droz, L., Dennielou, B., Baudin, F., Hermoso, M., de Rafelis, M., Sionneau, T., Cremer, M., Laurent, D., and Bez, M. (2019). "Monsoon control on channel avulsions in the Late Quaternary Congo Fan". In: *Quaternary Science Reviews* 204, pp. 149–171. DOI: 10.1016/j.quascirev.2018.11.033.
- Piper, D. J. W (1978). "Turbidite muds and silts on deepsea fans and abyssal plains". In: *Sedimentation in submarine canyons, fans, and trenches*.
- Piper, David J. W., Cochonat, Pierre, and Morrison, Martin L. (1999). "The sequence of events around the epicentre of the 1929 Grand Banks earthquake: initiation of debris flows and turbidity current inferred from sidescan sonar". In: *Sedimentology* 46.1, pp. 79–97. DOI: 10.1046/j.1365-3091.1999.00204.x.

- Piper, David J. W. and Savoye, Bruno (1993). "Processes of late Quaternary turbidity current flow and deposition on the Var deep-sea fan, north-west Mediterranean Sea". In: *Sedimentology* 40.3, pp. 557–582. DOI: 10.1111/j.1365-3091.1993.tb01350.x.
- Piper, David JW and Normark, William R (2009). "Processes that initiate turbidity currents and their influence on turbidites: a marine geology perspective". In: *Journal of Sedimentary Research* 79.6, pp. 347–362.
- Pittaluga, M. Bolla and Imran, J. (2014). "A simple model for vertical profiles of velocity and suspended sediment concentration in straight and curved submarine channels". In: *Journal of Geophysical Research: Earth Surface* 119 (3), pp. 483–503. DOI: 10.1002/2013JF002812.
- Pohl, Florian, Eggenhuisen, Joris T., Kane, Ian A., and Clare, Michael A. (2020). "Transport and Burial of Microplastics in Deep-Marine Sediments by Turbidity Currents". In: *Environmental Science and Technology* 54.7, pp. 4180–4189. DOI: 10.1021/acs.est.9b07527.
- Pope, N.D., Widdows, J., and Brinsley, M.D. (2006). "Estimation of bed shear stress using the turbulent kinetic energy approach—comparison of annular flume and field data". In: *Continental Shelf Research* 26.8, pp. 959–970. DOI: 10.1016/j.csr.2006.02.010.
- Pope, Stephen B. (2000). *Turbulent Flows*. Cambridge University Press. DOI: 10.1017/CB09780511840531.
- Postma, George and Cartigny, Matthieu JB (2014). "Supercritical and subcritical turbidity currents and their deposits—A synthesis". In: *Geology* 42.11, pp. 987–990. DOI: 10.1130/G35957.1.
- Postma, George, Nemeč, Wojciech, and Kleinspehn, Karen L. (1988). "Large floating clasts in turbidites: a mechanism for their emplacement". In: *Sedimentary Geology* 58.1, pp. 47–61.
- Prandtl, L. (1925). "Bericht über Untersuchungen zur ausgebildeten Turbulenz". In: *Z. Angew. Math. Mech.* 5, pp. 136–139.
- Pratson, LE, Imran, Jasim, Parker, Gary, Syvitski, James PM, and Hutton, Eric (2000). "Debris flows vs. turbidity currents: a modeling comparison of their dynamics and deposits". In: *Special Publication-SEPM* 68, pp. 57–72.
- Rastogi, Ashok K. and Rodi, Wolfgang (1978). "Predictions of Heat and Mass Transfer in Open Channels". In: *Journal of the Hydraulics Division* 104.3, pp. 397–420. DOI: 10.1061/JYCEAJ.0004962.
- Rijn, Leo C. van (1984). "Sediment Transport, Part II: Suspended Load Transport". In: *Journal of Hydraulic Engineering* 110.11, pp. 1613–1641. DOI: 10.1061/(ASCE)0733-9429(1984)110:11(1613).

- Rothwell, RG, Thomson, J, and Kähler, G (1998). “Low-sea-level emplacement of a very large Late Pleistocene ‘megaturbidite’ in the western Mediterranean Sea”. In: *Nature* 392.6674, p. 377. DOI: 10.1038/32871.
- Rouse, Hunter (1937). “Modern conceptions of the mechanics of fluid turbulence”. In: *Trans ASCE* 102, pp. 463–505.
- (1939). “An analysis of sediment transportation in the light of fluid turbulence”. In: *United States Department of Agriculture. Soil Conservation Services Report*.
- Rozovskii, IL (1957). “Flow of Water in Bends of Open Channels, Acad. of Sci. of the Ukr”. In: *SSR, Kiev*, p. 233.
- Ryan, William B F and Heezen, Bruce C (1965). “Ionian Sea submarine canyons and the 1908 Messina turbidity current”. In: *Geological Society of America Bulletin* 76.8, pp. 915–932. DOI: 10.1130/0016-7606(1965)76[915:ISSCAT]2.0.CO;2.
- Salinas, Jorge S., Balachandar, S., Shringarpure, M., Fedele, J., Hoyal, D., Zuñiga, S., and Cantero, M. I. (2021). “Anatomy of subcritical submarine flows with a lutocline and an intermediate destruction layer”. In: *Nature Communications* 12 (1), p. 1649. DOI: 10.1038/s41467-021-21966-y.
- Sequeiros, Octavio E., Mosquera, Rodrigo, and Pedocchi, Francisco (2018). “Internal Structure of a Self-Accelerating Turbidity Current”. In: *Journal of Geophysical Research: Oceans* 123.9, pp. 6260–6276. DOI: 10.1029/2018JC014061.
- Sequeiros, Octavio E., Naruse, Hajime, Endo, Noritaka, Garcia, Marcelo H., and Parker, Gary (2009). “Experimental study on self-accelerating turbidity currents”. In: *Journal of Geophysical Research: Oceans* 114.C5. DOI: 10.1029/2008JC005149.
- Sequeiros, Octavio E., Spinewine, Benoit, Beaubouef, Rick T., Sun, Tao, Garcia, Marcelo H., and Parker, Gary (2010a). “Bedload transport and bed resistance associated with density and turbidity currents”. In: *Sedimentology* 57.6, pp. 1463–1490. DOI: 10.1111/j.1365-3091.2010.01152.x.
- (2010b). “Characteristics of Velocity and Excess Density Profiles of Saline Underflows and Turbidity Currents Flowing over a Mobile Bed”. In: *Journal of Hydraulic Engineering* 136.7, pp. 412–433. DOI: 10.1061/(ASCE)HY.1943-7900.0000200.
- Shimizu, Hiroyuki A., Koyaguchi, Takehiro, and Suzuki, Yujiro J. (2019). “The run-out distance of large-scale pyroclastic density currents: A two-layer depth-averaged model”. In: *Journal of Volcanology and Geothermal Research* 381, pp. 168–184. DOI: 10.1016/j.jvolgeores.2019.03.013.

- Simmons, S. M., Azpiroz-Zabala, M., Cartigny, M. J.B., Clare, M. A., Cooper, C., Parsons, D. R., Pope, E. L., Sumner, E. J., and Talling, P. J. (2020). “Novel Acoustic Method Provides First Detailed Measurements of Sediment Concentration Structure Within Submarine Turbidity Currents”. In: *Journal of Geophysical Research: Oceans* 125.5. DOI: 10.1029/2019JC015904.
- Simpson, J. E. (1997). *Gravity Currents in the Environment and the Laboratory*. 2nd ed. Cambridge University Press, pp. 1–3.
- Simpson, J. E. and Britter, R. E. (1979). “The dynamics of the head of a gravity current advancing over a horizontal surface”. In: *Journal of Fluid Mechanics* 94.3, pp. 477–495. DOI: 10.1017/S0022112079001142.
- Simpson, John E. (1972). “Effects of the lower boundary on the head of a gravity current”. In: *Journal of Fluid Mechanics* 53.4, pp. 759–768. DOI: 10.1017/S0022112072000461.
- Skene, Kenneth I., Mulder, Thierry, and Syvitski, James P.M. (1997). “INFLO1: A model predicting the behaviour of turbidity currents generated at river mouths”. In: *Computers & Geosciences* 23.9, pp. 975–991. DOI: 10.1016/S0098-3004(97)00064-2.
- Skene, Kenneth I., Piper, David J. W., and Hill, Paul S. (2002). “Quantitative analysis of variations in depositional sequence thickness from submarine channel levees”. In: *Sedimentology* 49.6, pp. 1411–1430. DOI: 10.1046/j.1365-3091.2002.00506.x.
- Smellie, J. L. and Hole, M. J. (1997). “Products and processes in Pliocene–Recent, subaqueous to emergent volcanism in the Antarctic Peninsula: examples of englacial Surtseyan volcano construction”. In: *Bulletin of Volcanology* 58.8, pp. 628–646. DOI: 10.1007/s004450050167.
- Smellie, J.L. (1999). “Lithostratigraphy of Miocene–Recent, alkaline volcanic fields in the Antarctic Peninsula and eastern Ellsworth Land”. In: *Antarctic Science* 11.3, pp. 362–378. DOI: 10.1017/S0954102099000450.
- Smith, Douglas P, Ruiz, Genoveva, Kvittek, Rikk, and Iampietro, Pat J (2005). “Semiannual patterns of erosion and deposition in upper Monterey Canyon from serial multibeam bathymetry”. In: *GSA Bulletin* 117.9-10, pp. 1123–1133. DOI: 10.1130/B25510.1.
- Smith, Douglas P., Kvittek, Rikk, Iampietro, Pat J., and Wong, Kendra (2007). “Twenty-nine months of geomorphic change in upper Monterey Canyon (2002–2005)”. In: *Marine Geology* 236.1, pp. 79–94. DOI: 10.1016/j.margeo.2006.09.024.
- Smith, J.D. and Hopkins, T.S. (1971). “Sediment transport on the continental shelf off of Washington and Oregon in light of recent current measurements.” In: pp. 143–179.
- Soulsby, Richard (1997). *Dynamics of marine sands*. T. Telford London.

- Spalart, P.R. and Allmaras, S.R. (1994). “One-equation turbulence model for aerodynamic flows”. In: *Recherche aerospatiale* 1, pp. 5–21.
- Stacey, Michael W. and Bowen, Anthony J. (1988a). “The vertical structure of density and turbidity currents: Theory and observations”. In: *Journal of Geophysical Research: Oceans* 93.C4, pp. 3528–3542. DOI: 10.1029/JC093iC04p03528.
- (1988b). “The vertical structure of turbidity currents and a necessary condition for self-maintenance”. In: *Journal of Geophysical Research: Oceans* 93.C4, pp. 3543–3553. DOI: 10.1029/JC093iC04p03543.
- (1990). “A comparison of an autosuspension criterion to field observations of five turbidity currents”. In: *Sedimentology* 37.1, pp. 1–5. DOI: 10.1111/j.1365-3091.1990.tb01979.x.
- Stokes, G. G. (1845). “On the theories of the internal friction of fluids in motion and of the equilibrium and motion of elastic solids”. In: *Trans. Cambridge Philos. Soc.* 8, pp. 287–319.
- Stow, Dorrik A.V and Mayall, Mike (2000). “Deep-water sedimentary systems: New models for the 21st century”. In: *Marine and Petroleum Geology* 17.2, pp. 125–135. DOI: 10.1016/S0264-8172(99)00064-1.
- Stow, Dorrik A.V. and Shanmugam, Ganapathy (1980). “Sequence of structures in fine-grained turbidites: Comparison of recent deep-sea and ancient flysch sediments”. In: *Sedimentary Geology* 25.1, pp. 23–42. DOI: 10.1016/0037-0738(80)90052-4.
- Straub, Kyle M, Mohrig, David, McElroy, Brandon, Buttles, James, and Pirmez, Carlos (2008). “Interactions between turbidity currents and topography in aggrading sinuous submarine channels: A laboratory study”. In: *GSA Bulletin* 120.3-4, pp. 368–385. DOI: 10.1130/B25983.1.
- Straub, Kyle M., Mohrig, David, Buttles, James, McElroy, Brandon, and Pirmez, Carlos (2011). “Quantifying the influence of channel sinuosity on the depositional mechanics of channelized turbidity currents: A laboratory study”. In: *Marine and Petroleum Geology* 28.3, pp. 744–760. DOI: 10.1016/j.marpetgeo.2010.05.014.
- Sumner, E. J., Peakall, J., Dorrell, R. M., Parsons, D. R., Darby, S. E., Wynn, R. B., McPhail, S. D., Perrett, J., Webb, A., and White, D. (2014). “Driven around the bend: Spatial evolution and controls on the orientation of helical bend flow in a natural submarine gravity current”. In: *Journal of Geophysical Research: Oceans* 119.2, pp. 898–913. DOI: 10.1002/2013JC009008.
- Sun, Tao and Parker, Gary (2005). “Transportational cyclic steps created by flow over an erodible bed. Part 2. Theory and numerical simulation”. In: *Journal of Hydraulic Research* 43.5, pp. 502–514. DOI: 10.1080/00221680509500148.

- Talling, P. J., Amy, L. A., Wynn, R. B., Peakall, J., and Robinson, M. (2004). "Beds comprising debrite sandwiched within co-genetic turbidite: origin and widespread occurrence in distal depositional environments". In: *Sedimentology* 51.1, pp. 163–194. DOI: 10.1111/j.1365-3091.2004.00617.x.
- Talling, Peter J., Allin, Joshua, Armitage, Dominic A., Arnott, Robert W.C., Cartigny, Matthieu J.B., Clare, Michael A., Felletti, Fabrizio, Covault, Jacob A., Girardclos, Stephanie, Hansen, Ernst, Hill, Philip R., Hiscott, Richard N., Hogg, Andrew J., Clarke, John Hughes, Jobe, Zane R., Malgesini, Giuseppe, Mozzato, Alessandro, Naruse, Hajime, Parkinson, Sam, Peel, Frank J., Piper, David J.W., Pope, Ed, Postma, George, Rowley, Pete, Sguazzini, Andrea, Stevenson, Christopher J., Sumner, Esther J., Sylvester, Zoltan, Watts, Camilla, and Xu, Jingping (2015). "Key Future Directions For Research On Turbidity Currents and Their Deposits". In: *Journal of Sedimentary Research* 85.2, pp. 153–169. DOI: 10.2110/jsr.2015.03.
- Talling, Peter J., Masson, Douglas G., Sumner, Esther J., and Malgesini, Giuseppe (2012). "Subaqueous sediment density flows: Depositional processes and deposit types". In: *Sedimentology* 59.7, pp. 1937–2003. DOI: 10.1111/j.1365-3091.2012.01353.x.
- Talling, Peter. J., Paull, Charles K., and Piper, David J.W. (2013). "How are subaqueous sediment density flows triggered, what is their internal structure and how does it evolve? Direct observations from monitoring of active flows". In: *Earth-Science Reviews* 125, pp. 244–287. DOI: 10.1016/j.earscirev.2013.07.005.
- Talling, PJ, Wynn, RB, Masson, DG, Frenz, M, Cronin, BT, Schiebel, Ralf, Akhmetzhanov, AM, Dallmeier-Tiessen, S, Benetti, S, Weaver, PPE, et al. (2007). "Onset of submarine debris flow deposition far from original giant landslide". In: *Nature* 450.7169, p. 541. DOI: 10.1038/nature06313.
- Tesaker, Einar (1969). "Uniform turbidity current experiments". PhD dissertation. The Technical University of Norway.
- Thorpe, S. A. (2010). "Turbulent hydraulic jumps in a stratified shear flow". In: *Journal of Fluid Mechanics* 654, pp. 305–350. DOI: 10.1017/S0022112010000625.
- Thorpe, S. A. and Li, Lin (2014). "Turbulent hydraulic jumps in a stratified shear flow. Part 2". In: *Journal of Fluid Mechanics* 758, pp. 94–120. DOI: 10.1017/jfm.2014.502.
- Tilston, Mike, Arnott, Richard WC, Rennie, Colin D, and Long, Bernard (2015). "The influence of grain size on the velocity and sediment concentration profiles and depositional record of turbidity currents". In: *Geology* 43.9, pp. 839–842. DOI: 10.1130/G37069.1.
- Toniolo, Horacio, Lamb, Michael, and Parker, Gary (2006a). "Depositional turbidity currents in diapiric minibasins on the continental slope: formulation and theory". In: *Journal of Sedimentary Research* 76.5, pp. 783–797.

- Toniolo, Horacio, Parker, Gary, and Voller, Vaughan (2007). "Role of Ponded Turbidity Currents in Reservoir Trap Efficiency". In: *Journal of Hydraulic Engineering* 133.6, pp. 579–595. DOI: 10.1061/(ASCE)0733-9429(2007)133:6(579).
- Toniolo, Horacio, Parker, Gary, Voller, Vaughan, and Beaubouef, RT (2006b). "Depositional turbidity currents in diapiric minibasins on the continental slope: experiments—numerical simulation and upscaling". In: *Journal of Sedimentary Research* 76.5, pp. 798–818.
- Traer, M. M., Fildani, A., McHargue, T., and Hilley, G. E. (2015). "Simulating depth-averaged, one-dimensional turbidity current dynamics using natural topographies". In: *Journal of Geophysical Research: Earth Surface* 120.8, pp. 1485–1500. DOI: 10.1002/2015JF003638.
- Ungarish, Marius and Hogg, Andrew J. (2018). "Models of internal jumps and the fronts of gravity currents: unifying two-layer theories and deriving new results". In: *Journal of Fluid Mechanics* 846, pp. 654–685. DOI: 10.1017/jfm.2018.219.
- Van Den Berg, Jan H., Van Gelder, André, and Mastbergen, Dick R. (2002). "The importance of breaching as a mechanism of subaqueous slope failure in fine sand". In: *Sedimentology* 49.1, pp. 81–95. DOI: 10.1111/j.1525-139X.2006.00168.x-i1.
- Van Maren, D. S., Winterwerp, J. C., Wang, Z. Y., and Pu, Q. (2009). "Suspended sediment dynamics and morphodynamics in the Yellow River, China". In: *Sedimentology* 56.3, pp. 785–806. DOI: 10.1111/j.1365-3091.2008.00997.x.
- van Maren, D.S. (2007). "Grain size and sediment concentration effects on channel patterns of silt-laden rivers". In: *Sedimentary Geology* 202.1, pp. 297–316. DOI: 10.1016/j.sedgeo.2007.04.001.
- Vanoni, Vito A. (1946). "Transportation of Suspended Sediment by Water". In: *Transactions of the American Society of Civil Engineers* 111.1, pp. 67–102. DOI: 10.1061/TACEAT.0005975.
- Vanoni, Vito A. and Nomicos, George N. (1960). "Resistance Properties Of Sediment-Laden Streams". In: *Transactions of the American Society of Civil Engineers* 125.1, pp. 1140–1167. DOI: 10.1061/TACEAT.0007902.
- Varjavand, Peyman, Ghomeshi, Mehdi, Dalir, Ali Hosseinzadeh, Farsadizadeh, Davood, and Gorgij, Alireza Docheshmeh (2015). "Experimental observation of saline underflows and turbidity currents, flowing over rough beds". In: *Canadian Journal of Civil Engineering* 42.11, pp. 834–844. DOI: 10.1139/cjce-2014-0537.
- Velikanov, M.A. (1954). "Gravitational theory of sediment transport". In: *J. Sci. Soviet Union* 4.

- Velikanov, MA et al. (1954). “Gravitational theory of sediment transport”. In: *Journal of Science of the Soviet Union, Geophysics* 4.GTS translation 62-15004.
- Vitton, Stanley J and Sadler, Leon Y (1997). “Particle-size analysis of soils using laser light scattering and X-ray absorption technology”. In: *Geotechnical Testing Journal* 20.1, pp. 63–73.
- Von Karman, Th. (1930). “Mechanische Ahnlichkeit und Turbulenz”. In: *Math. -Phys. Klasse*.
- Von Karman, Théodore et al. (1940). “The engineer grapples with nonlinear problems”. In: *Bulletin of the American Mathematical Society* 46.8, pp. 615–683.
- Vrolijk, Peter and Southard, John (1997). “Experiments on Rapid Deposition of Sand from High-velocity Flows”. In: *Geoscience Canada* 24.1.
- Walker, R. G. (1965). “The origin and significance of the internal sedimentary structures of turbidites”. In: *Proceedings of the Yorkshire Geological Society* 35.1, pp. 1–32. DOI: 10.1144/pygs.35.1.1.
- Wan, Z. H. and Wang, Z. Y. (1994a). “Hyperconcentrated flow, IAHR monograph series”. In: *Balkema: Rotterdam*.
- Wan, Zhaohin and Wang, Zhaoyin (1994b). “Hyperconcentrated Flow”. In: *Journal of Hydraulic Engineering* 120.10, pp. 1234–1234. DOI: 10.1061/(ASCE)0733-9429(1994)120:10(1234).
- Weimer, Paul and Buffler, Richard T (1988). “Distribution and seismic facies of Mississippi fan channels”. In: *Geology* 16.10, pp. 900–903. DOI: 10.1130/0091-7613(1988)016<0900:DASFOM>2.3.CO;2.
- Weimer, Paul and Link, Martin H. (1991). “Global Petroleum Occurrences in Submarine Fans and Turbidite Systems”. In: *Seismic Facies and Sedimentary Processes of Submarine Fans and Turbidite Systems*. Ed. by Paul Weimer and Martin H. Link. New York, NY: Springer New York. DOI: 10.1007/978-1-4684-8276-8_2.
- Weimer, Paul, Slatt, Roger M, Bouroullec, Renaud, et al. (2007). *Introduction to the petroleum geology of deepwater setting*. Vol. 111. AAPG/Datapages Tulsa.
- Wells, M. G. and Dorrell, R. M. (2021). “Turbulence Processes Within Turbidity Currents”. In: *Annual Review of Fluid Mechanics* 53.1. DOI: 10.1146/annurev-fluid-010719-060309.
- White, James D. L. (1996). “Pre-emergent construction of a lacustrine basaltic volcano, Pahvant Butte, Utah (USA)”. In: *Bulletin of Volcanology* 58.4, pp. 249–262. DOI: 10.1007/s004450050138.
- White, JDL and Houghton, B (2000). “Surtseyan and related phreatomagmatic eruptions”. In: *Encyclopedia of volcanoes*. Academic, San Diego, pp. 495–513.

- Wilcox, David C. (1988). "Reassessment of the scale-determining equation for advanced turbulence models". In: *AIAA Journal* 26.11, pp. 1299–1310. DOI: 10.2514/3.10041.
- Wright, L. D. (1977). "Sediment transport and deposition at river mouths: A synthesis". In: *GSA Bulletin* 88.6, pp. 857–868. DOI: 10.1130/0016-7606(1977)88<857:STADAR>2.0.CO;2.
- Wynn, Russell B, Piper, David J.W, and Gee, Martin J.R (2002a). "Generation and migration of coarse-grained sediment waves in turbidity current channels and channel-lobe transition zones". In: *Marine Geology* 192.1, pp. 59–78. DOI: 10.1016/S0025-3227(02)00549-2.
- Wynn, Russell B., Cronin, Bryan T., and Peakall, Jeff (2007). "Sinuous deep-water channels: Genesis, geometry and architecture". In: *Marine and Petroleum Geology* 24.6, pp. 341–387. DOI: 10.1016/j.marpetgeo.2007.06.001.
- Wynn, Russell B., Kenyon, Neil H., Masson, Douglas G., Stow, Dorrik A. V., and Weaver, Philip P. E. (2002b). "Characterization and Recognition of Deep-Water Channel-Lobe Transition Zones". In: *AAPG Bulletin* 86.8, pp. 1441–1462. DOI: 10.1306/61EEDCC4-173E-11D7-8645000102C1865D.
- Wynn, Russell B., Weaver, Philip P. E., Masson, Douglas G., and Stow, Dorrik A. V. (2002c). "Turbidite depositional architecture across three interconnected deep-water basins on the north-west African margin". In: *Sedimentology* 49.4, pp. 669–695. DOI: 10.1046/j.1365-3091.2002.00471.x.
- Xu, J. P., Noble, M. A., and Rosenfeld, L. K. (2004). "In-situ measurements of velocity structure within turbidity currents". In: *Geophysical Research Letters* 31.9. DOI: 10.1029/2004GL019718.
- Xu, J.P., Swarzenski, Peter W., Noble, Marlene, and Li, An-Chun (2010). "Event-driven sediment flux in Hueneme and Mugu submarine canyons, southern California". In: *Marine Geology* 269.1, pp. 74–88. DOI: 10.1016/j.margeo.2009.12.007.
- Xu, J.P., Wong, Florence L., Kvitek, Rikk, Smith, Douglas P., and Paull, Charles K. (2008). "Sandwave migration in Monterey Submarine Canyon, Central California". In: *Marine Geology* 248.3, pp. 193–212. DOI: 10.1016/j.margeo.2007.11.005.